

**UNIVERSIDAD COMPLUTENSE DE MADRID**

FACULTAD DE INFORMÁTICA

Departamento de Ingeniería del Software e Inteligencia Artificial



**TESIS DOCTORAL**

**Técnicas de minería de datos para una base de datos masivas:  
una aplicación a los dispositivos de fusión JET y TJ-II**

**Data mining techniques for massive databases : an application  
to JET and TJ-II fusion devices**

MEMORIA PARA OPTAR AL GRADO DE DOCTOR

PRESENTADA POR

Sergio González Sanz

Directores

Jesús A. Vega Sánchez  
Gonzalo Pajares Martinsanz

**Madrid, 2013**

---

Técnicas de Minería de Datos para Bases de  
Datos Masivas: una Aplicación a los  
Dispositivos de Fusión JET y TJ-II

Data Mining Techniques for Massive Databases:  
an Application to JET and TJ-II Fusion Devices

---

**Ciemat**  
Centro de Investigaciones  
Energéticas, Medioambientales  
y Tecnológicas



Tesis Doctoral / PhD Thesis

Sergio González Sanz

•

Dirigida por / Supervised by

Dr. Jesús A. Vega Sánchez

Dr. Gonzalo Pajares Martinsanz

•

Grupo de Adquisición de Datos del TJ-II

Laboratorio Nacional de Fusión

Centro de Investigaciones Energéticas, Medioambientales y  
Tecnológicas (CIEMAT)

•

Departamento de Ingeniería del Software e Inteligencia Artificial

Facultad de Informática

Universidad Complutense de Madrid (UCM)

•

2012



**Técnicas de Minería de Datos para  
Bases de Datos Masivas: una  
Aplicación a los Dispositivos de  
Fusión JET y TJ-II**

**Data Mining Techniques for Massive  
Databases: an Application to JET  
and TJ-II Fusion Devices**

*Memoria presentada para obtener el título de Doctor por  
Dissertation submitted to obtain the Ph. D. Degree by*

**Sergio González Sanz**

*Dirigida por / Supervised by*

**Dr. Jesús A. Vega Sánchez  
Dr. Gonzalo Pajares Martinsanz**

**Grupo de Adquisición de Datos del TJ-II  
Laboratorio Nacional de Fusión  
Centro de Investigaciones Energéticas, Medioambientales y  
Tecnológicas (CIEMAT)**

•

**Departamento de Ingeniería del Software e Inteligencia  
Artificial**

**Facultad de Informática  
Universidad Complutense de Madrid (UCM)**

•

**2012**



*To everyone with a challenge ahead*



*It would appear that we have reached the  
limits of what it is possible to achieve  
with computer technology, although one  
should be careful with such statements, as  
they tend to sound pretty silly in 5 years*

John von Neumann



# Agradecimientos

Tras cuatro años trabajando en esta tesis, resulta complicado condensar mis agradecimientos a todas aquellas personas que me ha apoyado durante este tiempo, tanto en los buenos como en los malos momentos. Sin ellos, esta tesis jamás hubiera llegado a realizarse.

En primer lugar, quiero agradecerle al Dr. Jesús A. Vega haberme dado la oportunidad de descubrir el mundo de la investigación, compartir sus conocimientos conmigo y alentarme durante estos cuatro años para que esta tesis saliese adelante. Sin su inestimable ayuda y constancia, esta tesis no hubiera sido posible por lo que gran parte del mérito es suyo.

En segundo lugar, me gustaría dar las gracias al Dr. Gonzalo Pajares, quien me puso tras la pista de la beca FPI que me permitió realizar esta tesis. Además quiero reconocer su plena disponibilidad y conocimientos siempre que he necesitado su ayuda.

También quiero reconocer la gran ayuda que me ha prestado durante este tiempo el Dr. Andrea Murari. Sin él, el trabajo en el JET hubiera sido mucho más arduo y las estancias que realicé allí probablemente no hubiesen sido posibles. Asimismo, quiero destacar al Dr. Sebastián Dormido Canto con quien he compartido ideas y experiencias.

Por otra parte, quiero reconocer aquí a varios profesores de la Universidad Complutense de Madrid con los que, en distintos momentos del proceso que me llevó a escribir esta tesis, he tenido el honor de trabajar. Se trata del Dr. Jesús Manuel de la Cruz con quien tuve el placer de realizar el proyecto de fin de carrera y de los Drs. Belén Díaz y Juan Antonio Recio quienes me guiaron durante la realización del proyecto del máster de investigación. Sin ellos tampoco podría estar ahora escribiendo estas líneas.

Otra parte de esta tesis se la debo a las personas que han compartido el día a día conmigo. Se trata de los miembros del *Grupo de Adquisición de Datos* del TJ-II: Ana Belén Portas, Augusto Pereira, el Dr. Rodrigo Castro y Raúl Moreno. Ellos me han demostrado su valía y me han enseñado que todo es más fácil trabajando juntos.

Me gustaría también destacar a mis amigos dentro del CIEMAT: Pablo Blazquez, Eduardo Mejuto, Esther Montes, Beatriz Romo y Andrés Yuste. Con ellos he compartido buenos momentos y me han prestado su apoyo siem-

pre que lo he necesitado. Tampoco puedo olvidarme de mis amigos de Soria, con quienes siempre puedo contar para lo que necesite: Ana Belén Abad, Javier Asensio, Víctor Cervero, María Domínguez, Elisa Jimeno, Eleazar Ortega, Carmen Ovejero, María Pastora, Nerea Rodríguez y Andrés Vergara. Sin ellos, regresar cada fin de semana a Soria no sería lo mismo.

También debo dar las gracias a Marco Antonio Gómez y Pedro Pablo Gómez, autores de la plantilla  $\text{T}_{\text{E}}\text{X}_{\text{I}}\text{S}$  v.1.0+ con la que ha sido maquetada esta tesis. Recomiendo encarecidamente a todo el mundo que se disponga a escribir una tesis, incluso a aquellos que no conozcan  $\text{L}^{\text{A}}\text{T}_{\text{E}}\text{X}$ , su uso.

Y por último, y especialmente, quiero agradecer a mi familia haberme dado todo lo que tengo: mis padres Gloria y Odorcio, mi hermana Marta, y Ana, mi novia, quien merece una mención especial por apoyarme cada día en Madrid. Siempre estaré en deuda con vosotros.

A todo ellos, gracias de todo corazón.

Sergio González Sanz  
Madrid, octubre de 2012

# Structure - Estructura

## English

This Thesis is made of three Parts:

- Part I (English version) is the main part of the Thesis and it is written in English. It describes: (1) the goals of this thesis and its structure, (2) the main concepts of plasma physics (3) some relevant methods and techniques from data mining and artificial intelligence, (4) an event locator in waveforms and images, (5) two dimensionality reduction techniques (one for multi-dimensional feature spaces and one for images), (6) a automated L/H transition locator and (7) the conclusions and the future work of this Thesis.
- Part II (Resumen en español) is a summary of Part I written in Spanish. It contains: (8) the goals of this Thesis and its structure, (9) a summary of plasma physics, (10) a description of the event locator in waveforms and images, (11) a brief explanation of the developed dimensionality reduction techniques, (12) an overview of the automated L/H transition locator and (13) the conclusions and the future work of this Thesis.
- Part III includes a set of appendices with additional information written in English. Appendix A contains the publications that support this Thesis.

## Español

Esta tesis está formada por tres Partes:

- La Parte I (English version) es la parte principal de la Tesis y está escrita en inglés. Esta parte describe: (1) los objetivos de la tesis y su estructura, (2) los principales conceptos de la física de plasmas, (3) algunos métodos relevantes de minería de datos e inteligencia artificial, (4) un localizador de eventos en señales e imágenes, (5) dos técnicas de reducción de dimensionalidad (una para espacios de características

multi-dimensionales y otra para imágenes), (6) un localizador de transiciones L/H automático y (7) las conclusiones y el trabajo futuro de esta Tesis.

- La Parte II (Resumen en español) es un resumen de la Parte I escrito en español. Esta parte contiene: (8) los objetivos de esta Tesis y su estructura, (9) un resumen de la física de plasmas, (10) una descripción del localizador de eventos en señales e imágenes, (11) una breve explicación de las técnicas de reducción de dimensionalidad desarrolladas, (12) un repaso del localizador automático de transiciones L/H y (13) las conclusiones y el trabajo futuro de esta Tesis.
- La Parte III incluye un conjunto de apéndices con información adicional escritos en inglés. El Apéndice A contiene las publicaciones que avalan esta Tesis.

# Contents

<b>Agradecimientos</b>	<b>ix</b>
<b>Structure - Estructura</b>	<b>xi</b>
<b>I English version</b>	<b>1</b>
<b>1 Introduction</b>	<b>3</b>
1.1 Goals . . . . .	4
1.2 Contents . . . . .	5
<b>2 Nuclear Fusion: a promising source of clean energy</b>	<b>7</b>
2.1 A brief introduction to plasma physics . . . . .	10
2.2 Plasma phenomena . . . . .	12
2.2.1 L & H Modes . . . . .	13
2.2.2 ELMs . . . . .	14
2.2.3 Sawteeth . . . . .	17
2.2.4 Disruptions . . . . .	19
2.3 Fusion devices . . . . .	20
2.3.1 JET . . . . .	21
2.3.2 TJ-II . . . . .	25
2.3.3 DIII-D . . . . .	27
2.3.4 ITER . . . . .	28
2.3.5 DEMO . . . . .	29
<b>3 Data Mining: from data to knowledge</b>	<b>31</b>
3.1 Classification . . . . .	32
3.1.1 Support Vector Machines . . . . .	32
3.1.1.1 First step: optimal separating hyperplane . .	33
3.1.1.2 Second step: mapping the data into a higher dimensional space . . . . .	36
3.1.1.3 Third step: SVM . . . . .	37

3.1.1.4	SVM example: classification of the Fisher's Iris Data . . . . .	38
3.1.2	Conformal Predictors . . . . .	39
3.1.2.1	Inductive Conformal Prediction . . . . .	41
3.1.2.2	Conformal Prediction example: handwritten digit recognition . . . . .	42
3.2	Feature selection and dimensionality reduction . . . . .	45
3.2.1	The Receiver Operating Characteristic curve . . . . .	46
3.2.1.1	The ROC curve . . . . .	47
3.2.1.2	The Area Under the ROC curve . . . . .	49
3.2.1.3	The ROC convex hull . . . . .	50
3.2.1.4	Example of feature selection using the ROC curves . . . . .	51
3.2.2	Principal Component Analysis . . . . .	54
3.2.2.1	Representation of data using PCs . . . . .	55
3.2.2.2	Determining the optimal number of PCs . . . . .	55
3.2.2.3	The Singular Value Decomposition . . . . .	57
3.2.2.4	Example of Principal Component Analysis for dimensionality reduction . . . . .	58
3.2.3	Wavelet analysis . . . . .	59
3.2.3.1	Wavelet application to images . . . . .	62
3.2.3.2	Example of image decomposition using wavelets . . . . .	63
3.3	Regression . . . . .	64
3.3.1	Ordinary Least Squares . . . . .	65
3.3.2	Robust Regression . . . . .	66
3.3.2.1	Ordinary Least Squares versus Robust Regression example . . . . .	69
3.3.3	Ridge Regression . . . . .	69
3.3.3.1	Estimation of the $k$ parameter . . . . .	70
3.3.3.2	Ridge Regression example . . . . .	71
3.3.4	Support Vector Regression . . . . .	72
3.3.4.1	SVR example: the Mexican hat . . . . .	73
<b>4</b>	<b>Location of relevant events in waveforms and images</b>	<b>77</b>
4.1	A Universal Multi-Event Locator . . . . .	78
4.1.1	Sawteeth location using UMEL . . . . .	83
4.1.2	Disruption location using UMEL . . . . .	86
4.1.3	ELMs location using UMEL . . . . .	87
4.1.3.1	Location of the temporal interval with ELMs . . . . .	88
4.1.3.2	Location of single ELMs . . . . .	90

4.1.3.3	Results of ELMs detection in JET . . . . .	92
4.1.4	Analysis of the temperature profiles during ELMs . . .	93
4.1.4.1	Degradation of the temperature gradient between two times . . . . .	96
4.1.4.2	Degradation of the ETG during ELMs . . . . .	96
4.1.5	Discussion . . . . .	99
4.2	Analysis of 2D using UMEL . . . . .	100
4.2.1	Event location in films . . . . .	103
4.2.2	Detection of ROIs . . . . .	104
4.2.3	ROIs' evolution: Heat Maps . . . . .	105
4.2.4	Location of hot spot in JET infrared films . . . . .	107
4.2.5	Discussion . . . . .	108
4.3	Conclusions . . . . .	111
<b>5</b>	<b>Dimensionality reduction techniques</b>	<b>115</b>
5.1	SVM Feature Extractor System . . . . .	116
5.1.1	L/H transition feature extraction . . . . .	119
5.1.1.1	L/H feature extractor using ROC . . . . .	123
5.1.1.2	L/H feature extractor using PCA . . . . .	124
5.1.2	Discussion . . . . .	125
5.2	Image dimensionality reduction . . . . .	127
5.2.1	Region Selection and Image Classification methodology	128
5.2.1.1	Step 1: image division . . . . .	128
5.2.1.2	Step 2: models building . . . . .	129
5.2.1.3	Step 3: region evaluation . . . . .	130
5.2.1.4	Step 4: region selection . . . . .	131
5.2.1.5	Step 5: image classification . . . . .	132
5.2.2	Analysis of the TJ-II Thomson Scattering Images . . .	133
5.2.3	Discussion . . . . .	139
5.3	Conclusions . . . . .	140
<b>6</b>	<b>Analysis of L/H &amp; H/L transitions</b>	<b>143</b>
6.1	Automated location of L/H transitions . . . . .	147
6.1.1	ATD workflow . . . . .	148
6.1.1.1	Readout loop . . . . .	150
6.1.1.2	Discrimination loop . . . . .	150
6.1.1.3	Model creation . . . . .	155
6.1.1.4	Prediction module . . . . .	157
6.1.1.5	Validation of L/H transition times . . . . .	159
6.1.2	Location of L/H transitions in JET . . . . .	161
6.1.2.1	Scaling laws for the power threshold . . . . .	164

6.1.3	Location of L/H transitions in DIII-D . . . . .	167
6.1.4	Discussion . . . . .	169
6.2	Data-driven models of L/H and H/L transitions using CP . .	172
6.2.1	Experiment's set-up . . . . .	173
6.2.2	L/H & H/L models' results . . . . .	174
6.2.3	Discussion . . . . .	174
6.3	Conclusions . . . . .	175
<b>7</b>	<b>Conclusions &amp; Future Work</b>	<b>179</b>
<b>II</b>	<b>Resumen en español</b>	<b>185</b>
<b>8</b>	<b>Introducción</b>	<b>187</b>
8.1	Objetivos . . . . .	188
8.2	Contenidos . . . . .	190
<b>9</b>	<b>Fusión Nuclear: una prometedora fuente de energía limpia</b>	<b>191</b>
9.1	Una breve introducción a la física de plasmas . . . . .	194
9.2	Fenómenos del plasma . . . . .	196
9.2.1	Modos L & H . . . . .	196
9.2.2	ELMs . . . . .	198
9.2.3	Dientes de sierra . . . . .	199
9.2.4	Disrupciones . . . . .	200
9.3	Dispositivos de fusión . . . . .	202
9.3.1	JET . . . . .	203
9.3.2	TJ-II . . . . .	205
9.3.3	DIII-D . . . . .	207
9.3.4	ITER . . . . .	207
9.3.5	DEMO . . . . .	208
<b>10</b>	<b>Localización de eventos relevantes en señales e imágenes</b>	<b>211</b>
10.1	Un localizador de eventos universal . . . . .	212
10.1.1	Localización de dientes de sierra usando UMEL . . . .	215
10.1.2	Localización de disrupciones usando UMEL . . . . .	215
10.1.3	Localización de ELMs usando UMEL . . . . .	216
10.1.4	Análisis de los perfiles de temperatura durante los ELMs	219
10.1.4.1	Degradación del gradiente de temperatura . .	220
10.1.4.2	Degradación del ETG durante los ELMs . . .	220
10.1.5	Discusión . . . . .	222
10.2	Análisis en 2D usando UMEL . . . . .	223
10.2.1	Localización de eventos en películas . . . . .	225

10.2.2	Detección de ROIs . . . . .	225
10.2.3	Evolución de las ROIs: mapas de calor . . . . .	226
10.2.4	Localización de puntos calientes . . . . .	226
10.2.5	Discusión . . . . .	228
10.3	Conclusiones . . . . .	229
<b>11</b>	<b>Técnicas de reducción de dimensionalidad</b>	<b>233</b>
11.1	Sistema de extracción de características SVM . . . . .	233
11.1.1	Extracción de características de la transición L/H . . .	235
11.1.2	Discusión . . . . .	237
11.2	Reducción de la dimensionalidad en imágenes . . . . .	238
11.2.1	Metodología para la Selección de Regiones y la Clasi- ficación de Imágenes . . . . .	239
11.2.1.1	Paso 1: división de las imágenes . . . . .	239
11.2.1.2	Paso 2: construcción de los modelos . . . . .	240
11.2.1.3	Paso 3: evaluación de las regiones . . . . .	240
11.2.1.4	Paso 4: selección de las regiones . . . . .	242
11.2.2	Análisis de las imágenes del Thomson scattering del TJ-II . . . . .	242
11.2.3	Discusión . . . . .	247
11.3	Conclusiones . . . . .	247
<b>12</b>	<b>Análisis de transiciones L/H y H/L</b>	<b>251</b>
12.1	Localización automatizada de transiciones L/H . . . . .	253
12.1.1	Flujo de trabajo del ATD . . . . .	254
12.1.1.1	Bucle de lectura . . . . .	254
12.1.1.2	Bucle de discriminación . . . . .	255
12.1.1.3	Creación del modelo . . . . .	257
12.1.1.4	Módulo de predicción . . . . .	258
12.1.2	Localización de transiciones L/H en JET . . . . .	259
12.1.2.1	Leyes de escala para el umbral de potencia . . . . .	261
12.1.3	Localización de las transiciones L/H en DIII-D . . . . .	263
12.1.4	Discusión . . . . .	264
12.2	Modelos basados en datos de transiciones L/H y H/L usando CP . . . . .	265
12.2.1	Configuración del experimento . . . . .	266
12.2.2	Resultados de los modelos L/H y H/L . . . . .	267
12.2.3	Discusión . . . . .	268
12.3	Conclusiones . . . . .	268
<b>13</b>	<b>Conclusiones y Trabajo Futuro</b>	<b>271</b>

---

<b>III Appendices</b>	<b>277</b>
<b>A List of Journal Papers &amp; Conferences</b>	<b>279</b>
<b>B Fisher's Iris Data Set</b>	<b>283</b>
<b>C Wine Data Set</b>	<b>285</b>
<b>D Semeion Handwritten Digit Data Set</b>	<b>287</b>
<b>E Concrete Compressive Strength Data Set</b>	<b>289</b>
<b>F List of signals and results of the SVM-FES in JET</b>	<b>291</b>
<b>G PCA loadings of the L/H transition in JET</b>	<b>303</b>
<b>H List of signals required by the ATD models in JET</b>	<b>307</b>
<b>I List of signals required by the ATD models in DIII-D</b>	<b>309</b>
<b>References</b>	<b>311</b>

# List of Figures

2.1	Cross-section of the most common reactions in plasma fusion	11
2.2	Trajectories of a charged particle in a magnetic field . . . . .	12
2.3	Plasma pedestal and transport barriers . . . . .	14
2.4	Example of L & H modes, JET pulse 73336 . . . . .	15
2.5	Example of four ELMs, JET pulse 70355 . . . . .	16
2.6	Example of the $D_\alpha$ signal of three different ELMs types . . . . .	17
2.7	Sawteeth examples . . . . .	18
2.8	Sawteeth explanatory models . . . . .	18
2.9	JET original design . . . . .	22
2.10	JET coil systems and iron transformer . . . . .	23
2.11	JET magnetic configurations . . . . .	24
2.12	JET geometry and internal view . . . . .	25
2.13	TJ-II design . . . . .	26
2.14	TJ-II in 2009 . . . . .	27
2.15	DIII-D tokamak . . . . .	28
2.16	ITER design . . . . .	29
3.1	Example of an optimal hyperplane in a two dimensional space	34
3.2	Data mapping using a kernel function . . . . .	36
3.3	SVM example using four different models . . . . .	38
3.4	Credibility distribution of the Semeion test set . . . . .	45
3.5	Samples and error probability distributions as a function of the credibility in the Semeion test set . . . . .	45
3.6	Errors with high credibility in the Semeion test set . . . . .	46
3.7	Example of a ROC graph . . . . .	48
3.8	ROC curves examples . . . . .	49
3.9	ROCCH and iso-performance lines example . . . . .	51
3.10	ROC analysis of the Fisher's Iris Data features . . . . .	52
3.11	Example of PCA . . . . .	56
3.12	Example of two scree plots . . . . .	57
3.13	PCA results of the wine data set . . . . .	58

3.14	Visualization of the wine data set using PCs . . . . .	59
3.15	Wavelet hierarchical representation . . . . .	62
3.16	2-D Wavelet hierarchical representation . . . . .	63
3.17	2-D wavelet decomposition example . . . . .	65
3.18	M-estimator functions . . . . .	67
3.19	Regression example using OLS and RR . . . . .	70
3.20	Ridge trace of the concrete compressive strength data set . . . . .	71
3.21	$\epsilon$ -insensitive loss function . . . . .	72
3.22	SVR of the Mexican hat function using four kernels . . . . .	74
4.1	SVs retrieved by four SVR fits . . . . .	79
4.2	Comparison of UMEL using different types of kernel . . . . .	80
4.3	Examples of UMEL analysis . . . . .	82
4.4	Sawteeth activity example . . . . .	84
4.5	Location of sawteeth using UMEL . . . . .	85
4.6	Plasma diffusivity example . . . . .	85
4.7	Example of a disruptive and a non-disruptive plasma . . . . .	86
4.8	ELMs location, step 1. H-mode location . . . . .	88
4.9	ELMs location, step 2. $D_\alpha$ peaks location and ESVs combination . . . . .	90
4.10	ELMs location, step 2. Division of the diamagnetic energy . . . . .	92
4.11	ELMs location, step 2. Diamagnetic energy drops location . . . . .	92
4.12	Measurements of the electron temperature profile using the ECE diagnostics . . . . .	94
4.13	Examples of temperature profiles in L and H modes . . . . .	95
4.14	Example of the evolution of the temperature profile during an ELM . . . . .	97
4.15	Distribution of the ETG degradation results . . . . .	99
4.16	Comparison of UMEL versus wavelets . . . . .	100
4.17	Example of UMEL application to images . . . . .	103
4.18	Infrared film analysis using UMEL . . . . .	104
4.19	Visible film analysis using UMEL . . . . .	105
4.20	Location of ROIs using SVs and ESVs . . . . .	106
4.21	Heat maps using ESVs . . . . .	106
4.22	Comparison of hot spots location using UMEL and wavelets . . . . .	107
4.23	Heat maps examples from a visible light film . . . . .	110
5.1	JET diagnostics . . . . .	116
5.2	Example of a linearly separable data set in a two dimensional space . . . . .	117
5.3	Dimension reduction in two dimensional data sets . . . . .	118
5.4	Success rates and numbers of SVs of the L/H models trained in the SVM-FES . . . . .	121

5.5	PCA results of the L/H transition . . . . .	124
5.6	Example of an ill-conditioned data set . . . . .	125
5.7	Example of the division of images into six regions in a 4-class classification problem . . . . .	128
5.8	Example of the region selection in a 4-class classification problem	131
5.9	Example of the division of the TJ-II Thomson scattering im- ages into regions . . . . .	134
5.10	Results of the classification of the Thomson scattering images	135
5.11	RSIC regions obtained for each Thomson scattering image class	136
5.12	Example of a classification with multiple regions and a voting schema . . . . .	139
5.13	Distribution of the L/H samples in the BT and TE08 space .	141
6.1	Different patterns of the L/H transition in JET . . . . .	146
6.2	Visual location of the L/H transition . . . . .	147
6.3	ATD workflow . . . . .	149
6.4	L/H transition signature types examples . . . . .	150
6.5	Readout loop examples . . . . .	151
6.6	L/H Transition Interval (LHTI) example . . . . .	152
6.7	Discrimination loop, detection of the power injection . . . . .	153
6.8	Discrimination loop, detection of the ELMs region . . . . .	154
6.9	L/H transition signature types and their wavelet detail coef- ficients . . . . .	155
6.10	JET two-layer L/H model . . . . .	155
6.11	Example of the prediction module . . . . .	158
6.12	Reliability and PCI computation schema . . . . .	159
6.13	Examples of PCI . . . . .	160
6.14	Distribution of the results obtained in the location of the non- clear signature transitions . . . . .	164
6.15	Examples of pulses with a large PCIs . . . . .	165
6.16	DIII-D two-layer L/H model . . . . .	167
6.17	Relation of the uncertainty interval lengths and the input power	171
6.18	Pulse trajectory for L/H and H/L transitions in $T_e$ and $n_e$ . .	175
D.1	Three different sets of the Semeion handwritten characters . .	288
F.1	Success rates and numbers of SVs of the models trained in the SVM-FES discarding 3 features per step . . . . .	302



# List of Tables

2.1	Fusion by magnetic confinement devices . . . . .	21
3.1	Semeion data set classification results . . . . .	44
3.2	$z$ value of the Fisher's Iris Data features . . . . .	53
3.3	Coefficients (loadings) of the three first PCs of the wine data set . . . . .	60
3.4	M-estimator functions . . . . .	68
4.1	Results of the disruptions location . . . . .	87
4.2	Distribution of the periods of the located ELMs . . . . .	93
4.3	ETG degradation results at ELM time + 2 ms in JET . . . . .	98
4.4	Results of the location of hot spots . . . . .	109
5.1	Signals selected by the SVM-FES and their coefficients for the $\pm 100$ ms and the $\pm 500$ ms models . . . . .	122
5.2	ROC results of the L/H transition . . . . .	123
5.3	Comparison of the RSIC results versus the ones obtained using the entire images SVM . . . . .	137
5.4	Comparison of the CPU times of the RSIC method versus the entire images SVM . . . . .	138
6.1	JET two-layer L/H model classification results . . . . .	161
6.2	JET coefficients of the first layer hyperplanes . . . . .	162
6.3	Results of non-clear transitions in JET . . . . .	163
6.4	JET $P_\tau$ scaling laws using $n_e$ , $B_T$ and $S$ . . . . .	165
6.5	JET $P_\tau$ scaling laws using $n_e$ , $B_T$ and $q_{95}$ . . . . .	166
6.6	Comparison of the JET scaling laws obtained using clear and non-clear signature transitions . . . . .	167
6.7	DIII-D coefficients of the first layer hyperplanes . . . . .	168
6.8	L/H & H/L experiments' results summary . . . . .	173
D.1	Number of examples of each character in the Semeion handwritten digit data set . . . . .	288

---

F.1	JET $\pm 100$ ms model hyperplanes' coefficients . . . . .	294
F.2	JET $\pm 100$ ms model hyperplanes' coefficients, cont. 1 . . . . .	295
F.3	JET $\pm 100$ ms model hyperplanes' coefficients, cont. 2 . . . . .	296
F.4	JET $\pm 500$ ms model hyperplanes' coefficients . . . . .	297
F.5	JET $\pm 500$ ms model hyperplanes' coefficients, cont. 1 . . . . .	298
F.6	JET $\pm 500$ ms model hyperplanes' coefficients, cont. 2 . . . . .	299
F.7	JET $\pm 100$ ms model hyperplanes' coefficients discarding 3 features per step . . . . .	300
F.8	JET $\pm 500$ ms model hyperplanes' coefficients discarding 3 features per step . . . . .	301
G.1	JET $\pm 100$ ms model PCA loadings . . . . .	304
G.2	JET $\pm 500$ ms model PCA loadings . . . . .	305

Part I

English version



# Chapter 1

## Introduction

Plasma is the fourth state of the matter (liquid, solid, gas and plasma). It is a nearly neutral ionised gas in which ions and electrons are moving independently. If the plasma is heated sufficiently (and the right conditions are met), the atoms in the plasma fuse together creating heavier atoms and releasing energy. This process is called *plasma fusion*.

Plasma fusion is a promising source of clean energy. Unfortunately, the technology required to produce cheap and safe energy from plasma fusion is still under development. There are two main approaches to obtain energy from plasma fusion:

1. **Fusion by magnetic confinement:** the plasma is trapped by a magnetic field inside a vacuum vessel. Then, it is heated until it reaches thermonuclear conditions and the atoms fuse together. This thesis is focused on the computer analysis of the data generated by fusion by magnetic confinement devices.
2. **Fusion by inertial confinement:** fuel pellets (about the size of a pin head) are heated and compressed by laser beams. The fuel's atoms (usually deuterium and tritium) fuse together releasing energy.

Several different diagnostics quantify the plasma state during operation. These diagnostics generate waveforms and images that must be evaluated by experts. As the diagnostics have improved their performance in the last years, the amount of data generated has grown exponentially. It is no longer possible for the experts to examine the data by means of visual analysis.

The analysis of data retrieved from fusion by magnetic confinement devices has become a “big numbers” problem. Data mining and artificial intelligent techniques must play a relevant role in the data analysis during the following years. These techniques are:

- **Accurate:** the precision obtained by these methods can be hardly equalled by humans.

- **Fast:** most of these techniques are designed to handle large data sets and they can be parallelised. Their results can be available shortly after each plasma pulse.
- **Cheap:** although the initial cost of an application that uses data mining or artificial intelligence techniques could be expensive, they require little maintenance and they can be executed thousands of times without additional cost.
- **Free from human errors:** it does not mean that these techniques are error-free but they are free from absent-mindedness.

On the other hand, they have the disadvantages:

- **Complexity of fusion databases:** the large number of different phenomena taking place inside fusion devices and their correlation make the application of these methods difficult.
- **Expert knowledge:** most of these applications require expert knowledge during its design and execution. Sometimes, it is difficult to obtain the required knowledge from the experts.
- **Resistance to change:** data have been analysed by means of visual analysis since the beginning of plasma fusion research. The introduction of a new tool of data analysis and validation can encounter the resistance of experts that are not familiarized with these new techniques.

## 1.1 Goals

The purpose of this thesis is to develop a set of data mining and artificial intelligent techniques with a general scope and then, to apply them to plasma fusion databases. More precisely, this thesis attempts to:

- **Locate relevant events inside waveforms:** one of the most relevant aspects of data analysis in plasma fusion is the location of plasma phenomena using waveforms. In order to study the plasma behaviour, it is necessary to locate these events. Currently, their location is carried out manually by experts. This thesis explains UMEL—a novel method to locate plasma phenomena inside waveforms (Vega et al., 2010a). One of the goals of UMEL was the automated location of ELMs in JET (González et al., 2010a). In addition, the automated location of ELMs enabled the study of the degradation of the plasma edge temperature gradient during the ELMs' crashes (González et al., 2012c).

- **Locate relevant events inside images:** cameras are one of the newest plasma diagnostics. They provide a useful view of the vacuum vessel during operation. Therefore, the automated analysis of plasma films has become a key issue in the analysis of fusion databases. UMEL was adapted to locate events in plasma films, providing a powerful tool to identify, for example, hot spots in infrared films (González et al., 2010).
- **Select the main dimension in a multi-dimensional space:** several different diagnostics measure the state of the plasma during a pulse. Unfortunately, some of the signals are uninformative and thus, the best signals / features to describe a plasma phenomenon should be chosen. This thesis introduces a novel technique—SVM-FES—to select the best features in a classification problem using Support Vector Machines. The best signals to describe the L/H transition in JET (González et al., 2010b) and DIII-D (Farias et al., 2012) were identified using SVM-FES.
- **Select the main features in images:** in an image, all the pixels do not contain the same degree of information. Since the image processing is usually very time consuming, it should be focused in the most informative regions. This thesis develops RSIC, a technique to identify these regions in an image using a non-conformity measure. The TJ-II Thomson scattering images were analysed using RSIC (González et al., 2012d).
- **Analyse L/H transitions:** high energy mode is a key feature to reach a commercial fusion reactor. The transition between low and high energy mode (L/H transition) is then, one of the most relevant phenomenon in a pulse. This thesis describes an automated technique to locate L/H transitions in plasma waveforms. JET (González et al., 2012a) and DIII-D (Farias et al., 2012) L/H transitions were located using this method. This thesis also aims to study of the L/H and H/L transitions using data-driven models (González et al., 2012b).

## 1.2 Contents

This thesis is structured as follows:

- **Chapter 2** reviews the main topics of plasma fusion by magnetic confinement and exposes why plasma fusion should play a key role in the future energy market. It includes an introduction to plasma physics (Section 2.1), a description of some of the main phenomena that take place in fusion by magnetic confinement devices (Section 2.2), and information about current and future fusion devices (Section 2.3).

- A set of existing data mining and artificial intelligence techniques is reviewed in **Chapter 3**. Section 3.1 is focused in classification methods. The features selection and dimensionality reduction techniques are described in Section 3.2. Finally, Section 3.3 introduces four regression techniques.
- A Universal Multi-Event Locator is introduced in **Chapter 4**. It has been applied to the location of events in waveforms (Section 4.1) and images (Section 4.2). Sawteeth, disruptions and edge localised modes in waveform and hot spots and regions of interest in images have been sought using this method.
- **Chapter 5** describes two dimensionality reduction techniques: the first one (Section 5.1) is oriented to feature selection in a multi-dimensional space and the second one (Section 5.2.1) extracts the most important regions in images. Using the first one, the main features of the L/H transition have been found. The Thomson scattering images have been analysed using the second one.
- **Chapter 6** is devoted to the analysis of L/H and H/L transitions. Section 6.1 explains an automated locator of L/H transitions in plasma waveforms. It has been successfully applied to different fusion devices. Section 6.2 describes the use of conformal predictors to improve the classification of the plasma confinement mode.
- Finally, **Chapter 7** reviews the conclusions and the future work of this Thesis.

## Chapter 2

# Nuclear Fusion: a promising source of clean energy

From the very beginning of the human species history, humankind has been looking for opportunities to improve its living conditions. As hunters and pickers, humans depended on their environment to survive. The natural resources limited the number of humans –the Malthusian trap (Malthus, 1798). Later on, in 10.000 BC approx., the development of the husbandry and the animal husbandry allowed humankind to produce their own resources. As a result, the world population grew significantly. It is known as Neolithic Revolution.

12,000 years after the Neolithic Revolution, between the middle of the 18<sup>th</sup> century and the middle of the 19<sup>th</sup> century, England held a set of transformations in science, and specially, in technology that triggered an amazing rise of the capacity of production. It was the Industrial Revolution. According to United Nations data (United Nations, 1999), in 1750 –at the beginning of the Industrial Revolution–, the world population was 790 million people. In 1900, it was 1.650 million people. The population doubled in just 250 years due to the improved living conditions.

Both revolutions have a common factor: the increase of energy available for humankind (Cipolla, 1972). In the Neolithic, domestic plants and animals produced more (they were more energetically efficient) than the ones in nature. The increase in the production allowed a rise in the population, establishing a new limit for the Malthusian trap. In the Industrial Revolution, fossil fuels granted the access to a new source of energy that could be used to generate work. The Malthusian trap was broken again and the population grew rapidly. At the end of 2011, the world population has reached 7.000 million people. The population forecast of the UN predicts that in 2100 the world population will be 10.000 million people (United Nations, 2010).

The energy market must answer the future growth of the population. Moreover, it must answer the growth of energy demand accounted for the

development of the non-OECD (Organization for Economic Co-operation and Development) countries. According to the International Energy Agency (IEA) Outlook 2011 (International Energy Agency, 2010), the energy use will grow by 33% from 2010 to 2035. The non-OECD countries will account the 90% of this energy growth. China, India, Indonesia, Brazil and the Middle East are the regions where the energy demand grows faster. China's energy demand grows at 2.1% per year and by 2035 it will be a 70% larger than the demand in the USA.

In 2010, the 81% of the energy mix was produced by fossil fuels. Without new policies in energy production and environment protection, the average temperature will increase of more than 6°C. Despite the great effort on developing clean energies, fossil fuels will maintain the 74% of the global energy production in 2035 –and the global energy production will be 33% larger than in 2010. Only the OECD countries will reduce their demand of coal and oil.

The development of the transport sector in the non-OECD countries will cause an increase in the consumption of oil. Electric and hybrid cars will need time to penetrate in the markets. In the meanwhile, the number of cars will rise to 1,700 million in 2035 –almost the double than in 2010. The demand of oil will jump from 87 million barrels per day (mb/d) in 2010 to 99 mb/d in 2035. Electric vehicles will reach the 39% of new sales by 2035.

In this context, renewable energy should play a key role. Unfortunately, the prospects are not good enough. By 2035, the use of renewable energy will increase significantly but it will not be enough to respond to the growth of the energy demand. By regions, the EU will be in the head of the renewable primary energy demand, followed by the USA and China. Studies point out that there will be a reduction in the price of the electricity generated by renewable energy (de Vries et al., 2007).

Other important issue to take into consideration is the availability of resources (World Energy Council, 2010). On the one hand, fossil fuels have limited resources. The production of the currently producing oil fields has already peaked and the supplies for the next years will depend on the fields not yet developed and not yet discovered. The currently producing oil fields are not supposed to last longer than the mid of this century. Coal resources are supposed to last for about 100 years. Uranium stock is not very large but the new resources are supposed to produce enough resources for more than a millennium. The lack of resources will cause tension between different countries looking for cheap energy to fuel their economies (World Energy Council, 2007). On the other hand, the resources of the renewable energies are unlimited but they have the problems of minimum wind speed or land availability, among others, that limit their location.

Humankind is at the crossroads of fossil and renewable energies. On the one hand, fossil energy guarantees a cheap power supply for a few decades but

---

it compromises the future of our environment. On the other hand, renewable energy is an unlimited source of energy that does not risk the environment but it is still not able to fuel the whole world. Nuclear fusion is intended to fill the gap between a renewable energy and a source of energy able to replace fossil fuels.

Nuclear fusion is the energy source of stars. In the 1920s, Sir Arthur Eddington proposed that stars were spheres of hot gas, mainly composed of hydrogen (Eddington, 1926). The gravitational force raises the pressure and the temperature and therefore, gases turn into plasma. In 1927, Lewi Tonks and Irving Langmuir gave the name *plasma* to a nearly neutral ionised gas in which ions and electrons were moving independently (Tonks and Langmuir, 1929). The temperature and the pressure in stars make possible for hydrogen nuclei in plasma to fuse together releasing helium and energy.

The idea behind nuclear fusion is to use the energy in stars to generate electricity. Future fusion reactors will use tritium (an isotope of hydrogen that can be obtained from lithium) as fuel. The lithium in one laptop computer battery would generate 200,000 kWh of electricity (as much as 40 tons of coal) that is enough for lifetime personal electricity needs (McCracken and Stott, 2005, p. XV).

Other important factor to take into consideration is the carbon dioxide emission (in grams) per kWh (Cg/kWh). Fusion is one of the energy sources with lowest specific carbon dioxide emission (6-12 Cg/kWh) next to hydroelectricity (4.8 Cg/kWh) and light water reactors (5.7 Cg/kWh). Photo-voltaic (16 Cg/kWh) and Wind (33.7 Cg/kWh) energies also have low CO<sub>2</sub> emissions but they are penalised by their manufacture processes. Oil (200 Cg/kWh) and coal (270 Cg/kWh) are most contaminant energy sources (Kikuchi, 2011, p. 183).

Nuclear fusion advantages nuclear fission in safety. Unlike fission, fusion does not occur naturally in Earth. Thus, in the case of an accident, the fusion reaction will stop. Studies on fusion power plant safety show that the cost associated with an accident in a fusion power plant is limited due to the low radiological impacts of the accident (Schneider et al., 2001). In the case of an accident, the low amount of radioactivity released to the atmosphere will not make the evacuation of the nearby population necessary. Moreover, it seems that bans on food products will be limited to a small area around the power plant (within a radius of less than 10 km) for a few days (less than a week) and only for milk and cow meat products. Therefore, the cost of an accident varies from 78 million € to 1,950 million € considering risk aversion. The safety studies of future fusion power plants conclude that it is possible to achieve a safe and economically acceptable fusion power plant on the basis of plasma physics and technology to be reached in the next few years (Ward et al., 2001).

This chapter is structured as follows: Section 2.1 includes a brief in-

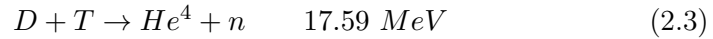
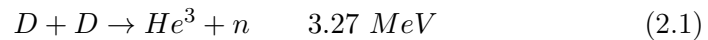
roduction to plasma physics and describes the main phenomena occurring in the plasma. These phenomena are analysed in the following chapters. Section 2.3 introduces some present and future fusion devices.

## 2.1 A brief introduction to plasma physics

When a gas is heated sufficiently, the electrons are separated from the atoms. When all the atoms have lost their electrons, the gas is fully ionised and it is known as plasma, the fourth state of matter. Plasma physics is the science that studies the behaviour of the plasma. There are many different types of plasma (e.g. solar plasma, industrial plasma, neon signs, lightnings, flames) that differ in their density and temperature.

Stars obtain their energy from nuclear fusion processes. The hydrogen atoms fuse to form helium, releasing  $6 \times 10^8$  MJ per kilogram of hydrogen, about 60 million times the energy per kilogram available from chemical fuels (Wesson, 2000, p. 2). Heavy elements are formed by fusion of lighter elements.

Most of the studies of plasma fusion start with deuterium (D), either alone or in a mixture with the heavier hydrogen isotope, tritium (T). Three possible reactions can take place (Wesson, 2000, p. 3):



where H is a proton,  $n$  is a neutron and  $He^4$  is an  $\alpha$ -particle.

The cross-section (the likelihood of interaction between particles) for these reactions only becomes large enough to be useful at high energies. If the required nuclear reactions were to be generated through the thermal motions of the nuclei, it would be necessary to achieve extremely high temperatures. Figure 2.1 (EFDA-JET<sup>©</sup>) shows the cross-section for the reactions in Equations 2.1, 2.2 and 2.3. At a temperature of  $100 \text{ keV}^1$ , the cross-section of the D-T reaction is much larger than the ones of the D-D and D- $He^3$  reactions.

In stars, the high temperature particles are held together by the gravitational force arising from their masses. Unfortunately, the gravitational force in Earth is not strong enough to avoid the particles to fly apart due to their thermal velocities (i.e. the gravity in the Sun is 27.9 times larger than in Earth). So the question was: how to reproduce / simulate the stars' conditions in Earth? Moreover, if the temperature of the particles must be extremely high, how to handle particles at temperatures tens of times larger

---

<sup>1</sup>An  $eV$  is the energy an electron would receive in falling through an electric potential of one volt.  $1 \text{ eV} = 11,600 \text{ K}$  and  $10 \text{ keV} \approx 100 \text{ million K}$

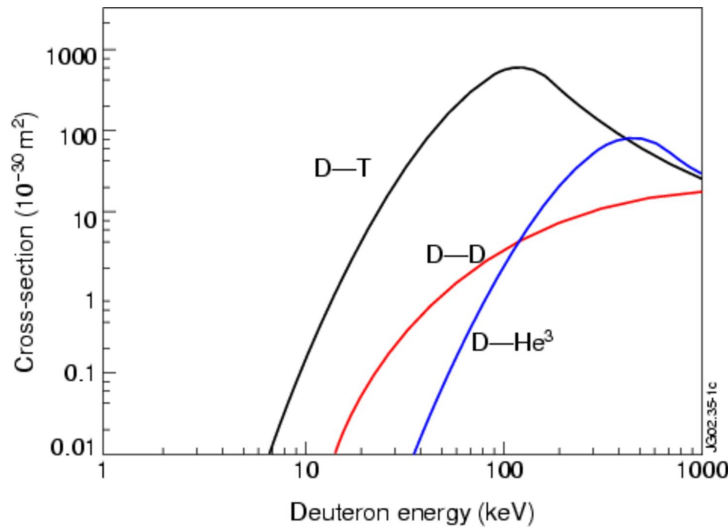


Figure 2.1: Cross-section of the most common reactions in plasma fusion

than the Sun's temperature? For example, the temperature in the core of the Sun is 15 million K in contrast to the temperature in the centre of the plasma in JET that can reach 200 million K.

The answers to these questions came up studying the plasma properties. Since plasma is made up of electrical charged particles, it is subjected to a magnetic force: the Lorenz force. Then, a magnetic field in Earth can replace the gravitational forces that trap the particles in the Sun. When a charged particle is affected by an uniform magnetic field, its movement has two parts:

1. A circular motion perpendicular to the magnetic field, the radius of the circle being called the Larmor radius (Figure 2.2a).
2. A parallel motion along the magnetic field (Figure 2.2b).

Figure 2.2 (EFDA-JET<sup>©</sup>) shows the motion of a charged particle along an uniform magnetic field. In the compound motion (Figure 2.2c), the particle follows a helical trajectory.

Once the plasma is trapped in a magnetic field, it is necessary to heat it until it reaches thermonuclear conditions. The toroidal current induced by the toroidal field coil system generates ohmic heating. Unfortunately, the resistance of the plasma falls with increasing temperature and therefore the ohmic heating is self-limiting. Using only ohmic heating, the plasma temperature is far from the temperature needed to reach an acceptable cross-section for the nuclear fusion reactions. Thus, alternative heating methods were proposed:

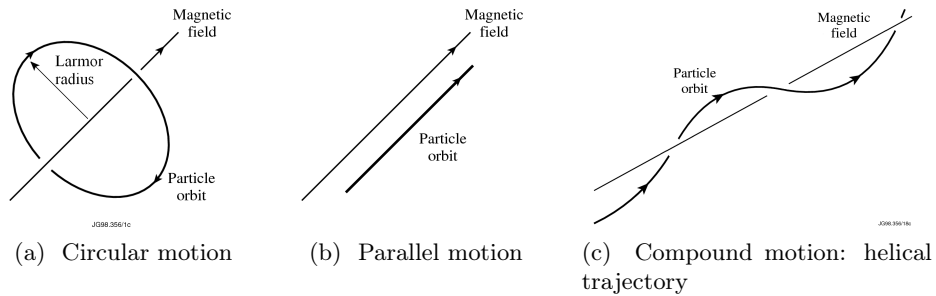


Figure 2.2: Trajectories of a charged particle in a magnetic field

- **Neutral Beam Injection (NBI):** high energy beams of hydrogen ions are injected into the plasma increasing the plasma temperature. These particles must be neutral atoms because they could not cross the magnetic field around the plasma otherwise.
- **Radio-Frequency (RF) heating:** an antenna inside of the vacuum vessel generates high frequency electromagnetic waves. The RF heating includes two different methods:
  - **Ion-Cyclotron Resonant Heating (ICRH):** the ICRH system uses a frequency between 23 MHz (wavelength  $\lambda = 13$  m) and 57 MHz ( $\lambda = 5$  m) resonant to the second harmonic of deuterium or first harmonic of tritium and helium.
  - **Electron-Cyclotron Resonant Frequency (ECRH):** it heats only the electrons in the plasma. It uses a frequency between 140 GHz ( $\lambda = 2.136$  mm) and 170 GHz ( $\lambda = 1.759$  mm).
  - **Lower-Hybrid Current Drive (LHCD):** the LHCD heating uses a frequency of approx. 3.7 GHz ( $\lambda = 0.1$  m) in between ion and electron cyclotron frequencies.

## 2.2 Plasma phenomena

Unfortunately, plasma operation is not smooth and different events take place from the beginning of a pulse to its end. Some of these events, such as L/H transitions, help scientists to achieve better plasma performance but some of them, such as disruptions, are harmful and potentially dangerous for the integrity of fusion devices and hence, they must be avoided.

This section describes four plasma phenomena that have a key role in the following chapters. L & H modes and the changes of plasma confinement are described in Section 2.2.1. Section 2.2.2 contains an explanation of a plasma instability called *edge localised mode*. Sawteeth are analysed in Section 2.2.3.

Finally, Section 2.2.4 describes probably the most dangerous instability: the disruption.

### 2.2.1 L & H Modes

L (for Low confinement mode) and H (for High confinement mode) modes are two different confinement regimes of plasma in fusion machines. H-mode was firstly discovered by Wagner in 1982 (Wagner et al., 1982). During the heating of plasma in the ASDEX tokamak, while the gas valve was closed, Wagner noticed that there was an increase in density caused by a sudden improvement in particle confinement. This phenomenon was completely unexpected since theoretical models did not predict it. Fortunately, Wagner's team was able to reproduce the experiment and, in the following years, the H-mode was reached in other tokamak devices e.g. PDX in 1984 (Kaye et al., 1984), DIII-D in 1986 (Burrell et al., 1987), JET in 1987 (Tanga et al., 1987) and even stellarator devices e.g. W 7-AS in 1993 (Erckmann et al., 1993) demonstrating that the H-mode is a generic feature of fusion by magnetic confinement (Wagner, 2007).

During H-mode, the plasma confinement enhances –the energy confinement increases typically by a factor of 2. At the edge of the plasma, there is an increase in density and temperature, raising the pressure gradient. This edge steep gradient is known as Edge Transport Barrier (ETB) (Wagner et al., 1984). The difference on the plasma pressure caused by the ETB is known as *pedestal*. Figure 2.3 (EFDA-JET<sup>©</sup>) shows a diagram of the L & H modes, the ETB and the pedestal. The normalised plasma radius is shown on the  $x$  axis and the plasma pressure is represented on the  $y$  axis. When the ETB is created, the plasma pressure increases significantly and the ETB appears close to the plasma edge. The pedestal raises the pressure of the plasma between the core and the ETB.

The transition from L-mode to H-mode (L/H transition) requires the heating power to be above a certain threshold  $P_\tau$ . It is known to depend on the plasma density, magnetic field and plasma size.  $P_\tau$  is a crucial parameter in the design of future fusion devices such as ITER and DEMO. ITER's  $P_\tau$  has been predicted using scaling laws computed using a wide range of existing tokamaks (Martin et al., 2008).

An abrupt fall of the  $D_\alpha$  signal at the edge of the plasma characterises the L/H transition. The  $D_\alpha$  signal measures the recycling of deuterium between the plasma and the surrounding surfaces. Thus, the abrupt fall in this signal points out a decreasing in recycling (Wesson, 1987, p. 188). A raise in the slope of the plasma density (caused by the ETB) accompanies the  $D_\alpha$  abrupt fall. Figure 2.4b shows an example of the L/H transition from JET pulse 73336. The L/H transition takes place at 15.793 s. Figure 2.4b includes the  $D_\alpha$  signal (top) and the density at edge of the plasma (bottom). The characteristic abrupt fall of the  $D_\alpha$  signal after the L/H transition can be

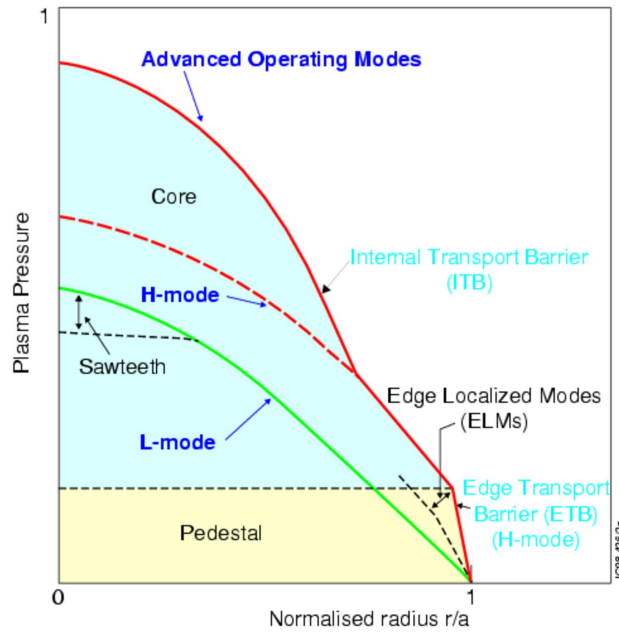


Figure 2.3: Plasma pedestal and transport barriers

clearly seen. At this time, the slope of the plasma density rises.

The typical JET plasma time evolution can be seen in Figure 2.4a. At the beginning of the figure (15 s), plasma is in L-mode (the heating power is lower than  $P_\tau$ ). The NBI and the ICRH heating systems work from 15.459 s to 23.805 s. A short time after the injected power is above the power threshold  $P_\tau$ , the L/H transition takes place and the plasma enters in H-mode (grey time slice). The plasma continues in H-mode until the heating stops. Then, a short time after it, the plasma returns to L-mode (H/L transition, time  $\approx$  24.089 s).

Although the advantages of the H-mode are extremely important for the achievement of a fusion reactor, it also has a few negative aspects such as the uncontrolled increased in the density, an enhancement in impurity confinement and the Edge Localised Modes (ELMs). ELMs are fully described in Section 2.2.2 and can be recognised as spikes in the  $D_\alpha$  emission signal in Figure 2.4a.

### 2.2.2 ELMs

During the operation of ASDEX in H-mode in 1982, scientists realised that there were bursts in the  $H_\alpha$  signal (Wagner et al., 1982). These bursts or spikes were associated with a MHD instability at the edge of the plasma and, in 1984, they were named *Edge Localised Modes* (ELMs) (Keilhacker et al.,

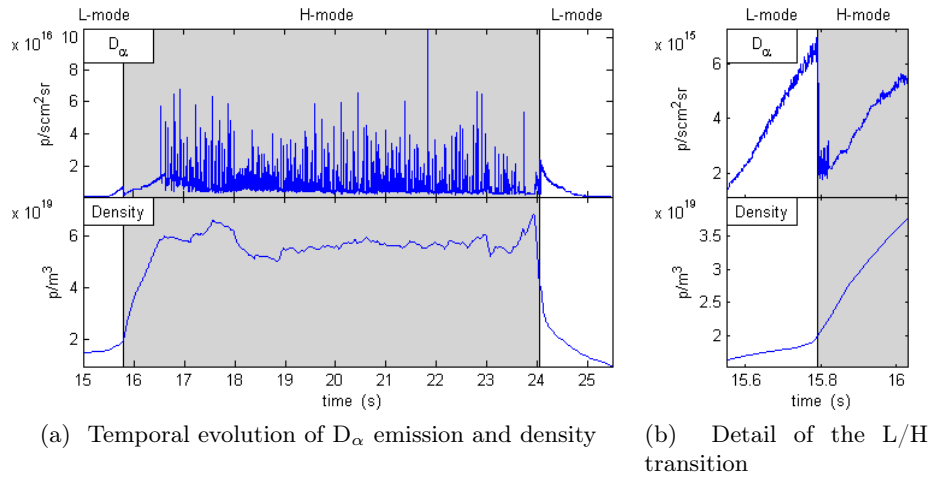


Figure 2.4: Example of L &amp; H modes

1984).

ELMs are instabilities associated with the H-mode in tokamaks. They are recognised as bursts in the  $H_\alpha$  or  $D_\alpha$  signal that cause a reduction in density and temperature in the outer zone of the plasma (edge). This reduction in density and temperature leads to a deterioration of the plasma confinement through the reduction of the ETB.

Originally, scientists identified three different types of ELMs in the DIII-D tokamak in 1991 (Doyle et al., 1991):

- **Type I, *giant* ELMs:** the plasma edge is close to the stability limit  $\alpha \approx \alpha_{crit}$ . The Type I ELMs repetition frequency increases with power and target density, and drops with increasing current. They appear as large isolated sharp bursts on the emissivity signal ( $H_\alpha$  or  $D_\alpha$ ). An example of Type I ELMs in JET can be found in Figure 2.6a. Type I ELMs are the most dangerous ones since the large heat loss pulse involved and the consequent unacceptable high heat load on the divertor (Wesson, 1987, p. 409).
- **Type II, *grassy* ELMs:** they appear when the plasma edge is in the connection regime between the first and the second stable ballooning regimes. They are irregular and low-amplitude ELMs (Figure 2.6b).
- **Type III:** they are medium amplitude ELMs which repetition frequency decreases as the power is increased. The plasma edge pressure gradient is below the ideal ballooning limit ( $0.3 \leq \alpha/\alpha_{crit} \leq 0.5$ ). Figure 2.6c includes an example of Type III ELMs in JET.

Since Type II ELMs can only be observed under certain conditions, a

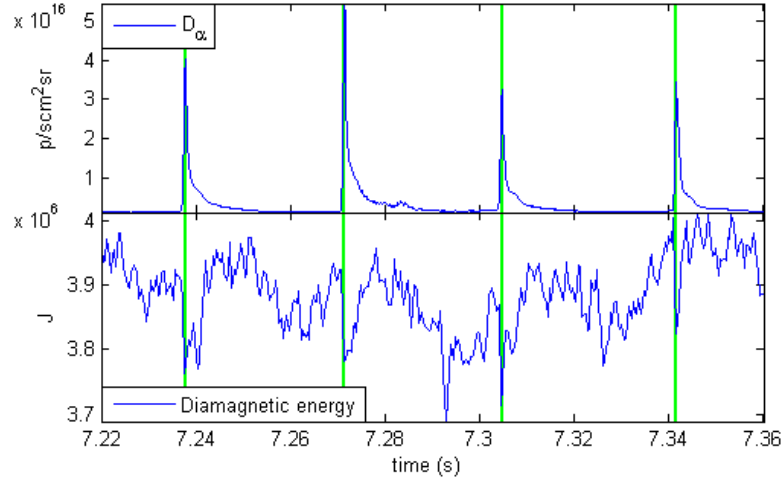


Figure 2.5: Example of four ELMs

different ELM classification has been proposed (Zohm, 1996a):

- **Type I:** the ELM repetition frequency  $v_{ELM}$  increases with the energy flux through the separatrix<sup>2</sup> ( $P_{sep}$ ):

$$\frac{dv_{ELM}}{dP_{sep}} > 0 \quad (2.4)$$

- **Type III:** the ELM repetition frequency decreases with  $P_{sep}$ :

$$\frac{dv_{ELM}}{dP_{sep}} < 0 \quad (2.5)$$

- **Dithering cycles:** for  $P_{sep} \approx P_{\tau}$ , where  $P_{\tau}$  is the power threshold to move the plasma from L-mode to H-mode, repetitive L-H-L transitions may occur. The repetition frequency shows a slight decrease with increasing  $P_{sep}$ .

Experiments have shown that it is possible to obtain an ELMs-free H-mode. Unfortunately, the ELMs-free H-mode is not stationary. Considering  $P_{\tau}^{HL}$  the power limit for the H-L transition, the power in the separatrix  $P_{sep}$  is given by (Zohm, 1996b):

$$P_{sep} = P_{heat} - dW/dt - P_{rad}(core) \quad (2.6)$$

The power radiated from the core ( $P_{rad}(core)$ ) increases with the density and the impurity content of ELMs-free H-mode, decreasing the power in the

<sup>2</sup>**Separatrix:** last closed flux surface. Surface that divides the plasma confined by the closed magnetic lines from the Scrape Off Layer (SOL, see Figure 2.11c)

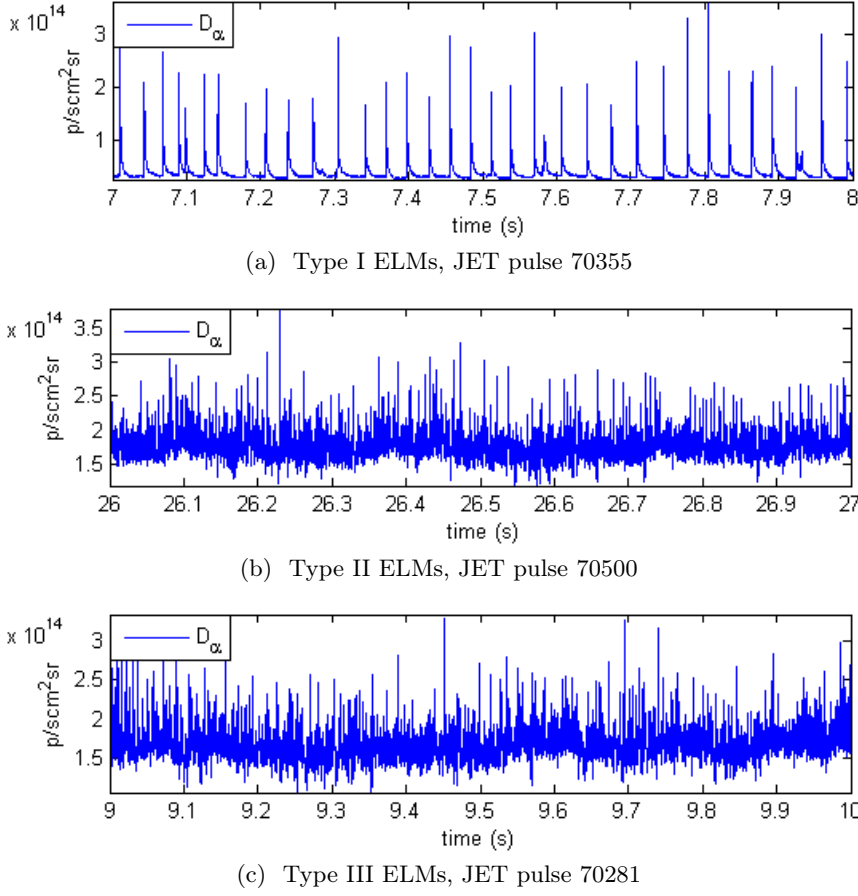


Figure 2.6: Example of the  $D_\alpha$  signal of three different ELMs types

separatrix  $P_{sep}$  (Eq. 2.6).  $P_\tau^{HL}$  also rises with density and there is a time when  $P_{sep} < P_\tau^{HL}$  and thus, the plasma returns to L-mode. In contrast to the ELMs-free H-mode, in the ELMy H-mode pulses density reaches a steady-state level due to the effect of ELMs. Therefore,  $P_{rad}(core)$  does not rise,  $P_{sep} > P_\tau^{HL}$  and the plasma reaches a steady-state.

### 2.2.3 Sawteeth

Sawteeth are instabilities that cause a loss of energy from the plasma core. The plasma temperature and density follow a regular cycle of slow rises and rapid falls (McCracken and Stott, 2005, p. 98). At the temperature collapse, the core of the plasma releases thermal energy to the plasma edge in the form of a heat pulse (Wesson, 1987, p. 365).

Figure 2.7 depicts two examples of sawteeth from JET pulses 60903 (Figure 2.7a) and 60906 (Figure 2.7b). In the examples, the electron temperature at the plasma core shows an oscillatory behaviour similar to the teeth of a

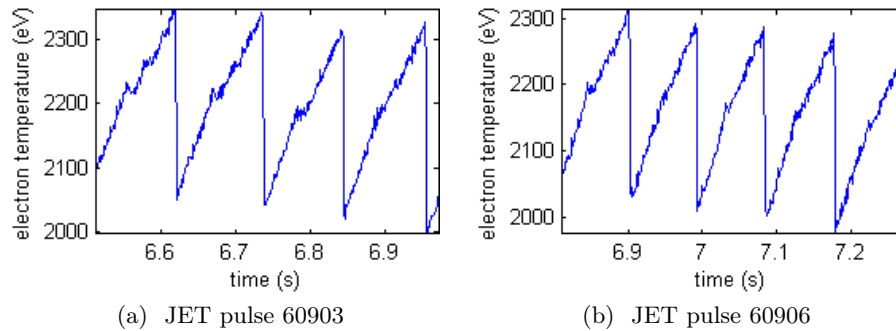


Figure 2.7: Sawteeth examples

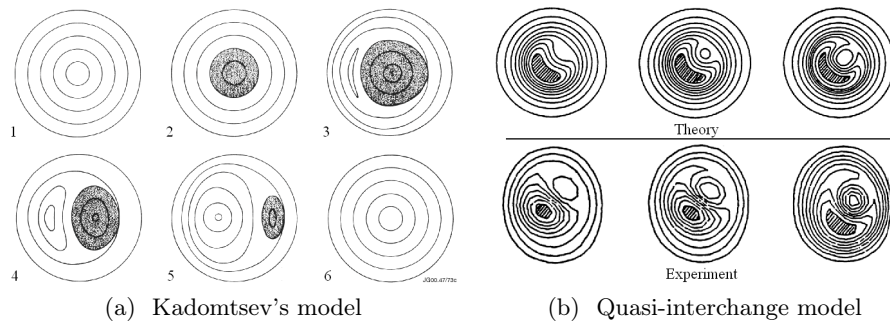


Figure 2.8: Sawteeth explanatory models

saw. The frequency of the oscillations is slightly faster in pulse 60906.

Different explanatory theories have arisen since the first observation of the sawteeth instability in the 70s. One of the first ones was the Kadomtsev's model (Kadomtsev, 1975). It stated that the sawteeth instability starts when the central value of  $q^3$  falls below one. Then, a magnetic island appears in the plasma core and it causes a magnetic reconnection of the field lines. As a result, the plasma temperature and density collapse. They slowly rise again as the  $q$  profile diffuses back toward its natural state with its central value falling below one. When this profile becomes unstable, the next fall occurs and the cycle starts again (Wesson, 2000, p. 90). Figure 2.8a (EFDA-JET<sup>©</sup>) illustrates the cycle of the magnetic reconnection of the field lines in the plasma core during a sawtooth. Lately, it was found that the diffusion of the  $q$  profile during the ramp phase of the sawteeth is very low (against what was predicted by the Kadomtsev's model).

<sup>3</sup>**q**: safety factor. Ratio of the times a magnetic field line travels around the torus toroidally to the times it travels around poloidally. It is dubbed *safety* because plasmas that rotate around the torus poloidally about the same number of times as toroidally are inherently less susceptible to certain instabilities

After the Kadomtsev's model, the quasi-interchange theory (Wesson, 1986) tried to explain the sawteeth phenomenon. It proposed that instead of magnetic reconnection through the growth of a magnetic island, there would be a convective motion involving the interchange of almost parallel magnetic field lines, resulting in the formation of a cold bubble surrounded by hotter plasma (Wesson, 2000, p. 91). The X-ray image seemed to confirm the quasi-interchange theory (Figure 2.8b, EFDA-JET<sup>©</sup>) but after the measurements of the  $q$  profile in the plasma core, the scientist found that the  $q$  value was far from 1 and this theory was discarded.

The discrepancy between the  $q$  profile observed in the experiments and the theoretical one is still unsolved.

### 2.2.4 Disruptions

Disruptions are probably the most dangerous instabilities for the safety of fusion devices. During a disruption, the plasma current abruptly decays away and the plasma confinement is lost.

The dynamic of the disruptions consists of four phases (Schuller, 1995):

1. **Initial event:** the plasma conditions change leading to an unstable plasma configuration.
2. **Precursor phase:** the unstable plasma configuration leads to a MHD instability.
3. **Thermal quench:** the plasma temperature plummets.
4. **Current quench:** the magnetic energy of the poloidal magnetic field is dissipated as thermal energy. The deposition of this energy can be harmful for the integrity of the vessel.

It is possible to distinguish, at least, eight types of disruptions (Savtchikov, 2003), (Murari et al., 2008):

1. **Low  $q$ :** when the  $q$  at the plasma edge reaches the value of 2, a current density gradient appears inside the  $q = 2$  surface. The difference of temperature between the plasma core and the colder plasma at the edge leads to a rapid fall in electron temperature and a loss of plasma current.
2. **Density limit:** the plasma density limit is a consequence of the plasma configuration. When the plasma density is above this limit, the radiated power increases. It causes a reduction of the electron temperature at the plasma edge and finally, when the radiated power exceeds the local heating power, the plasma current shrinks and the plasma disrupts.

3. **H/L transition:** they are a particular case of the previous type. When a H/L transition occurs at high density, sometimes caused by a reduction of the additional heating, it can lead to a density limit disruption.
4. **High radiated power:** this type is similar to the previous one, but in this case, the rise of the radiated power takes place before the increment in the plasma density. The presence of impurities seems the cause of the rise of the radiated power.
5. **Vertical displacement event:** this type of disruptions only occurs in elongated plasmas. These plasmas have better performance (higher plasma current at a given  $q$ ) but they are vertically unstable and thus, their position must be controlled. If the control system fails, the plasma hits the vessel's wall producing a disruption.
6.  **$\beta$  limit:** these disruptions are the consequence of the simultaneous presence of a low  $q$  value and a high local pressure gradient that causes kink and ballooning modes.
7. **Mode lock:** they are caused by external perturbations of the magnetic field. These perturbations can create unstable pressure or current gradients leading to the formation of rotating magnetic islands (modes). If these instabilities ceases to rotate and *locks* to the wall, it can lead to a disruption.
8. **Internal Transport Barrier:** the Internal Transport Barrier (ITB) is a steep temperature and pressure gradient that appears in advanced scenarios (Figure 2.3). The ITB reduces the transport of particles and energy from the centre to the edge of the plasma and can cause a disruption.

The disruption prediction is a key issue in the development of future fusion devices. (Rattá, 2010) has developed a successful predictor based on the combination of three SVM classifiers. It has predicted the disruptions in JET during the carbon wall campaigns and it is being upgraded to analyse the pulses of the new ITER-like wall.

## 2.3 Fusion devices

At the beginning of the fusion research, plasma was trapped inside lineal vessels. To avoid the loss of particles at the ends of the linear vessel, Peter Thonemann (Thonemann and Cowhig, 1951) and Sir George Thomson (Thomson and Blackman, 1946) suggested to make the vessel toroidal (like a ring or a doughnut). In a toroidal vessel, the confinement has no limits and

Name	Location	Name	Location
<b>Conventional tokamak</b>			
ALCATOR C-Mod	USA	ASDEX Upgrade	Germany
COMPASS	Czech Republic	DIII-D	USA
EAST	China	FTU	Italy
ISTTOK	Portugal	JET	UK
J-TEXT	China	KSTAR	South Korea
TCV	Switzerland	TEXTOR	Germany
Tore Supra	France	JT-60U	Japan
<b>Spherical tokamak</b>			
LTX	USA	MAST	UK
NSTX	USA	TST-2	Japan
<b>Stellarator</b>			
H1	Australia	HSX	USA
LHD	Japan	NCSX	USA
TJ-II	Spain	W 7-X	Germany

Table 2.1: Fusion by magnetic confinement devices

thus there are no particle leaks. Alan Ware carried out the first experiments using toroidal vessels in the late 1940s.

In the 1950s, a new design came up: the *stellarator* (steady-state generator). Lyman Spitzer suggested a configuration in which currents in external windings –rather than in the plasma– created the magnetic field (Spitzer, 1951). The Spanish fusion device, the TJ-II (Section 2.3.2), is a stellarator.

Soviet Union scientists Sakharov and Tamm designed the *tokamak*. It was similar to the toroidal pinch configuration designed by Thonemann and Thomson but having a larger toroidal magnetic field. The name *tokamak* came from the Russian name “toroidalnaya kamera ee magnitnaya katushka”, that means “toroidal chamber and magnetic coil”. JET (Section 2.3.1), DIII-D (Section 2.3.3) and ITER (Section 2.3.4) are tokamak fusion devices.

This section also describes DEMO (Section 2.3.5), that will be the first fusion by magnetic confinement power plant. Table 2.1 lists the most important fusion devices, their location and their type.

### 2.3.1 JET

The Joint European Torus (JET) is the world largest tokamak at present. It is located in Culham, Oxfordshire, UK. The design process started in 1973 leded by P. H. Rebut and finished in 1975 with the publication of the *JET Design Proposal* (Rebut and JET design team, 1976) also known as R5. The JET construction lasted for four years, between 1979 and 1983. The JET first pulse was the 25<sup>th</sup> of June 1983, at 13:44 local time.

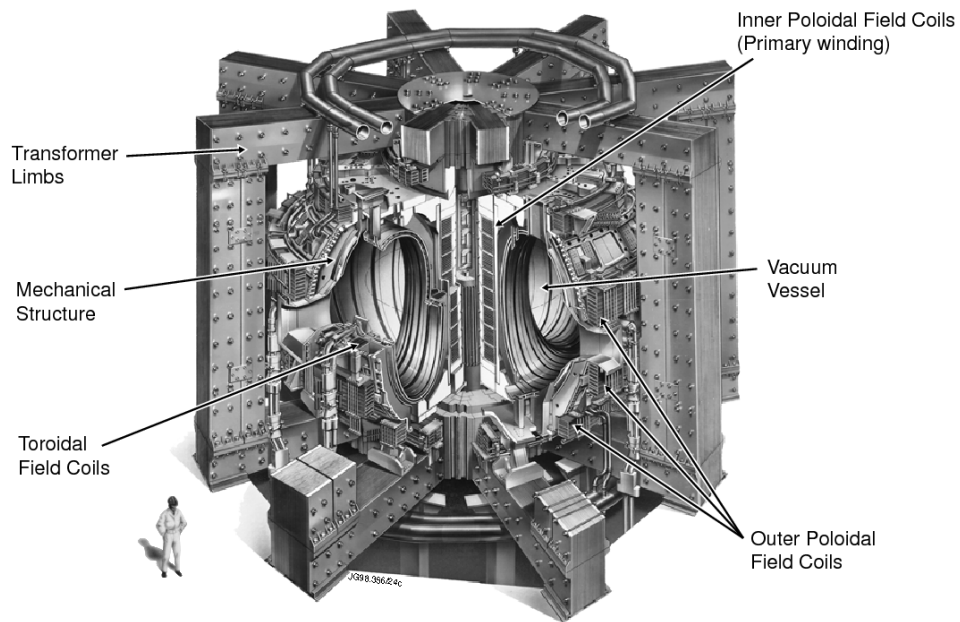


Figure 2.9: JET original design

The aim of JET was stated in the JET design proposal: *“the essential objective of JET is to obtain and study a plasma in conditions and dimensions approaching those needed in a thermonuclear reactor. These studies will be aimed at defining the parameters, the size and the working conditions of a Tokamak reactor. The realisation of this objective involves four main areas of work:*

1. *The scaling of plasma behaviour as parameters approach the reactor range.*
2. *The plasma-wall interaction in these conditions.*
3. *The study of plasma heating.*
4. *The study of  $\alpha$ -particle production, confinement and consequent plasma heating.”*

Figure 2.9 (EFDA-JET<sup>©</sup>) contains the original design of the JET tokamak. The plasma volume in the vacuum vessel is ranging between 80 m<sup>3</sup> and 100 m<sup>3</sup>. The initial plasma current was design to be 3.8 MA and later it was upgraded up to 4.8 MA. The toroidal magnetic field at the centre of the plasma that was initially 2.8 T has been extended to 3.5 T.

The JET coils have a characteristic D-shape. This design obeyed to physical reasons: the magnetic field inside the toroidal field coils falls off

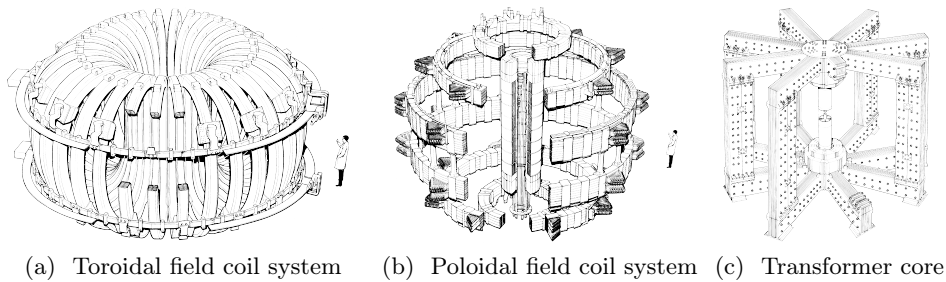


Figure 2.10: JET coil systems and iron transformer

with major radius as  $1/R$  and therefore there is a larger magnetic force on the inboard side (the straight part of the D-shape) of the coils than on the outboard side (Wesson, 2000, p. 22). The primary winding of the transformer borne the magnetic force on the inboard side of the coils. The outboard side of the coils was designed to bear the magnetic force by itself. The curvature provided a balancing force from the tensile stress. 32 D-shape coils produced the JET *toroidal magnetic field* (Figure 2.10a, EFDA-JET<sup>©</sup>). Each one of the toroidal field coils weighed 12 tonnes and was wound with 24 turns of copper. The combined current carrying capacity of all the coils was 51MA. The magnetic fields could cause a total force on each coil that would be almost 2,000 tones, directed toward the major axis of the torus.

The *poloidal magnetic field* coils consisted of 7 circular coils enclosing the toroidal field coils (Figure 2.10b, EFDA-JET<sup>©</sup>). The purpose of the inner coil wound around the central column of the iron transformer core (Figure 2.10c, EFDA-JET<sup>©</sup>) was to act as the primary of the transformer. The other 6 coils allowed scientists to modify the plasma shape and position. The largest coil was 11 metres in diameter.

Combining the magnetic fields created by the toroidal and the poloidal coils systems, it is possible to generate plasmas with different shapes. Figure 2.11 includes three different JET magnetic configurations. Figure 2.11a depicts a view of a circular plasma in the vacuum vessel. Modifying the magnetic configuration it is possible to obtain an elliptical plasma like the one shown in Figure 2.11b.

Figure 2.11c contains a special magnetic configuration: the *X-point* magnetic configuration. Using this magnetic configuration, two types of magnetic surfaces appear: open magnetic surfaces and close magnetic surfaces. The magnetic flux surface that separates the open and the close magnetic surfaces is called *separatrix*. The layer between the separatrix and the wall of the vacuum vessel is called *scrape-off layer* (SOL). The magnetic lines outside the separatrix cross the vacuum vessel's wall and therefore the particles in the SOL hit the wall. The surface below the X-point where the particles hit the wall is called *divertor*.

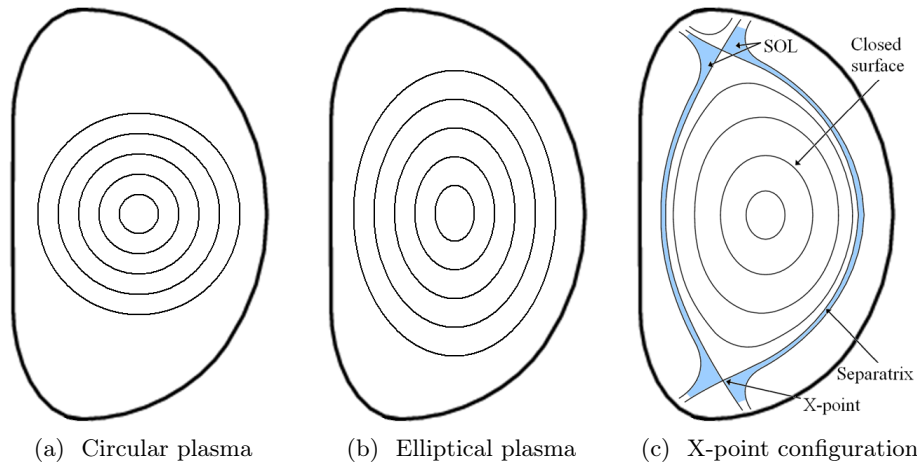


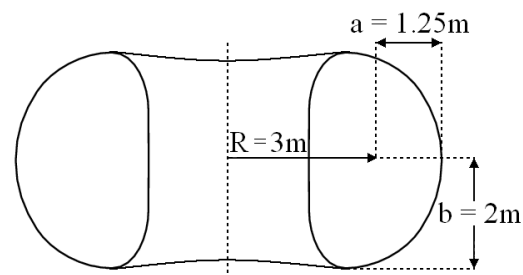
Figure 2.11: JET magnetic configurations

The vacuum vessel maximised the space inside the toroidal coils. It held a vacuum in which the pressure was less than one millionth of the atmospheric pressure (Wesson, 2000, p. 23). Hence, it borne an atmospheric pressure of 10 tonnes per square metre over an area of 200 square metres. The vacuum vessel could hold up to 100 m<sup>3</sup> of plasma. Figure 2.12b (United Kingdom Atomic Energy Authority<sup>©</sup>) contains a real image from the JET vacuum vessel taken in 1998.

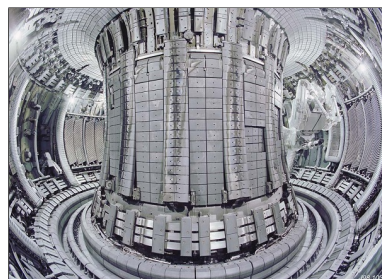
The D-shape of the toroidal field coils determined the geometry of the vacuum vessel (Figure 2.12a). The height-width ratio ( $b/a$ ) of the vacuum vessel was 1.6. The optimum value of the aspect ratio ( $R/a$ ) was found to be between 2 and 3. The chosen value of the aspect ratio was 2.4 on the basis of minimizing the cost of the tokamak.

The JET heating is composed of three different systems: a NBI system with 23 MW of total power, an ICRH antenna up to 32 MW and a LHCD antenna of 12 MW of power.

The diagnostic systems allow the JET scientists to measure plasma properties such as density or temperature and to study the physical phenomena taking place in the fusion device. Nowadays, there are more than 90 diagnostics operational and more than 20 in the design phase. On each JET pulse, the diagnostics generate up to 40 GBytes of data –in contrast to the 243 KBytes generated in the first JET pulse. The JET pulse database contains more than 80 TBytes of data. The JET diagnostics include Thomson scattering spectroscopy (measurements of electron temperature and density profiles), visible, UV and X-ray spectrometers (temperatures and densities measurements), bolometers (measurements of energy loss from the plasma), magnetic coils (magnetic field, current and energy measurements) or electron cyclotron emission (fast, high resolution electron temperature profiles



(a) JET geometry



(b) JET internal view

Figure 2.12: JET geometry and internal view

measurements). The JET diagnostics also include visible and infra-red light cameras that obtain video recordings and images of the plasma during a pulse.

More information about JET can be found at the EFDA-JET's webpage (EFDA-JET, 2012).

### 2.3.2 TJ-II

The TJ-II is a low magnetic shear stellarator of the heliac type with an average major radius ( $R$ ) of 1.5 m and average minor radius ( $a$ )  $\leq 0.22$  m (Alejalde et al., 1999). It is located in the *Laboratorio Nacional de Fusion* (LNF) in Madrid, Spain. A team of physicists and engineers of CIEMAT in collaboration with the Oak Ridge National Laboratory designed the TJ-II (Hender et al., 1987). This proposal was based in a previous one of a flexible heliac configuration stellarator (Harris et al., 1985).

Figure 2.13 shows the TJ-II design. The vertical field coils control the horizontal position of the plasma. 32 toroidal coils generate the toroidal field (up to 1.2 T). Two central coils (one circular and one helical) create the three-dimensional twist of the central axis of the configuration. The vacuum vessel holds a vacuum lower than  $1 \cdot 10^{-8}$  mbar.

The design process of the TJ-II started in 1986 when the Association EURATOM-CIEMAT was created. The flexible heliac project TJ-II was

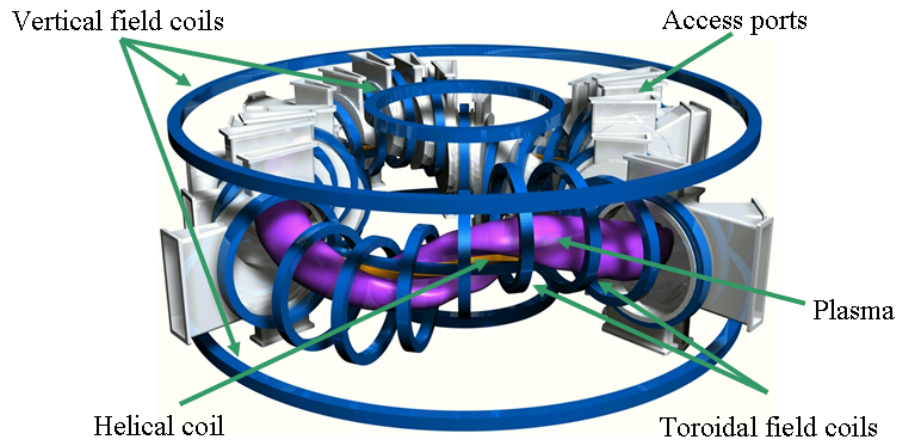


Figure 2.13: TJ-II design

introduced to demonstrate its scientific interest and it received preferential support from EURATOM for phase I (physics). In 1990, it received support for phase II (engineering). The first plasma in the TJ-II stellarator took place in December, 1997. Figure 2.14 contains an image of the state of the TJ-II stellarator in 2009.

One of the most important characteristics of the TJ-II stellarator is its flexible heliac configuration. The rotational transform can vary between 0.9 and 2.2 obtaining plasma volumes from  $0.3 \text{ m}^3$  to  $1.2 \text{ m}^3$ . For large values of the rotational transform, the plasma is bean-shaped. The average plasma radius oscillates between 0.12 m and 0.22 m. This flexibility gives scientists an extensive range of different configurations to develop their experiments.

The TJ-II pulses last between 200 ms and 300 ms with a repetition frequency of 7 minutes. The electric supply consists of a 15 kV, 100 Hz pulse generator of 140 MVA, 100 MJ. The 96 access points in the vacuum vessel allows scientists to use a wide range of plasma diagnostics such as bolometry, soft X-ray, interferometry, reflectometry, Thomson scattering, spectrometry or visible and infra-red cameras. In order to minimize the impurities in the plasma, the vacuum vessel wall is coated with lithium or boron.

In the TJ-II device, two different systems heat the plasma: ECRH and NBI. The ECRH heating uses two gyrotrons at 53.2 GHz. The maximum power per gyrotron is 300 kW. There are two NBI injectors installed in the TJ-II, each one provides a heating power up to 500kW (Estrada et al., 2010). Using the NBI heating, it has been possible to obtain H-mode, reaching densities of  $8 \cdot 10^{19} \text{ m}^{-3}$  and electron temperatures of 250 eV - 300 eV (Sánchez et al., 2009).

More information about the TJ-II and the LNF can be found in its web-

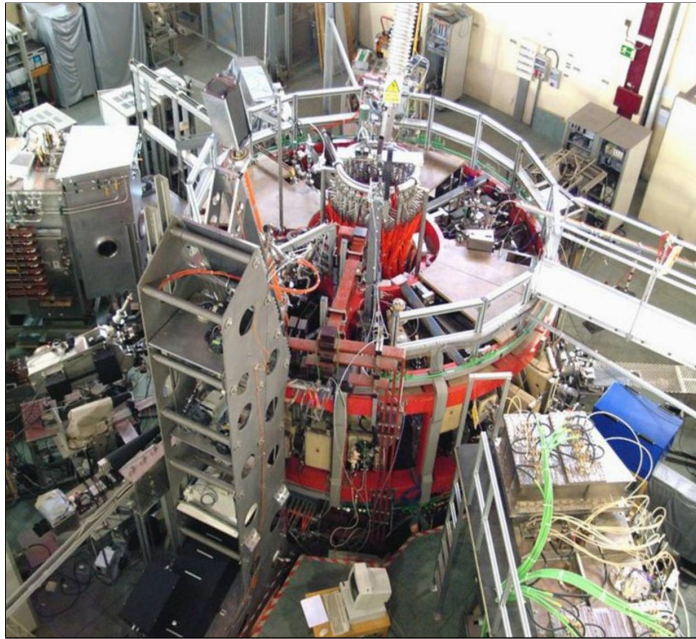


Figure 2.14: TJ-II in 2009

page (Laboratorio Nacional de Fusion, 2012).

### 2.3.3 DIII-D

DIII-D is a tokamak fusion device located in San Diego, USA. It is operated by General Atomics. DIII-D is the update of the Doublet III device and it was dubbed DIII-D because of its new D-shape vessel. Currently, it is the third largest tokamak after JET and JT-60U (Japan).

The main features of the DIII-D fusion device are (Brooks et al., 1987): major radius ( $R$ ) 1.67 m, minor radius ( $a$ ) 0.67 m, plasma area  $2 \text{ m}^2$ , plasma volume  $30 \text{ m}^3$ , maximum plasma current 5 MA and maximum toroidal field on axis 2.2 T.

The goal of the DIII-D research program is to establish the scientific basis for the optimization of the tokamak approach to fusion energy production. In the near term, it aims to enable the success of ITER by providing solutions to main physics issues such as the steady-state operation (General Atomics, 2012).

Figure 2.15a contains a pictorial view of the DIII-D tokamak. It is possible to get an idea of the size of the device comparing it to the scientist next to it. Figure 2.15b shows an image from the inside of the DIII-D vessel.

The DIII-D website (General Atomics, 2012) provides more information about this tokamak.

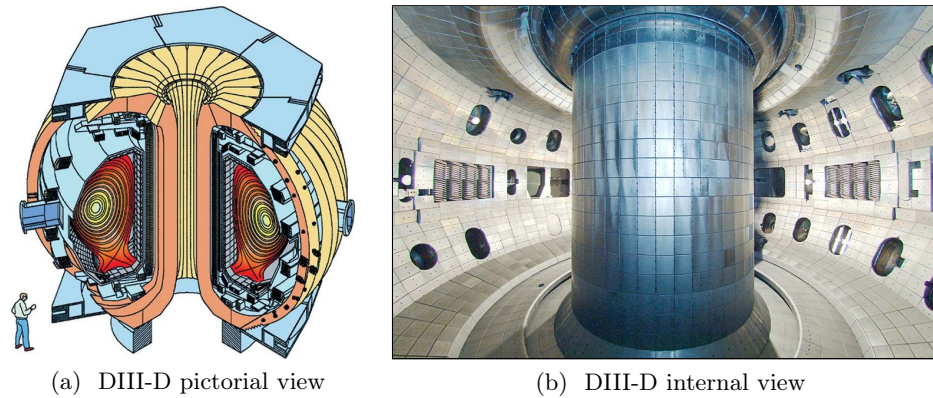


Figure 2.15: DIII-D tokamak

### 2.3.4 ITER

ITER (International Thermonuclear Experimental Reactor) is a tokamak fusion device that is being built in Cadarache, France. It is intended to fill the gap between the experimental fusion devices and the first commercial power plant (DEMO). The members of the ITER project are: EU, China, India, Japan, South Korea, Russia and USA.

Figure 2.16 depicts the design of ITER. Its main features are: major radius ( $R$ ) 6.2 m, minor radius ( $a$ ) 2.0 m, maximum plasma current 15 MA and toroidal field 5.3 T. The scientific goal of ITER is to obtain  $Q^4 \geq 10$ .

The ITER magnetic field is created by means of superconducting coils: 18 toroidal field coils, 6 poloidal field coils, a central solenoid and additional coils to mitigate the effect of ELMs. In order to achieve superconductivity, supercritical helium –in the range of  $-269^\circ\text{C}$ – cools the coils. The magnetic field created by the ITER magnets will be around 200,000 times the magnetic field on Earth. The cost of the ITER’s magnets is estimated in 298.18 million € (Fusion for Energy, 2011).

Its vacuum vessel has a volume of  $1,400 \text{ m}^3$ . It will hold a vacuum one millionth of the atmospheric pressure (similar to JET). The vessel includes 44 ports to provide access to the inside for plasma diagnostics and remote handling. The price of the vacuum vessel will be 147.30 million €.

The temperature inside ITER will reach 150 million K. In order to achieve this temperature, 50 MW of heating power will be installed. ITER will use two NBI injectors and one additional for diagnostic purposes (133.36 million €) and ICRH and ECRH heating systems (66.72 million €). Since scientists aim to obtain  $Q \geq 10$ , ITER is expected to generate 500 MW of fusion power.

The ITER diagnostics include 50 different systems to analyse the state of

---

<sup>4</sup> $Q$  is the ratio of fusion power to auxiliary power injected into the plasma

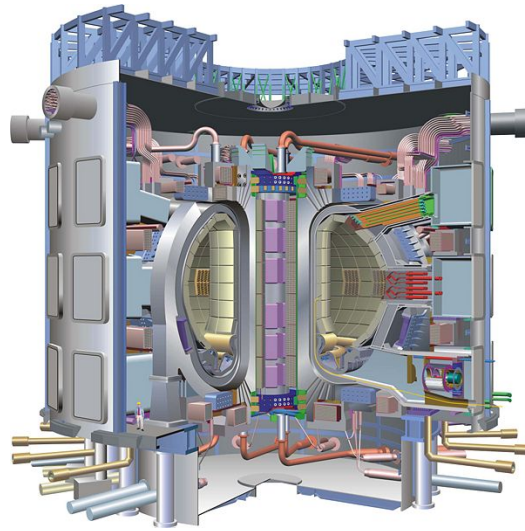


Figure 2.16: ITER design

plasma. They include X-rays, cameras, lasers, impurity monitors, bolometers, etc. The diagnostic systems are priced at 56.78 million €.

The plasma facing components are crucial for the success of ITER. An ITER-like wall made of tungsten is currently being tested in JET. 440 tiles of size  $1\text{ m} \times 1.5\text{ m}$  will cover the ITER's wall. The price of the blankets and other in-vessel components is 130.88 million €. Since the extreme heat can activate the plasma face components, it is necessary a remote handling system to deal with repair and replacement issues. The remote handling system that will be implemented in ITER costs 71.36 million €.

The ITER site preparation started in January 2007 and the construction of the scientific buildings and facilities began in July 2010. The assembly of the tokamak is expected to start in 2015. It will be finished by 2018 and the first plasma in ITER will be held by 2019. The site, buildings and power supplies costs will be 776.27 million €.

More information about the ITER project can be found in its webpage (ITER Organization, 2012).

### 2.3.5 DEMO

DEMO (DEMOstration power plant) will be the next step towards a commercial fusion device. DEMO will belong to the 5<sup>th</sup> generation of experimental fusion devices. It will demonstrate the reliability of a *commercial size* fusion device.

There are still many unknowns in the design of DEMO. Its final features will be based on the results obtained by ITER and other fusion devices.

The European Power Plant Conceptual Study (PPCS) has analysed the different alternatives of the design of DEMO based on the tokamak concept (Maisonnier et al., 2005). The PPCS is focused on four power plant models, named PPCS-A to PPCS-D, which are illustrative of a wider spectrum of possibilities (Maisonnier et al., 2006). The PPCS plant models have been designed using the PROCESS code. It was firstly written for the conceptual design of ITER and it has been updated to incorporate recent scaling laws using the data obtained by existing fusion devices. The models PPCS-A and PPCS-B are near-term devices (about 30% better than the design basis of ITER) while the models PPCS-C and PPCS-D are based on advanced plasma configurations and material technologies.

For (Ward, 2010), DEMO must be based on a tokamak device whose main characteristics are: 8.5 m major radius with a toroidal field of 6 T and a fusion power of 3 GW. The main difference between DEMO and the existing fusion devices is its energy production: while existing fusion devices have a pulse length not longer than a minute, DEMO must be steady state or at least it must work in very long pulses.

In DEMO, the energy production will be larger. It can be obtained by two different alternatives:

- **Using a higher density:** in this case the DEMO plasma will be highly shaped or DEMO will run at very high magnetic field.
- **Using a higher temperature:** this is the most feasible option. If the density of DEMO is similar to the ITER density then the plasma temperature in DEMO will be higher (average 10 keV, around 25 keV in the plasma core). At this temperature, the fusion cross section no longer varies with  $T^2$  (see Fig. 2.1).

In order to provide DEMO with data of the materials that will be used for its construction, the International Fusion Materials Irradiation Facility (IFMIF) is being built in Japan. Its focus is to shrink the design and construction time of DEMO and then achieving a commercial prototype in the shortest time (*fast track*).

## Chapter 3

# Data Mining: from data to knowledge

Fusion devices generate large quantities of raw data. Several plasma diagnostics measure plasma properties during operation, generating time series in the form  $(t, x)$  where  $t$  are the times when the data  $x$  are collected. These data aim to increase the knowledge about the physical processes taking place inside the fusion devices. Unfortunately, raw data are not commonly useful for scientific purposes. Therefore, they must be processed in order to be analysed.

Data mining techniques are a set of statistical and artificial intelligence techniques that aim to generate knowledge from raw data. They analyse massive databases to seek hidden patterns and to create behaviour models. Then, they transform the information retrieved into understandable data for further use. Data mining techniques have been applied to a wide range of fields, for example business, science or medicine.

This chapter reviews the most important data mining techniques that will be applied to fusion databases in the following chapters. These techniques have been classified into three groups:

- **Classification (Section 3.1):** given a set of training samples, the classification methods predict the label of new samples. Support Vector Machines (Section 3.1.1) and Conformal Predictors (Section 3.1.2) belong to this group.
- **Feature Selection and Dimensionality Reduction (Section 3.2):** given a data set in a  $p$ -dimensional space, these techniques aim to find a reduced or a transformed feature space of dimension  $q$  where  $q \ll p$ . The representation of the data set in the new feature space must be the best possible (in terms of classification rates or variance covered). The use of a lower dimension feature space simplifies the interpretation of the data, saves storage space and increases the performance of

other data mining methods. The techniques described in this section are the Receiver Operating Characteristic curve (Section 3.2.1), Principal Component Analysis (Section 3.2.2) and Wavelet analysis (Section 3.2.3).

- **Regression (Section 3.3):** the regression methods compute the relationship between a dependent variable and a set of explanatory variables. The ones analysed in this chapter are Ordinary Least Squares (Section 3.3.1), Robust Regression (Section 3.3.2), Ridge Regression (Section 3.3.3) and Support Vector Regression (Section 3.3.4).

## 3.1 Classification

Given a set of training samples together and labels  $(x_1, y_1), (x_2, y_2), \dots, (x_n, y_n)$ , a classifier predicts the label  $\hat{y}_{n+1}$  of a new sample  $x_{n+1}$ . It is possible to distinguish two classification paradigms (Gamerman and Vovk, 2007):

- **Induction:** a general rule is created using the training data (inductive step). This general rule is called *predictor*, *model* or *decision rule*. It is applied to generate  $\hat{y}_{n+1}$  using only  $x_{n+1}$  (deductive step). In the inductive paradigm, the bulk of the computations is carried out in the inductive step while the deductive step is usually much faster. Examples of this paradigm are *Support Vector Machines* (Section 3.1.1) and *Inductive Conformal Predictors* (Section 3.1.2.1).
- **Transduction:** the prediction is carried out in a single step. The training samples and  $x_{n+1}$  are used to generate  $\hat{y}_{n+1}$ . Since all the sample are used to generate  $\hat{y}_{n+1}$  for each new sample  $x_{n+1}$ , this process is usually longer than the deductive step and it is unfeasible for large training sets. *Conformal Predictors* (Section 3.1.2) are an example of transduction.

In fusion science, classifiers are applied to the determination of the plasma confinement (González et al., 2012b), (Vega et al., 2009b), (Murari et al., 2006), the classification of disruptions (Cannas et al., 2006) and the classification of ELMs (Duro et al., 2009), among others.

### 3.1.1 Support Vector Machines

Support Vector Machines (SVM) is a statistical learning method to build predictive models. It was created by V. Vapnik et al. between 1964 and 1995.

SVM is based on the idea of mapping the input feature space (the space where the training samples are defined) into a higher dimensionally space

(called transformed input space or image space) where the data can be separated by a hyperplane<sup>1</sup> –optimal separating hyperplane.

Three steps make up the theory of SVM: formulation of the optimal separating hyperplane (Section 3.1.1.1), mapping of the data into a higher dimensional space (Section 3.1.1.2) and computation of SVM (Section 3.1.1.3).

### 3.1.1.1 First step: optimal separating hyperplane

The first step of SVM theory was the formulation of the optimal separating hyperplane between 1964 and 1974 (Vapnik, 2006, p. 430).

Given a linearly separable training data

$$(x_1, y_1), (x_2, y_2), \dots, (x_n, y_n), \quad x \in \mathbb{R}$$

belonging to two different classes  $y \in \{-1, 1\}$ , an *optimal separating hyperplane* or a *maximal margin hyperplane* separates the data without errors and maximises the distance to the closest samples (Vapnik, 2000, p. 131). The optimal separating hyperplane can be written as:

$$(w \cdot x) - b = 0 \tag{3.1}$$

The label of a sample  $i$  is equal to the sign of the distance from the optimal separating hyperplane to  $i$ :

$$y_i = 1 \quad \text{if } (w \cdot x_i) - b \geq 1 \tag{3.2}$$

$$y_i = -1 \quad \text{if } (w \cdot x_i) - b \leq -1 \tag{3.3}$$

Equations 3.2 and 3.3 can be rewritten as an unique equation in the form:

$$y_i [(w_i \cdot x_i) - b] \geq 1, \quad i = 1, \dots, n \tag{3.4}$$

The optimal hyperplane satisfies the conditions in Equation 3.4 and minimises:

$$\Phi(w) = \|w\|^2 \tag{3.5}$$

Figure 3.1 shows an example of a two-class classification problem in a two dimensional space. The training data are linearly separable. All the hyperplanes in the figure separate the data without errors but only one of them (solid lines) is the optimal separating hyperplane (the one that maximises the distance to the closest samples).

In order to find the optimal hyperplane, the following quadratic programming problem has to be solved: minimise the functional

$$\Phi(w) = \frac{1}{2}(w \cdot w) \tag{3.6}$$

---

<sup>1</sup>**hyperplane:** generalisation of a plane in a higher dimensional space. It divides the space into two regions

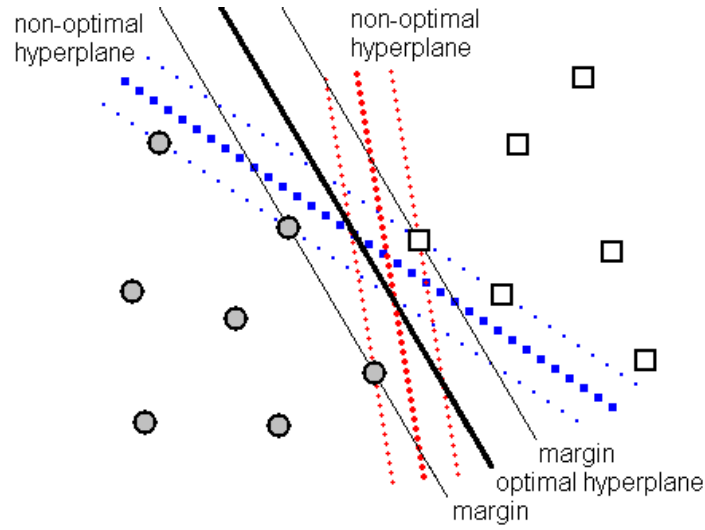


Figure 3.1: Example of an optimal hyperplane in a two dimensional space

under the constraints of Equation 3.4.

The solution of this optimisation problem is given by the Lagrangian:

$$L(w, b, \alpha) = \frac{1}{2}(w \cdot w) - \sum_{i=1}^n \alpha_i \{y_i [(x_i \cdot w) - b] - 1\} \quad (3.7)$$

where the  $\alpha_i$  are Lagrange multipliers. The Lagrangian has to be minimised with respect to  $w$  and  $b$  and maximised with respect to  $\alpha_i > 0$ .

At the saddle point, the solutions  $w_0$ ,  $b_0$ , and  $\alpha^0$  should satisfy the conditions:

$$\frac{\partial L(w_0, b_0, \alpha^0)}{\partial b} = 0 \quad (3.8)$$

$$\frac{\partial L(w_0, b_0, \alpha^0)}{\partial w} = 0 \quad (3.9)$$

Using Equations 3.8 and 3.9 it is possible to obtain the following properties of the optimal hyperplane (Vapnik, 2000, p. 134):

1. The coefficients  $\alpha_i^0$  of the optimal hyperplane should satisfy the constraints:

$$\sum_{i=1}^n \alpha_i^0 y_i = 0, \quad \alpha_i^0 \geq 0, \quad i = 1, \dots, n \quad (3.10)$$

2. The optimal separating hyperplane ( $w_0$ ) is a linear combination of the vectors in the training set:

$$w_0 = \sum_{i=1}^n y_i \alpha_i^0 x_i, \quad \alpha_i^0 \geq 0, \quad i = 1, \dots, n \quad (3.11)$$

It is possible to obtain the equation of the optimal separating hyperplane in terms of the Lagrange multipliers substituting Equation 3.11 into Equation 3.1:

$$\sum_{i=1}^n y_i \alpha_i^0 x_i + b_0 = 0 \quad (3.12)$$

3. Only a subset of the vectors in the training set has non-zero  $\alpha_i^0$  coefficients in Equation 3.11. The vectors in this subset are called *Support Vectors* (SV) and they are the vectors for which Equation 3.4 is equal to 1. Thus, Equation 3.11 can be rewritten as:

$$w_0 = \sum^{SV} y_i \alpha_i^0 x_i, \quad \alpha_i^0 \geq 0 \quad (3.13)$$

**The Nonseparable Case.** In the case of linearly non-separable data, the error in the classification of the training set is minimised and the margin for the correctly classified vectors is maximised. For this purpose, the slack variables  $\xi_i \geq 0$  and the function

$$F_\sigma(\xi) = \sum_{i=1}^n \xi_i^\sigma, \quad \sigma > 0 \quad (3.14)$$

are introduced. Now, the functional  $F_\sigma(\xi)$  is minimised subject to the constraints:

$$\begin{cases} y_i ((w \cdot x_i) - b) \geq 1 - \xi_i, & i = 1, 2, \dots, n \\ (w \cdot w) \leq \Delta^{-2} \end{cases} \quad (3.15)$$

This hyperplane is called  *$\Delta$ -margin separating hyperplane* (Vapnik, 2000, p. 136). It is important to note that the  $\Delta$ -margin hyperplane is equal to the optimal separating hyperplane in the case of a linearly separable training set. The  $\Delta$ -margin separating hyperplane is equal to:

$$w = \frac{1}{C^*} \sum_{i=1}^n \alpha_i y_i x_i \quad (3.16)$$

The values of  $\alpha_i$  and  $C^*$  are obtained maximising the functional:

$$W(\alpha, C^*) = \sum_{i=1}^n \alpha_i - \frac{1}{2C^*} \sum_{i,j=1}^n \alpha_i \alpha_j y_i y_j (x_i \cdot x_j) - \frac{C^*}{2\Delta^2} \quad (3.17)$$

subject to the constraints

$$\begin{cases} \sum_{i=1}^n y_i \alpha_i = 0, & C^* \geq 0 \\ 0 \leq \alpha_i \leq 1, & i = 1, \dots, n \end{cases} \quad (3.18)$$

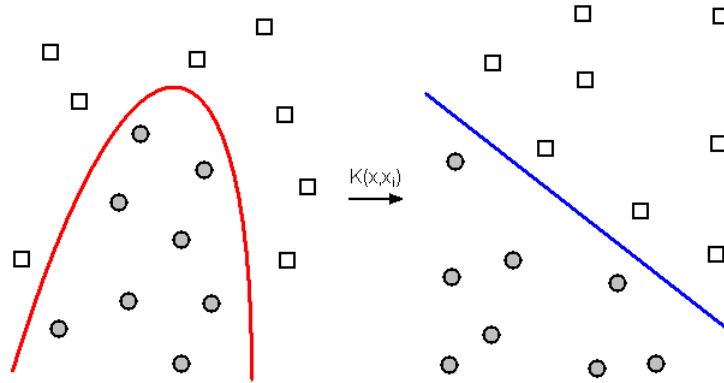


Figure 3.2: Data mapping using a kernel function

The *soft-margin separating hyperplane* (or generalised optimal hyperplane) introduced in (Cortes and Vapnik, 1995) simplifies the computations of the  $\Delta$ -margin hyperplane. In this case,  $C$  is a given value and  $\sigma = 1$ . The soft-margin hyperplane is determined by the vector  $w$  that minimises the functional:

$$\Phi(w, \xi) = \frac{1}{2}(w \cdot w) + C \left( \sum_{i=1}^n \xi_i \right) \quad (3.19)$$

### 3.1.1.2 Second step: mapping the data into a higher dimensional space

The next step of the SVM theory was the mapping of the data from the input space into a transformed input space (Vapnik, 2006, p. 432). This step tries to find a transformed input space where the input data are linearly separable.

According to the Mercer's theorem (Minh et al., 2006), the optimal separation hyperplane (3.12) can be written in the transformed space as (Boser et al., 1995):

$$\sum_{i=1}^n y_i \alpha_i^0 K(x, x_i) + b_0 = 0 \quad (3.20)$$

where  $K(x, x_i)$  is a function called *kernel function* (Schölkopf and Smola, 2002, p. 25). Kernel functions map the input vectors into the image space.

Figure 3.2 shows an example of a non-separable data that have been mapped into a transformed input space where a linear separating hyperplane can be built.

### 3.1.1.3 Third step: SVM

Finally, V. Vapnik and C. Cortes developed the SVM theory in 1995 (Vapnik, 2006, p. 433). It is a generalisation of the non-separable case mapping the data into an image space.

Following from Equation 3.20,  $\alpha$  values are calculated by maximising the functional:

$$W(\alpha) = \sum_{i=1}^n \alpha_i - \frac{1}{2} \sum_{i,j=1}^n \alpha_i \alpha_j y_i y_j K(x_i, x_j) \quad (3.21)$$

subject to the constraints:

$$\begin{cases} \sum_{i=1}^n y_i \alpha_i = 0 \\ 0 \leq \alpha_i \leq C, \quad i = 1, \dots, n \end{cases} \quad (3.22)$$

As in the separable case, the hyperplane in Equation 3.20 can be written as a function of the Support Vectors:

$$\sum^{SV} y_i \alpha_i^0 K(x, x_i) + b_0 = 0 \quad (3.23)$$

Then, the decision function given by the hyperplane in Equation 3.23 is:

$$D(x) = \sum^{SV} y_i \alpha_i^0 K(x, x_i) + b_0 \quad (3.24)$$

The value of  $D(x)$  is the distance from a sample  $x$  to the separating hyperplane in the transformed feature space.

Some of the most widely used kernel functions are (Schölkopf and Smola, 2002):

1. **Linear:**

$$K(x, x_i) = x \cdot x_i \quad (3.25)$$

2. **Polynomial:**

$$K(x, x_i) = (x \cdot x_i + 1)^d \quad (3.26)$$

where  $d$  is the degree of the polynomial function.

3. **Radial-Basis Function (RBF):**

$$K(x, x_i) = e^{-\frac{|x - x_i|^2}{2\sigma^2}} \quad (3.27)$$

where  $\sigma$  determines the area of influence of SVs. The larger the value of  $\sigma$ , the smoother the hyperplane generated

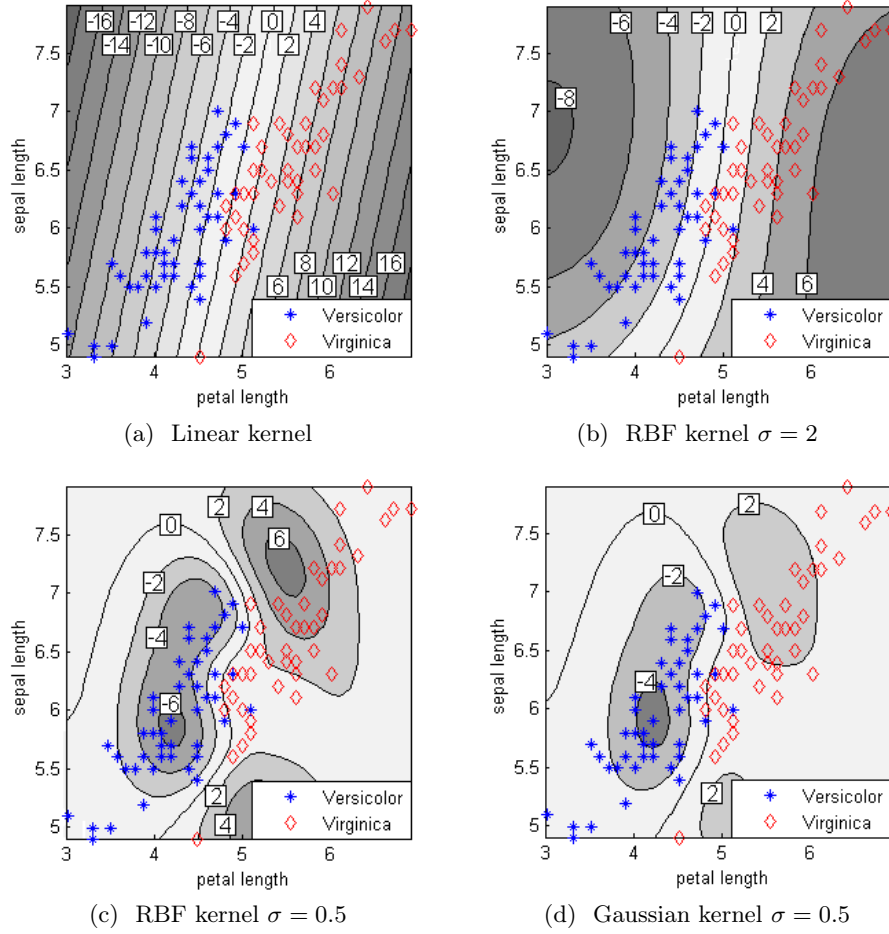


Figure 3.3: SVM example using four different models

#### 4. Gaussian:

$$K(x, x_i) = \frac{1}{2\pi^{N/2}\sqrt{\sigma}} e^{-\frac{|x - x_i|^2}{2\sigma^2}} \quad (3.28)$$

where  $\sigma$  determines the area of influence of SVs and  $N$  is the total number of samples

#### 3.1.1.4 SVM example: classification of the Fisher's Iris Data

This section illustrates the classification of the Fisher's Iris Data (see Appendix B) using SVM. It was carried out using *The Spider* toolbox (Weston et al., 2011) and *Matlab*®.

This example classified the species *Iris versicolor* and *Iris virginica*. The input space was a two dimensional space that used the features *sepal length*

and *petal length*. Using these features, this was a linearly non-separable problem.

Four different models were trained using the Fisher’s Iris Data: a linear kernel model ( $C = 100$ ), two RBF kernel models ( $C = 100$ ,  $\sigma = 2$  and  $C = 100$ ,  $\sigma = 0.5$ ) and a Gaussian kernel model ( $C = 100$ ,  $\sigma = 0.5$ ). Figure 3.3 shows the distances to the separating hyperplanes in the feature spaces. The separating hyperplanes coincide with the line of distance 0.

The classification success rates of the training set were: 95% linear kernel, 95% RBF kernel  $\sigma = 2$ , 97% RBF kernel  $\sigma = 0.5$  and 96% Gaussian kernel.

The linear kernel model (Figure 3.3a) created a linear separating hyperplane between the *Iris versicolor* and *Iris virginica* classes. Therefore, it was not able to classify some of the samples in the border of both classes (it was a non-separable problem). On the other hand, it had a high generalization ability.

The RBF kernel model ( $\sigma = 2$ ) in Figure 3.3b created a non-linear separating hyperplane between classes. Despite the non-linear separating hyperplane, the model was not able to classify the samples in the frontier of both classes.

In contrast to the previous models, the RBF kernel model ( $\sigma = 0.5$ ) in Figure 3.3c was able to properly classify some of the samples in the border of both classes. On the other hand, the generalization capability of the model decreased. For example, a sample with a *sepal length* = 7.0 and a *petal length* = 3.1 was classified as *Iris virginica* although it probably belonged to the *Iris versicolor* class.

Finally, the Gaussian kernel model in Figure 3.3d defined the margin between classes better than the linear one but, as the previous case, it also lost some generalization ability.

### 3.1.2 Conformal Predictors

Conformal prediction (CP) was firstly introduced by A. Gammerman, V. Vovk and V. Vapnik as an addition to SVM that hedged the prediction labels with supportiveness values (Gammerman et al., 1998). Later on, conformal prediction theory was developed as an independent theory to hedge the prediction of any classification method. CP uses past experience to determine precise levels of confidence and credibility in new predictions. Given an error probability  $\epsilon$  and a method that makes a prediction  $\hat{y}_{n+1}$  of a label  $y_{n+1}$ , it produces a set of labels that also contains  $y_{n+1}$  with a probability  $1 - \epsilon$  (Shafer and Vovk, 2008).

Let’s assume a set of samples  $(x_1, y_1), (x_2, y_2), \dots, (x_n, y_n)$  where  $x_i \in X$  ( $X$  is the object space) and  $y_i \in Y$  ( $Y$  is the label space). The sample space is defined as:

$$Z := X \times Y \tag{3.29}$$

A traditional predictor is a function  $f$  that given a new object  $x_{n+1}$ , generates a predicted label  $\hat{y}_{n+1}$  using the information available in  $(x_1, y_1), (x_2, y_2), \dots, (x_n, y_n)$ :

$$f : Z^* \times X \rightarrow Y \quad (3.30)$$

On the other hand, conformal predictors predict a subset of  $Y$  large enough to contain  $y_{n+1}$  with a probability  $1 - \epsilon$ .  $\epsilon$  is called significance level and  $1 - \epsilon$  is called confidence level (Vovk et al., 2005, p. 19). Given a significance level  $\epsilon$ , a conformal predictor  $\Gamma$  outputs a subset of predicted labels:

$$\Gamma^\epsilon(\underbrace{x_1, y_1, \dots, x_n, y_n}_{\text{training samples}}, \underbrace{x_{n+1}}_{\text{new}}) \quad (3.31)$$

of  $Y$ .

The size of the predicted subset varies with  $\epsilon$ . As the confidence level ( $1 - \epsilon$ ) increases, the subset of predicted labels must be larger enough to contain  $y_{n+1}$  with higher probability. In contrast, if  $\epsilon$  increases, it is possible to give more specific predictions (smaller subsets of  $Y$ ). Therefore, the predicted subset of labels are nested, and  $\Gamma$  must satisfy (Vovk et al., 2005, p. 19):

$$\Gamma^{\epsilon_1}(x_1, y_1, \dots, x_n, y_n, x_{n+1}) \subseteq \Gamma^{\epsilon_2}(x_1, y_1, \dots, x_n, y_n, x_{n+1}), \quad \epsilon_1 \geq \epsilon_2 \quad (3.32)$$

$\Gamma$  can be defined as a function (Vovk et al., 2005, p. 19):

$$\Gamma : Z^* \times X \times (0, 1) \rightarrow 2^Y \quad (3.33)$$

( $2^Y$  is the set of all subsets of  $Y$ ) that satisfies Eq. 3.32 for all values of  $\epsilon$  and all sets in  $Z^*$ .

The predicted set of labels in Eq. 3.31 can be summarised by two numbers (Gammerman and Vovk, 2007):

$$\text{Confidence: } \sup \{1 - \epsilon : |\Gamma^\epsilon| \leq 1\} \quad (3.34)$$

$$\text{Credibility: } \inf \{\epsilon : |\Gamma^\epsilon| = 0\} \quad (3.35)$$

Confidence and credibility require a way of scoring how different a sample is from a bag of samples. A bag of size  $n \in \mathbb{N}$  is a collection of  $n$  elements where repetitions are allowed and its content is not ordered. The bag of the elements  $z_1, z_2, \dots, z_n$  is written as  $\{z_1, z_2, \dots, z_n\}$ . The set of all bags of size  $n$  of elements of a measurable space  $\mathbb{Z}$  is called  $\mathbb{Z}^{(n)}$ .  $\mathbb{Z}^{(*)}$  is the set of all bags of elements of  $\mathbb{Z}$  (the union of all the  $\mathbb{Z}^{(n)}$ ).

Nonconformity measures evaluate how different a sample is from a bag of old samples. A nonconformity measure is a measurable mapping (Vovk et al., 2005, p. 23):

$$A : \mathbb{Z}^{(*)} \times \mathbb{Z} \rightarrow \bar{\mathbb{R}} \quad (3.36)$$

A scores the new sample indicating how different it is from the old ones. Given a bag of elements  $\{z_1, z_2, \dots, z_n\}$  and a new sample  $z_{n+1}$ , the nonconformity score of  $z_{n+1}$  is written as  $\alpha_{n+1} := A(\{z_1, z_2, \dots, z_n\}, z_{n+1})$ .

Unfortunately, the value  $\alpha_{n+1}$  does not characterise, by itself, how unusual the sample  $z_{n+1}$  is. Since the nonconformity measure may be scaled, it is necessary to compare the value  $\alpha_{n+1}$  with the nonconformity scores of the samples in the bag  $\{z_1, z_2, \dots, z_n\}$ . This statistical value is called *p-value* and it is computed as (Vovk et al., 2005, p. 25):

$$p\text{-value} = \frac{\#\{j = 1, \dots, n : \alpha_j \geq \alpha_{n+1}\}}{n + 1} \quad (3.37)$$

The new sample  $z_{n+1}$  is very conforming if its *p-value* is large (close to 1) and it is very unusual if its *p-value* is low (close to  $1/(n + 1)$ ).

In an  $d$ -class classification problem, it is necessary to compute  $d$  different *p-values*, one assuming that  $z_{n+1}$  belongs to each class. Using the largest ( $P_1$ ) and the second largest ( $P_2$ ) *p-values*, the conformal scores are defined as (Saunders et al., 1999):

$$\text{Confidence} = 1 - P_2 \quad (3.38)$$

$$\text{Credibility} = P_1 \quad (3.39)$$

The predicted label— $\hat{y}_{n+1}$ —is equal to the class of the largest *p-value* ( $P_1$ ).

This approach of CP is transductive. Given a training set  $t$  and a new sample  $z_{n+1}$ , a transductive algorithm generates a label  $\hat{y}_{n+1}$  using all the information in  $t$ . In contrast, an inductive algorithm generates a classification rule  $r$  using  $t$  only once and then it uses  $r$  to predict  $\hat{y}_{n+1}$  for every new sample. In the case of transductive algorithms, the bulk of the computations is performed once per each new sample and in the case of inductive algorithms it is performed only once to create  $r$ .

Since CP is a transductive algorithm, it is highly inefficient when the number of samples to classify is high. Next section includes a modification in CP to create an inductive version of the method.

### 3.1.2.1 Inductive Conformal Prediction

Inductive Conformal Prediction (ICP) is a modification of CP. In contrast to it, using ICP, the bulk of the computation is performed only once, no matter the number of samples to be classified.

The initial training set in CP ( $\{z_1, z_2, \dots, z_n\}$ ) is divided into two different bags: the *proper training set* ( $\{z_1, z_2, \dots, z_k\}$ ,  $k < n$ ) and the *calibration set* ( $\{z_{k+1}, z_{k+2}, \dots, z_n\}$ ) (Saunders et al., 1999). A classification rule  $r$  is computed only once using the samples in the proper training set.  $r$  remains unchanged during the life of the inductive conformal predictor.

The samples in the calibration set are used to compute the conformity scores of the new samples. Then, in order to classify a new sample  $x_{n+1}$ , a conformity score:

$$\alpha_l = A(\{z_{k+1}, z_{k+2}, \dots, z_n\}, (x_{n+1}, y)) \quad (3.40)$$

and its  $p$ -value:

$$p\text{-value}_y = \frac{\#\{j = k + 1, \dots, n : \alpha_j \geq \alpha_{n+1}\}}{n - k + 2} \quad (3.41)$$

are computed for each  $y \in Y$  (for each different class in the classification problem). The reason of computing an  $\alpha$  value for each  $y \in Y$  is because the value of the non-conformity measure of  $z_{n+1}$  depends on both, the object  $x_{n+1}$  and its predicted label  $\hat{y}_{n+1}$ . Then, for each value of  $\alpha_{n+1}$  a different  $p$ -value is obtained.

Conformal values are computed using Equation 3.38 and 3.39. The predicted label  $\hat{y}_{n+1}$  is the label of the largest  $p\text{-value}_y$ .

There are two versions of ICP:

- **Semi-off-line ICP:** after classifying a new sample  $x_{n+1}$ , it is added to the calibration set. Then, the calibration set is made up of the elements:  $\{z_{k+1}, z_{k+2}, \dots, z_n, (x_{n+1}, \hat{y}_{n+1})\}$ . The advantage of semi-off-line ICP is that the conformal measures are improved when new samples are classified and initially it requires a calibration set smaller than the one required by off-line ICP.
- **Off-line ICP:** new samples are not added to the calibration set. Its advantage is that, in contrast to semi-off-line ICP, it is independent of the order of the new samples classified by the predictor (its calibration set is not modified).

### 3.1.2.2 Conformal Prediction example: handwritten digit recognition

This section includes an example to illustrate the use of inductive conformal predictors. It consists in the recognition of handwritten digits from 0 to 9. This experiment was developed using *Matlab*®, *The Spider* toolbox (Weston et al., 2011) and the Semeion Handwritten Digit Data Set (see Appendix D). The classification rule was created using SVM (Section 3.1.1). The focus of this experiment was not to design an error-free classifier but to demonstrate the usefulness of the conformal values (credibility and confidence).

The Semeion data set contains 1,593 samples of handwritten digits. It was split into a training set containing the 35% of the samples of each character (553 digits), a calibration set containing the 15% of the samples of each

character (234 digits) and a test set containing the 50% of the samples (806 digits).

The nonconformity measure chosen to solve this problem was:

$$\alpha(x) = \begin{cases} -|distance(H, x)| & \text{if } x \text{ is properly classified} \\ |distance(H, x)| & \text{if } x \text{ is misclassified} \end{cases} \quad (3.42)$$

where  $distance(H, x)$  is the Euclidean distance from the hyperplane  $H$  to the sample  $x$ . The sign of this distance gives the predicted label of  $x$ . Therefore,  $x$  is properly classified if  $sign(distance(H, x)) = y$  where  $y$  is the real label of  $x$  and misclassified otherwise.

Table 3.1 shows the results obtaining on the classification of the Semeion data set using two different kernels: a linear kernel (Eq. 3.25,  $C = 2000$ ) and a RBF kernel (Eq. 3.27,  $C = 2000$ ,  $\sigma = 5$ ). The best results were achieved using the RBF kernel. This table contains the number of samples in the Semeion data set for each digit and the number of samples in the training, calibration and test sets. For each kernel, Table 3.1 includes the number of properly classified instances (# success), the number of errors (# errors), the number of unknown samples (# unknowns, the samples whose largest  $p_{values}$  are equal) and the mean values of credibility and confidence for each digit and for the whole test set.

Figure 3.4 depicts the credibility values obtained by the 806 samples in the test set. The samples corresponding to each character are divided by vertical lines. The errors are circled in red. The unknown samples are plotted on the 0 credibility line. It is important to note that all the errors are located in the low credibility area of the figure (the highest credibility value of a error is 0.3362, character 6). The mean credibility value of the errors is 0.1270 whereas the mean credibility value of the properly classified samples is 0.5378.

Figure 3.5 includes three different graphs of the samples and the error probability distributions as a function of the credibility. Figure 3.5a shows the distribution of the samples as a function of the credibility. In this example, there is not a tendency in the distribution of the samples. Figure 3.5b includes the distribution of the errors in the credibility. In this case, it is possible to observe that the probability of making an error increases when the credibility of the classified samples decreases. Finally, Figure 3.5c contains the error probability in the credibility interval  $[\theta, 1]$ . Using Figure 3.5c, it is possible to obtain the error probability if only the samples with credibility above the threshold  $\theta$  are classified. For example, if only the samples with credibility higher or equal to 0.5 ( $\theta = 0.5$ ) are classified, the error probability is 0.00%. Using  $\theta = 0.225$ , the error probability is 1.95%

Figure 3.6 contains five examples of errors with credibility values between 0.24 and 0.34. Figure 3.6a corresponds to a sample from character 1 that was classified as 7 (credibility = 0.2979). The sample in Figure 3.6b belongs

	Total	Character											
		0	1	2	3	4	5	6	7	8	9		
# samples	1593	161	162	159	159	161	159	161	158	155	158	155	158
# training	553	56	56	55	55	56	55	56	55	56	55	55	54
# calibration	234	24	24	23	23	24	23	24	23	24	23	23	23
# test	806	81	82	81	81	81	81	81	80	81	80	78	80
Linear kernel ( $C = 2000$ )													
# success	711	78	70	75	69	67	76	78	71	62	65	62	65
	88.21%	96.30%	85.37%	92.59%	85.19%	82.72%	93.83%	96.30%	88.75%	79.49%	81.25%	79.49%	81.25%
# errors	91	3	12	5	12	14	5	3	8	15	14	15	14
	11.29%	3.70%	14.63%	6.17%	14.81%	17.28%	6.17%	3.70%	10.00%	19.23%	17.50%	19.23%	17.50%
# unknowns	4	0	0	1	0	0	0	0	1	1	1	1	1
	0.50%	0.00%	0.00%	1.24%	0.00%	0.00%	0.00%	0.00%	1.25%	1.28%	1.25%	1.28%	1.25%
credibility	0.525	0.652	0.402	0.497	0.514	0.547	0.474	0.664	0.509	0.483	0.506	0.483	0.506
confidence	0.952	0.971	0.939	0.945	0.959	0.962	0.957	0.936	0.964	0.971	0.916	0.964	0.971
RBF kernel ( $C = 2000, \sigma = 5$ )													
# success	747	79	72	78	75	72	78	79	74	70	70	70	70
	92.68%	97.53%	87.80%	96.30%	92.59%	88.89%	96.30%	97.53%	92.50%	89.74%	87.5%	92.50%	87.5%
# errors	49	2	8	3	6	9	3	2	5	5	6	5	6
	6.08%	2.47%	9.76%	3.70%	7.41%	11.11%	3.70%	2.47%	6.25%	6.41%	7.50%	6.25%	7.50%
# unknowns	10	0	2	0	0	0	0	0	1	3	4	1	4
	1.24%	0.00%	2.44%	0.00%	0.00%	0.00%	0.00%	0.00%	1.25%	3.85%	5.00%	1.25%	5.00%
credibility	0.513	0.765	0.484	0.482	0.485	0.542	0.501	0.598	0.471	0.384	0.395	0.471	0.384
confidence	0.988	0.993	0.977	0.984	0.991	0.988	0.986	0.991	0.991	0.993	0.981	0.991	0.981

Table 3.1: Semeion data set classification results

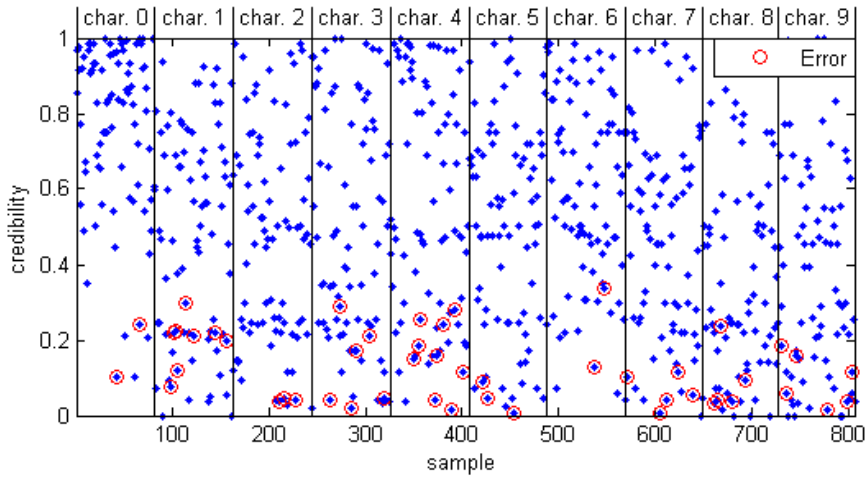
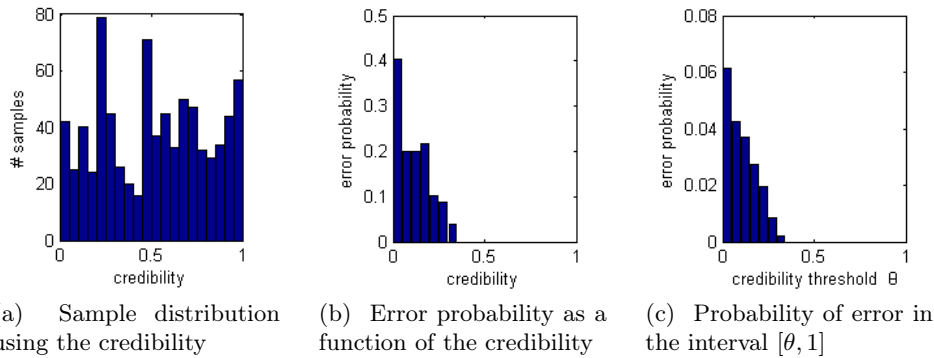


Figure 3.4: Credibility distribution of the Semeion test set



(a) Sample distribution using the credibility    (b) Error probability as a function of the credibility    (c) Probability of error in the interval  $[\theta, 1]$

Figure 3.5: Samples and error probability distributions as a function of the credibility in the Semeion test set

to character 3 but it was classified as 5 (credibility = 0.2894). The character of the sample in Figure 3.6c is 4 but it was classified as 7 (credibility = 0.2809). Figure 3.6d contains a sample from character 6 that was classified as 0 (credibility = 0.3362, the highest credibility of an error). Finally, Figure 3.6e shows a sample from character 8 that was classified as 9 (credibility = 0.2383).

### 3.2 Feature selection and dimensionality reduction

High-dimensionality is a big issue that slows down the analysis and hinders scientists from reaching appropriate conclusions. High-dimensional data is usually correlated and it commonly contains useless dimensions.

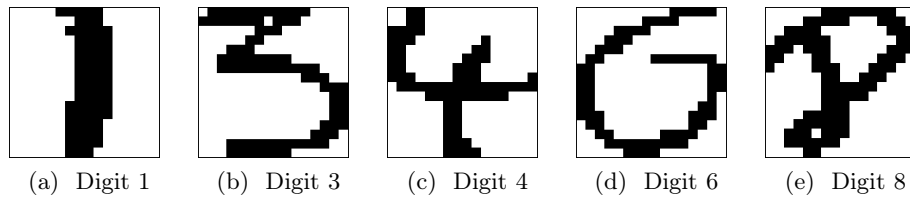


Figure 3.6: Errors with high credibility in the Semeion test set

The techniques introduced in this section are designed to reduce the dimensionality of a data set, maximising the variance covered by the transformed dimensions, the classification rates of the new feature space or finding the most appropriate representation of the data. Section 3.2.1 introduces the Receiver Operating Characteristic Curve. It was initially designed to evaluate classifiers and it can be used to choose the most relevant dimensions of a feature space to classify a given data set. Section 3.2.2 reviews Principal Components analysis. This technique maximises the original variance covered by the data set in the transformed feature space where each new dimension is a linear combination of the dimensions of the original space. Finally, Section 3.2.3 describes Wavelets, a useful tool to data analysis and dimensionality reduction.

In fusion science, dimensionality reduction techniques have been applied, for example, to the dimensionality reduction of the L/H transition (González et al., 2010b), (Vagliasindi et al., 2008), or to the extraction of the most relevant precursors of disruptions in JET (Rattá et al., 2012).

### 3.2.1 The Receiver Operating Characteristic curve

The Receiver Operating Characteristic curve (ROC curve) was introduced by J. P. Egan (Egan, 1975) for the analysis of the tradeoff between hit rates and false alarm rates of classifiers (Fawcett, 2006). Later on, it was applied to the evaluation of algorithms by Spackman (Spackman, 1989). Nowadays, it has several applications e.g. the evaluation of medical diagnostics, the evaluation of classification models or the selection of features.

The ROC curve is a powerful graphing method to explore, analyse and select classifiers based on their performance. In some cases, it is not enough to assess a classifier using only its accuracy (e.g. problems where the class distribution is skewed). The usage of accuracy implies the assumption of equal error costs for false positive and false negative samples and it is not always true. Let's imagine the case of a patient whose health is checked by an automatic classifier. In the case that the patient is healthy, if the classifier fails and predicts that he is ill (false positive), the costs of this error are the negative effects of the medicines in a healthy person. In contrast, if the

patient is ill and the system predicts that he is healthy (false negative) the costs of the error are the consequences of the illness in the patient.

### 3.2.1.1 The ROC curve

Let's consider a discrete classifier as a function  $f$ :

$$f : \mathbb{R}^n \rightarrow \{-1, 1\} \quad (3.43)$$

Given a sample  $s = (x, y)$  where  $x \in \mathbb{R}^n$  is the object space and  $y \in \{-1, 1\}$  is the label space, there are four possible outcomes on classifying  $s$  using  $f$ :

1.  **$f(\mathbf{x}) = -1$  and  $\mathbf{y} = -1$** : the predicted label ( $f(x)$ ) and the real label ( $y$ ) are equal to  $-1$ . The sample  $s$  is called **true negative (TN)**.
2.  **$f(\mathbf{x}) = -1$  and  $\mathbf{y} = 1$** : the classification of the sample  $s$  is  $-1$  but the real label is  $1$ . It is an error and it is called **false negative (FN)**.
3.  **$f(\mathbf{x}) = 1$  and  $\mathbf{y} = 1$** : the prediction  $f(x)$  and the real label  $L$  coincide and they are equal to  $1$ . It is called **true positive (TP)**.
4.  **$f(\mathbf{x}) = 1$  and  $\mathbf{y} = -1$** : the prediction and the real label are different ( $y = -1$ ). It is called **false positive (FP)**.

The most well-known classifier performance metrics are (Fawcett, 2006):

$$FP\ rate = \frac{FP}{N} \quad (3.44)$$

$$FN\ rate = \frac{FN}{P} \quad (3.45)$$

$$TP\ rate = Recall = \frac{TP}{P} = 1 - FN\ rate \quad (3.46)$$

$$TN\ rate = \frac{TN}{N} = 1 - FP\ rate \quad (3.47)$$

$$Precision = \frac{TP}{TP + FP} \quad (3.48)$$

$$Accuracy = \frac{TP + TN}{P + N} \quad (3.49)$$

$$F\text{-measure} = 2 \cdot \frac{Precision \cdot Recall}{Precision + Recall} \quad (3.50)$$

where  $P$  is the number of samples that belong to the class  $1$  and  $N$  is the number of samples of the class  $-1$ .

A ROC graph is a 2D graph in which TP rate is plotted on the Y axis and FP rate is plotted on the X axis. A discrete classifier like  $f$  is plotted in a ROC graph as a single point. The location of the classifier in the ROC graph is  $(FP_{rate}, TP_{rate})$  where  $FP_{rate}$  is the FP rate and  $TP_{rate}$  is the TP rate obtained by the classifier in a test set.

Figure 3.7 includes an example of a ROC graph. There are three different discrete classifiers (A, B and C). The diagonal dashed line represents the performance of randomly guessing the label of the test samples. Since classifiers

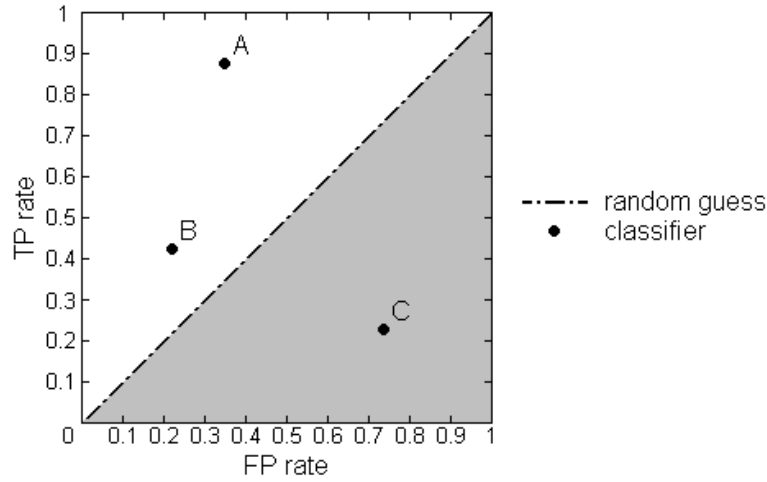


Figure 3.7: Example of a ROC graph

are trained, their performance should be larger than the performance of the random guess and thus, they should appear in the white area of the graph. Classifiers in the grey area (classifier C) may be using some information but they are using it incorrectly (Flach and Wu, 2003). A perfect classifier would be located in the upper-left corner of the graph (FP rate = 0, TP rate = 1).

ROC curves can be obtained only for continuous classifiers or those ones that hedge their predictions with a continuous value:

$$f' : \mathbb{R}^n \rightarrow \mathbb{R} \quad (3.51)$$

Given a threshold  $t \in [-\infty, \infty]$ , a test sample  $s = (x, y)$  is a:

$$\mathbf{True\ Negative:} \quad f'(x) < t \text{ and } y = -1 \quad (3.52)$$

$$\mathbf{False\ Negative:} \quad f'(x) < t \text{ and } y = 1 \quad (3.53)$$

$$\mathbf{True\ Positive:} \quad f'(x) \geq t \text{ and } y = 1 \quad (3.54)$$

$$\mathbf{False\ Positive:} \quad f'(x) \geq t \text{ and } y = -1 \quad (3.55)$$

Given a test set  $S = (x_1, y_1), (x_2, y_2), \dots, (x_m, y_m)$  where  $m$  is the number of samples in  $S$  and a threshold  $t$ , the plot of the classifier in a ROC graph is again a single point  $(FP_{rate}, TP_{rate})$  where  $FP_{rate}$  is the FP rate (Eq. 3.44) and  $TP_{rate}$  is the TP rate (Eq. 3.46) of the test set  $S$  computed using  $t$  (Equations 3.52, 3.53, 3.54 and 3.55).

In order to obtain the complete ROC curve of a classifier, a single ROC point should be computed for every value of  $t$  in the range  $[-\infty, \infty]$ . An efficient algorithm to compute the ROC curve can be found in (Fawcett, 2006). The closer the points of a ROC curve to the point (0,1), the better the classifier.

Four examples of ROC curves can be found in Figure 3.8.

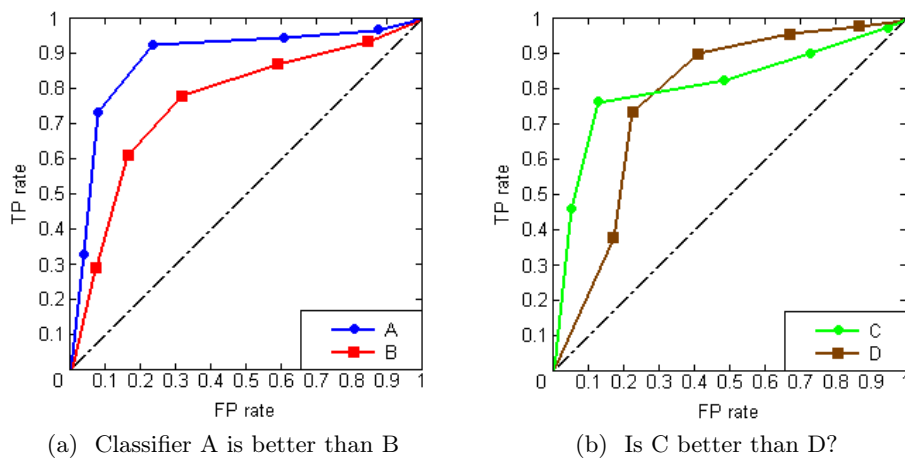


Figure 3.8: ROC curves examples

### 3.2.1.2 The Area Under the ROC curve

On comparing two different classifiers, it is not always possible to decide which one is better just looking at their ROC curves. Let's imagine two classifiers A and B where B's ROC curve is completely enveloped by A's ROC curve (all the points of A's ROC curve are closer to the point (0,1) than the points of B's curve, Figure 3.8a). In this case, classifier A is better than classifier B.

Let's now analyse classifiers C and D in Figure 3.8b. Some points of C's ROC curve are closer to (0,1) than D's points but there are points where D's curve is closer. Therefore, it is not possible to decide which classifier is better. In this case, it is worth using the Area Under the ROC curve to compare the classifiers.

The Area Under the ROC curve (AUC) measures the performance of a classifier. Given two test samples  $s_1 = \{x_1, -1\}$  and  $s_2 = \{x_2, 1\}$ , the meaning of the AUC is the probability of correctly classifying  $s_1$  and  $s_2$  (Hanley and McNeil, 1982). The AUC is within the range  $[0, 1]$  but, since the AUC of the randomly guessing strategy is 0.5, the AUC of a classifier should not be smaller than 0.5.

The AUC value can be computed using the trapezoidal integration (Bradley, 1997):

$$AUC = \sum_{i=2}^n (FP_i - FP_{i-1}) \left( \frac{TP_i + TP_{i+1}}{2} \right) \quad (3.56)$$

where  $n$  is the number of points in the ROC curve.

In order to compare the AUC of two different classifiers, it is important

to measure their Standard Error (SE). SE is computed as (Bradley, 1997):

$$SE = \sqrt{\frac{\hat{\theta}(1 - \hat{\theta}) + (P - 1)(Q_1 - \hat{\theta}^2) + (N - 1)(Q_2 - \hat{\theta}^2)}{P \cdot N}} \quad (3.57)$$

$$Q_1 = \frac{\hat{\theta}}{2 - \hat{\theta}} \quad (3.58)$$

$$Q_2 = \frac{2\hat{\theta}^2}{1 + \hat{\theta}} \quad (3.59)$$

where  $\hat{\theta}$  is the maximum likelihood estimate of AUC (if there are infinite points in the ROC curve then  $\hat{\theta} = AUC$ ),  $P$  is the number of samples belonging to class 1 and  $N$  is the number of samples in class  $-1$ .

To decide whether the difference in the area of two classifiers (A and B) is real or caused by randomness, it is possible to use a critical ratio  $z$  defined as (Hanley and McNeil, 1983):

$$z = \frac{\hat{\theta}_A - \hat{\theta}_B}{\sqrt{SE_A^2 + SE_B^2 - 2rSE_ASE_B}} \quad (3.60)$$

where  $r$  is the estimated correlation between the areas of the classifiers (a correlation table for value  $r$  can be found in Hanley and McNeil, 1983). Values of  $z$  above a certain threshold ( $z = 1.96$  is proposed in the previous article) indicate that the difference between the area of the classifiers is real.

On comparing two different classifiers using the same test set, if their  $z$  value is above the threshold, the best classifier is the one with a larger AUC. In the case that their  $z$  value is below the threshold, the difference of the AUCs is not significant and the systems are equivalent.

### 3.2.1.3 The ROC convex hull

ROC curves are specially adequate in problems where the cost of a false positive classification  $-c_{FP}$  is not equal to the cost of a false negative classification  $-c_{FN}$  (unequal error cost).

A classifier's expected cost can be computed as (Provost and Fawcett, 1997):

$$C = FP \text{ rate} \cdot c_{FP} + FN \text{ rate} \cdot c_{FN} \quad (3.61)$$

A *iso-performance* line represents the points in a ROC graph with the same expected cost (Provost and Fawcett, 2001). Therefore, two classifier in the same *iso-performance* line are equal in terms of expected cost. Given the costs  $c_{FP}$  and  $c_{FN}$ , the slope of a *iso-performance* line is calculated as:

$$m = \frac{c_{FP} \cdot N}{c_{FN} \cdot P} \quad (3.62)$$

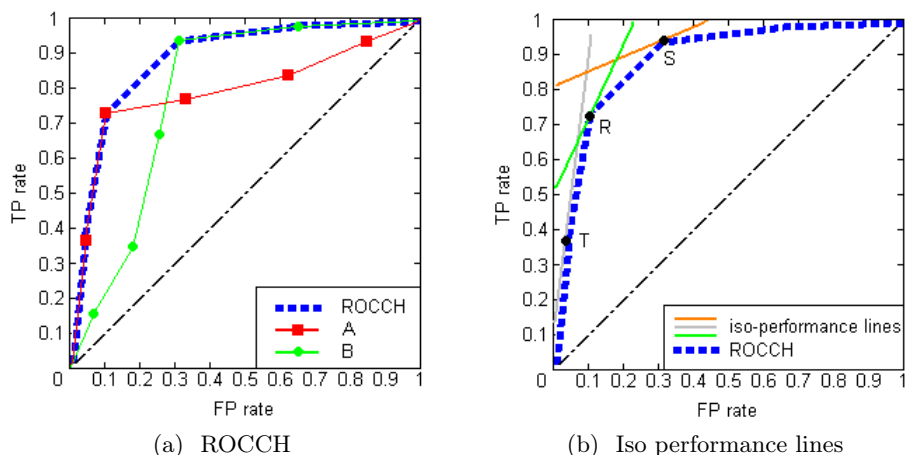


Figure 3.9: ROCCH and iso-performance lines example

where  $P$  is the total number of samples of class 1 and  $N$  is the total number of samples of class  $-1$ . On comparing two iso-performance lines with the same slope  $m$ , the best one is the closest to the point  $(0,1)$  of the ROC graph since it corresponds to classifiers with lower expected cost.

The convex hull of a set of points in a ROC graph is called ROC convex hull (ROCCH, Figure 3.9a). A classifier is potentially optimal if and only if it lies on the ROCCH (Fawcett, 2006).

Given the costs  $c_{FP}$  and  $c_{FN}$  and a ROCCH, the optimal classifier is the one that lies in the tangency point between the best iso-performance line (defined by  $c_{FP}$  and  $c_{FN}$ ) and the ROCCH. Figure 3.9b shows three different iso-performance lines with different slopes. The best classifier of each iso-performance line is in the tangency point of the lines and the ROCCH (points R, S and T). Then, the best classifier selected by the ROC curve varies with the cost of the errors.

#### 3.2.1.4 Example of feature selection using the ROC curves

The ROC curves can select the most important features of a classification problem. Considering each feature as a single classifier, it is possible to plot their performance in a ROC graph and compare them (Theodoridis and Koutroubas, 2009, p. 275). The most significant features are the ones with the largest ROC areas.

This section includes an example of the use of ROC curves for the feature selection of the Fisher's Iris Data (see Appendix B). In this example, the best features to distinguish the *Iris Versicolor* and the *Iris Virginica* classes were identified and the best classifiers for a set of costs functions were found. It has been carried out using *Matlab*®.

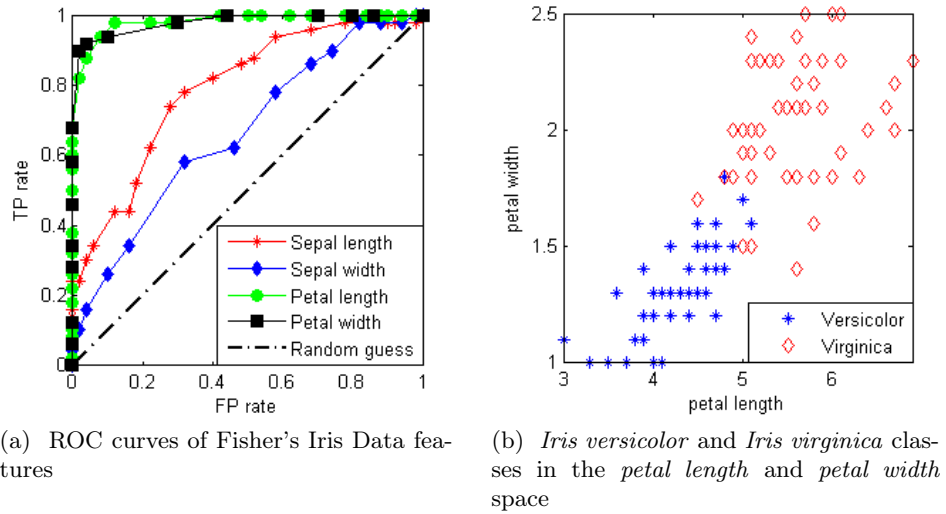


Figure 3.10: ROC analysis of the Fisher's Iris Data features

A feature's ROC curve can be obtained by sweeping the threshold in Equations 3.52, 3.53, 3.54 and 3.55 along the feature's range. The ROC curves obtained by the features in the Fisher's Iris Data can be seen in Figure 3.10a. Analyzing these ROC curves, it was possible to conclude that:

- The classifier using the *sepal width* feature was the worst one. All the points of the other curves were closer to the point (0,1) than its points.
- Classifiers using the *petal length* and the *petal width* features were better than the classifier using the *sepal length* feature.
- It was not possible to assure which one of the classifiers using the *petal length* and *petal width* features was better.

In order to discover which one of the classifiers using the *petal length* and the *petal width* features was more accurate, it was necessary to compute their AUCs: 0.7896 *sepal length*, 0.6636 *sepal width*, 0.9822 *petal length* and 0.9804 *petal width*. The values of AUC certified the analysis of the ROC curves: the shortest area corresponded to the *sepal width* feature (the worst classifier), the AUC value of the *petal width* and the *petal length* classifiers were larger than the *sepal length* AUC. There was a small difference in the areas of the *petal width* and the *pedal length* classifiers and thus it was necessary to compute their  $z$  value (Eq. 3.60) to decide if it was real or caused by randomness.

The standard errors (Eq. 3.57) obtained by the classifiers were: *sepal length* = 0.0455, *sepal width* = 0.0542, *petal length* = 0.0135 and *petal width* = 0.0142. Using these standard errors, it was possible to compute the  $z$

Feature	<i>Petal width</i>	<i>Petal length</i>	<i>Sepal width</i>
<i>Sepal length</i>	4.2670	4.7971	2.1185
<i>Sepal width</i>	6.2254	6.1086	
<i>Petal length</i>	0.1036		

Table 3.2:  $z$  value of the Fisher's Iris Data features

value for each pair of classifiers using Eq. 3.60. Table 3.2 contains the results obtained. As it has been explained in Section 3.2.1.2, values of  $z$  above a certain threshold ( $z = 1.96$ ) indicate that the difference between the area of the classifiers is real. Since the  $z$  value of the *petal width* and the *petal length* classifiers was 0.1036, the difference between their ROC areas was not significant and the classifiers were considered equivalent.

Figure 3.10b shows a plot of the samples of the Fisher's Iris Data in the *petal width* and *pedal length* space. The main reason why these features obtained a large value of the AUC is because it was possible to set a threshold (1.65 for the *petal width* and 4.85 for the *pedal length* approx.) that divided the samples into two classes with a few errors.

Finally, the best classifiers for three different sets of costs values were found. In this example, the number of samples of both classes is the same ( $P = N = 50$ ) and therefore the Equation 3.62 only depended on the values  $c_{FP}$  and  $c_{FN}$ . The results were:

- **$c_{FP} = 2$  and  $c_{FN} = 1$ :** the slope of the iso-performance line was  $m = 2$ . The tangency point between the iso-performance line and the ROCCH was the point  $(0.02, 0.9)$  –  $FP$  rate = 0.02 and  $TP$  rate = 0.9 –. According to Equation 3.61, the cost of the classifier was  $c = 0.02 \cdot 2 + (1 - 0.9) \cdot 1 = 0.14$ . In this case, the best feature was the *petal width* (the tangency point was on the *petal width* ROC curve) using a threshold  $t = 1.7$ . It meant that all the flowers with a *petal width* larger than 1.7 were classified as *Iris Virginica* and all the flowers with a *petal width* smaller or equal to 1.7 were classified as *Iris Versicolor*.
- **$c_{FP} = 1$  and  $c_{FN} = 2$ :** the slope of the iso-performance line was  $m = 0.5$  and the tangency point was  $(0.12, 0.98)$ . The cost of the classifier was  $c = 0.12 \cdot 1 + (1 - 0.98) \cdot 2 = 0.16$ . In this case, the best feature was the *petal length* and the value of the threshold was  $t = 4.7$ . All the flowers with a *petal length* larger than 4.7 were classified as *Iris Virginica* and all the flowers with a *petal length* smaller or equal to 4.7 were classified as *Iris Versicolor*.
- **$c_{FP} = 1$  and  $c_{FN} = 1$ :** this was the special case where the costs of the errors were equal. The slope of the iso-performance line was  $m = 1$  and there were two tangency points on the *petal width* curve:  $P_1 = (0.02, 0.9)$  and  $P_2 = (0.04, 0.92)$ . Since both points were on the same

iso-performance line, their costs coincide:  $c_1 = 0.02 \cdot 1 + (1 - 0.9) \cdot 1 = 0.12$  and  $c_2 = 0.04 \cdot 1 + (1 - 0.92) \cdot 1 = 0.12$ . The points corresponded to the threshold values of the *petal width* feature:  $t_1 = 1.7$  and  $t_2 = 1.6$ .

### 3.2.2 Principal Component Analysis

Principal Component Analysis (PCA) is a statistical methodology for dimensionality reduction. Hotelling is the author of the modern PCA theory and he also coined the term Principal Component (PC) (Hotelling, 1933). However, it is possible to track the origin of PCA back to Pearson (Pearson, 1901) although the approaches of the papers are not the same—Pearson was concerned with finding lines and planes that best fit a set of points in  $p$ -dimensional space and Hotelling defined the standard algebraic derivation of PCs (Jolliffe, 2002).

Given a data set in a  $p$ -dimensional space (there are  $p$  coordinates, dimensions or features), the main idea behind the method is to create a new set of  $q$  orthonormal features ( $q \ll p$ ) that are a linear combination of the original ones, retaining most of the variation present in the original dimensions. The PCs are ordered so that the first PC retains more variation than next ones. The total number of PCs is equal to the number of dimensions in the original space  $p$ . The reduced space is made up of the first  $q$  PCs (the first  $q$  PCs with the highest variation). PCs are calculated as follows (Jolliffe, 2002):

Let's assume a vector of variables  $x$  of dimension  $p$  with a known covariance matrix  $\Sigma$  where the element  $(i, j)$ ,  $i \neq j$  is the covariance between the  $i^{th}$  and  $j^{th}$  dimensions of  $x$  ( $i, j \leq p$ ) and the variance of the  $j^{th}$  dimension of  $x$  if  $i = j$ . The  $k^{th}$  PC of  $x$  ( $PC_k$ ) is given by:

$$z_k = \alpha'_k x \quad (3.63)$$

where  $\alpha_k$  is the eigenvector of  $\Sigma$  corresponding to its  $k^{th}$  largest eigenvalue ( $\lambda_k$ ). If  $\alpha'_k \alpha_k = 1$  then  $var(z_k) = \lambda_k$  where  $var(z_k)$  is the variance of  $z_k$ .

Finding the first PC ( $PC_1$ , the PC with the largest variance) is the same as finding the vector  $\alpha_1$  that maximises  $var(z_k) = \alpha'_1 \Sigma \alpha_1$  subject to the constraint  $\alpha'_1 \alpha_1 = 1$ . This optimisation problem can be solved using the Lagrange multipliers:

$$\alpha'_1 \Sigma \alpha_1 - \lambda (\alpha'_1 \alpha_1 - 1), \quad (3.64)$$

deriving with respect to  $\alpha_1$

$$(\Sigma - \lambda I_p) \alpha_1 = 0 \quad (3.65)$$

where  $I_p$  is the identity matrix of size  $p$ . Therefore,  $\lambda$  is an eigenvalue of  $\Sigma$  and  $\alpha_1$  is its corresponding eigenvector.

In order to obtain the eigenvector that gives  $\alpha_1'x$  with maximum variance,  $\alpha_1'\Sigma\alpha_1$  must be maximised:

$$\alpha_1'\Sigma\alpha_1 = \alpha_1'\lambda\alpha_1 = \lambda\alpha_1'\alpha_1 = \lambda \quad (3.66)$$

therefore  $\lambda$  must be as large as possible. Then,  $PC_1$  is computed using the eigenvector corresponding to the largest eigenvalue of  $\Sigma$ :  $PC_1 = \alpha_1'x$ . The variance of  $PC_1$  is:  $var(\alpha_1'x) = \alpha_1'\Sigma\alpha_1 = \lambda_1$ , its eigenvalue.

The  $k^{th}$ ,  $k = 1, \dots, p$  PC can be obtained using Equation 3.63. The  $\alpha$  matrix is commonly known as PCs coefficients or loadings.

### 3.2.2.1 Representation of data using PCs

One of the goals of PCA is to simplify the description of a data set (Abdi and Williams, 2010). It is achieved in two different ways:

1. **Reducing the number of dimensions:** given a data set in a  $p$ -dimensional space, it is possible to represent it using only the first  $q$  PCs. The representation of the original data in a reduced subspace of  $q$  dimensions is good if the total variance covered by the  $q$  PCs is close to the total amount of variance of the data in the  $p$ -dimensional space.
2. **Finding the best representation of the data:** the representation of a data set in a  $q$ -dimensional subspace made up of the first  $q$  PCs is the best possible in the sense that this representation minimises the sum of squared perpendicular distances of the data set from the subspace (Jolliffe, 2002).

Figure 3.11 includes an example of the analysis of a data set using PCA. The data set in the original two dimensional space  $(X_1, X_2)$  is shown in Figure 3.11a. Figure 3.11b contains a plot of the data set in the PCs space  $(PC_1, PC_2)$ . The first PC ( $PC_1$ ) is defined along the maximum variance axis of the data. The second PC ( $PC_2$ ) is an orthonormal axis to  $PC_1$ . This example illustrates how PCA can be used to find the best representation of the data. An example of the reduction of the data dimensionality can be found in the section 3.2.2.4.

### 3.2.2.2 Determining the optimal number of PCs

Given a data set in a  $p$ -dimensional space, it is possible to use PCA to find a  $q$ -dimensional space ( $q \ll p$ ) that retains most of the data variance. The problem, now, is to decide how many PCs ( $q$ ) are necessary to use in order to obtain a good representation of the data set in the  $q$ -dimensional space. There are several methods to choose the value of  $q$ . Some of the most important ones are described below (Jackson, 1993), (Peres-Neto et al., 2005):

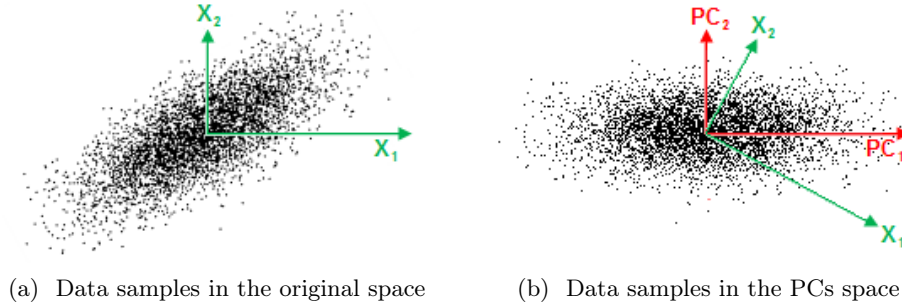


Figure 3.11: Example of PCA

**Proportion of the total variance.** It is probably the easiest method for choosing  $q$ . It simply consists of including the first  $q$  PCs up to some arbitrary proportion of the total variance. Therefore, given a proportion of the total variance  $\tau$  ( $0 < \tau < 1$ ),  $q$  is the smallest value for which:

$$\sum_{k=1}^q \lambda_k \geq \tau \cdot \sum_{k=1}^p \lambda_k \quad (3.67)$$

where  $p$  is the number of dimensions of the original data space and  $\lambda_k$  is the variance of  $PC_k$ .

**Kaiser-Guttman method.** The basic idea of the Kaiser-Guttman method is to retain those PCs with a variance larger than the variance of any single original component (computed as the total variance divided between the number of components). A  $PC_k$  is retained if:

$$\lambda_k > \frac{1}{p} \sum_{i=1}^p \lambda_p \quad (3.68)$$

where  $p$  is the number of dimensions of the original data space and  $\lambda_k$  is the variance of  $PC_k$ .

**The broken-stick rule.** If the total variance of a data set is divided randomly amongst the dimensions of the space, the variance values are supposed to follow a broken-stick distribution. Only PCs with variance values larger than the generated by the broken-stick distribution are retained.

The value of the broken-stick model of the  $PC_k$  can be calculated as:

$$b_k = \frac{1}{p} \sum_{i=k}^p \frac{1}{i} \quad (3.69)$$

where  $p$  is the number of dimensions of the original data space.

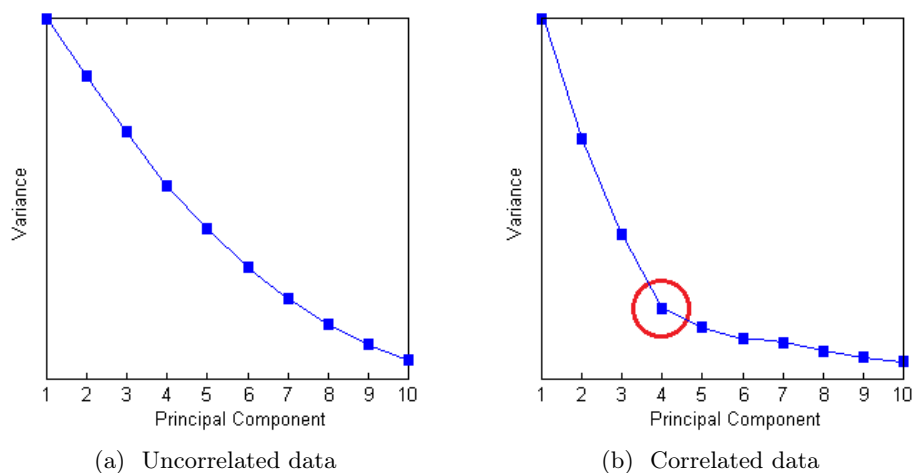


Figure 3.12: Example of two scree plots

**The Scree Plot.** This is a visual method for determining the value of  $q$ . It consists of a plot of the variance (eigenvalue) of all the PCs in decreasing order. If the data in the original space is correlated, then, the first  $q$  PCs cover a high amount of the total variance while the other  $p - q$  PCs just cover a little. In the scree plot an *elbow* appears in the point  $q$ . Therefore, the new subspace is made up of the PCs 1 to  $q$ . If the data are not correlated, no elbow appears in the scree plot.

Figure 3.12 includes an example of the scree plots of two different data sets. Data in 3.12a is uncorrelated and therefore, there is not an elbow in the scree plot. It is not possible to choose the number of PCs using the scree plot. On the contrary, data in Figure 3.12b is correlated and thus an elbow appears in the scree plot ( $q = 4$ ).

### 3.2.2.3 The Singular Value Decomposition

The Singular Value Decomposition (SVD) method gives a computationally efficient method of computing PCs (Jolliffe, 2002).

Let's assume a matrix  $X$  of  $n$  observations on a  $p$ -dimensional space centred in their means. Then,  $X$  can be expressed as:

$$X = ULA', \quad \text{where:} \quad (3.70)$$

$U$ ,  $A$  are matrices of size  $U = (n \times r)$  and  $A = (p \times r)$  so that  $U'U = I_r$  and  $A'A = I_r$ ;  $L$  is a diagonal matrix of size  $L = (r \times r)$  where  $r$  is the rank of  $X$  and  $ULA'$  is the transpose matrix of  $ULA$ .

Finding  $U$ ,  $L$  and  $A$  satisfying 3.70, the coefficients and standard deviation of the PCs are given by  $A$  and  $L$ .  $U$  contains a scaled version of the PCs scores. The PCs scores are given by  $Z = UL$ .

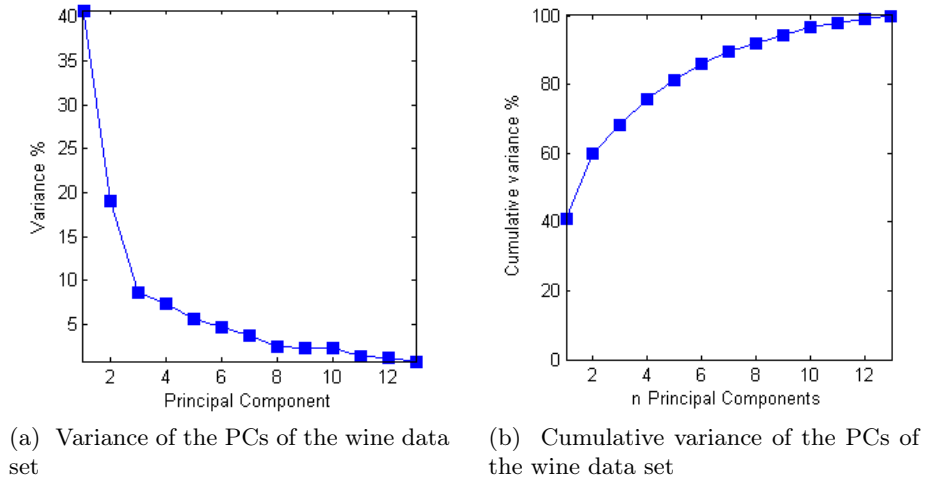


Figure 3.13: PCA results of the wine data set

### 3.2.2.4 Example of Principal Component Analysis for dimensionality reduction

This section includes an example of the use of PCA for the reduction of the dimensionality of a wine data set (see Appendix C).

The original data set contains 13 features and 178 samples. The features were normalised between 0 and 1 and then their mean value were subtracted (as a result the features were centred in 0). The PCA analysis was carried out using *Matlab*®.

Figure 3.13a includes a plot of the total amount of variance covered by each one of the principal components. Figure 3.13b includes the cumulative variance covered by the first  $n$  principal components.

Using the scree plot technique for determining the number of PCs, it was possible to observe that there was an elbow in Figure 3.13a at  $PC = 3$ . Thus, the optimal subspace was made up of the three first PCs. Figure 3.14 includes the visualization of the data in the PCs subspace using the first two (Figure 3.14a) and three (Figure 3.14b) PCs.

The percentages of total variance covered by the first three PCs were 40.75%, 18.97% and 8.56% respectively. The cumulative total variance covered by these PCs was 68.28%. Using the method of the proportion of the total variance for determining the number of PCs, if 90% of the total variance was retained ( $\tau = 0.9$ ), then the number of PCs was 8, much larger than using the scree plot method. In the case of using the Kaiser-Guttman method, only the PCs with a variance larger than  $1/13 = 7.69\%$  were retained (the first three PCs).

Table 3.3 contains the loadings of the three first PCs obtained analysing

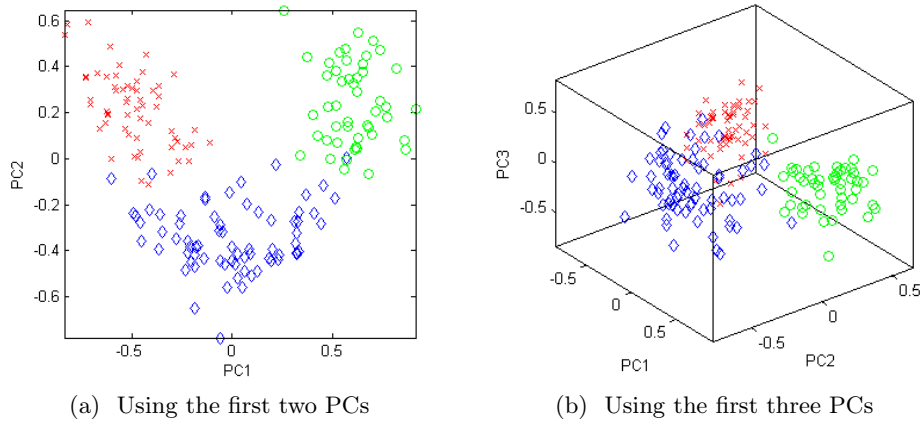


Figure 3.14: Visualization of the wine data set using PCs

the wine data set. All the PCs are orthonormal vectors and therefore  $PC_1 \cdot PC_2 = PC_1 \cdot PC_3 = PC_2 \cdot PC_3 = 0$ .

### 3.2.3 Wavelet analysis

Wavelet analysis is a technique to analyse 1-D data (waveforms) and 2-D data (images). Using wavelets, it is possible to decompose the original data into different frequency subspaces. It has many applications e.g. de-noising and compressing data, detecting discontinuities, breakdown points and long-term evolutions or acoustic signals compression.

Wavelets are an extension of Fourier analysis (Burke, 1996, p. 5). The advantage of wavelets versus Fourier analysis is that wavelets have good location properties in both, the time and the frequency domains (Fourier analysis does not give much information about the time domain of the data).

It is possible to define a wavelet as a function  $\psi \in \mathbf{L}^2(\mathbb{R})$ , normalised ( $\|\psi\| = 1$ ), centred in the neighbourhood of  $t = 0$  and with a zero average:

$$\int_{-\infty}^{+\infty} \psi(t) dt = 0 \quad (3.71)$$

where  $\mathbf{L}^2(\mathbb{R})$  denotes the vector space of functions  $f(x)$  squared-integrable (Mallat, 1999, p. 79).

After translating  $\psi$  by  $u$  and scaling it by  $s$ , it is given by:

$$\psi_{u,s}(t) = \frac{1}{\sqrt{s}} \psi\left(\frac{t-u}{s}\right) \quad (3.72)$$

where  $\psi_{u,s}$  is still normalised ( $\|\psi_{u,s}\| = 1$ ).

Attribute	PC <sub>1</sub>	PC <sub>2</sub>	PC <sub>3</sub>
Alh	-0.1334	0.5509	0.0838
MAc	0.2485	0.2274	-0.4920
Ash	-0.0007	0.1631	-0.4030
Alc	0.1778	-0.0798	-0.4772
Mag	-0.0887	0.1882	-0.0066
TPh	-0.3951	0.0741	-0.2531
Fla	-0.4146	0.0010	-0.1961
NFl	0.3331	0.0100	-0.2860
Pan	-0.2529	0.0314	-0.2283
Cln	0.0923	0.5197	0.0331
Hue	-0.2511	-0.2372	0.1066
ODW	-0.4735	-0.2156	-0.2978
Pli	-0.2869	0.4439	0.1520

Table 3.3: Coefficients (loadings) of the three first PCs of the wine data set

Given a one-dimensional function  $f \in \mathbf{L}^2$ , a time  $u$  and a scale  $s$ , the wavelet transform of  $f$  is defined by:

$$Wf(u, s) = \langle f, \psi_{u,s} \rangle = \int_{-\infty}^{+\infty} f(t) \frac{1}{\sqrt{s}} \psi^* \left( \frac{t-u}{s} \right) dt \quad (3.73)$$

Equation 3.73 can be written as the convolution product of  $f$  and  $\psi$ :

$$Wf(u, s) = f * \bar{\psi}_s(u) \quad (3.74)$$

where:

$$\bar{\psi}_s(t) = \frac{1}{\sqrt{s}} \psi^* \left( \frac{-t}{s} \right) \quad (3.75)$$

The Fourier transform of  $\bar{\psi}_s(t)$  is:

$$\hat{\bar{\psi}}_s(w) = \sqrt{s} \hat{\psi}^*(sw) \quad (3.76)$$

$\hat{\psi}$  is the transfer function of a band-pass filter ( $\hat{\psi}(0) = \int_{-\infty}^{+\infty} \psi(t) dt = 0$ ).

To construct a translation-invariant wavelet representation, the scale  $s$  is discretised along a dyadic sequence  $\{2^j\}_{j \in \mathbb{Z}}$ . The dyadic wavelet transform of  $f \in \mathbf{L}^2(\mathbb{R})$  is given by (Mallat, 1999, p. 148):

$$Wf(u, 2^j) = \int_{-\infty}^{+\infty} f(t) \frac{1}{\sqrt{2^j}} \psi \left( \frac{t-u}{2^j} \right) dt = f * \bar{\psi}_{2^j}(u) \quad (3.77)$$

where

$$\bar{\psi}_{2^j}(t) = \psi_{2^j}(-t) = \frac{1}{\sqrt{2^j}} \psi \left( \frac{-t}{2^j} \right) \quad (3.78)$$

Using the wavelet analysis, it is possible to build a multi-resolution representation of data based on the differences of information available at two successive resolutions (detail levels)  $2^j$  and  $2^{j+1}$  (Mallat, 1989). The multi-resolution representation provides a scale-invariant hierarchical representation of data. Each one of these detail levels contains different information of the data being analysed. On the one hand, levels with a low resolution contain information about the larger patterns in the data (low frequency phenomena) such as long-term evolutions. On the other hand, levels with a high resolution represent the smaller details of the data (high frequency phenomena) such as peaks or heart-beats.

Let's suppose two finite impulse response filters  $h$  and  $g$  where  $h$  is a low-pass filter whose transfer function satisfies  $\hat{h}(0) = \sqrt{2}$ . We design a scaling function whose Fourier transform is:

$$\hat{\phi}(w) = \prod_{p=1}^{+\infty} \frac{\hat{h}(2^{-p}w)}{\sqrt{2}} = \frac{1}{\sqrt{2}} \hat{h}\left(\frac{w}{2}\right) \hat{\phi}\left(\frac{w}{2}\right) \quad (3.79)$$

Assuming that  $\phi \in \mathbf{L}^2(\mathbb{R})$ , its wavelet transform  $\psi$  has a Fourier transform defined by (Mallat, 1999, p. 150):

$$\hat{\psi}(w) = \frac{1}{\sqrt{2}} \hat{g}\left(\frac{w}{2}\right) \hat{\phi}\left(\frac{w}{2}\right) \quad (3.80)$$

The relation between  $h$  and  $g$  obtained from Equation 3.80 is (Mallat, 1989):

$$g(n) = (-1)^{1-n} h(1-n) \quad (3.81)$$

where  $g$  is the mirror filter of  $h$  and therefore  $g$  is a high-pass filter.

For each level of resolution  $j$  two different types of structures are obtained:  $a_j$  and  $d_j$ .  $a_j$  is the approximation of the signal  $f(x)$  at the resolution  $2^j$ , and it is equal to (Mallat, 1989):

$$a_j = ((f(u) * \phi_j(-u)) (2^{-j}n))_{n \in \mathbb{Z}} \quad (3.82)$$

Since  $\phi(x)$  is a low-pass filter,  $a_j$  is a low-pass filtering of  $f(x)$  followed by a uniform sampling at the rate  $2^j$  (the number of samples in  $a_j$  has been reduced by  $2^j$ ). Therefore, the details of  $f(x)$  smaller than  $2^{-j}$  are removed (higher frequency details).

$d_j$  is the detail signal at the resolution  $2^j$ . It contains the difference of information between the approximation coefficients at the levels  $j$  and  $j+1$  ( $a_j$  and  $a_{j+1}$ ).  $d_j$  is defined as (Mallat, 1989):

$$d_j = ((f(u) * \psi_j(-u)) (2^{-j}n))_{n \in \mathbb{Z}} \quad (3.83)$$

$d_j$  describes  $f(x)$  in the frequency bands:

$$[-2^{-j-1}\pi, -2^{-j}\pi] \cup [2^{-j}\pi, 2^{-j-1}\pi] \quad (3.84)$$

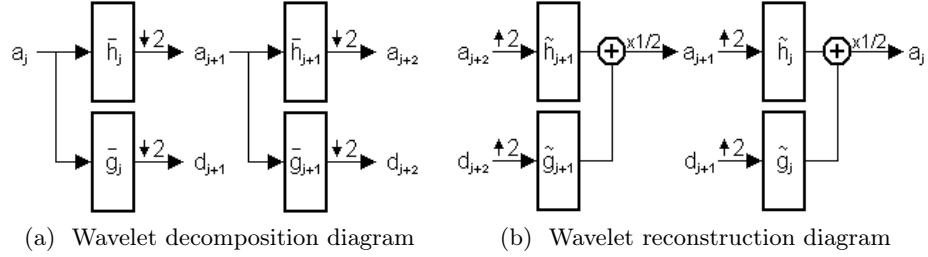


Figure 3.15: Wavelet hierarchical representation

Figure 3.15 includes a representation of the wavelet hierarchy. Figure 3.15a represents the wavelet multi-resolution decomposition process. Starting from the approximation coefficients of level  $j$  ( $a_j$ ), it is possible to obtain the approximation and the detail coefficients of level  $j + 1$  using the filters  $h_j$  and  $g_j$ . The coefficients  $a_{j+1}$  and  $d_{j+1}$  have half of the points of  $a_j$ . Repeating this process, it is possible to obtain the coefficients  $a_{j+2}$  and  $d_{j+2}$  from  $a_{j+1}$  applying  $h_{j+1}$  and  $g_{j+1}$ .

In order to reconstruct the coefficients of  $a_{j+1}$  from  $a_{j+2}$  and  $d_{j+2}$  (Figure 3.15b),  $a_{j+2}$  and  $d_{j+2}$  must be resampled adding zeros between each one of their coefficients. Then, the filters  $h_{j+1}$  and  $g_{j+1}$  are applied and their sum times  $1/2$  is equal to  $a_{j+1}$ . The process can be iterated until the original data is obtained.

### 3.2.3.1 Wavelet application to images

The wavelet multi-resolution decomposition can be extended to 2-D data. This enables us to use the properties of wavelets in images. Let's assume a 1-D wavelet  $\psi(x)$  generated using a scaling function  $\phi(x)$ . The three 2-D wavelets:

$$\Psi^V(x, y) = \phi(x)\psi(y) \quad (3.85)$$

$$\Psi^H(x, y) = \psi(x)\phi(y) \quad (3.86)$$

$$\Psi^D(x, y) = \psi(x)\psi(y) \quad (3.87)$$

are an orthonormal basis of  $\mathbf{L}^2(\mathbb{R}^2)$  (Mallat, 1989).

In this case, each decomposition level  $j$  contains the approximation coefficients ( $a_j$ ) and three different detail coefficients vectors:  $d_j^V$  is the vector of the vertical high frequencies coefficients,  $d_j^H$  is the vector containing the horizontal high frequencies and  $d_j^D$  is the vector of the high frequencies in both directions. The 2-D wavelet gives a set of independent and spatially oriented frequency channels. Thus, in  $d_j^V$  we obtain the horizontal edges of the image, in  $d_j^H$  we obtain the vertical edges and  $d_j^D$  contains the corners of the image.

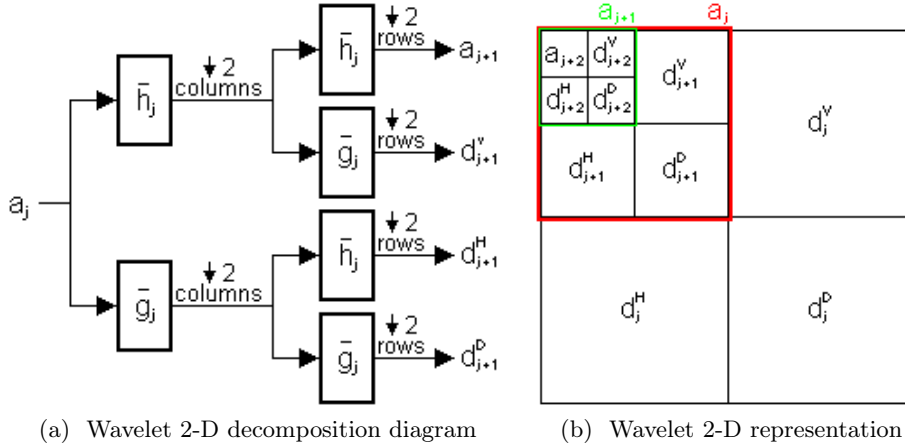


Figure 3.16: 2-D Wavelet hierarchical representation

The values of the coefficients of a 2-D wavelet decomposition can be obtained by (Mallat, 1989):

$$a_j = ((f(x, y) * \phi_j(-x)\phi_j(-y)) (2^{-j}n, 2^{-j}m))_{(n,m) \in \mathbb{Z}^2} \quad (3.88)$$

$$d_j^V = ((f(x, y) * \phi_j(-x)\psi_j(-y)) (2^{-j}n, 2^{-j}m))_{(n,m) \in \mathbb{Z}^2} \quad (3.89)$$

$$d_j^H = ((f(x, y) * \psi_j(-x)\phi_j(-y)) (2^{-j}n, 2^{-j}m))_{(n,m) \in \mathbb{Z}^2} \quad (3.90)$$

$$d_j^D = ((f(x, y) * \psi_j(-x)\psi_j(-y)) (2^{-j}n, 2^{-j}m))_{(n,m) \in \mathbb{Z}^2} \quad (3.91)$$

Figure 3.16a includes a diagram of the wavelet decomposition applied to 2-D data. Figure 3.16b shows the wavelet representation of images. The original image is decomposed reducing its size by 2 in two directions (columns and rows). Thus, the size of the approximation ( $a_1$ ) and the detail coefficients is a quarter of the original image's size. The sum of the size of all the coefficients is the size of the original image. The size of the coefficients of level 2 is a quarter of the size of the  $a_1$  coefficients and a sixteenth part of the size of the original image. Using this representation, the approximation coefficients (or their wavelet decomposition) are placed in the upper-left corner of the resulting image. The  $d_j^V$  coefficients are placed in the upper-right corner, the  $d_j^H$  coefficients are placed in the lower-left corner and finally the  $d_j^D$  coefficients are placed in the lower-right corner of the resulting image.

### 3.2.3.2 Example of image decomposition using wavelets

This section includes an example of the use of the wavelets to decompose an image. The image analysed in this example can be found in Figure 3.17a. It is a photograph of the acropolis in Calton Hill, Edinburgh. This example used *Matlab*©.

The Haar wavelet (Haar, 1910) was chosen to analyse this image. This wavelet is given by:

$$\psi(t) = \begin{cases} 1 & \text{if } 0 \leq t < 1/2 \\ -1 & \text{if } 1/2 \leq t < 1 \\ 0 & \text{otherwise} \end{cases} \quad (3.92)$$

The image was decomposed to level 2 obtaining the results in Figure 3.17b. The sum of the size of the level 1 coefficients ( $a_1, d_1^V, d_1^H$  and  $d_1^D$ ) is equal to the size of the original image. The value of the  $d_1^V$  coefficients (upper-right corner) is higher in the points of the image where there is an horizontal edge. As it can be seen in the image, the roof and the steps contained the largest horizontal edges. In the case of the  $d_1^H$  coefficients (lower-left corner), they are higher where there is a vertical edge and therefore, the columns appeared clearly delimited. The  $d_1^D$  coefficients (lower-right corner) contain the corners of the original image. The approximation coefficients at level 1 ( $a_1$ ) were decomposed obtaining the coefficients of level 2 that appear in the upper-left corner of Figure 3.17b. Again, the highest values of the  $d_2^V, d_2^H$  and  $d_2^D$  coefficients correspond to the horizontal and vertical edges and the corners of the  $a_1$  coefficients. The approximation coefficients of level 2 ( $a_2$ ) appear in the upper-left corner of the resulting image.

### 3.3 Regression

Regression is a statistical tool to explain the behaviour of a dependent variable ( $Y$ ) as a function of a set of explanatory variables ( $X_1, X_2, \dots, X_p$ ). The general regression equation is given by (Chatterjee and Hadi, 2006, p. 2):

$$Y = f(X_1, X_2, \dots, X_p) + \epsilon \quad (3.93)$$

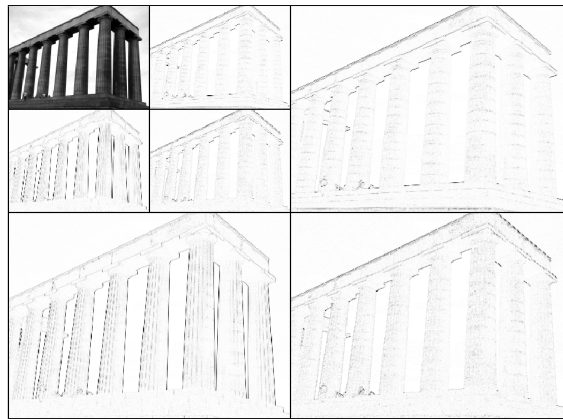
where  $\epsilon$  is the estimation error between the regression function and the dependent variable.

When the dependent variable  $Y$  is a linear function of the explanatory variables, Ordinary Least Squares (Section 3.3.1) can be applied to obtain a regression function. Unfortunately, this method is largely biased by outlier samples. Robust Regression (Section 3.3.2) is a linear regression technique that obtains better results than Ordinary Least Squares in the presence of outliers. Ridge Regression (Section 3.3.3) is also a linear regression technique that solves the problem of collinearity among explanatory variables. The last method described in this section, Support Vector Regression, is a regression technique that can obtain non-linear regression functions.

In fusion science, regression is commonly applied to compute scaling laws. These laws are intended to predict the behaviour of future fusion devices (usually bigger than the existing ones) using data from current experiments.



(a) Original image



(b) Wavelet decomposition

Figure 3.17: 2-D wavelet decomposition example

For example, scaling laws for the H-mode power threshold  $P_\tau$  (see Section 2.2.1) have been computed in (González et al., 2012a) and (Martin et al., 2008).

### 3.3.1 Ordinary Least Squares

Ordinary Least Squares (OLS), or simply Least Squares (LS), is a linear regression technique that finds the regression coefficients ( $\beta$ ) that minimise the sum of square errors (the differences between the dependent variable  $Y$  and the estimation  $\hat{Y}$ ).

Given a set of  $n$  observations and  $p$  predictor or explanatory variables ( $X$ ), the relation between  $Y$  and  $X$  is given by (Chatterjee and Hadi, 2006, p. 53):

$$Y = \beta_0 + \beta_1 X_1 + \beta_2 X_2 + \dots + \beta_p X_p + \epsilon \quad (3.94)$$

Equation 3.94 can be written in matrix notation as:

$$Y = X\beta + \epsilon \quad (3.95)$$

The error in the estimation of a sample  $i$ ,  $1 \leq i \leq n$  is given by:

$$\epsilon_i = y_i - \beta_0 - \beta_1 x_{i,1} - \dots - \beta_p x_{i,p} \quad (3.96)$$

and the sum of square errors is equal to:

$$S(\beta_0, \beta_1, \dots, \beta_p) = \sum_{i=1}^n \epsilon_i^2 = \sum_{i=1}^n (y_i - \beta_0 - \beta_1 x_{i,1} - \dots - \beta_p x_{i,p})^2 \quad (3.97)$$

OLS finds an estimation of the regression coefficients ( $\hat{\beta}$ ) that minimises the sum of square errors in Equation 3.97. Using the matrix notation, the estimated regression coefficients are obtained as (Draper and Smith, 1998, p. 136):

$$\hat{\beta} = (X'X)^{-1} X'Y \quad (3.98)$$

The term  $\hat{\beta}_0$  is called constant and the coefficients  $\hat{\beta}_1, \dots, \hat{\beta}_p$  are called the estimators of the regression coefficients. The fitted regression values ( $\hat{Y}$ ) are computed using the estimator of the regression coefficients:

$$\hat{Y} = \hat{\beta}_0 + \hat{\beta}_1 X_1 + \dots + \hat{\beta}_p X_p \quad (3.99)$$

The residuals are given by:

$$\epsilon = Y - \hat{Y} \quad (3.100)$$

### 3.3.2 Robust Regression

One problem of OLS is that it is heavily conditioned by outlier samples (samples far from the regression hyperplane). The square errors of the outliers are significantly larger than the ones of the samples close to the regression hyperplane. As a result, OLS tries to minimise these quantities and the regression model can be not good enough.

Robust Regression (RR) solves this problem using a weight function called *M-estimator*. This function gives a specific weight to the samples in the data set based on their residuals. The weights oscillate between 0 and 1. In contrast to OLS where the sum of square errors is minimised (Equation 3.97), given a set of  $n$  observations ( $X$ ), RR minimises the sum of the weights given by the M-estimator (Draper and Smith, 1998, p. 569):

$$\sum_{i=1}^n \rho\left(\frac{\epsilon_i}{s}\right) = \sum_{i=1}^n \rho\left(\frac{y_i - x_i' \beta}{s}\right) \quad (3.101)$$

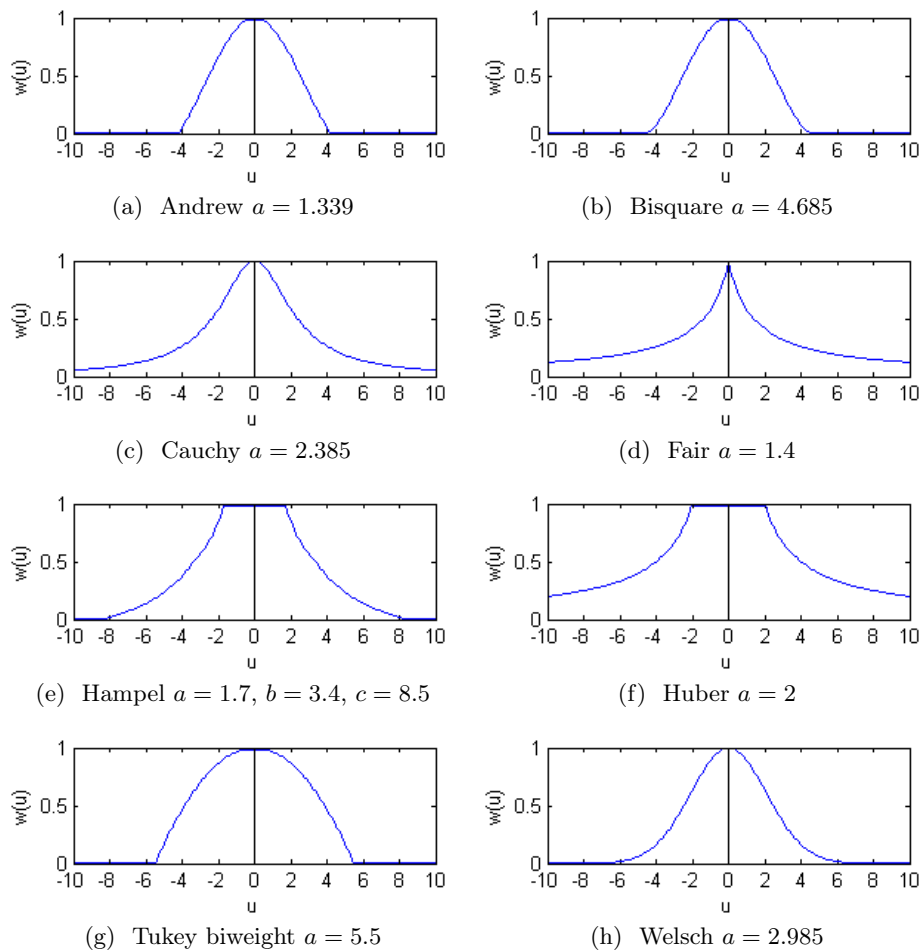


Figure 3.18: M-estimator functions

where:

- $\rho$  : is a M-estimator
- $\epsilon_i$  : is the residual of the sample  $i$
- $s$  : is an estimate of scale
- $y_i$  : is the value of the dependent variable  $Y$  for the sample  $i$
- $\beta$  : is the vector of regression coefficients

The drawback using RR is that if the distribution of residuals is unknown, no assumption can be made in order to choose an appropriate M-estimator. Table 3.4 contains 8 functions that can be used as M-estimators. Figure 3.18 shows the weights generated by the functions in Table 3.4 for values of  $u = \epsilon_i/s$  between  $-10$  and  $+10$ .

Name	$\rho(u)$	$w(u) = \frac{1}{u} \cdot \frac{\partial \rho(u)}{\partial u}$	Range
Andrew	$\begin{cases} a[1 - \cos(u/a)] \\ 2a \end{cases}$	$\begin{cases} \sin(u/a)/(u/a) \\ 0 \end{cases}$	$\begin{cases} -a\pi \leq u \leq a\pi \\ u \leq -a\pi \text{ and } u \geq a\pi \end{cases}$
Bisquare	$\begin{cases} a^2/6 \left\{ 1 - \left[ 1 - (u/a)^2 \right]^3 \right\} \\ a^2/6 \end{cases}$	$\begin{cases} \left[ 1 - (u/a)^2 \right]^2 \\ 0 \end{cases}$	$\begin{cases} -a \leq u \leq a \\ u \leq -a \text{ and } u \geq a \end{cases}$
Cauchy	$\frac{a^2}{2} \log(1 + (u/a)^2)$	$\frac{1}{1 + (u/a)^2}$	$-\infty \leq u \leq \infty$
Fair	$a^2 \left[ \frac{ u }{a} - \log\left(1 + \frac{ u }{a}\right) \right]$	$\frac{1}{1 +  u /a}$	$-\infty \leq u \leq \infty$
Hampel	$\begin{cases} u^2/2 \\ a u  - a^2/2 \\ a \frac{c u  - u^2/2}{c-b} - \frac{7a^2}{6} \\ a \frac{c-b}{a(b+c-a)} \end{cases}$	$\begin{cases} 1 \\ a/ u  \\ \frac{(c/ u  - 1)a}{c-b} \\ 0 \end{cases}$	$\begin{cases} -a \leq u \leq a \\ -b \leq u \leq -a \text{ and } a \leq u \leq b \\ -c \leq u \leq -b \text{ and } b \leq u \leq c \\ u \leq -c \text{ and } u \geq c \end{cases}$
Huber	$\begin{cases} u^2/2 \\ a u  - a^2/2 \end{cases}$	$\begin{cases} 1 \\ a/ u  \end{cases}$	$\begin{cases} -a \leq u \leq a \\ u \leq -a \text{ and } u \geq a \end{cases}$
Tukey biweight	$\begin{cases} u^2/2 - \frac{u^4}{4a^2} \\ a^2/4 \end{cases}$	$\begin{cases} 1 - u^2/a^2 \\ 0 \end{cases}$	$\begin{cases} -a \leq u \leq a \\ u \leq -a \text{ and } u \geq a \end{cases}$
Welsch	$\frac{a^2}{2} \left( 1 - e^{-(u/a)^2} \right)$	$e^{-(u/a)^2}$	$-\infty \leq u \leq \infty$

Table 3.4: M-estimator functions

The regression coefficients  $\beta$  are obtained minimising Equation 3.101.  $\beta$  can be computed using the iterative equation (Draper and Smith, 1998, p. 572):

$$\hat{\beta}_{q+1} = (X'W_qX)^{-1}X'W_qY \quad (3.102)$$

where  $W_q$  is the diagonal matrix whose diagonal elements are  $(w_{1\beta}, w_{2\beta}, \dots, w_{n\beta})$  and:

$$w_{i\beta}(u) = \frac{1}{u} \cdot \frac{\partial \rho(u)}{\partial u} \quad (3.103)$$

Next section includes an example illustrating the advantages of RR versus OLS.

### 3.3.2.1 Ordinary Least Squares versus Robust Regression example

This Section illustrates the difference in the results obtained by OLS and RR in the presence of outliers in the data.

The explanatory variable was  $X = [4.1, 5.3, 3.2, 3.9, 3.6, 5.5, 5.7, 7.3, 9.1, 7.3, 8.2]$  and the dependent variable was  $Y = [2.0, 2.1, 1.9, 0.2, 7.9, 2.4, 4.1, 5.9, 6.2, 3.5, 4.0]$ . The point  $[3.6, 7.9]$  was an outlier.

Four regressions were computed: one using OLS and three using RR and the M-estimators *Huber*, *Cauchy* and *bisquare*. The data set and the regression lines obtained by the methods are shown in Figure 3.19. It is important to note that the regression line obtained using OLS is biased by the presence of the outlier in the data set. In contrast, RR obtained good results thanks to the weights given to the regression samples. Since the weights given by RR are a function of the M-estimation, the regression lines computed by the three RR methods were different.

The regression equations obtained are:

OLS:	$Y = 0.4568X + 1.0303$
RR Huber $a = 1.345$ :	$Y = 0.6969X - 0.7456$
RR Cauchy $a = 2.385$ :	$Y = 0.741X - 0.8384$
RR bisquare $a = 4.685$ :	$Y = 0.8071X - 1.5849$

### 3.3.3 Ridge Regression

In 1970, Arthur E. Hoerl and Robert W. Kennard introduced Ridge Regression (Hoerl and Kennard, 1970a) and (Hoerl and Kennard, 1970b), as an alternative to OLS in ill-conditioned problems (problems where the matrix  $X'X$  in Eq. 3.98 is close to be singular). In this kind of problems, the coefficients  $\hat{\beta}$  given by OLS are very sensitive to data errors (and they tend to be large).

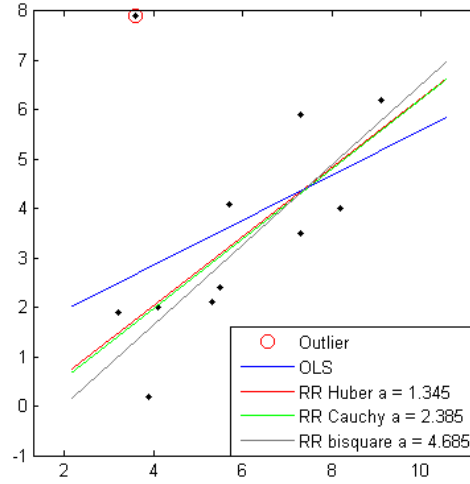


Figure 3.19: Regression example using OLS and RR

The method proposed by Hoerl and Kennard to compute the regression coefficients is:

$$\hat{\beta}^* = [X'X + kI]^{-1} X'Y = WX'Y, \quad k \geq 0 \quad (3.104)$$

where the parameter  $k$  is known as *bias parameter*.

The relationship between the Ridge Regression coefficients ( $\hat{\beta}^*$ ) and the OLS coefficients ( $\hat{\beta}$ ) is given by:

$$\hat{\beta}^* = [I_p + k(X'X)^{-1}]^{-1} \hat{\beta} = Z\hat{\beta} \quad (3.105)$$

### 3.3.3.1 Estimation of the $k$ parameter

There are several method to estimate the best value of the  $k$  parameter. Some of these methods are (Chatterjee and Hadi, 2006, p. 271):

- **Fixed point (Hoerl et al., 1975):**

$$k = \frac{p\hat{\sigma}^2(0)}{\sum_{j=1}^p [\hat{\beta}_j(0)]^2} \quad (3.106)$$

where  $\hat{\beta}$  are the OLS coefficients and  $\hat{\sigma}^2(0)$  is the corresponding residual mean square.

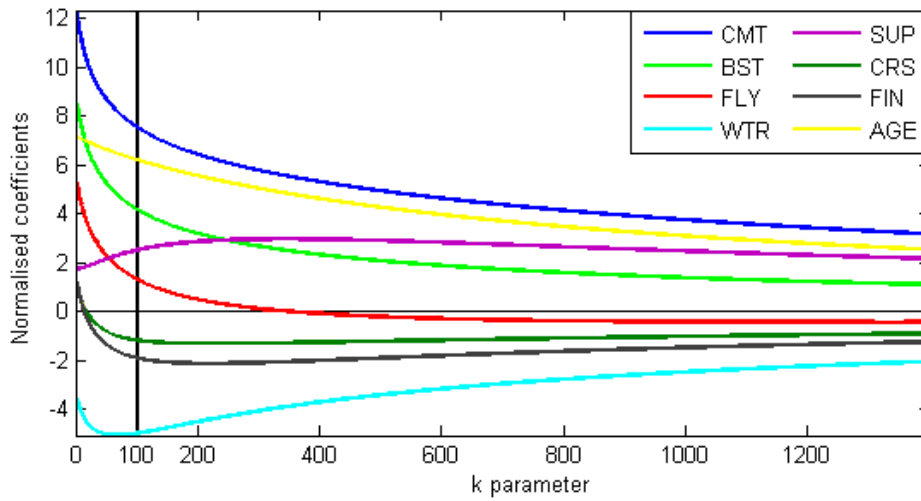


Figure 3.20: Ridge trace of the concrete compressive strength data set

- **Iterative method (Hoerl and Kennard, 1976):** starting from the  $k$  value computed from Eq. 3.106, a new  $k_i$  value is computed using:

$$k_i = \frac{p\hat{\sigma}^2(0)}{\sum_{j=1}^p [\hat{\beta}_j(k_{i-1})]^2} \quad (3.107)$$

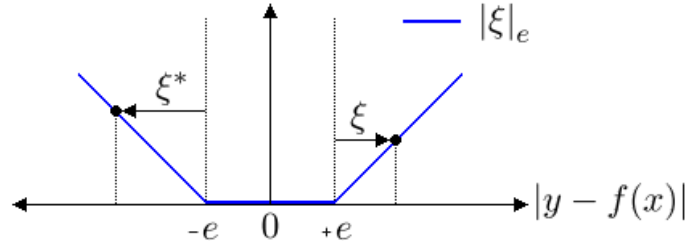
until the difference between  $k_i$  and  $k_{i-1}$  is negligible.

- **Ridge trace:** the Ridge Trace is a two-dimensional plot of the  $\hat{\beta}^*$  values for several values of the  $k$  parameter. If the  $\hat{\beta}^*$  coefficients show large fluctuations for the first values of  $k$ , it means that the explanatory variables are probably correlated. When  $k$  is increased, the fluctuations of the  $\hat{\beta}^*$  coefficients decrease. The smallest value of  $k$  for which the fluctuations decrease must be chosen. For larger values of  $k$ , the regression is overfitted.

### 3.3.3.2 Ridge Regression example

This example shows the use of Ridge Regression to fit a concrete compressive strength data set (see Appendix E). This data set contains 1,030 samples and 8 explanatory variables.

The ridge trace of this data set can be seen in Figure 3.20. Using the ridge trace, it was possible to decide that  $k = 100$  is a valid value of the

Figure 3.21:  $e$ -insensitive loss function

ridge parameter. Using this value, the regression equation obtained was:

$$\begin{aligned} strength &= 78.6552 + 0.0725 \cdot CMT + 0.0487 \cdot BST + \\ &+ 0.021 \cdot FLY - 0.2331 \cdot WTR + 0.4214 \cdot SUP + \\ &- 0.0149 \cdot CRS - 0.0235 \cdot FIN + 0.0986 \cdot AGE \quad (3.108) \end{aligned}$$

Using OLS, the coefficients obtained were:

$$\begin{aligned} strength &= -23.1638 + 0.1198 \cdot CMT + 0.1038 \cdot BST + \\ &+ 0.0879 \cdot FLY - 0.1503 \cdot WTR + 0.2907 \cdot SUP + \\ &+ 0.0180 \cdot CRS + 0.0202 \cdot FIN + 0.1142 \cdot AGE \quad (3.109) \end{aligned}$$

It is possible to observe that the signs of the explanatory variables CRS and FIN change. It can also be observed using the ridge trace in Figure 3.20 for  $k = 0$ . It is due to the correlation between these explanatory variables, partly solved by Ridge Regression.

### 3.3.4 Support Vector Regression

Support Vector Regression (SVR) is a version of SVM (see Section 3.1.1) for function estimation.

SVR uses the  $e$ -insensitive loss function (Figure 3.21):

$$|\xi|_e := \begin{cases} 0 & \text{if } |\xi| \leq e \\ |\xi| - e & \text{otherwise} \end{cases} \quad (3.110)$$

The goal of SVR is to find the flattest function that fits the training data. The errors lower than  $e$  are not taking into consideration (the value of the  $e$ -insensitive loss function is 0 is the region  $[-e, +e]$ ) but the errors higher than  $e$  are minimised (Smola and Schölkopf, 2004). Then, being  $\xi$  and  $\xi^*$  non-negative slack variables (Figure 3.21), the functional in Eq. 3.6 is now (Cherkassky and Mulier, 1998, p. 441):

$$\Phi(w) = \frac{1}{2}(w \cdot w) + \frac{C}{n} \sum_{i=1}^n (\xi_i + \xi_i^*) \quad (3.111)$$

subject to the constraints:

$$\begin{cases} y_i - (w \cdot x_i) - b \leq e + \xi_i \\ (w \cdot x_i) + b - y_i \leq e + \xi_i^* \\ \xi_i, \xi_i^*, \quad i = 1, \dots, n \end{cases} \quad (3.112)$$

where  $n$  is the number of samples in the data set and  $w$  are the coefficients of the estimated linear function.

This functional can be solved in the dual form using the Lagrangian:

$$\begin{aligned} L(\alpha_i, \beta_i) = & -e \sum_{i=1}^n (\alpha_i + \beta_i) + \sum_{i=1}^n y_i (\alpha_i - \beta_i) + \\ & -\frac{1}{2} \sum_{i,j=1}^n (\alpha_i - \beta_i) (\alpha_j - \beta_j) (x_i \cdot x_j) \end{aligned} \quad (3.113)$$

subject to the constraints:

$$\begin{cases} \sum_{i=1}^n \alpha_i = \sum_{i=1}^n \beta_i \\ 0 \leq \alpha_i \leq C/n, \quad 0 \leq \beta_i \leq C/n \end{cases} \quad (3.114)$$

Only SVs have non-zero coefficients in the solution of the Lagrangian in Eq. 3.113 ( $\alpha^*$  and  $\beta^*$ ). Therefore, the regression function is given by

$$f(x) = \sum_{i=1}^{SV} (\alpha_i^* - \beta_i^*) (x_i, x) + b_0 \quad (3.115)$$

The bias ( $b_0$ ) is given by:

$$b_0^* = y_s - \sum_{i=1}^{SV} (\alpha_i^* - \beta_i^*) (x_i \cdot x_s) \quad (3.116)$$

In the case of non-linear kernels, the regression function is given by:

$$f(x) = \sum_{i=1}^n (\alpha_i^* - \beta_i^*) K(x_i, x) + b_0 \quad (3.117)$$

Next section includes an example of the use of SVR to compute a regression function of the Mexican hat.

### 3.3.4.1 SVR example: the Mexican hat

The Mexican hat is a well-known function, given by the equation:

$$f(x) = \frac{2}{\sqrt{3\sigma\pi^{1/4}}} \cdot \left(1 - \frac{x^2}{\sigma^2}\right) \cdot e^{\frac{-t^2}{2\sigma^2}} \quad (3.118)$$

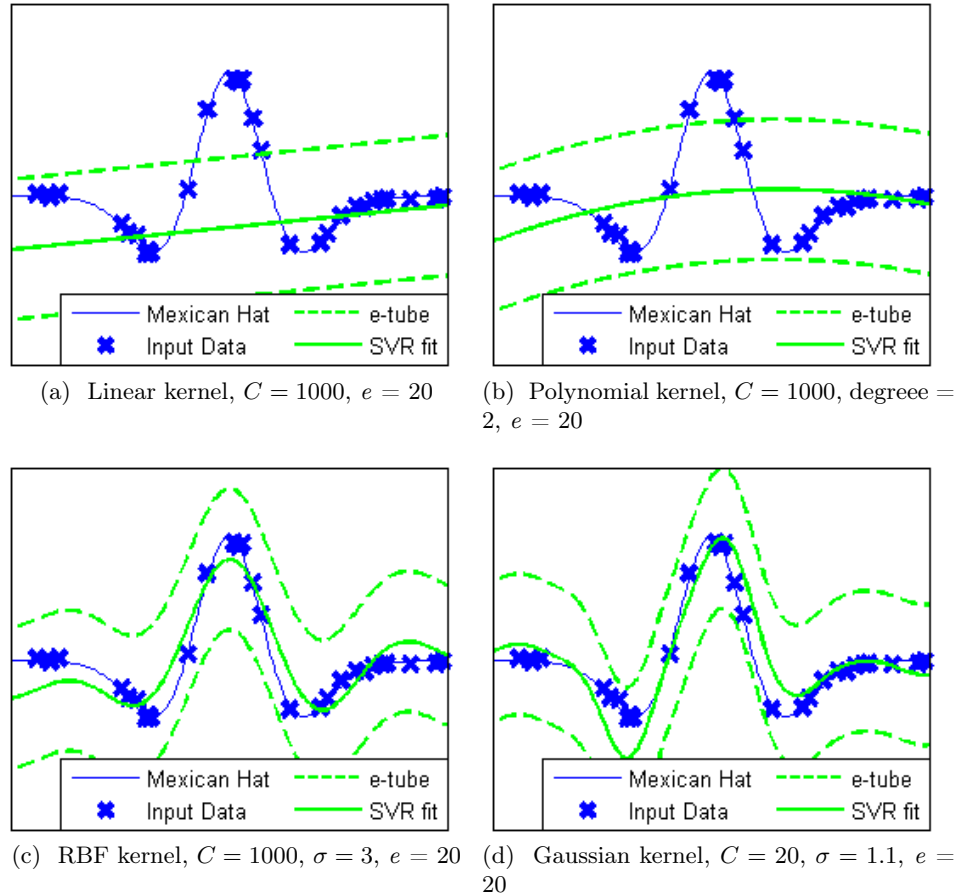


Figure 3.22: SVR of the Mexican hat function using four kernels

In this example, a data set of 30 points from the Mexican hat was chosen to illustrate the use of SVR. The points were randomly chosen from the function and white Gaussian noise was added to the samples. This example was carried out using *The Spider* toolbox (Weston et al., 2011) and *Matlab*®.

Four different kernels were tested: linear (Eq. 3.25,  $C = 1000$ ,  $e = 20$ ), polynomial (Eq. 3.26,  $C = 1000$ , degree = 2,  $e = 20$ ), RBF (Eq. 3.27,  $C = 1000$ ,  $\sigma = 3$ ,  $e = 20$ ) and Gaussian (Eq. 3.28,  $C = 20$ ,  $\sigma = 1.1$ ,  $e = 20$ ). The kernels were trained using the same data set.

Figure 3.22 depicts the results obtained by the kernels. The regression function obtained by the linear kernel is shown in Figure 3.22a. The blue line represents the Mexican hat given by Eq. 3.118 ( $\sigma = 2$ ). The blue crosses are the data set points. The green solid line is the regression function and the green dashed lines are the bounds of the  $e$ -tube. Since it used a linear kernel, the regression function computed by SVR was a straight line. The result obtained by the polynomial kernel of degree 2 is depicted in Figure

3.22b. Figures 3.22c and 3.22d shows the results of the RBF and Gaussian kernels respectively.



## Chapter 4

# Location of relevant events in waveforms and images

The energy production of future fusion power plants is a function of the plasma pulse length (the longer the pulse length, the higher the energy produced). Present fusion devices have short pulse lengths (e.g. the TJ-II pulses are shorter than a second and JET pulses usually last 10-20 seconds, and even one minute under certain conditions). These pulse lengths will be overcome by future fusion devices. ITER is intended to maintain plasma in steady state up to 400 seconds with  $Q \sim 5$ . But the ITER pulse length can be even longer. The Hybrid Mode is intended to last up to an hour with  $Q \sim 10$  and the Advance Mode will last up to 30 minutes with  $Q \sim 40$  (Stambaugh, 2006).

During the pulse length, hundreds of physical events take place. The identification and the location of these events is carried out by means of visual analysis of plasma waveforms. Experts devote their time examining in great detail each waveform in order to determine the event type (e.g. ELMs, sawteeth, disruptions) and its temporal location. Present fusion devices require several expert manpower to analyse the data generated during each pulse and it will be unaffordable in future devices when the pulse length will be up to 100 times longer.

Recently, data mining and artificial intelligence tools have been applied to fusion databases. These methods provide fast and accurate results on locating and identifying plasma phenomena. Moreover, they can predict dangerous plasma phenomena (such as disruptions) before they occur (Ratta et al., 2010). They will become essential in the next years and specially after the first ITER plasma expected by 2019.

An important issue to take into consideration is the cost of the analysis of the data. The visual analysis of the waveforms requires a lot of manpower and hence, it is expensive. Computer codes are much cheaper. Their price includes their design and maintenance / update but then, they can be run

thousands of times without additional cost. They allow the analysis of large quantities of data in a low-cost basis.

Another advantage of data mining techniques is their speed. Computer codes are faster than any visual analysis carried out by experts. Visual analysis is time-intensive and the only way to speed up the process is increasing the number of experts and thus, increasing the cost.

The deterministic behaviour of computer codes is also one of their benefits. The results of an analysis using a computer code are always the same, no matter the number of times that the program is executed. It is important to note that it does not imply that the codes are error-free, it does just mean that the same errors (if exist) are made. It cannot be assured by the analysis carried out by experts. The same event can be located by two experts in two slightly different times and even the same expert can determine two different times for the same event. The reasons of these differences can be, among others, a different detail level in the analysis (the higher the level of detail, the longer the analysis time) or just an error.

Fusion experts also have a key role in the design of data mining tools. Since they held the most extensive knowledge about plasma phenomena, their assistance is indispensable in the development of these computer codes. The tools that integrate the expertise in their systems are called *expert systems*. On the one hand, expert systems are fast and accurate and, on the other hand, they apply expert knowledge. Since expert systems combine the best attributes of experts and computer codes, they are valuable tools.

This chapter introduces a Universal Multi-Event Locator, a data mining technique to determine plasma events within waveforms (Section 4.1) and films (Section 4.2). It allows the location of single events and the location of time slices (in waveforms) and regions (in images) of interest. It has been applied to create expert system to locate plasma phenomena such as sawteeth (Section 4.1.1), disruptions (Section 4.1.2) and ELMs (Section 4.1.3) in plasma signals, hot spots in infrared films, the identification of the most relevant frames in visible light films (Section 4.2.1) and the identification of regions of interest in images (Section 4.2.2) and their evolution (Section 4.2.3).

## 4.1 A Universal Multi-Event Locator

This Section describes an Universal Multi-Event Locator (UMEL), a technique to locate events in plasma waveforms and films (Vega et al., 2010a). UMEL is a universal technique because it is independent from the type of the pattern sought (peaks, drops or slope changes) and the type of waveforms analysed (time domain or frequency domain).

UMEL provides a double capability:

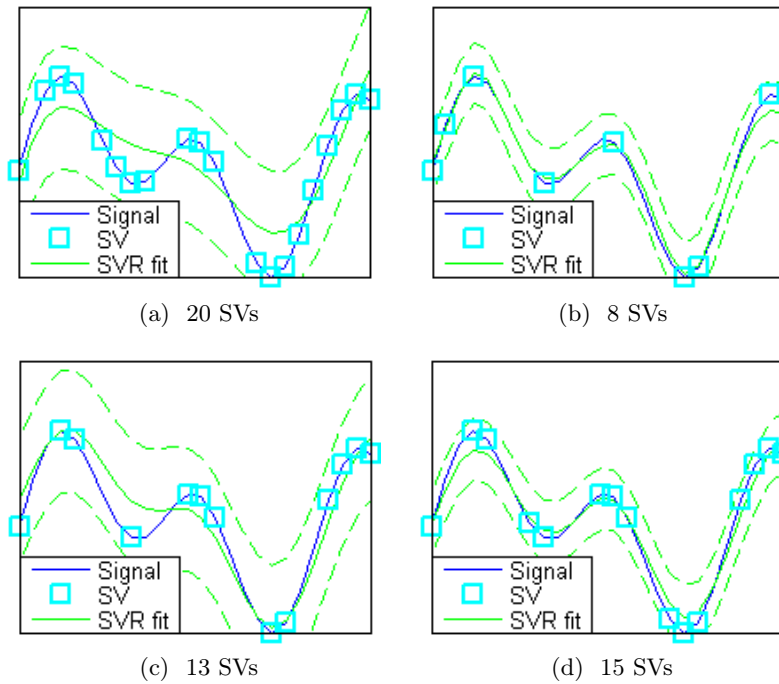


Figure 4.1: SVs retrieved by four SVR fits

1. It can be used as a filter to recognise signal segments or image areas with relevant behaviour. The use of UMEL as a filter allows establishing the presence of physical events even without identifying their type.
2. It can be applied as an exact locator of singular points within signals. UMEL can locate physical events in a high number of experiments and, therefore, big databases with large statistical significance can be created in an automatic way.

UMEL bases its searching capabilities on a specific regression technique: SVR (see Section 3.3.4). SVR fits the training data without depending on factors such as sampling rate or noise distribution. This technique computes a fitting function and, in addition, it retrieves a list of the points from the training set that become Support Vectors (SVs). UMEL provides a novel interpretation of these SVs: for the most SVs, they are the most difficult samples to regress.

In SVM and SVR, the complexity of the model determines the number of SVs (the higher the complexity, the larger the number of SVs). The regression of complex data sets requires large numbers of SVs. In contrast, simple data sets require smaller numbers of SVs. But the number of SVs does not only depend on the complexity of the data set to regress. It also depends on the

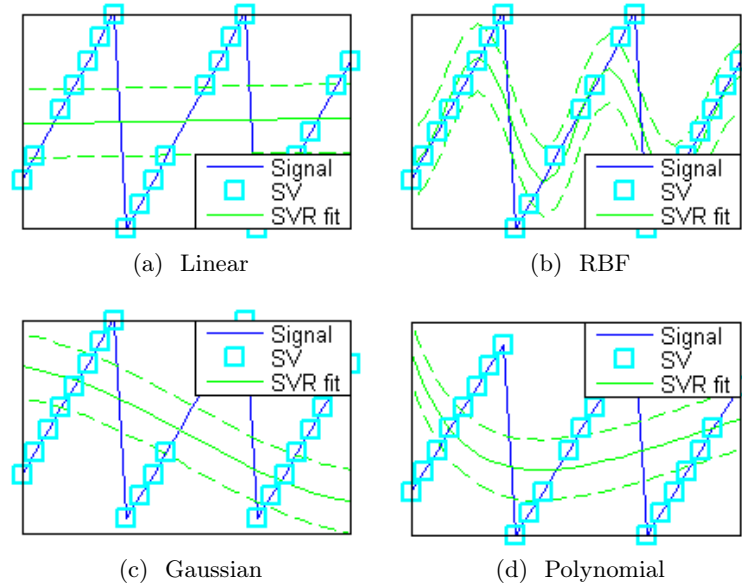


Figure 4.2: Comparison of UMEL using different types of kernel

smoothness of the regression function. Smoother functions require fewer SVs than crispy functions.

Figure 4.1 contains four examples of SVR regressions of the same function using a RBF kernel (Eq. 3.27). The only difference between the examples is the set of SVM parameters ( $C$ ,  $\sigma$  and  $e$ ) chosen. The number of SVs varies between 8 and 20 as function of the complexity of each one of the fits. But a good fit does not mean a large number of SVs. For example, the fit shown in Figure 4.1b is the best one (in terms of  $\text{MSE}^1$ ) and it only contains 8 SVs. In contrast, the fit depicted by Figure 4.1a is poor and it contains 20 SVs. The SVM parameters influence both, the quality of the fit and the number of SVs. It is also possible to obtain similar fits with different number of SVs. Figure 4.1b and Figure 4.1d shows two similar fits with different number of SVs. The same effect can be seen comparing Figure 4.1a and Figure 4.1c.

Despite their differences, all the examples in Figure 4.1 have something in common: the location of the SVs. In all the fits, the SVs appear in the most difficult samples to regress (the function local maximums and minimums and the beginning and the end of the signal). No SVs appear in the straight intervals of the function between its local maximums and minimums. Therefore, different sets of SVM parameters obtain different sets of SVs but all of them located in close points of the original signal.

The smoothness of a SVR fit is function of four parameters:

<sup>1</sup>**MSE:** Mean Square Error

1. **Kernel type:** it determines the equation of the SVR fit and hence, its smoothness. There are many different kernel types e.g. linear, Gaussian, polynomial or RBF. Figure 4.2 contains four examples of regressions using these kernels. Figure 4.2a depicts the fit obtained using a linear kernel. It cannot resemble the original function and it only follows the global tendency (almost an horizontal straight line). Figure 4.2b shows a fit computed using a RBF kernel. This is the best fit in terms of MSE. Figure 4.2c contains an example of a Gaussian kernel and finally, Figure 4.2d plots a regression computed using a polynomial kernel.
2. **Regularization parameter C:** it controls the model complexity (Eq. 3.19). Large values of  $C$  produce crispy fits. On the other hand, low values of  $C$  produce smooth regressions. Its value can be estimated using the following equation (Cherkassky and Mulier, 1998, p. 449):

$$C = K_C \cdot \max(|\bar{y} + 3 \cdot \text{std}(y)|, |\bar{y} - 3 \cdot \text{std}(y)|) \quad (4.1)$$

where:

- $\bar{y}$  : is the mean of the function to regress
- $\text{std}(y)$  : is the standard deviation of the function to regress
- $K_C$  : is a constant that can vary for different kind of signals

3. **epsilon ( $e$ ):** it determines the width of the  $e$ -insensitive zone (also called  $e$ -tube since it seems to be a tube around the fit). It can be determined using the equation (Cherkassky and Mulier, 1998, p. 449):

$$e = K_e \cdot \text{std}(\text{noise}) \cdot \sqrt{\frac{\ln n}{n}} \quad (4.2)$$

where:

- $\text{std}(\text{noise})$  : is the standard deviation of the noise of the function
- $n$  : is the number of samples
- $\ln n$  : is the natural logarithm of  $n$
- $K_e$  : is a proportionality constant

From a practical point of view, and since the value of the noise is not usually known, the value of  $\text{std}(\text{noise})$  is replaced by  $\text{std}(y)$  where  $y$  is the function to be fitted. Then, the value of  $e$  is tuned using the proportionality constant  $K_e$ .

The  $e$ -tube can be identified in Figures 4.1 and 4.2 as the area surrounded by green dashed lines.

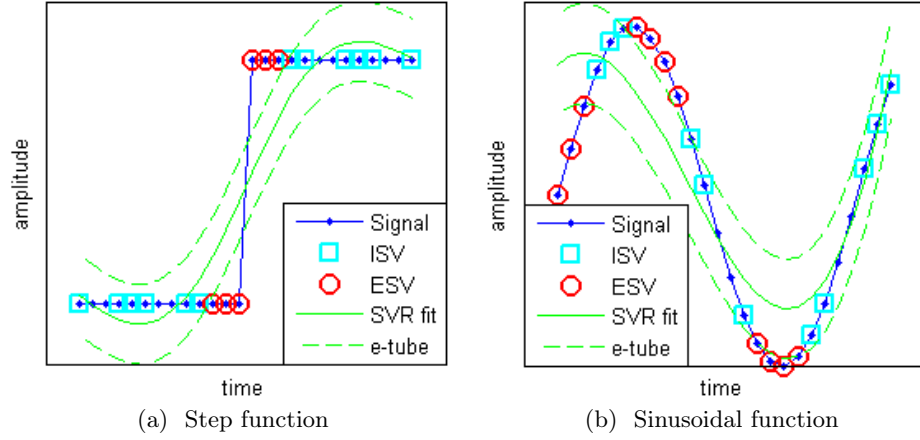


Figure 4.3: Examples of UMEL analysis

4. **Kernel parameter(s):** some kernels include a parameter, for example the  $\sigma$  parameter of the RBF kernel. It is one of the most commonly used kernels and thus, there is an equation to estimate the  $\sigma$  parameter (Martinez and Martinez, 2008, p. 325):

$$\sigma_k = K_\sigma \cdot 1.06 \cdot \text{std}(y) \cdot n^{-1/5} \quad (4.3)$$

where:

- $\text{std}(y)$  : is the standard deviation of the function to regress  
 $n$  : is the number of samples  
 $K_\sigma$  : constant dependent on the type of signal to fit

Therefore, given a certain signal to regress, there are four parameters that define the results obtained using UMEL: the kernel type, the regularization constant  $K_C$ , the  $e$  proportionality constant  $K_e$  and the kernel parameter constant (if exist)  $K_\sigma$ . From here on, all the UMEL analyses will use the RBF kernel and the following notation:

$$(\text{RBF kernel}, K_C, K_e, K_\sigma) \quad (4.4)$$

Using UMEL, not all the SVs have the same degree of relevance. The SVs that lie on or outside the  $e$ -tube are called External Support Vectors (ESVs). In contrast, the SVs within the  $e$ -tube are called Internal Support Vectors (ISVs):

$$ESV \subseteq SV \quad \forall i \in ESV, \quad |y_i - f(x_i)| \geq e \quad (4.5)$$

$$ISV \subseteq SV \quad \forall i \in ISV, \quad |y_i - f(x_i)| < e \quad (4.6)$$

ISVs are necessary samples for the regression estimation, but they do not provide the same degree of relevance that can be assigned to ESVs. UMEL proposes a novel interpretation of ESVs: the SVs that become ESVs are the *most difficult samples to regress* (they cannot be fitted inside the  $e$ -tube) and these SVs provide *essential information* in the regression process. ESVs reveal the occurrence of special patterns inside a signal: peaks, high gradients or segments with different morphological structure in relation to the bulk of the signal.

Figure 4.3 depicts two examples of UMEL using a step function and a sinusoidal function. The green dashed lines delimit the  $e$ -tube. Then, the SVs within these lines are ISVs (cyan squares) and the SVs outside the  $e$ -tube are ESVs (red circles). The ESVs appear in the most difficult samples to regress. In the case of the step function (Figure 4.3a), the samples around the step become ESVs. Some ISVs can be found inside the  $e$ -tube. In the case of the sinusoidal function (Figure 4.3b), the ESVs appear at the beginning of the function and at the maximum and the minimum of the function.

Most of the plasma phenomena are characterised by high frequency components in the time domain (spikes, drops, rapid slope changes, etc.). For example, an ELM is recognised as a spike in the  $D_\alpha$  signal accompanied by a drop in the diamagnetic energy as well as a drop of the plasma density at the plasma edge. A disruption is identified by a fast drop in the plasma current at the same time that the plasma voltage peaks. Therefore, it is possible to apply UMEL to locate these events. Next sections contain the application of UMEL to the location of plasma phenomena such as sawteeth (Section 4.1.1), disruptions (Section 4.1.2) and ELMs (Section 4.1.3).

#### 4.1.1 Sawteeth location using UMEL

Sawteeth are instabilities at the plasma core that cause a release of energy from the core to the edge (see Section 2.2.3). Sawteeth can be identified, for example, using the plasma temperature or density, as a regular cycle of rises and falls. It is also possible to detect sawteeth using the X-ray emission. In addition, using different chords of soft X-ray emission at different plasma radii, it is possible to measure the plasma diffusivity as function of the time difference between a sawtooth at the different radii.

Figure 4.4 contains an example of soft X-ray signals at different radii. The plots are sorted in ascending radius order (the waveform at the top corresponds to the plasma core and the one at the bottom is the X-ray emission at the plasma edge). The central plot corresponds to the inversion radius ( $q = 1$ ). At the inversion radius, the sawteeth drops are revealed by small spikes. For larger radii, the X-ray emission crash up to a maximum (heat pulse) followed by a slow decreasing.

Using the central chords (Figure 4.4 upper graph), it is possible to deter-

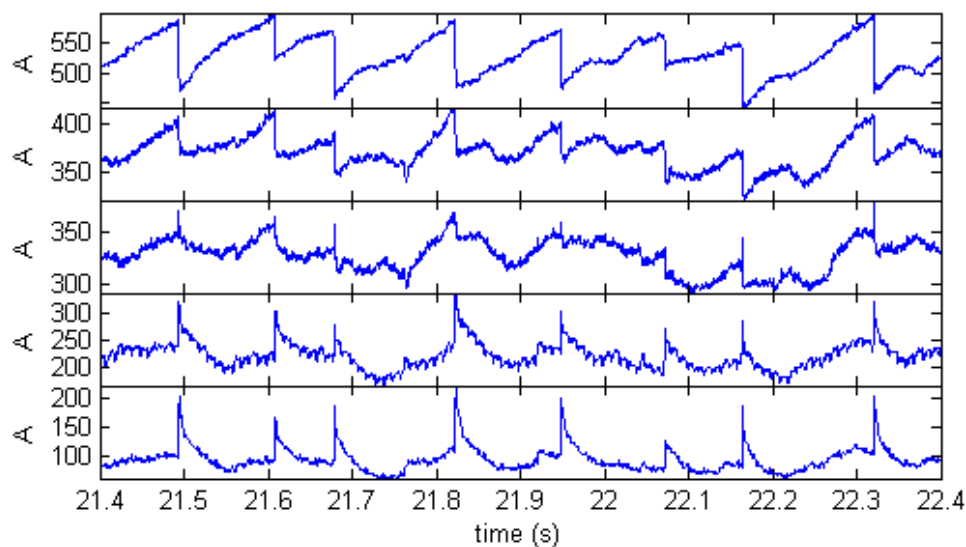


Figure 4.4: Sawteeth activity, JET pulse 60906

mine the exact time of the sawteeth crashes. UMEL can be applied to locate the X-ray emission falls and hence, to determine the times of the sawteeth. The ESVs appear in the most difficult samples to regress, in this case, the points around every single fall.

Figure 4.5 depicts the location of sawteeth using UMEL. The exact times of the sawteeth are determined using the central chord (upper graph). The times of the sawteeth are also computed at the different radii in order to quantify the plasma diffusivity. The solid green line represent the SVR fit (using a RBF kernel) and the green dashed lines are the bounds of the  $e$ -tube. The ESVs (red circles) appear in the most difficult samples to regress (the ones located close to the falls). In the case of the chords at the plasma edge, the ESVs are located in the samples of the X-ray emission spikes.

If the times of the sawteeth are determined at different radii, they can be used to quantify the plasma diffusivity. According to the time-to-peak method, it is possible to compute the plasma diffusivity as (Soler and Callen, 1979):

$$\chi_e = \frac{r^2 - r_{inversion}^2}{8t_p} \quad (4.7)$$

where:

- $r$  : is the plasma radius where the  $\chi_e$  is measured
- $r_{inversion}$  : is the radius where the sawtooth inversion takes place
- $t_p$  : is the sawtooth time difference between the inversion radius and  $r$

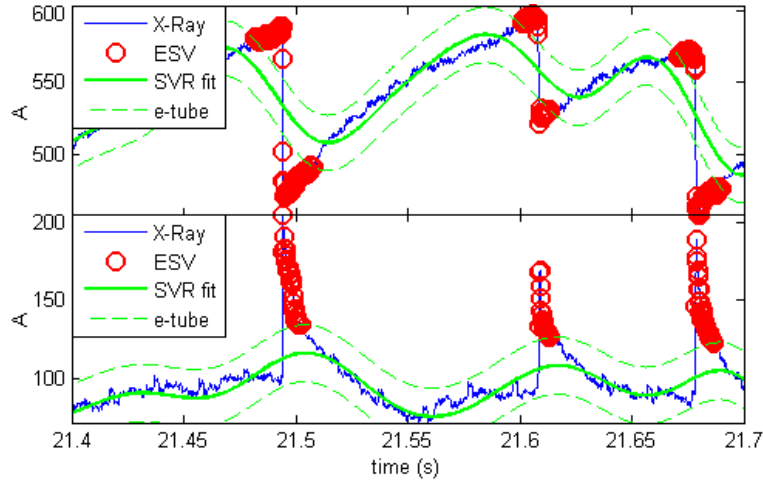


Figure 4.5: Location of sawteeth using UMEL, JET pulse 60906

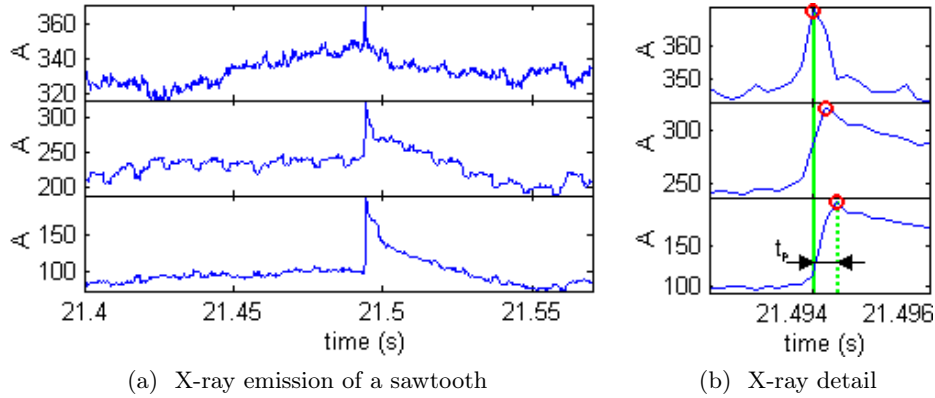
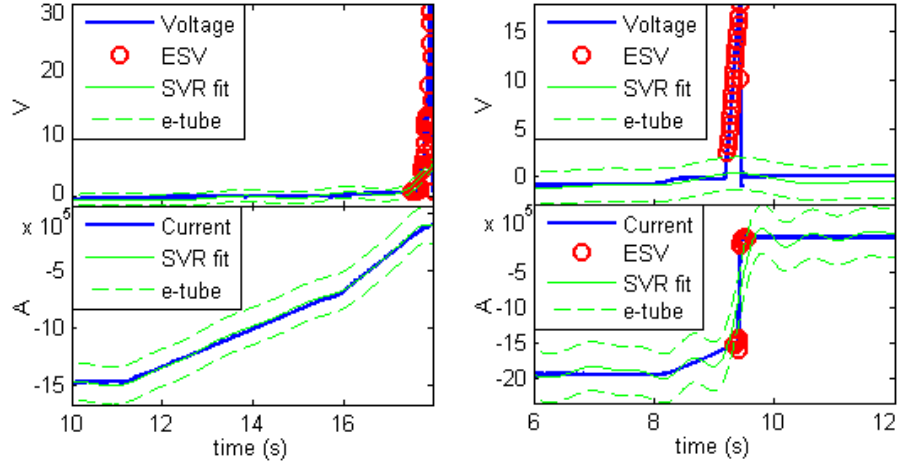


Figure 4.6: Plasma diffusivity, JET pulse 60906

Since the radial coordinates of the soft X-ray chords are known beforehand, UMEL allows the automatic determination of  $\chi_e$ .

Figure 4.6 contains an example of the measurement of  $t_p$ . Figure 4.6a shows the time evolution of a sawtooth in an interval of 170 ms. If we zoom in an interval of 4 ms around the sawtooth, it is possible to check that the sawtooth is slightly delayed in the edge chords (Figure 4.6b). Then, the time  $t_p$  is measured as the time difference between the sawtooth time at the inversion radius (Figure 4.6b upper graph,  $t_{inversion} = 21.4940$  s) and the sawtooth time at the edge (Figure 4.6b lower graph,  $t_r = 21.4944$  s). In this case,  $t_p = 0.4$  ms.



(a) Non-disruptive plasma, JET pulse 71023 (b) Disruptive plasma, JET pulse 71025

Figure 4.7: Example of a disruptive and a non-disruptive plasma

#### 4.1.2 Disruption location using UMEL

Disruptions are plasma instabilities that cause a loss of confinement (see Section 2.2.4). During plasma operation, different types of disruptions can appear. The most dangerous ones can be hazardous to the integrity of the fusion device and hence, they must be avoided.

Disruption times can be recognised in plasma waveform using the plasma current and the loop voltage. When a disruption takes place, the plasma current plummets and a spike appears in the loop voltage signal. Figure 4.7b shows the loop voltage and the plasma current of a disruptive discharge (JET pulse 71025). In non-disruptive discharges, it is also possible to observe a spike in the loop voltage, but the plasma current gradually decreases until it reaches 0 (Figure 4.7a, JET pulse 71023).

Both signals (plasma current and loop voltage) are necessary for the recognition of disruptions. For example, a spike appears at the beginning of every pulse in the plasma loop voltage but there is not loss of the plasma current. In addition, sometimes it is possible to find a fast reduction of the plasma current but without a peak of the plasma loop voltage. These cases are not disruptions and can be misjudged if only one of the signals is used in the identification of the disruptions.

In order to locate disruptions using UMEL, both signals are fitted using the parameters (RBF kernel,  $K_C = 1$ ,  $K_e = 30$ ,  $K_\sigma = 1$ ). Since the most difficult samples to regress are the points located in the loop voltage spikes and the plasma current drops, ESVs appear in these samples. Figure 4.7 shows the fit of the plasma current and loop voltage in a non-disruptive

<b>Disruptive</b>	<b>343 pulses</b>
Detected (true positives)	321 (93.59%)
Missed (false negatives)	22 (6.41%)
<b>Non-disruptive</b>	<b>4,057 pulses</b>
Successes (true negatives)	4,036 (99.48%)
Errors (false positives)	21 (0.52%)
<b>Total</b>	<b>4,400 pulses</b>
Successes	4,357 (99.02%)
Errors	43 (0.98%)

Table 4.1: Results of the disruptions location

discharge and in a disruptive one. The disruptive discharge can be recognised due to the simultaneous presence of ESVs in the plasma current and loop voltage.

UMEL can be applied to the off-line location of the existing disruptions in the JET database. The determined disruption times can be used to build automatic on-line disruption predictors (Ratta et al., 2010). Since the number of samples in both signal is low (average 1000 samples per signal), the computation times are very short (0.33 s per signal using an Intel® Core™ 2 Quad CPU Q9300 2.50GHz, 1.95GB RAM).

The disruptions from a JET database of 4,400 discharges (in the pulse range from 65115 to 70722) were located using UMEL. The database contained 343 disruptive pulses and 4,057 non-disruptive ones. The results obtained by the method can be seen in Table 4.1. The success rate was 99.02% (4,357 discharges properly recognised) and the error rate was 0.98% (43 discharges misclassified).

### 4.1.3 ELMs location using UMEL

Edge Localised Modes (ELMs) are instabilities occurring in the edge of H-mode plasmas (see Section 2.2.2). Most ELMs taking place in tokamak experiments are not indexed and thus it is not easy to study them. Average ELMs' studies contain dozens of ELMs, a reduce set of the ELMs available in the JET database. For example, JET pulses can contain more than one hundred ELMs each and the JET database currently contains more than 80,000 pulses (not all the pulses contain ELMs).

Previous work has been done in developing an automatic ELM classification system (Duro et al., 2009). This tool uses the ELMs times as an input and classifies them as Type I or Type III. It has been tested using a small set of 256 ELMs (122 training and 143 test) manually located by experts. In order to apply this system to a wide range of discharges, it is necessary to provide an automatic tool to locate ELMs without human intervention.

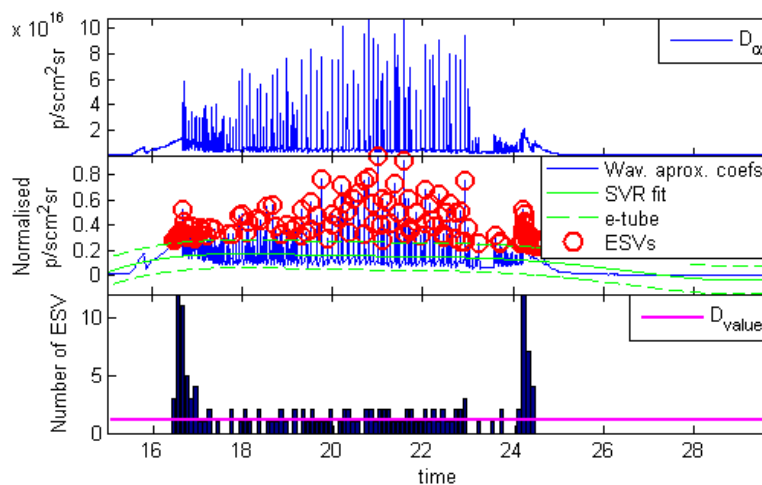


Figure 4.8: ELMs location, step 1. H-mode location. JET pulse 73337

Present software codes to locate ELMs are completely dependent on waveform amplitudes and noise. Therefore, if the amplitude or noise changes from one discharge to another (or even in a single discharge), the software must be tuned.

This section describes the application of UMEL to the location of ELMs in plasma pulses (González et al., 2010a). The method described here can be applied to a wide range of plasma discharges without human intervention or modification of the code. It is made up of two steps: the location of the temporal interval with ELMs (Section 4.1.3.1) and the location of individual ELMs (Section 4.1.3.2). This method has been applied to a JET databases of more than 1,200 JET pulses, locating more than 220,000 ELMs.

#### 4.1.3.1 Location of the temporal interval with ELMs

The typical sequence of a plasma pulse starts with the plasma in L-mode. Then, when auxiliary power is injected to the plasma above a certain power threshold, the plasma reaches H-mode. The plasma returns to L-mode after the injected power is stopped. ELMs take place only during the time the plasma is in H-mode and, in JET, there is no H-mode without ELMs. Therefore, the location of the H-mode implies the determination of the region where ELMs appear and vice versa. The focus of this step is to delimit the time interval in which ELMs appear rather than the location of every single ELM, so this phase is actually a gross H-mode locator system.

This step save computational time in the individual ELMs location carried out in the next step. It makes no sense to look for ELMs in L-mode segments and thus, ELMs are only sought in the H-mode region. Three

sequential tasks are carried out within this step:  $D_\alpha$  normalisation, dimensionality reduction and H-mode location.

**Normalisation of the  $D_\alpha$  waveform.** In order to optimise the computation of the SVR regression and allow the use of the same UMEL parameters in a wide range of discharges, the  $D_\alpha$  signal is normalised between 0 and 1. The normalisation chosen is:

$$D_\alpha, \text{ normalised} = \frac{D_\alpha - \min(D_\alpha)}{\max(D_\alpha) - \min(D_\alpha)} \quad (4.8)$$

**Dimensionality reduction.** The computation time of the SVR regression can be reduced significantly reducing the number of samples to regress. Since this is a gross H-mode locator, a high decomposition level of the Wavelet transform (see Section 3.2.3) can be used to reduce the number of samples to regress without precision problems. The approximation coefficients of the wavelet transform are used as approximation of the  $D_\alpha$  waveform. These coefficients retain the most relevant signal information in both, the time and frequency domains.

The wavelet decomposition level has been set to 5. For example, a signal with 150,000 samples is reduced to 4,688 samples.

**H-mode location.** The capability of UMEL to locate time segments with relevant behaviour has been applied to locate the H-mode time interval in a plasma discharge. Given a pulse number, a SVR regression is computed using the wavelet approximation coefficients of the  $D_\alpha$  signal. The chosen UMEL parameters are (RBF kernel,  $K_C = 1$ ,  $K_e = 10$ ,  $K_\sigma = 20$ ). The upper graph in Figure 4.8 shows an example of the ESVs obtained by UMEL in JET pulse 73337.

Then, an histogram of the ESVs in time windows of 0.1 s length is computed (Figure 4.8, lower graph). This histogram defines the temporal segment that has been more difficult to regress, and therefore, the time slice where the  $D_\alpha$  signal contains high frequency components (peaks). This temporal slice corresponds to the H-mode region and therefore, the time slice with ELM activity. The borders of this region are the first and the last bins with more ESVs than a certain decision value. This decision value is computed as:

$$d_{value} = K \cdot \frac{\sum_{i=1}^N ESV_i}{N} \quad (4.9)$$

where:

- $K$  : constant depending on the discharge range
- $ESV_i$  : number of ELMs in the bin  $i$
- $N$  : number of bins with ELMs

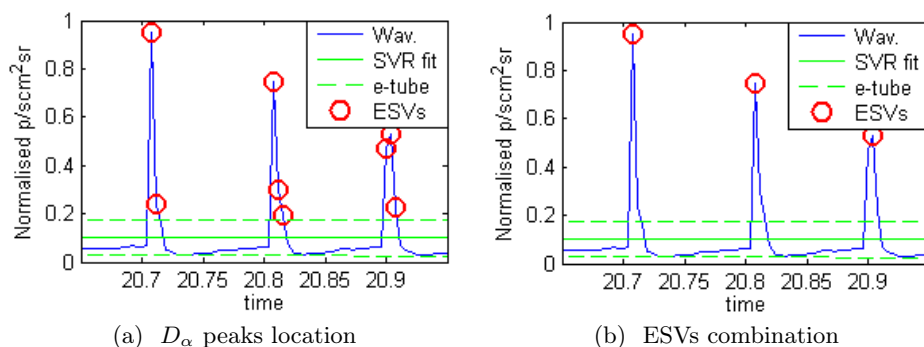


Figure 4.9: ELMs location, step 2. Example of  $D_\alpha$  peak location and ESVs combination, JET pulse 73337

The constant  $K$  has been set to 0.5. It is important to note that this value has been used for the detection of the time interval with ELMs in all the discharges in the pulses analysed in Section 4.1.3.3.

The outputs of this step are the borders of the time interval with ELMs. This time interval can be also computed without using the wavelet transform. On the one hand, the borders of the time slice are more accurately determined (it is not needed here since this is just a gross estimation of the H-mode region) but on the other hand, the computation time is significantly larger. For example, using a waveform with 121,072 samples, the SVR takes 379 s while the SVR of a waveform with 4,096 samples plus the wavelet transform computation time is 6.32 s (using a Intel® Core™ 2 Quad CPU Q9300 2.50GHz, 1.95GB RAM).

#### 4.1.3.2 Location of single ELMs

Usually, ELMs are localised by means of visual analysis. The process consists of recognizing peaks in the  $H_\alpha/D_\alpha$  signals that are synchronous with a drop in the stored diamagnetic energy. This step executes this process. Since the  $D_\alpha$  signal typically has a better signal-to noise ratio, the ELMs location process begins searching peaks in this signal. Then, simultaneous drops in the diamagnetic energy are sought. This searching process is limited to the time interval determined in the previous step.

The location of ELMs is carried out in four steps:  $D_\alpha$  peak location, ESVs combination, diamagnetic energy division and combination of information.

**$D_\alpha$  peak location.** Since the  $D_\alpha$  signal has a better signal-to noise ratio than the diamagnetic energy signal, the location of the peaks caused by ELMs in the  $D_\alpha$  signal is easier. This step locates the peaks in the  $D_\alpha$  signal that are candidates to be ELMs. It is important to note that not all

these peaks are ELMs (it must be checked using the diamagnetic energy). The location of peaks in the  $D_\alpha$  waveform is performed using UMEL (RBF kernel,  $K_C = 1$ ,  $K_e = 8$ ,  $K_\sigma = 50$ ).

Figure 4.9a shows the location of ELMs in JET pulse 73337. The points of the waveform outside the  $e$ -tube become ESVs. Although the SVR fit can seem a straight line, it is adapted to the low frequency shape of the  $D_\alpha$  waveform. The identification of peaks as the points above a certain threshold is not valid since ELMs have different amplitudes and the  $D_\alpha$  amplitude can vary from one pulse to another. The main advantage of using UMEL resides in the fact that UMEL looks for samples that do not fit a smooth regression, independently of their amplitudes.

**ESVs combination.** As it can be observed in Figure 4.9a, more than one ESV appears on each peak of the  $D_\alpha$  signal. This step concentrates all the ESVs of each peak in a single one. The selected point is the  $D_\alpha$  sample with the highest amplitude. After this task, each peak is represented by just one ESV.

Figure 4.9b contains the result of this step using the peaks in Figure 4.9a as inputs. After this step, only one ESV remains on each peak, located in the maximum of the  $D_\alpha$  waveform.

**Diamagnetic energy division.** The diamagnetic energy waveform is divided into small segments around the time of each  $D_\alpha$  peak located in the previous step. These segments must allow the identification of the drops of the diamagnetic energy without possible confusion from signal noise. It has been empirically determined that a segment of 35 ms is enough for a clear recognition of the diamagnetic energy drops. Then, the time windows of the diamagnetic energy are determined as [ $D_\alpha$  peak - 0.005,  $D_\alpha$  peak + 0.03].

Figure 4.10 shows the time windows computed for the  $D_\alpha$  peaks located in the previous tasks. As it can be seen, the peaks of the  $D_\alpha$  waveform is not located in the centre of the windows. It simplifies the recognition of the drops of the diamagnetic energy carried out in the next task.

**Combination of information.** The last step of this method locates drops in the diamagnetic time windows determined in the previous step. UMEL is used again as event locator (RBF kernel,  $K_C = 100$ ,  $K_e = 1$ ,  $K_\sigma = 100,000$ ). It is not possible to set a simple threshold to determine the drop in the diamagnetic energy because the amplitude of the waveform changes from one pulse to another.

On the one hand, if one or more ESVs are found in the diamagnetic energy at a maximum distance of 5 ms from the  $D_\alpha$  peak, it is recognised as an ELM. In this case, the time instant of the ELM is determined as the time of the maximum value of the diamagnetic energy just before the drop.

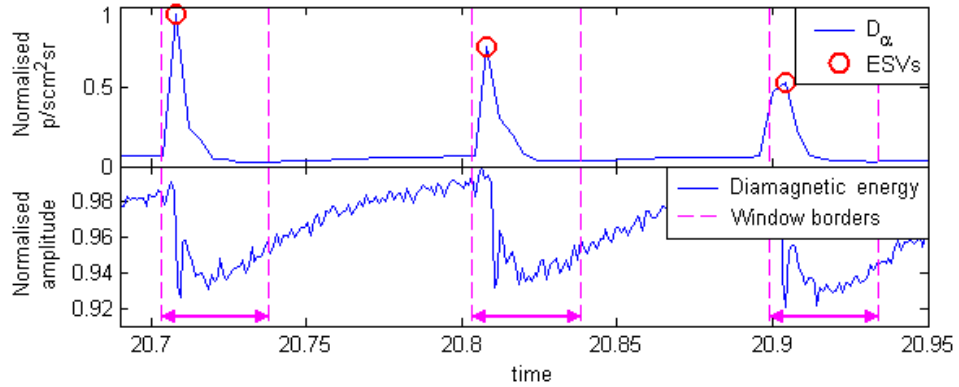


Figure 4.10: ELMs location, step 2. Division of the diamagnetic energy example, JET pulse 73337

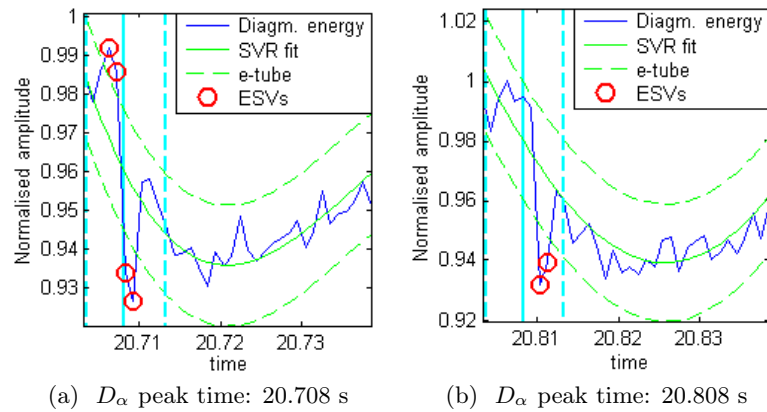


Figure 4.11: ELMs location, step 2. Example of the diamagnetic energy drops location, JET pulse 73337

On the other hand, if not ESVs are found in the diamagnetic energy within 5 ms from the  $D_\alpha$  peak, it is discarded.

Figure 4.11 contains two examples of the analysis of the diamagnetic energy drop for two of the  $D_\alpha$  peaks (solid cyan lines) previously located. In both cases, ESVs appear within 5 ms (cyan dashed lines) from the  $D_\alpha$  peaks and therefore, these peaks are recognised as ELMs.

#### 4.1.3.3 Results of ELMs detection in JET

The ELM location method was applied to a JET database of more than 1,200 pulses in the range [73337, 78156]. 226,751 ELMs were identified in these pulses.

Due to the lack of a large ELMs database, the performance of the ELM

Period (s)	Number of ELMs	Period (s)	Number of ELMs
< 0.01	3,200	0.04 to 0.05	19,809
0.01 to 0.02	56,550	0.05 to 0.06	11,409
0.02 to 0.03	61,373	0.06 to 0.07	6,800
0.03 to 0.04	30,100	0.07 to 0.08	4,000

Table 4.2: Distribution of the periods of the located ELMs

location method was tested comparing its results with the ELMs manually located by experts in 20 JET discharges from the above range. The method reached a success rate of 95% in the location of ELMs.

Table 4.2 shows the number of ELMs located for different time periods (the time difference between one ELM and the next one). The most common period was between 0.02 and 0.03 s with 61,373 ELMs.

#### 4.1.4 Analysis of the temperature profiles during ELMs

The automated determination of the ELMs' times carried out in Section 4.1.3 allows the study of the ELMs' phenomenology using a large database of ELMs. One relevant topic related to the ELMs is the study of the dynamics of the electron temperature profile during an ELM crash and more specifically, the study of the ETB (see Section 2.2.1) during an ELM (González et al., 2012c).

As it has been explained in Section 4.1.3, ELMs cause a reduction in density and temperature in the edge of the plasma. It deteriorates the ETB<sup>2</sup> and therefore, the plasma confinement degrades. Different plasma configurations lead to different confinement degradation during ELMs and therefore, it is worth studying the effect of each parameter in the degradation of the ETB.

The *electron temperature* (ET) profile measure the temperature of the plasma electrons along the major radius of the fusion device. In JET, the ET can be measured using the electron cyclotron emission (ECE) diagnostic (de la Luna et al., 2004). At each time, the ECE measures the ET at 96 different radial positions and a bandwidth of 5 kHz. Using a sampling rate of 250 kHz, it provides up to 3 s of data collection. Figure 4.12 contains two examples of the ET profile using the ECE diagnostic from JET pulse 733326. The measurement in Figure 4.12a shows a L-mode instant ( $t = 11.630$  s) and the one in Figure 4.12b depicts a H-mode instant ( $t = 19.000$  s). Each dot represents a measurement of the ECE diagnostic. It is possible to observe that the temperature raises from the plasma edge to the centre and the temperature reached in H-mode is higher than in L-mode.

The ETB can be recognised as a high step gradient in the ET close to the plasma edge in H-mode plasmas. Here, this gradient has been called *edge*

<sup>2</sup>**ETB:** Edge Transport Barrier (recall)

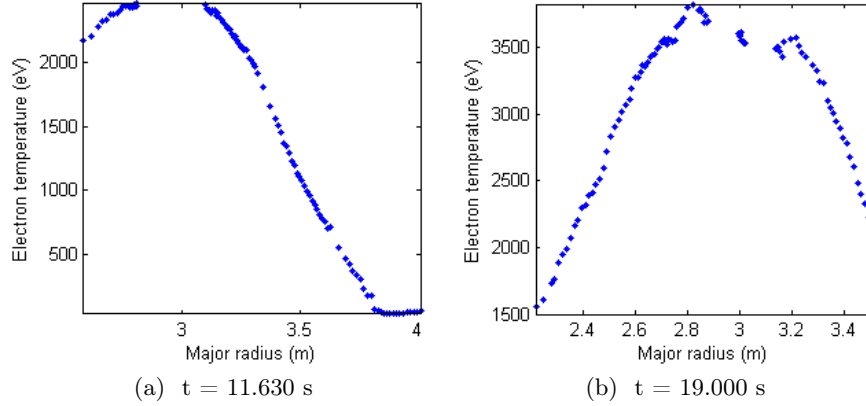


Figure 4.12: Two measurements of the electron temperature profile using the ECE diagnostics, JET pulse 73326

*temperature gradient* (ETG). It causes an increment of the plasma pressure at the centre and therefore, the temperature of the electrons raises. Figure 4.13 contains two examples from JET pulse 78073. In Figure 4.13a, the plasma is in L-mode ( $t = 8.100$  s) and thus, the ETG does not appear. In contrast, Figure 4.13b depicts a H-mode instant ( $t = 9.400$  s). The ETG appears close to the plasma edge (approx. 3.819 m). It has been emphasised using a red circle. The scale of the ET has been plotted in blue on the left of Figures 4.13a and 4.13b.

In order to simplify the automated recognition of the ETG, a new parameter called *Steep Gradient Temperature* (SGT) has been introduced. It estimates the steepness of the ET and it is equal to the ET difference between two consecutive radial points:

$$SGT(i) = \frac{ET(i) - ET(i+1)}{r(i+1) - r(i)} \quad (4.10)$$

where  $r(i)$  is the plasma radius where  $ET(i)$  has been measured and  $i$  is a radial position ( $i = 1, \dots, 95$ ). In Figure 4.13, the SGT has been plotted using a green line with diamonds. The scale of the SGT appears in green on the right-hand side of Figures 4.13a and 4.13b.

Since the ETG has been defined as a high steep gradient of the ET close to the plasma edge, it can be easily located in H-mode plasmas at the radial position close to the plasma edge where the SGT peaks. In Figure 4.13b, there is a clear peak of the SGT at the ETB. In contrast, the SGT does not peak at the plasma edge in L-mode plasmas (Figure 4.13a).

The ET profile of the plasma steadily decreases from the plasma centre to its edge. As a result, the SGT oscillates around a certain value and finally it peaks at the ETG close to the plasma edge. The value around which

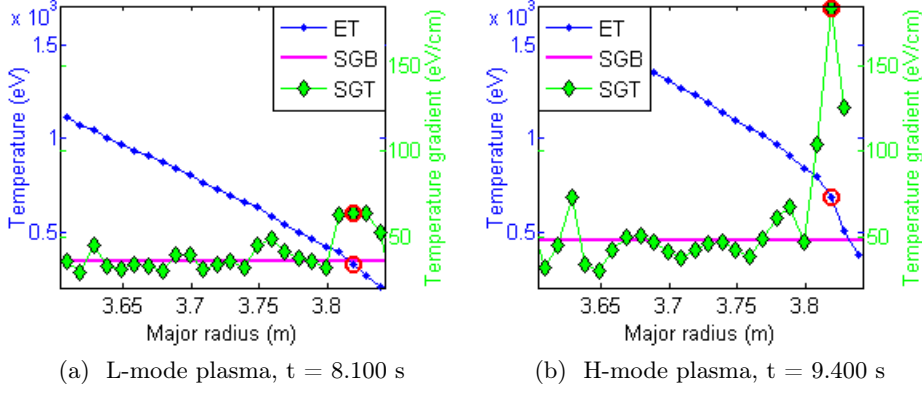


Figure 4.13: Examples of temperature profiles in L and H modes, JET pulse 78073

the SGT oscillates has been called *Steep Gradient Baseline* (SGB) and it is computed and the mean value of the SGT from the plasma centre to two radial positions before the ETG:

$$SGB = \text{mean}(SGT(c), SGT(c+1), \dots, SGT(j-2)) \quad (4.11)$$

where  $c$  is the radial position of the centre of the plasma and  $j$  is the radial position of the ETB. Since the SGB is a single value, it has been plotted using a magenta horizontal line in Figure 4.13. In Figure 4.13a the plasma is in L-mode. The ET decreases from the centre to the edge of the plasma without high gradients and therefore, there is a small difference between the SGB and the SGT at the plasma edge (27.94 eV). In contrast, the plasma in Figure 4.13b is in H-mode and therefore, there is a large difference between the SGB and the SGT at the plasma edge (136.11 eV).

It is possible to quantify the ETG of a H-mode plasma using the SGB as a reference of the temperature gradient. This value has been called *edge temperature gradient coefficient* ( $ETG_{coef}$ ) and it is estimated as the highest value of the SGT close to the plasma edge ( $SGT_{ETB}$ ) by the SGB:

$$ETG_{coef} = \frac{SGT_{ETB}}{SGB} \quad (4.12)$$

The larger difference between the  $SGT_{ETB}$  and the  $SGB$ , the higher value of the  $ETG_{coef}$ . The  $ETG_{coef}$  is equal to 1 if  $SGT_{ETG} = SGB$ . It implies that the SGT at the plasma core is equal to the SGT and the plasma edge (there is no ETB). The  $ETG_{coef}$  could be lower than 1 if the temperature gradient at the ETB is lower than the mean temperature gradient at the plasma core.

#### 4.1.4.1 Degradation of the temperature gradient between two times

In order to measure the degradation of the ETG at a certain time, it is necessary to determine a reference time to compare it. Here, the  $ETG_{coef}$  of the reference time have been called  $ETG_{coef}^{ref}$ . Then, the degradation of the ETG between a time  $t$  ( $ETG_{coef}^t$ ) and the reference time is computed as:

$$degrad\left(ETG_{coef}^{ref}, ETG_{coef}^t\right) = 1 - \frac{ETG_{coef}^t - 1}{ETG_{coef}^{ref} - 1} \quad (4.13)$$

The degradation of the ETG is equal to 1 (100%) if  $ETG_{coef}^t$  is equal to 1—there is no ETB. In contrast, the degradation is 0 (0%) if  $ETG_{coef}^{ref} = ETG_{coef}^t$ —the gradients at both times are similar. The degradation could be lower than zero if the gradient at the time  $t$  is higher than the gradient at the reference time—there is no degradation ( $ETG_{coef}^t > ETG_{coef}^{ref}$ ).

On studying two close times (within a few milliseconds) the ET at the plasma core is almost constant. Thus, the SGB is not altered and it is possible to consider that  $SGB^{ref} \approx SGB^t$ . Using this simplification and substituting the value of the  $ETG_{coef}$  from Eq. 4.12 into Eq. 4.13:

$$\begin{aligned} degrad\left(ETG_{coef}^{ref}, ETG_{coef}^t\right) &= 1 - \frac{\frac{SGT_{ETB}^t}{SGB} - 1}{\frac{SGT_{ETB}^{ref}}{SGB} - 1} \\ &= 1 - \frac{SGT_{ETB}^t - SGB}{SGT_{ETB}^{ref} - SGB} \\ &= \frac{SGT_{ETB}^{ref} - SGB - SGT_{ETB}^t + SGB}{SGT_{ETB}^{ref} - SGB} \\ &= \frac{SGT_{ETB}^{ref} - SGT_{ETB}^t}{SGT_{ETB}^{ref} - SGB} \end{aligned} \quad (4.14)$$

Using this equation, the degradation of the ETG between two times is computed as the difference between the  $SGT_{ETB}$  at the reference time and  $t$  by the difference between the  $SGT_{ETB}$  at the reference time and the SGB. As previously, the degradation is 1 (100%) if there is no ETB at  $t$  ( $SGT_{ETB}^t = SGB$ ) and 0 (0%) if the amplitude of the temperature gradient at the ETB at  $t$  is equal to the one at the reference ( $SGT_{ETB}^t = SGT_{ETB}^{ref}$ ).

#### 4.1.4.2 Degradation of the ETG during ELMs

The degradation of the ETG caused by an ELM's crash can be studied using the ET profile. The reduction in density and temperature in the edge of the

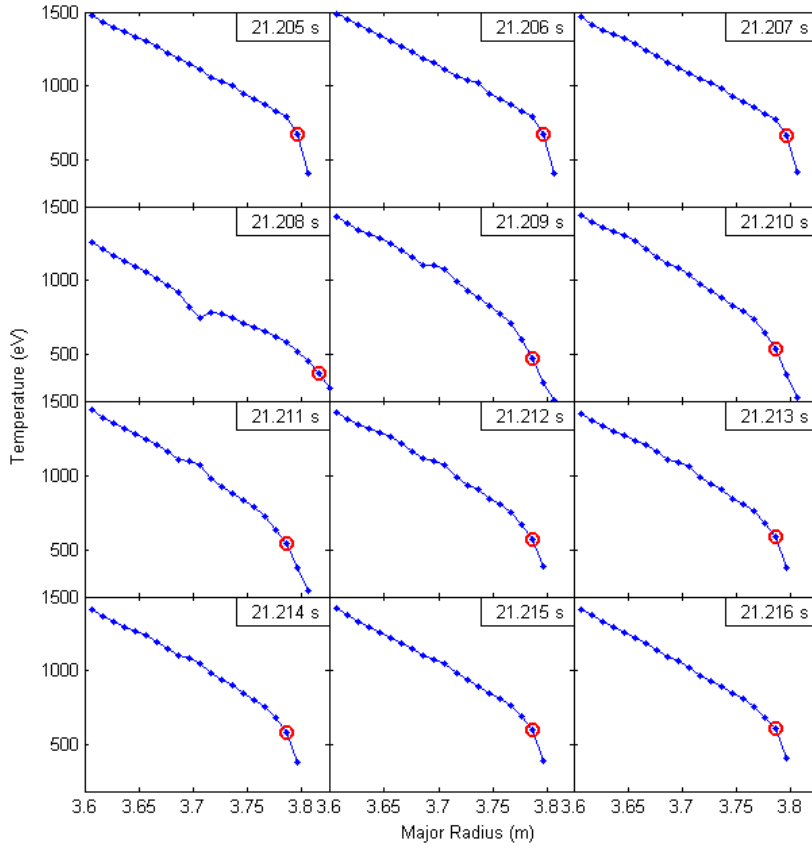


Figure 4.14: Example of the evolution of the temperature profile during an ELM, JET pulse 73337

plasma leads to a fall of the ETG. The density and temperature raise after the ELM and the ETG appears again at the plasma edge.

Figure 4.14 depicts the evolution of the electron temperature of an ELM of JET pulse 73337. The ELM takes place at  $t = 21.208$  s. Before the ELM, the ETG can be clearly seen in the ET profile (it has been emphasised using a red circle). At the ELM time, the ETG disappears and the ET profile is almost a straight line. After the ELM, the ETG slowly recovers its temperature gradient.

This technique of quantification of the degradation of the ETG was applied to analyse the ETG during ELMs in JET. The ELMs were automatically located using the methodology described in Section 4.1.3. Since the ET profile was not always available, only a subset of the ELMs located in Section 4.1.3.3 were studied (more than 700 pulses from JET campaigns from C15a to C26 and more than 46,000 ELMs). Here, the reference time was set to the ELM time minus 2 ms ( $ELM - 2$ ) and the time where the ETG degradation

Pulses	ELMs	ELMs with ETG recovered	mean ETG degradation (non-recovered cases)
<b>Campaign 15a</b>			
8	846	455 (53.786%)	22.710%
<b>Campaign 15b</b>			
23	1,136	463 (40.757%)	27.235%
<b>Campaigns 16, 17</b>			
138	8,893	3,088 (34.724%)	22.263%
<b>Campaign 18</b>			
19	863	283 (32.797%)	20.363%
<b>Campaign 19</b>			
5	74	14 (18.919%)	37.958%
<b>Campaign 20</b>			
67	3,762	509 (13.530%)	30.761%
<b>Campaign 21</b>			
39	2,425	635 (26.186%)	28.668%
<b>Campaign 22</b>			
49	2,594	408 (15.729%)	24.791%
<b>Campaign 23</b>			
108	6,293	1,233 (19.593%)	21.642%
<b>Campaign 24</b>			
10	436	48 (11.009%)	33.772%
<b>Campaign 25</b>			
60	2,586	527 (20.379%)	26.126%
<b>Campaign 26</b>			
222	16,279	3,687 (22.649%)	22.376%
<b>Total</b>			
748	46,187	11,350 (24.574%)	23.948%

Table 4.3: ETG degradation results at ELM time + 2 ms in JET

is quantified was set to the ELM time plus 2 ms ( $ELM + 2$ ).

Table 4.3 shows the results obtained after the analysis of the ETG. The first column contains the number of pulses of each campaign that were analysed. The second one shows the number of ELMs analysed for each campaign. The number of ELMs that had recovered the initial ETG 2 ms after the ELMs' times ( $degrad\left(ETG_{coef}^{ELM-2}, ETG_{coef}^{ELM+2}\right) \leq 0$ ) is shown in the third column. This experiment showed that 11,350 (24.574%) ELMs had recovered their ETG 2 ms after the ELMs' times. Therefore, there were 34,837 (75.426%) ELMs with a degradation higher than 0. Finally, the last column of Table 4.3 contains the ETG degradation of the ELMs with a degradation higher than 0, 2 ms after the ELMs' crashes. The mean ETG degradation was 23.948%.

Figure 4.15 depicts the results obtained in the experiment. Both graphs (4.15a and 4.15b) shows the histogram of the degradation of the ETG 2 ms after the ELMs' times (number of ELMs versus degradation). The difference

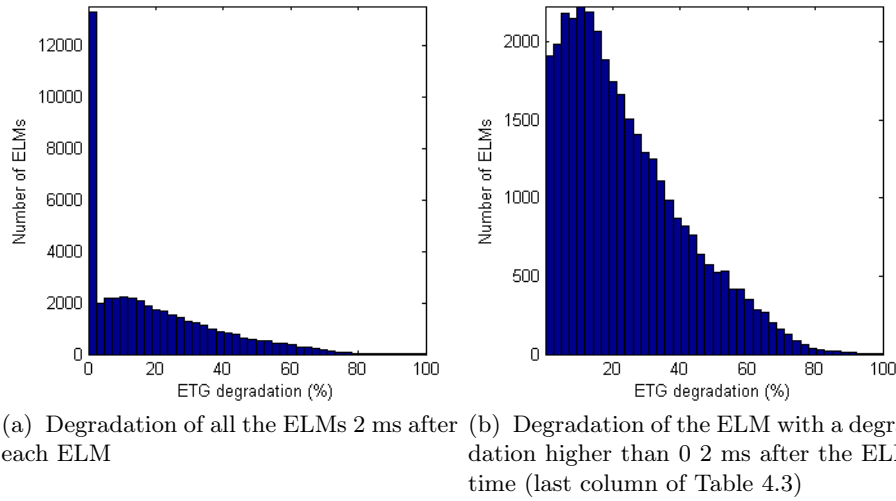


Figure 4.15: Distribution of the ETG degradation results

between both is that Figure 4.15a includes the ELMs where the degradation is lower or equal to zero and Figure 4.15b does not (these are the results shown in the last column of Table 4.3).

#### 4.1.5 Discussion

Section 4.1 has introduced UMEL, an Universal Multi-Event Locator. UMEL has been used to build three expert systems to locate ELMs, disruptions and sawteeth.

Usually, plasma phenomena is characterised by high frequency events in waveforms (spikes, peaks or falls). Then, it could be thought that other existing techniques to locate high frequency events in signals, such as wavelets (see Section 3.2.3), can provide similar results. Using wavelets, it is possible to find a local discriminant base as described in (Saito and Coifman, 1995). Using this base, high frequency events can be located. But the searching capabilities of UMEL are not restricted to high-frequency events. It also locates segments of waveforms that show special patterns although they have low frequencies.

Figure 4.16 contains an example of the analysis of a sinusoidal function using wavelets and UMEL. The absolute values of the detail coefficients of the sinusoidal function have been plotted in Figure 4.16a. It is possible to observe that the largest values of the detail coefficients are located in the straight segments of the sinusoidal function—these are the points with largest amplitude differences and therefore, their wavelet detail coefficients are the largest ones (vertical green lines). Unfortunately, these segments are not the ones that provide the most interesting information. Figure 4.16b depicts the

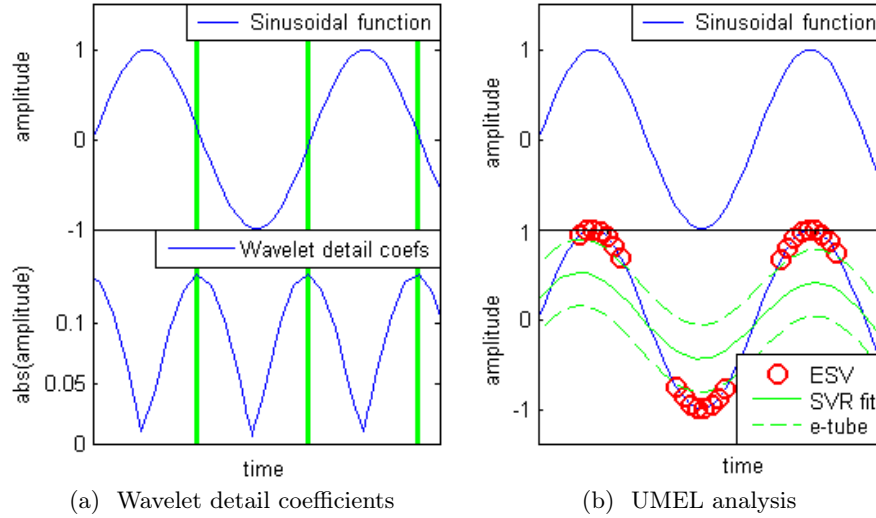


Figure 4.16: Comparison of UMEL versus wavelets

analysis performed using UMEL. In this case, ESVs appear exactly in the points where the wavelet detail coefficients have bottomed out. The points where the ESVs appear are the most relevant ones of the waveform.

It is also worth mentioning that UMEL cannot be computed using a different regression technique. In SVR, the regression fit is function of the width of the  $e$ -tube. As a consequence, the fit is different for different values of the  $e$  parameter. Therefore, the ESVs cannot be obtained using a different regression technique just by locating the samples with a residual value larger or equal than  $e$ . It is also important to bring up that ISVs cannot be determined using a different regression technique and they provide useful information as it will be explained in the next section.

Finally, the importance of the selection of the UMEL parameters should be pointed out. The SVR kernel,  $K_C$ ,  $K_e$  and  $K_\sigma$  must be chosen accordingly to the phenomena that are being located in waveforms. Each type of event requires different parameters that must be fixed before the analysis. Fortunately, once these parameters have been fixed, they can be applied to a wide range of plasma discharges without changes.

## 4.2 Analysis of 2D using UMEL

In the last few years, the use of cameras as plasma diagnostics has spread along the fusion community. Cameras allow the visualization of the processes taking place inside the vacuum vessel in both the visible and the infrared spectrum. These new diagnostics have been used, among others, for thermography of the Plasma Facing Components (PFCs) and the divertor

tiles, the analysis of power and energy fluxes deposition or the analysis of impurities.

ITER (see Section 2.3.4) is intended to use cameras as a main source of information for both data acquisition and control. The camera network planned for ITER consists of 36 infrared and visible views of the vacuum vessel that will generate data at a rate of 10 GByte/s. As a consequence, the analysis of the data generated by cameras in present and future devices is a daunting task.

The only option to interpret the data generated by cameras is probably the use of automatic analysis tools. These tools convert the sequences of frames into control signals, new entries in databases or intelligible figures for different plasma studies. It is possible to distinguish two main groups of image analysis applications:

1. **Real-time applications:** they monitor the plasma state in real time and they are able to send control signals, such as alarms, if they detect dangerous events.
2. **Off-line applications:** their calculations require more time and therefore they cannot be applied in on-line control. They locate and determine the existence of plasma events such as ELMs of Multifaceted Asymmetric Radiations From the Edge (MARFEs).

In the first group, it is worth mentioning the measure of the temperature of the PFCs using infrared cameras and the tracking of pellets<sup>3</sup>. The PFCs' temperature measurement is carried out using the intensity of the pixels in fixed image's areas. It has been applied in JET (Gauthier et al., 2007) and it has been implemented using FPGAs<sup>4</sup> in Tore Supra (Martin et al., 2010).

The variety of applications of the second group is higher. The off-line analysis allows more complex calculation and thus, more sophisticated studies. One of the problems addressed using off-line analysis is the tracking of dust inside the vacuum vessel. Most of this dust is generated by the erosion of the PFCs. When the concentration of dust is high, it risks the plasma operation. The tracking of dust during plasma operation has been carried out in ASDEX and Tore Supra in 2D (Hong et al., 2010) and in NSTX in 3D using two cameras simultaneously (Roquemore et al., 2007). These applications allow the study of dust trajectories and how plasma is affected by their existence.

MARFEs have also drawn the attention of scientists. They are instabilities that can reduce the plasma confinement and they can also cause disruptions. MARFEs can be identified using visible light cameras. This phenomenon has been identified in JET using optical flow methods (Craci-

---

<sup>3</sup>**Pellet:** millimetric ball of frozen hydrogen isotopes for fuelling plasma

<sup>4</sup>**FPGA:** Field Programmable Gate Array

unescu et al., 2011) and Cellular Nonlinear Networks (CNN) (Murari et al., 2011).

The pattern recognition techniques applied to images also belong to the second group. The search of patterns inside images is very time consuming and thus, it cannot be applied on-line. One example is the location of patterns in JET films (Vega et al., 2009a). The pattern selected by a user is sought in the frames database. The retrieved patterns are ordered using a similarity measure.

The methods of image classification lay in the border of both groups. The use of these methods can be on-line or off-line depending on the method used to solve the problem. An example of image classification is the classification of the Thomson scattering in the TJ-II stellarator using conformal predictors (Vega et al., 2010b).

The analysis of images using UMEL belongs to the group of off-line applications. It can be applied with a two-fold purpose (González et al., 2010):

1. **Temporal location of events:** it consists in locating the frames where single events or a set of events take place. The times of the events are given by the times of the frames where they have been located. It is described in Section 4.2.1.
2. **Detection of regions of interest (ROIs):** in an image, all the pixels do not contain the same amount of information and thus, they do not have the same relevance. For example, the pixels in the background of an image contain less information—they are less relevant—than the pixels in the focus of the image. A ROI is a set of connected (adjacent) pixels with a high degree of relevance. Using UMEL, the pixels where ESVs appear are the pixels with the highest relevance (see Section 4.2.2). In addition, it is possible to study the evolution of the ROIs using heat maps (see Section 4.2.3).

UMEL computes every single frame independently, so it is easily parallelisable. The frames are analysed one by one and once all frames have been processed, the results are put together and interpreted in order to identify events and to study the evolution of ROIs. It does not make any distinction between types of films and thus, it can be applied to infrared and visible light films.

A regression surface must be computed for every frame that is being analysed. Figure 4.17 contains a real example from JET visible light camera KL8, pulse 69787. Figure 4.17a shows the original frame. The 3D surface generated by this frame is shown in Figure 4.17b. The height of each pixel corresponds to its intensity. Then, a 3D fit of this surface is computed using SVR (Figure 4.17d). The pixels with a high-intensity gradient become ESVs because they are the most difficult points to fit. Figure 4.17c contains the

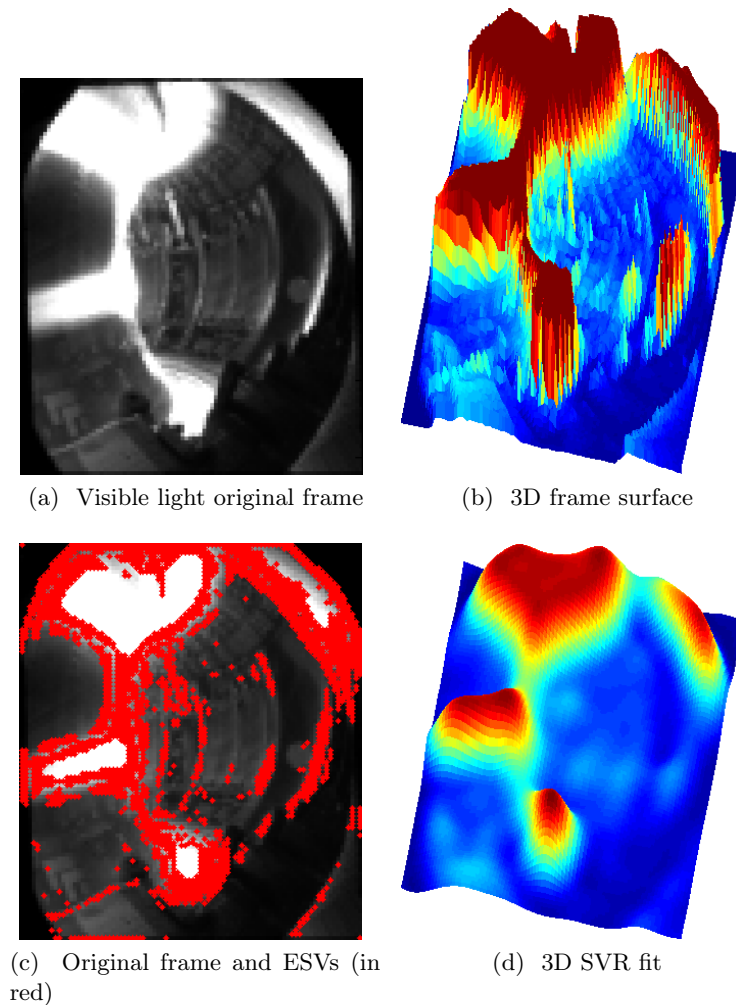


Figure 4.17: Example of UMEL application to images

ESVs found and their locations in the original image. In addition, some ISVs appear in the essential pixels to define the fitting surface.

#### 4.2.1 Event location in films

One of the UMEL capabilities is the location of events in plasma films. SVs appear in those areas with a high intensity gradient between pixels and those areas that are difficult to regress. In the case of visible light and infrared films, these high gradient zones correspond to high-emission areas.

In infrared films, the most interesting events are hot spots. These events are hits of the plasma against the PFCs that cause an increase of their temperature. In infrared films, hot spots are detected due to a sudden aug-

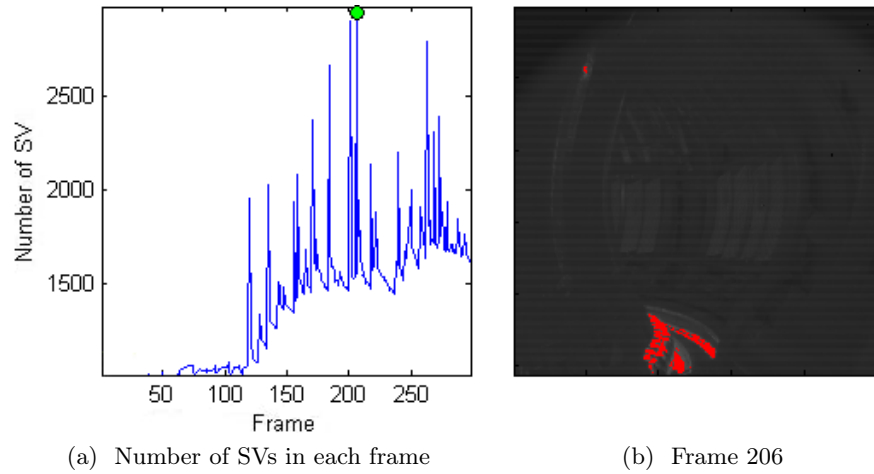


Figure 4.18: Infrared film analysis using UMEL, JET pulse 70231

mentation of the intensity of the pixels in the hottest areas. It makes the number of SVs rise abruptly. Figure 4.18 contains an example of the study of an infrared film (JET pulse 70231). Figure 4.18a shows the number of SVs found in each frame of the film. Each one of the peaks in this figure corresponds to a hot spot. Figure 4.18b depicts the frame with the maximum number of SVs (frame 206). Most of the SVs appear in the divertor tiles, the hottest area of the image.

It is also possible to locate events of interest in visible light films. In this case, these events can correspond to MARFEs, disruptions, pellets or Unknown Flying Objects (UFOs), among others. All these events cause an increase of the emission of light from the plasma and hence, a rise in the pixels intensity. Figure 4.19 contains an example of the analysis of a visible light film from JET pulse 69787. Figure 4.19a shows the number of SVs detected in each frame. Figure 4.19b depicts the frame with the highest number of SVs (frame 804). The time instant of this frame corresponds to the time of a plasma disruption.

The location of peaks and events in the graphs of Figure 4.18a and 4.19a can be addressed in an automatic way using UMEL. The number of SVs in each frame can be fitted using SVR as it has been explained in Section 4.1. The ESVs appear in the high frequency points, and in this case, these points correspond to hot spots in the infrared films and MARFEs, disruptions and other events in visible light films.

#### 4.2.2 Detection of ROIs

One important use of UMEL is the location of ROIs in images. Since all the pixels in an image do not contain the same amount of information, not all

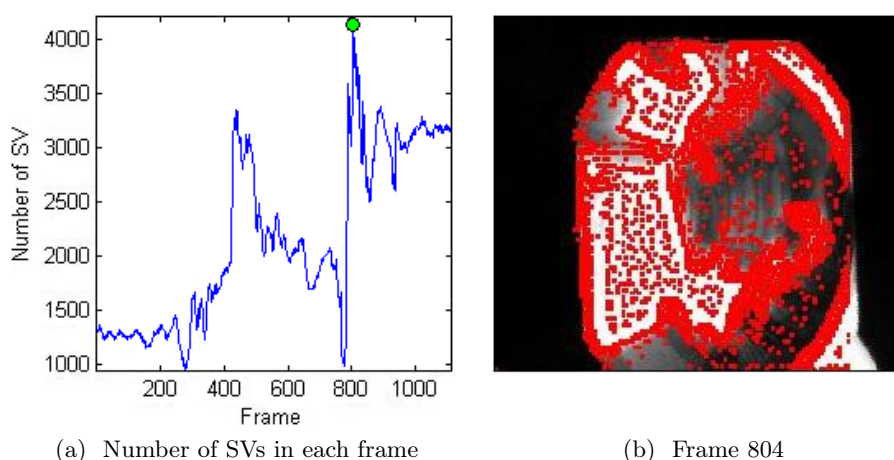


Figure 4.19: Visible light film analysis using UMEL, JET pulse 69787

the regions have the same degree of relevance. ROIs are areas of an image where a high number of SVs appear. SVs appear in the most difficult areas to regress and where there are large intensity differences between neighbouring pixels.

There are two different options to locate ROIs in images using UMEL:

1. **Using all the SVs:** SVs appear in areas where there is a high gradient between neighbouring pixels and in all the pixels of the images that are relevant to compute the regression surface. Using this alternative, SVs can appear in all the pixels of the ROI (edges and interior). Figures 4.20a and 4.19b contain two examples of the use of all the SVs to locate ROIs in infrared and visible light film. In Figure 4.20a, most of the SVs of the frame appear in the divertor tiles, the hottest area of the vessel.
2. **Using only the ESVs:** ESVs appear only in those areas with large intensity variation between neighbouring pixels. Therefore, they can be used to locate the edges of the emission areas. Figure 4.20b contains an example of edge detection using UMEL. In this case, no SVs appear inside the area of high emissions of the plasma. All the ESVs are concentrated in the areas with a high intensity gradient.

### 4.2.3 ROIs' evolution: Heat Maps

Heat maps are images that summarise the evolution of ROIs along the frames of a film. They are very useful to analyse a set of frames using only a single image. The intensity of a pixel in a heat map depends on the activity of this pixel in a set of frames (or the entire film). The more activity of the pixel,

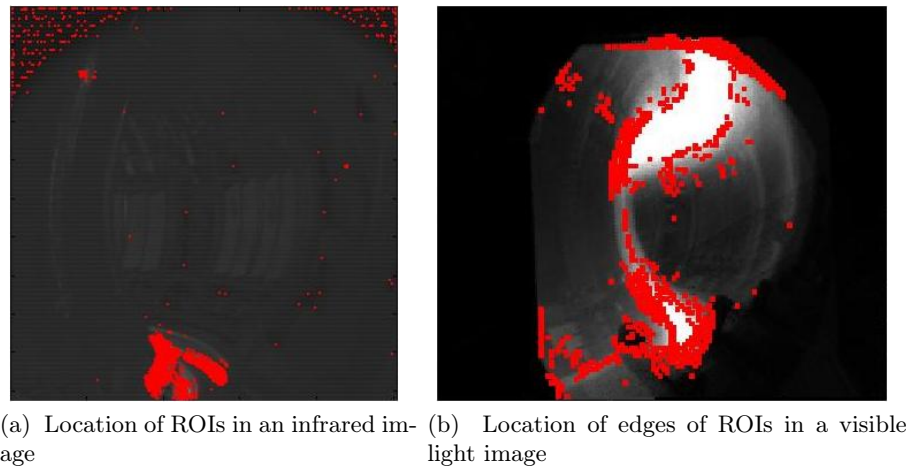


Figure 4.20: Location of ROIs using SVs and ESVs

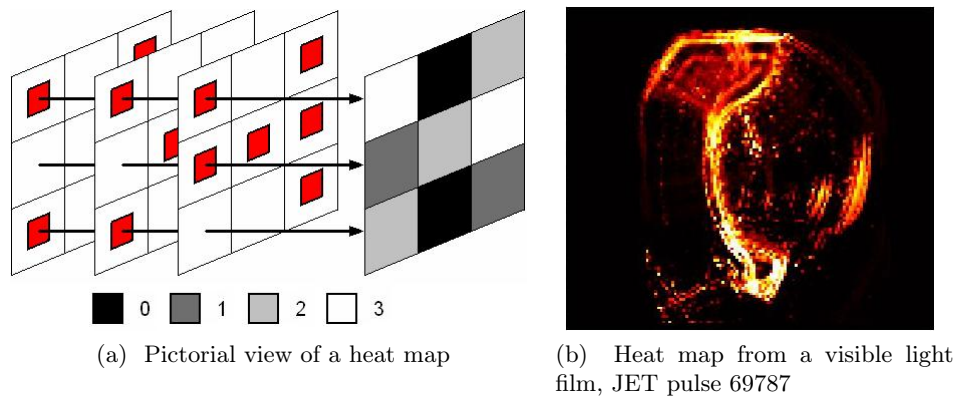


Figure 4.21: Heat maps using ESVs

the higher the intensity of this pixel in the heat map.

The activity of a pixel can be understood in many different ways, e.g. the absolute value of the intensity, a boolean value showing if the intensity is above a certain threshold, the mean value of the intensity of the neighbouring pixels, etc. Here, the presence or absence of a SV in a pixel is used as pixel activity. The intensity of the pixels of a heat map is a function of the number of SVs on each pixel. Given a pixel of a heat map, its intensity depends on the number of SVs that have appeared on this pixel in the analysed frames (the higher number of SVs, the lightest pixel in the heat map).

A pictorial view of a heat map can be found in Figure 4.21. The red points in Figure 4.21a symbolise SVs in a set of three frames. The SVs in each frame have been computed independently. The number of SVs in the sequence of

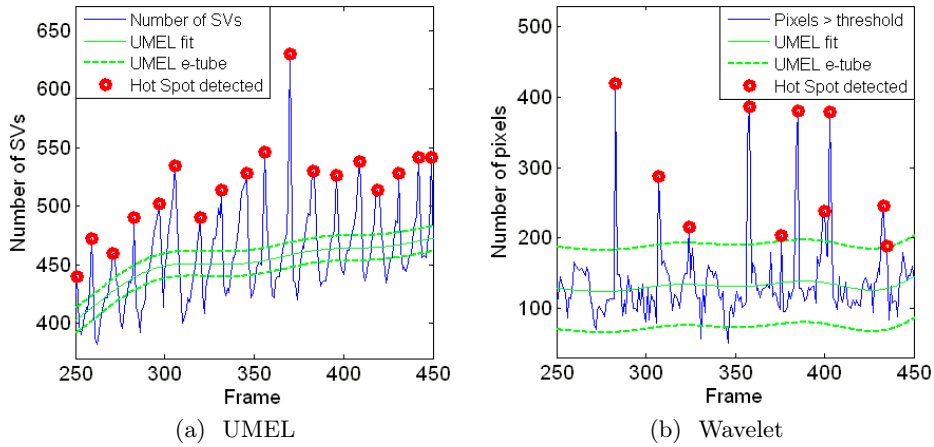


Figure 4.22: Comparison of hot spots location using UMEL and wavelets

frames is counted up. Then, the colour of each pixel of the heat map is function of these number. The pixels where no SVs appear are black while the ones with the maximum of SVs (3) are white. Figure 4.21b shows the heat map computed from a visible light camera KL8 of JET pulse 69787. 154 frames have been used to computed this heat map. The lightest areas of the image are the ones where the SVs have appear and therefore, the edges of the ROIs. This heat map resumes the high emission areas of the set of frames.

#### 4.2.4 Location of hot spot in JET infrared films

The location of events in plasma films using UMEL was tested in 10 JET infrared films. The hot spots were located using UMEL and the wavelet transform (see Section 3.2.3). The films contained 819 frames each.

The event location using wavelets was based on the values of the detail coefficients. For each frame of the films, a wavelet transform (order 2 Daubechies family) was computed. The horizontal, vertical and diagonal detail coefficients were summed and normalised between 0 and 1 using Eq. 4.8. For each frame, the number of pixels with a value of the sum of the detail coefficients above a certain threshold was counted up. The value of the threshold was empirically set to 0.45.

UMEL was applied again to automatically locate the hot spots in both, the number of SVs on each frame (Figure 4.22a) and the number of pixels in each frame with a wavelet value larger than the threshold (Figure 4.22b). ESVs appeared in the peaks of both graphs and therefore hot spots can be located without human intervention. It was possible to observe that the existence of hot spots in infrared films was better indicated by UMEL. The

number of pixels with a wavelet value larger than the threshold did not reproduce the hot spots behaviour as well as SVs do.

Table 4.4 contains the results obtained by both methods. This test was executed using an Intel® Core™ 2 Quad CPU Q9300 2.50GHz, 1.95GB RAM. The first column of the table corresponds to the method used. The second one is the number of hot spots detected by each one. These hot spots can contain errors and can miss real hot spots. The third column is the *True Positives*, i.e. the number of real hot spots detected by the methods. The fourth column is the number of *False Negatives*, i.e. the number of real hot spots missed by the methods. The fifth column contains the number of *False Positives*, i.e. the number of false alarms or the number hot spots detected by the methods that are not real. Finally, the sixth column shows the CPU time used in the analysis of each film.

The last row of Table 4.4 summarises the results obtained over the ten films. The average rate of *True Positives* was 91.64% using UMEL versus 68.17% using wavelets. The average *False Positives* rate was 3.46% using UMEL versus 14.18% using wavelets. In contrast, the CPU times of UMEL were much larger than the ones obtained using wavelets. This was a consequence of the quadratic optimization problem that must be solved for each frame in the films using UMEL.

#### 4.2.5 Discussion

The most important disadvantage of the application of UMEL to images is probably its time consumption. Due to the high resolution of the plasma cameras, the computation of the optimization problem needed to generate the fitting surface is slow. It makes UMEL unable to be applied to real time control. In spite of its time consumption, the application of UMEL to off-line analysis can be of great interest to analyse plasma phenomena. It is also possible to speed up the UMEL analysis in two different ways:

1. **Using the wavelet approximation coefficients:** it is possible to reduce the size of the images analysed by UMEL using wavelet analysis. Using an appropriate decomposition level, it is possible to obtain similar results to the ones obtained using the original images. The CPU times are significantly reduced using this method.
2. **Using paralellization:** as it has been previously explained, UMEL is applied independently to each frame. Then, the number of SVs in each frame is counted up and when all the frames have been computed, the peaks in the number of SVs are located. The CPU time of the location of the peaks is negligible compared to the CPU time of the analysis of the frames. UMEL can be easily paralellised if each frame is computed by a different computer. For example, the total computation time

Method	Hot spots detected	True positives	False negatives	False positives	Time (s)
<b>Pulse 73337, 97 hot spots</b>					
UMEL	96	90 (92.78%)	7 (7.22%)	6 (6.25%)	3,282
Wavelet	74	64 (65.98%)	33 (34.02%)	10 (13.51%)	65
<b>Pulse 73339, 152 hot spots</b>					
UMEL	143	142 (93.42%)	10 (6.58%)	1 (0.70%)	3,464
Wavelet	123	110 (72.37%)	42 (27.63%)	13 (9.76%)	64
<b>Pulse 73340, 143 hot spots</b>					
UMEL	132	130 (90.91%)	13 (9.09%)	2 (1.52%)	3,299
Wavelet	111	99 (69.23%)	44 (30.77%)	12 (10.81%)	64
<b>Pulse 73344, 134 hot spots</b>					
UMEL	129	127 (94.78%)	7 (5.22%)	2 (1.55%)	3,552
Wavelet	105	94 (70.15%)	40 (29.85%)	11 (10.48%)	64
<b>Pulse 73558, 91 hot spots</b>					
UMEL	86	84 (92.31%)	7 (7.69%)	2 (2.32%)	3,904
Wavelet	79	65 (71.43%)	26 (28.57%)	14 (17.72%)	68
<b>Pulse 73559, 107 hot spots</b>					
UMEL	91	90 (84.11%)	17 (15.89%)	1 (1.10%)	3,098
Wavelet	68	62 (57.94%)	45 (42.06%)	6 (8.82%)	68
<b>Pulse 73561, 98 hot spots</b>					
UMEL	98	88 (89.90%)	10 (10.20%)	10 (10.20%)	10,935
Wavelet	65	51 (52.04%)	47 (47.96%)	14 (21.54%)	66
<b>Pulse 74200, 45 hot spots</b>					
UMEL	46	44 (97.78%)	1 (2.22%)	2 (4.34%)	3,842
Wavelet	54	36 (80.00%)	9 (20.00%)	18 (33.34%)	64
<b>Pulse 74602, 134 hot spots</b>					
UMEL	127	119 (88.81%)	15 (11.19%)	8 (6.30%)	1,478
Wavelet	107	96 (71.64%)	38 (28.36%)	11 (10.28%)	64
<b>Pulse 74619, 64 hot spots</b>					
UMEL	63	62 (96.88%)	2 (3.12%)	1 (1.59%)	3,844
Wavelet	60	49 (76.56%)	15 (23.44%)	11 (18.33%)	65
<b>Total: 1,065 hot spots, 10 pulses</b>					
UMEL	1011	976 (91.64%)	89 (8.36%)	35 (3.46%)	40,698
Wavelet	846	726 (68.17%)	339 (31.83%)	120 (14.18%)	652

Table 4.4: Results of the location of hot spots

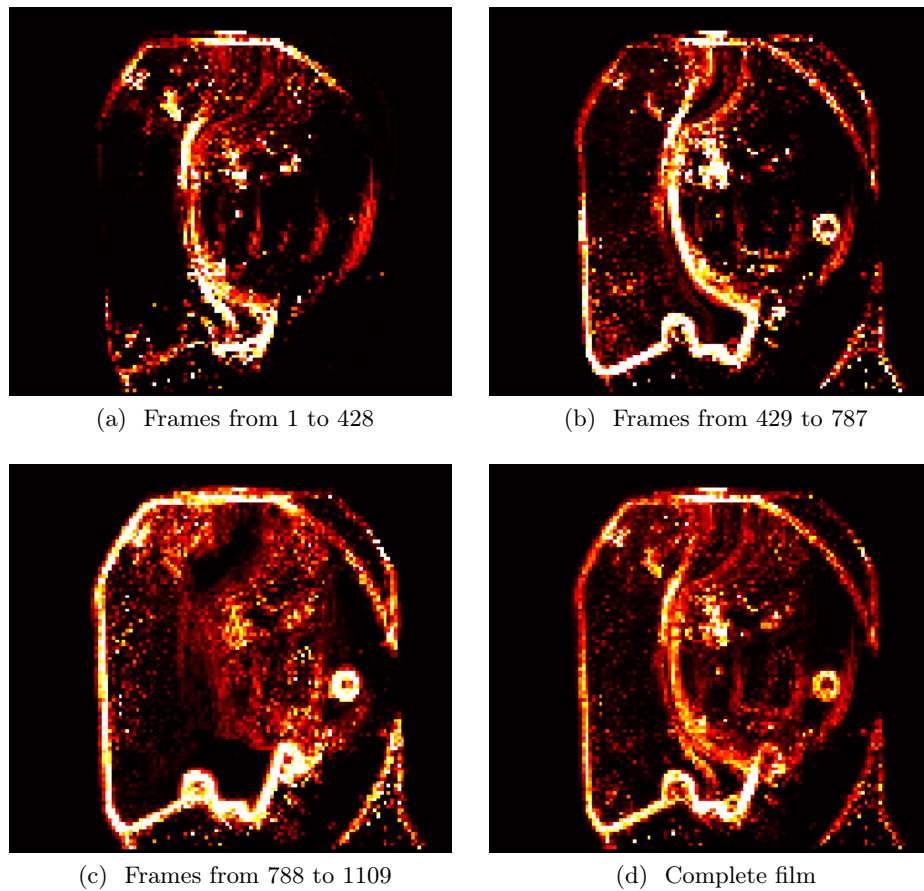


Figure 4.23: Heat maps examples from a visible light film, JET pulse 69787

can be reduced to 4,070 s using 10 computers and to 2,035 s using 20 computers.

There are interesting problems that can be addressed using UMEL. For example, the location of dust, pellets or UFOs in visible light films. All these phenomena are characterised by high emissivity in the visible light spectrum. Using UMEL, they can be located (they are high gradient areas) in 2D images. Using different views of the same sector of the vacuum vessel, the position of these particles can be tracked (Roquemore et al., 2007).

There is also an interesting discussion related to the use of heat maps. Since plasma films are quite long and the plasma passes through different states, it would be interesting to create one heat map per each state to summarise the different plasma behaviours. The determination of these plasma states can also be done automatically. Films can be analysed using UMEL and then, the number of SVs can be counted up. UMEL is able to detect relevant segments in the number of SVs and hence, it can determine the

different groups of frames where the heat map should be computed. For example, three different phases can be distinguished in Figure 4.19a:

1. **Frames from 1 to 428:** the plasma evolves without relevant instabilities. This heat map can be seen in Figure 4.23a. The lightest area is the divertor. Its contour appears in bright colours in the heat map.
2. **Frames from 429 to 787:** at the beginning of this phase, the number of SVs peaks, suddenly plummets and then it remains steady. It is caused by the existence of MARFEs. Since MARFEs appear as high emission areas in the inner wall of visible light films, the contour of the inner wall of the vacuum vessel is the lightest area in this heat map (Figure 4.23b).
3. **Frames from 788 to 1109:** this phase is characterised by the peak of the number of SVs at the beginning of the phase caused by a disruption. At this point, most of the plasma emits visible light. As a result, the lightest points of this heat map (Figure 4.23c) are the points of the contour of the area of vision (the area that the camera records), but the contour between the inner wall and the vacuum vessel in the middle of the image disappears.

Figure 4.23d contains the heat map computed using all the frames of the film. It is also possible to increase the level of detail increasing the number of phases.

### 4.3 Conclusions

This chapter has described UMEL (Vega et al., 2010a), a novelty technique to locate relevant behaviour in plasma waveforms and images. UMEL provides a new interpretation of SVs: they appear in relevant samples of the original waveform / image. Plasma phenomena are traditionally located by means of visual analysis. UMEL automates the location of these events and generates large databases of plasma phenomena. This technique is extremely important since later studies will use these databases to increase the statistical significance of their results.

UMEL implies the computation of a SVR fit. This fit defines the samples that become ESVs and ISVs. ISVs are SVs that lie inside the  $e$ -tube while ESVs lie outside. ISVs are necessary samples to compute the regression but they do not provide the same degree of relevance that ESVs do. ESVs are located in the most difficult samples to regress (the points of the original signal that lie outside the  $e$ -tube). Using these SVs, it is possible to locate relevant events and segments in waveforms and images.

In order to create expert systems to locate plasma phenomena without human interaction, the location capabilities of UMEL should be used to-

gether with expert knowledge. The experts must determine the events that characterise certain plasma phenomena and then, UMEL locates these events in plasma waveforms and images.

Three different expert systems have been built to locate plasma phenomena:

- **Sawteeth:** they can be located using the soft X-ray emission. The sawteeth pattern changes depending on the X-ray chord but the same UMEL code can be applied to any of them. Using UMEL, it is possible to automate the computation of the plasma diffusivity: using the times of a single sawtooth at the central cord and at the edge, the plasma diffusivity is given by Eq. 4.7.
- **Disruptions:** a simultaneous peak of the loop voltage and a drop of the plasma current determine the existence of a disruption. Using this information, an expert system has been built to locate disruptions using UMEL. A database of 343 JET pulses was analysed obtaining a success rate of 99.02% (Vega et al., 2010a). The located disruptions will help scientist to create better disruption models to increase the knowledge about disruptions and even to predict them before they occur.
- **ELMs:** an ELM can be identified as a drop of the diamagnetic energy accompanied by a spike in the  $D_\alpha$  signal. More than 1,200 JET pulses were analysed and 226,751 ELMs were located, obtaining a success rate of 95%. The most common period for ELMs was from 20 ms to 30 ms (61,373 ELMs) (González et al., 2010a). The located ELMs will be usefull to improve the theoretical models on ELMs and to increase the statistical significance of future studies.

One of the applications of the automated location of ELMs is the analysis of the temperature profiles during ELMs. The temperature profiles of 46,187 ELMs from 748 JET pulses were automatically analysed. The results showed that in 24.574% of the ELMs the temperature gradient was recovered 2 ms after the ELMs' crashes and the mean degradation value of the non-recovered cases was 23.948%. This automated method of analysis of the temperature profiles will be highly relevant in the analysis of the degradation caused by the ELMs' crashes under different plasma configurations, especially after the installation of the new ITER-like wall in JET.

Due to the great development of cameras as plasma diagnostics in the last few years, the analysis of films has become a hot topic in plasma fusion. UMEL will be a useful tool to study these films without human intervention (González et al., 2010). Using the number of SVs in each frame, UMEL located the occurrence of hot spots in JET infrared cameras. The location

of SVs in each frame revealed the hottest area of the vacuum vessel: the divertor tiles.

The behaviour of plasma in visible light films was also studied using UMEL. Plasma events are characterised by their high emissivity and thus, SVs appear in these areas. Using heat maps, it is possible to study the evolution of the plasma along the frames of a film. The heat maps can be computed using the frames in the regions of interest given by UMEL.

The most important drawback of UMEL is probably its time consumption. This problem has been mitigated using a SVM parallel version (Ramírez et al., 2010). This code speeds up the location of events in waveforms. In the case of films, the UMEL analysis can be sped up in an easy way: each single frame can be computed in a different CPU and then, the total number of SVs in each frame can be analysed using the SVM parallel version (if the number of analysed frames is very high). It is also possible to compute a SVR fit of each frame using the SVM parallel code.



## Chapter 5

# Dimensionality reduction techniques

During plasma operation, dozens of diagnostics measure plasma properties such as current, density or temperature. These diagnostics generate streams of data pairs or *samples*  $(t_i, x_i)$  where  $x_i$  is the magnitude of the measurement at the time  $t_i$ . These streams are usually called *waveforms* or *signals* and they can contain thousand of data pairs. For example, a typical signal of the  $D_\alpha$  emission in JET contains more than 100,000 samples. Some diagnostics produce multiple signals to describe the same plasma quantity, and hence, they generate information that is correlated. In addition, most of plasma magnitudes can be measured using different diagnostics.

Fusion massive databases contain TBytes of data. In JET, more than 5 GBytes of data are stored after each pulse of less than a minute. Figure 5.1 contains a picture of several JET diagnostics. It gives an idea of the complexity of this fusion device diagnostics. In TJ-II, there are more than 1,200 different signals that measure the plasma during operation. A detailed description of the TJ-II diagnostics can be found in (Laboratorio Nacional de Fusion, 2011).

Some signals are relevant to describe a certain physical phenomenon but others are not. Given a data set in a feature space of dimension  $p$ , the basic purpose of feature selection techniques is to determine a transformed or a reduced feature space of dimension  $q$ , where  $q < p$ , retaining the maximum variance of the original feature space. In the case of classification tasks, instead of the variance, the methods should maximise the classification success rate in the resulting feature space.

PCA (Section 3.2.1) and ROC (Section 3.2.2) are two of the most well-known and widely-used feature extraction methods. On the one hand, PCA transforms the feature space into a resulting space whose dimensions are orthonormal and a linear combination of the original feature space dimensions. It maximises the variance explained by the transformed dimensions. On the

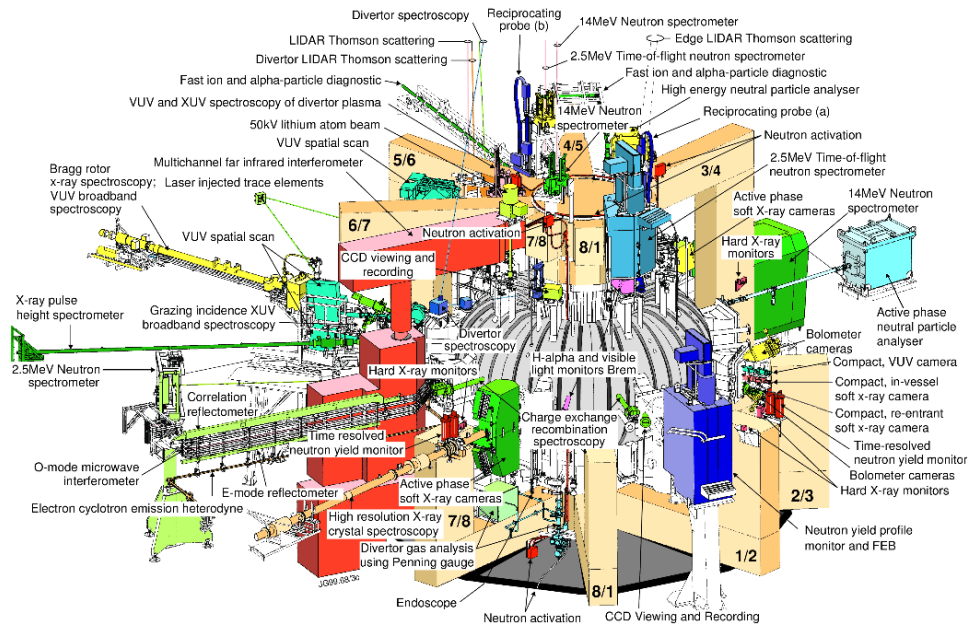


Figure 5.1: JET diagnostics

other hand, ROC selects the best dimensions to classify the samples of the data set. The dimensions of the resulting feature space are a subset of the original dimensions.

There are also non linear approaches to dimensionality reduction. (Tenenbaum et al., 2000) reports a technique of non linear dimensionality reduction that can be applied to complex data such as images or handwriting characters. This method is based on multidimensional scaling and it seeks to preserve the intrinsic geometry of the data.

This chapter describes two techniques developed for dimensionality reduction: a SVM feature extractor system for multidimensional data (Section 5.1) and a region extractor for classification of images (Section 5.2). The most important features of the L/H transition in JET have been analysed using the SVM feature extractor (Section 5.1.1) while the region extractor has been applied to the study of the TJ-II Thomson scattering images (Section 5.2.2). Section 5.3 contains the conclusions of this chapter.

## 5.1 SVM Feature Extractor System

In a multi-dimensional feature space, not all the dimensions (features) have the same degree of relevance. Given a classification problem, the most relevant features are the ones that allow the classification of the samples in the reduced feature space minimising the number of errors. The aim of

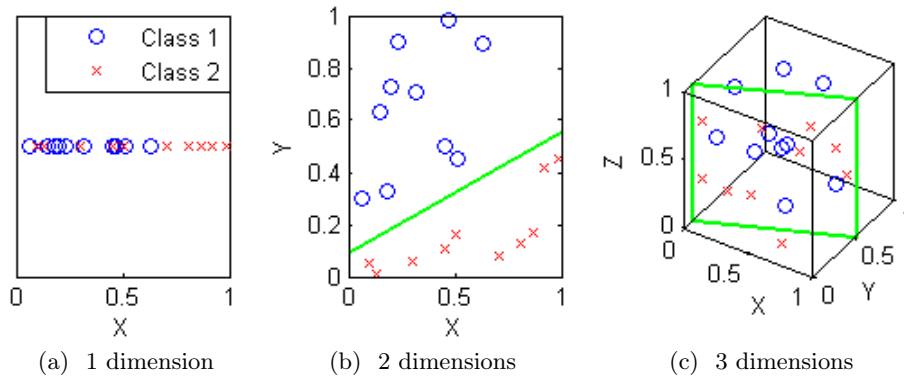


Figure 5.2: Example of a linearly separable data set in a two dimensional space

the *SVM Feature Extractor System* (SVM-FES) is to perform an automated identification of these features in large data sets.

Figure 5.2 contains an example of a three dimensional data set ( $\{X, Y, Z\}$ ) that is linearly separable in a two dimensional space ( $\{X, Y\}$ ). Figure 5.2a shows the data set in the space  $\{X\}$ . It cannot be linearly divided in any one dimensional space— $\{X\}$ ,  $\{Y\}$  or  $\{Z\}$ . It is possible to observe that there is not any value of  $X$  that divides the space without making errors in the classification of classes 1 and 2. Figure 5.2b depicts the space  $\{X, Y\}$ . In this case, it is possible to divide the space into two different regions, one per each class, without classification errors—it is impossible in the spaces  $\{X, Z\}$  or  $\{Y, Z\}$ . Figure 5.2c shows the three dimensional space. The  $Z$  dimension is irrelevant (it does not provide any information) and thus, it can be discarded.

The SVM-FES is based on the computation of a *separating hyperplane* that divides the feature space into two different regions (one per each class). The equation of the separating hyperplane is used to discard the less relevant dimension of the feature space. Given the general equation of a linear hyperplane in a  $n$  dimensional space:

$$C_1 \cdot X_1 + C_2 \cdot X_2 + \dots + C_n \cdot X_n + C_0 = 0 \quad (5.1)$$

where:

- $C_i$  : coefficient or weight of the  $i^{th}$  dimension ( $1 \leq i \leq n$ )
- $X_i$  :  $i^{th}$  dimension
- $C_0$  : bias

the most relevant features are those whose absolute  $C_i$  values are the largest ones.

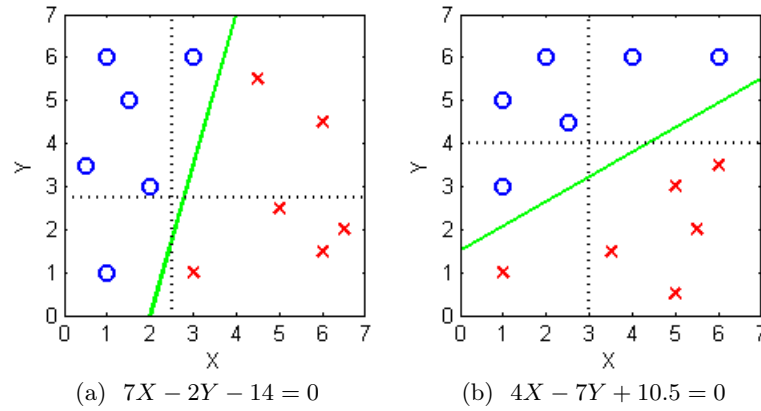


Figure 5.3: Dimension reduction in two dimensional data sets. In (a) the main feature is X while in (b) the main feature is Y

Figure 5.3 shows two examples of data sets in two dimensional spaces. A separating hyperplane has been computed for each one of the data sets (green solid lines). The equation of the hyperplane in Figure 5.3a is  $7X - 2Y - 14 = 0$ . The largest absolute coefficient is 7 and therefore, X is the most relevant dimension to classify this data set. The hyperplane  $X - 2.5 = 0$  (vertical dotted line) divides the feature space into two regions making only one classification error. In contrast, the best hyperplane using the Y dimension ( $Y - 2.75 = 0$ , horizontal dotted line) makes three classification errors. The equation of the hyperplane in Figure 5.3b is  $4X - 7Y + 10.5 = 0$ . In this case, the largest absolute coefficient belongs to the Y dimension and thus, this is the most suitable one to divide the feature space. The hyperplane  $Y - 4 = 0$  makes only one error while the hyperplane  $X - 3 = 0$  makes three errors.

Given a SVM model that uses a linear kernel (Eq. 3.25) the equation of the optimal separating hyperplane is given by Eq. 3.24:

$$\begin{aligned}
 D(x) &= \sum^{SV} \alpha_i y_i [X \cdot x_i] + b_0 \\
 D(x) &= \sum^{SV} \alpha_i y_i [(X_1, \dots, X_n) \cdot (x_{i,1}, \dots, x_{i,n})] + b_0 \\
 D(x) &= \sum^{SV} \alpha_i y_i [x_{i,1} X_1 + \dots + x_{i,n} X_n] + b_0 \\
 D(x) &= \sum^{SV} [\alpha_i y_i x_{i,1} X_1 + \dots + \alpha_i y_i x_{i,n} X_n] + b_0 \\
 D(x) &= \left( \sum^{SV} \alpha_i y_i x_{i,1} \right) X_1 + \dots + \left( \sum^{SV} \alpha_i y_i x_{i,n} \right) X_n + b_0 \quad (5.2)
 \end{aligned}$$

where:

$n$ :	number of dimensions of the input space
$y_i$ :	label of $SV_i$
$\alpha_i$ :	Lagrange multiplier of $SV_i$
$b_0$ :	bias

Therefore, given a SVM model that uses a linear kernel, it is possible to obtain the equation of its optimal separating hyperplane in the form of Eq. 5.1 where:

$$C_j = \sum_{i=1}^{SV} \alpha_i y_i x_{i,j}, \quad 1 \leq j \leq n, \quad C_0 = b_0 \quad (5.3)$$

In a  $n$  dimensional space, SVM-FES discards the dimension with the lowest absolute coefficient. Then, a new separating hyperplane is computed in a  $n - 1$  dimensional space and SVM-FES discards again the dimension with the lowest absolute coefficient. The process continues until there are no more dimensions to be discarded. The dimension of the resulting feature space can be determined using the success rate (the process is stopped when the success rate drastically drops) or, in the case of SVM, using the number of SVs. The number of SVs of a model is given by the complexity of the model and the number of misclassified samples. Therefore, using the number of SVs, the process is stopped when their number suddenly soars.

Next section includes the application of the SVM-FES to the extraction of the most important features of the L/H transition in JET.

### 5.1.1 L/H transition feature extraction

A L/H transition (see Section 2.2.1) is a change of the plasma confinement mode (from Low confinement mode to High confinement mode). The goal of this experiment was to find the set of signals (features) that better characterise this phenomenon. 28 signals were chosen as candidates to define the transition. A complete list of these signals can be found in Appendix F.

Previous work was done in analysing the relative importance of the different signals during the L/H transition in JET. Classification and Regression Trees (CART) method (Breiman et al., 1984) was applied to compute the weight of each feature in the L/H transition phenomenon (Vagliasindi et al., 2008). A set of 22 JET signals were classified and ranked based on their relative relevance given by CART.

Here, two different models were considered:

- **$\pm 100$  model:** a model trained in the interval  $\pm 100$  ms around the transitions.

- **$\pm 500$  model:** a model trained in the interval  $\pm 500$  ms around the transitions.

It had a two-fold purpose:

- Build a successful L/H classifier at different distances from the L/H transition.
- Study the influence of the distant from the L/H transition in the most relevant features to identify the confinement regime.

The original signals were resampled at 1 kHz (1000 samples per second). Thus, the  $\pm 100$  ms model uses 201 samples per discharge ( $0.1 \cdot 2 \cdot 1000 = 200$  samples + transition instant) and the  $\pm 500$  ms model uses 1001 samples per discharge ( $0.5 \cdot 2 \cdot 1000 = 1000$  samples + transition instant). The training set includes 551 JET pulses from campaigns C21 to C26. The samples where one or more signals were not sampled were discarded. As a consequence, the  $\pm 100$  ms model was trained using 110,174 samples and the  $\pm 500$  ms model was trained using 534,136 samples.

Since the amplitudes of the signals may differ, they must be normalised to avoid scaling problems in the selection of the main ones. Three different normalisations have been tested: in the first one, the signals were normalised between 0 and 1 using the equation:

$$S_{normalised} = \frac{S - \min(S)}{\max(S) - \min(S)}, \quad (5.4)$$

in the second one, the signals were transformed to have mean 0 and variance 1 using the equation:

$$S_{normalised} = \frac{S - \bar{S}}{\sigma_S^2}, \quad (5.5)$$

and in the third one, the signals were normalized in the interval  $[-1, 1]$  using the equation:

$$S_{normalised} = \frac{2S - \min(S) - \max(S)}{\max(S) - \min(S)}, \quad (5.6)$$

The best results were obtained using the first option (Eq. 5.4).

The complete SVM-FES process is shown in Tables F.1, F.2, F.3 ( $\pm 100$  ms model), F.4, F.5 and F.6 ( $\pm 500$  ms model). Each column of the tables represents an iteration of the SVM-FES. On each step, the signal with the lowest absolute coefficient was discarded and a new SVM model was trained without this signal. The process continued until all the signals were discarded.

Figure 5.4a shows the success rate and the number of SVs of the  $\pm 100$  ms model. Using this figure, the number of dimensions of the resulting feature

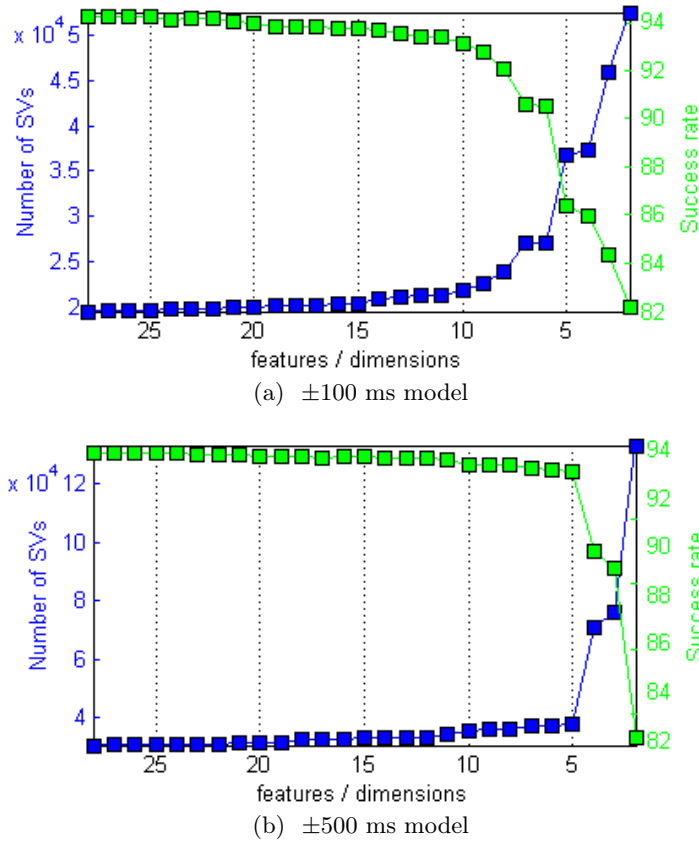


Figure 5.4: Success rates and numbers of SVs of the L/H models trained in the SVM-FES

space was set to 11. Therefore, the resulting space is made up of the last 11 signals discarded by the SVM-FES. These signals and their coefficients can be found in Table 5.1.

The results obtained by the  $\pm 500$  ms model are shown in Figure 5.4b. In this case, the number of SVs suddenly rockets at 5 dimensions and the success rate abruptly falls at the same point. Therefore, the resulting space is defined by the last 5 features discarded by the SVM-FES. Table 5.1 contains these signals and their coefficients.

It is important to note that the  $\pm 500$  ms features selected by the SVM-FES are a subset of the features chosen for the  $\pm 100$  ms model. It means that these signals are good enough for the phenomenological description of the decision function. However, since the classifier closer to the transition is more complex, it needs more information to obtain a high success rate.

The models success rates are 93.404% in the case of the  $\pm 100$  ms model and 97.436% in the case of the  $\pm 500$  ms model. It is worth noting that a higher success rate of the  $\pm 500$  ms model does not mean a more accurate

<b>Signal</b>	<b>Description</b>	<b>Coef.</b>
<b><math>\pm 100</math> ms model</b>		
<b>BT</b>	Toroidal magnetic field	8.129
<b>LI</b>	Plasma inductance	-5.022
<b>Q95</b>	Safety factor at $\text{PSI} = 0.95$	6.333
<b>RIG</b>	Radial inner gap	-2.507
<b>AD36</b>	$D_\alpha$ inner view	-9.636
<b>TOG</b>	Top outer gap	4.283
<b>RAD</b>	Radiated power	-83.827
<b>TE02</b>	Electron temperature at $\text{PSI} = 0.2$	8.851
<b>LAD3</b>	Line average electron density at the plasma core	-7.452
<b>LAD4</b>	Line average electron density at the plasma edge	32.191
<b>TE08</b>	Electron temperature at $\text{PSI} = 0.8$	91.244
<b><math>\pm 500</math> ms model</b>		
<b>BT</b>	Toroidal magnetic field	6.719
<b>AD36</b>	$D_\alpha$ inner view	-17.809
<b>LAD3</b>	Line average electron density at the plasma core	-27.102
<b>LAD4</b>	Line average electron density at the plasma edge	43.207
<b>TE08</b>	Electron temperature at $\text{PSI} = 0.8$	374.425

Table 5.1: Signals selected by the SVM-FES and their coefficients for the  $\pm 100$  ms and the  $\pm 500$  ms models

Signal	ROC area	Signal	ROC area	Signal	ROC area
<b>±100 ms model</b>					
BNDIAM	0.7631	XPRL	0.4424	TOG	0.4850
BT	0.5020	XPZL	0.4854	RAD	0.5304
ELO	0.5323	LSPRI	0.5310	TE02	0.7184
FDWDT	0.7357	LSPRI	0.4998	CR0	0.4810
IPLA	0.4843	LSPRO	0.4439	RGEO	0.6116
LI	0.4508	LSPZO	0.5560	LAD3	0.6470
PTOT	0.5955	RIG	0.5611	LAD4	0.7163
Q95	0.4932	ROG	0.3996	WDIA	0.6570
TRIL	0.5950	AD36	0.4631	TE08	0.8346
TRIU	0.5416				
<b>±500 ms model</b>					
BNDIAM	0.9916	XPRL	0.3205	TOG	0.4849
BT	0.5456	XPZL	0.5211	RAD	0.8477
ELO	0.6781	LSPRI	0.4639	TE02	0.9315
FDWDT	0.9640	LSPRI	0.6298	CR0	0.4869
IPLA	0.5221	LSPRO	0.4292	RGEO	0.7526
LI	0.4611	LSPZO	0.6655	LAD3	0.9046
PTOT	0.9062	RIG	0.6765	LAD4	0.9534
Q95	0.5629	ROG	0.4067	WDIA	0.9285
TRIL	0.7979	AD36	0.7496	TE08	0.9874
TRIU	0.6941				

Table 5.2: ROC results of the L/H transition

determination of the L/H transition times. In fact, the accuracy of the  $\pm 500$  ms model is lower than the  $\pm 100$  ms model. Their mean errors in the determination of the L/H transition times are<sup>1</sup>:

$$\pm 100 \text{ ms model: } (2 \cdot 100 + 1) \cdot (1 - 0.934041) = 13.258 \text{ ms}$$

$$\pm 500 \text{ ms model: } (2 \cdot 500 + 1) \cdot (1 - 0.974359) = 25.667 \text{ ms}$$

Due to the feature spaces high dimensionality and the large number of samples, the models have been trained using the CIEMAT computer cluster EULER (Acero et al., 2009). It uses a parallel version of SVM (Ramírez et al., 2010) that allows the training of models using several samples and dimensions in short times.

#### 5.1.1.1 L/H feature extractor using ROC

The results obtained by the SVM-FES were compared with the ones obtained using the ROC curve (see Section 3.2.1). The same process that the one applied to the analysis of the Fisher's Iris Data (Section 3.2.1.4) was applied

<sup>1</sup>since the signals have been interpolated at 1 kHz, each sample corresponds to 1 ms

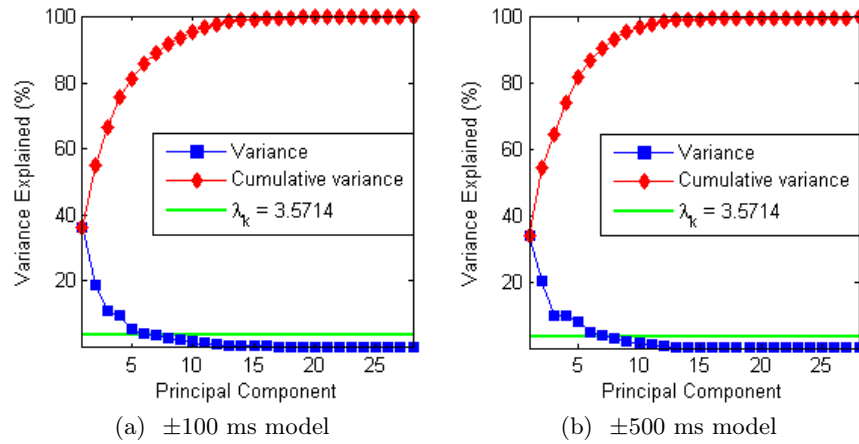


Figure 5.5: PCA results of the L/H transition

to the analysis of the L/H transition: each feature of the data was considered as a single continuous classifier and its performance was measured using the ROC curve. Then, the features with the largest ROC area were chosen to define the resulting feature space.

Table 5.2 contains the areas of the ROC classifiers of each signal for both models. In order to compare the results obtained using ROC and SVM-FES, a 11-dimensional space was built using the signals with the largest area in the case of the  $\pm 100$  ms model and a 5-dimensional space in the case of the  $\pm 500$  ms model (the same number of dimensions that have been obtained previously). The signals selected for each model have been marked in grey.

The ROC  $\pm 100$  ms model obtained a success rate of 87.852% versus 93.404% obtained by the  $\pm 100$  SVM-FES model. For its part, the  $\pm 500$  ms model obtained a success rate of 91.982% versus 97.436% obtained by the  $\pm 500$  SVM-FES model. The most important downside of the ROC feature extractor is probably that the signals are analysed independently and due to the complexity of the L/H transition, none of them is good enough to define the plasma confinement mode.

### 5.1.1.2 L/H feature extractor using PCA

This section contains the results of the analysis of the L/H transition using PCA (see Section 3.2.2). One analysis was performed per each one of the L/H models ( $\pm 100$  ms and  $\pm 500$  ms).

Figure 5.5a shows the percentage of the variance explained and the cumulative variance of each one of the PCs of the  $\pm 100$  ms model. Unfortunately, it is not possible to use the scree plot to choose the optimum number of PCs in the resulting space. Therefore, a different stopping criterion was used: the Kaiser-Guttman rule (see Section 3.2.2.2). In this case, the threshold

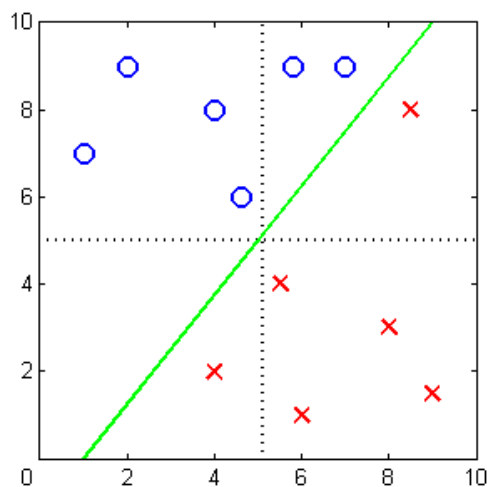


Figure 5.6: Example of an ill-conditioned data set

given by this rule (Eq. 3.68) was 3.5714 (horizontal green line). All the PCs with a percentage of the variance above this threshold were retained in the resulting feature space and hence, the remaining PCs were discarded. In the case of the  $\pm 100$  ms model, the resulting feature space was made up of 6 PCs. Their loadings can be found in Appendix G.

A L/H model was trained using the six first PCs of the  $\pm 100$  model, obtaining a success rate of 57.035% versus 93.404% obtained by the SVM-FES model. The total variance covered by these PCs was 85.567%.

The scree plot of the  $\pm 500$  ms model was not either useful to define the optimum number of PCs (Figure 5.5b). Using the Kaiser-Guttman rule, the number of PCs in the resulting feature space was set to 7. Appendix G contains their loadings. The success rate obtained by these PCs is 87.635% versus 97.436% obtained by the SVM-FES model. The total variance covered by the seven first PCs was 90.578%.

One of the disadvantages of PCA is that, although it is possible to define a reduce feature space using the PCs, all the signals of the original feature space are required to compute the PCs and thus, all of them must be stored.

### 5.1.2 Discussion

The SVM-FES assumes that the samples are randomly distributed in the feature space. If this assumption is not true, the features selected by the SVM-FES may not be the ones that allows the division of the feature space minimising the number of errors. Figure 5.6 contains an example of an ill-conditioned data set. The equation of the separating hyperplane is  $10X - 8Y - 10 = 0$ . Using the SVM-FES criterion, the most relevant feature is X.

The hyperplane  $X - 5.1 = 0$  (vertical dotted line) divides the space making three errors. In contrast, the hyperplane  $Y - 5 = 0$  (horizontal dotted line) makes only one error. This is a consequence of the distribution of the samples in the feature space. Specifically, it is a consequence of the sample located in  $[8.5, 8]$ , far from the samples of its same class.

The SVs considered in Figure 5.4 consist of the errors of the model and the samples that properly define the separating hyperplane. In order to allow a more accurate estimation of the complexity of the model generated by SVM, the number of errors should be subtracted from the total number of SVs.

On each step, the SVM-FES methodology discards the dimension with the lowest coefficient. It implies that in a  $n$ -dimensional space, the SVM-FES methodology makes  $n$  steps. Each step requires the computation of a SVM model and, if the data set is large, it can be very time consuming. The process can be sped up if more than one dimension is discarded on each step. For example, the dimensions with the lowest  $n/t$  coefficients can be discarded on each step so the SVM-FES would make only  $t$  steps. Tables F.7 ( $\pm 100$  ms model) and F.8 ( $\pm 500$  ms model) in Appendix F contain the results of the SVM-FES of the L/H transition where 3 features are discarded on each step. The resulting feature space of the  $\pm 100$  ms model contains 13 features ( $\{BT, LI, Q95, ROG, AD36, TOG, RAD, TE02, CR0, RGEO, LAD3, LAD4, TE08\}$ ) and it achieves a success rate of 93.403%. The resulting feature space of the  $\pm 500$  ms model is made up of 13 features ( $\{BT, ELO, TRIL, XPRL, RIG, ROG, AD36, ROG, CR0, RGEO, LAD3, LAD4, TE08\}$ ) and it has obtained a success rate of 97.750%. Since the signals are discarded in groups of 3, the results are not as accurate as the ones obtained in Section 5.1.1 where the features have been discarded one by one. It is also possible to fix a threshold value for the coefficients of the separating hyperplane,  $C_\tau$  and then, all the dimensions with a coefficient  $C_j < C_\tau$  are discarded on each step. The feature extraction process finishes when there are no more dimensions with coefficients shorter than  $C_\tau$ . This alternative has the disadvantage that the optimum value of  $C_\tau$  is unknown a priori.

The SVM-FES uses a linear equation to select the most relevant characteristics of the feature space. If the samples show a non-linear dependency in the feature space, the resulting space given by the SVM-FES cannot be the most appropriate one to classify the samples. Unfortunately, using for example a RBF kernel (Eq. 3.27) in Eq. 3.24 it is not possible to decide which ones are the most important features of the space.

Although the features have been selected for a linear model, a RBF kernel can also be applied to generate a model in the SVM-FES feature space. In the case of the  $\pm 100$  ms model, the RBF kernel obtained a success rate of 98.861% using  $C = 200$  and  $\sigma = 0.316$  and in the case of the  $\pm 500$  ms model, it obtained a success rate of 98.261% using the same parameters.

## 5.2 Image dimensionality reduction

In an image, all the pixels do not contain the same amount of information. Typically, the borders of an image contain less information than the centre. In the same way, the pixels from the background of an image are not as relevant as the ones in the focus.

The existing techniques to analyse images, such as the optical flow (Horn and Schunck, 1981), are heavy in terms of computational times. Focusing the attention in a SVM classification problem, it requires to solve a quadratic optimization problem to compute the optimal separating hyperplane (Eq. 3.6). Therefore, the complexity of the solution grows quadratically with the size of the data. Then, it is necessary to discard the useless regions of the images in order to speed up the computation of the different methods.

This section describes RSIC: a *Region Selection and Image Classification methodology* (González et al., 2012d). RSIC locates the most relevant image regions in a classification problem. A relevant region, or a Region Of Interest (ROI), is a set of connected (adjacent) pixels that allow the identification of an image class. The methodology is based on a novel interpretation of the *non-conformity measures*: they are used to identify the best ROI to classify an image class. The combination of the best ROIs (one per each class) is used to classify new images.

The goals of RSIC are:

1. **Image ROIs identification:** a ROI contains suitable information to recognise an image class versus the rest.
2. **Image dimensionality reduction:** the dimension of the original images is reduced to the dimension of the resulting ROIs. It has a two-fold objective:
  - (a) **Reduction of the training and classification times:** the systems are trained and the new images are classified using only a small subset of the images' pixels. It results in a CPU time reduction.
  - (b) **Reduction of the storage space of the images:** if the purpose of the images is its classification, only the pixels of the ROIs must be stored.
3. **Creation of a successful classifier:** although the CPU time and the storage space would be significantly reduced, the RSIC methodology is meaningless if the classifier built using the ROIs does not obtain high success rates. ICP (see Section 3.1.2.1) is used to build the resulting classifier. In addition to the prediction, ICP gives conformal measures (credibility and confidence).

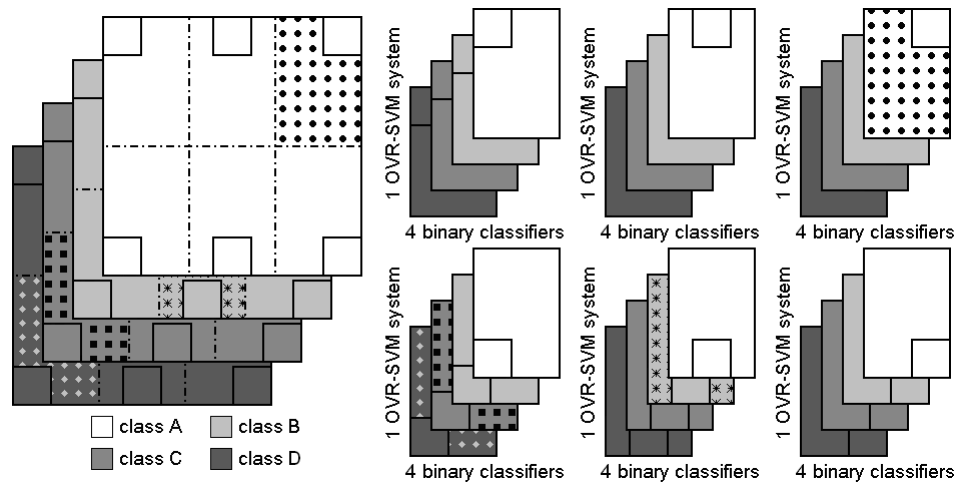


Figure 5.7: Example of the division of images into six regions in a 4-class classification problem

This section is structured as follows: section 5.2.1 describes the RSIC methodology. Section 5.2.2 contains the experiment carried out using the RSIC methodology: the analysis of the TJ-II Thomson scattering images. Finally, Section 5.2.3 raises some interesting points of the RSIC methodology that are worthy of discussion.

## 5.2.1 Region Selection and Image Classification methodology

The RSIC methodology consists of five steps: image division (Section 5.2.1.1), models building (Section 5.2.1.2), region evaluation (Section 5.2.1.3), region selection (Section 5.2.1.4) and image classification (Section 5.2.1.5).

### 5.2.1.1 Step 1: image division

The first step of the RSIC methodology implies the division of the images into regions. This step plays a key role in the RSIC methodology since the regions created here are the ones that will be evaluated in the next steps (some of them will contain suitable information to identify an image class and hence, they will become ROIs). A proper or an extensive—several different regions, hoping that some of them will contain relevant information— division of the images is required in order to obtain a good classification system.

Figure 5.7 depicts an example of the division of images into six regions. Each colour represents one image class. In this example, there are 4 different classes (A, B, C and D). The purpose of the small square on each region is the identification of the position of the region in the original image (e.g.

the region with a small square on its upper-left corner is located in the upper-left side of the original image). Each class has an unique feature that distinguishes it from the rest of the classes: dots in the upper-right region of class A, crosses in the lower-mid region of class B, squares in the lower-left region of class C and diamonds in the lower-left region of class D.

The image division can be carried out using expert knowledge. In this case, the ROIs are identified by an expert. These ROIs contain the a priori most relevant information. It helps the system to select the most suitable ones to identify each class. In contrast, if no expert knowledge is available, the images must be cut up in an extensive way. In this case, several regions must be generated, many of them probably overlap.

### 5.2.1.2 Step 2: models building

One versus rest SVM (OVR-SVM) has been chosen to solve this multi-class classification problem. In a  $k$ -class problem,  $k$  binary SVM classifiers are built. Each binary classifier generates a separation hyperplane between a class and the rest ( $k - 1$  classes). A new sample is assigned to the class for which the positive<sup>2</sup> distance from the hyperplane is maximal (Weston and Watkins, 1999).

The image pieces generated in the previous step are grouped together into regions (the pieces of all the images from a single region are grouped together). The number of groups is the same as the number of regions. An OVR-SVM system is trained using each one of these groups. The OVR-SVM systems are completely independent (they are trained using only the information of their regions and they must be able to classify images using only the information of the pixels contained in these regions). In a  $k$ -class classification problem, each OVR-SVM system is made up of  $k$  binary classifiers. The total number of binary classifiers is given by  $k \cdot r$  where  $r$  is the number of regions.

In order to compare the results generated by each OVR-SVM system, they are trained and calibrated using the same proper training set and calibration set. It is important to note that the non-conformity measures obtained by each OVR-SVM cannot be compared if they are trained using different sets.

The right-hand side of Figure 5.7 shows the OVR-SVM systems created to solve a 4-class classification problem where the images have been cut up into 6 regions. One OVR-SVM is created per each one of these 6 regions (6 OVR-SVM). Each OVR-SVM contains 4 binary classifiers (one per each class). The total number of binary classifier in the system is 24.

---

<sup>2</sup>in this case, the distance is positive if the sample belongs to this class and negative otherwise

### 5.2.1.3 Step 3: region evaluation

The goal of the third step of the RSIC methodology is to measure the performance of each OVR-SVM on classifying an image class. In multi-class classification problems, it is possible that a region that properly identifies a class would not be able to distinguish other classes. For example, in Figure 5.7, the upper-right region is able to recognise class A (the region is dotted for this class) but it cannot distinguish class B from C or D (the region is not filled with anything in these classes). Therefore, the performance of a region is computed separately for each class. It allows the RSIC methodology to select as many different regions as classes. In the example of Figure 5.7, four quality measures are obtained for each OVR-SVM system (one per each class).

The performance of an OVR-SVM system  $r$  (or what is the same, a region<sup>3</sup>) on the classification of a given class  $t$  is computed using the non-conformity values of the calibration set corresponding to the binary classifier that distinguishes the class  $t$  from the rest of the classes ( $\alpha^{rt}$ ). For example, if we want to measure the performance of the upper-right region in Figure 5.7 to classify class A, we will use the non-conformity values of the binary classifier that distinguishes class A from classes B, C and D ( $\alpha^{upper-right,A}$ ). Please remember that every OVR-SVM system contains  $k$  binary classifiers, where  $k$  is the number of classes.

The non-conformity measure proposed for the RSIC methodology is the one given by Eq. 3.42. Using this non-conformity measure, the  $\alpha$  values of the properly classified samples (True Positives —TP— and True Negatives —TN—) are equal or lower than zero ( $\alpha \leq 0$ ) and the  $\alpha$  values of the misclassified samples (False Positives —FP— and False Negatives —FN—) are positive ( $\alpha > 0$ ). On the one hand, in the region where the  $\alpha^{rt}$  values are positive, it has not been possible to build a good separating hyperplane between the class  $t$  and the other classes (there are classification errors). On the other hand, if the  $\alpha^{rt}$  values are negative, it means that the hyperplane built by the SVM classifier accurately defines the separation between classes (there are not classification errors).

The quality of a region  $r$  on classifying a class  $t$  is given by:

$$q(r, t) = \frac{\left( \sum_{i=1}^{\#FN} \alpha_{FN,i}^{rt} + \sum_{j=1}^{\#FP} \alpha_{FP,j}^{rt} \right) \cdot PF + \sum_{k=1}^{\#TP} \alpha_{TP,k}^{rt}}{\#FN + \#FP + \#TP} \quad (5.7)$$

where  $\#FN$ ,  $\#FP$  and  $\#TP$  are, respectively, the number of false negatives, false positives and true positives and  $PF$  is a *penalty factor*.

Equation 5.7 is composed of two different terms:

- **Positive term:**  $\alpha$  values of FP and FN samples in the calibration set.

<sup>3</sup>every OVR-SVM system corresponds to one, and only one region

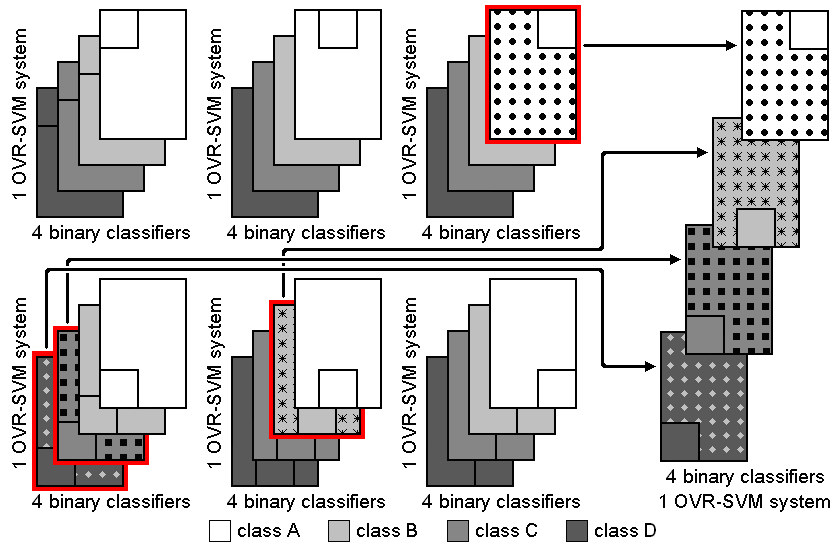


Figure 5.8: Example of the region selection in a 4-class classification problem

They are multiplied by the PF. The aim of the PF ( $PF \in [1, \infty]$ ) is to penalize the classifiers that make classification errors.

- **Negative term:** values of the TP samples.

Using Eq. 5.7, the smaller (a large negative value)  $q$  value, the better is the region  $r$  to classify the class  $t$ . A small value of  $q$  means that the binary classifier of the region  $r$  has computed a hyperplane that maximises the distance from the samples to the separating hyperplane, and thus, it is unlikely to make classification errors. In contrast, a large value of  $q$  (a positive value) means that the samples of the classes are very close one to the others in the transformed feature space, and thus, it is more likely to make a mistake in the classification of a new sample.

#### 5.2.1.4 Step 4: region selection

The output of the RSIC methodology is an OVR-SVM classifier made up of the best binary classifiers. For each class, all the binary classifiers of the different regions are compared and the best one is chosen (based on the quality measure computed in the previous step). The chosen binary classifiers are grouped together in a single OVR-SVM system. The resulting OVR-SVM system contains as many binary classifiers as image classes (in a  $k$ -class classification problem, it contains  $k$  binary classifiers, one per each class).

It is possible that the same region would be the best one to classify all the different classes of images. In this case, although the region used by

the binary classifiers is the same, the binary classifiers are different. It is important to take into account that they are *binary* classifiers (one versus the rest). Therefore, each one of the classifiers must identify a class from the rest. On the other hand, it is also possible that  $k$  different regions of the image would be required to build the OVR-SVM system. These regions can overlap or they can use different image pixels.

Figure 5.8 shows an example of the region selection step. The regions that allow the identification of each class have been selected. For example, the upper-right region has been chosen to identify class A. Thus, the binary classifier that identifies class A using the upper-right region of the images is part of the resulting OVR-SVM system. In the case of classes C and D, the same region has been chosen to identify them. Thus, the binary classifiers that identify these classes are included in the resulting OVR-SVM system (since the classifiers are different, both of them must be included).

### 5.2.1.5 Step 5: image classification

The result of the RSIC methodology is an OVR-SVM system made up of the best binary classifiers. Each binary classifier is responsible for identifying a single class from the rest of the classes of the problem.

When a new image is classified, the regions required by each binary classifier are extracted. As it was mentioned previously, since two or more regions can overlap, a single pixel of the image can belong to more than one region and therefore, it can be analysed by more than one classifier. On the other hand, there can be pixels that do not belong to any classifier and therefore, they are irrelevant. In the example shown in Figure 5.8, the upper-left, upper-mid and lower-right regions are not used by any of the binary classifiers in the resulting OVR-SVM system and therefore, they are irrelevant and they can be discarded. In this case, the size of the image can be reduced to the 50% of its original size (3 out of 6 regions).

Once the required regions have been extracted from the image, each one is classified by its corresponding binary classifier. In the example shown in Figure 5.8, the upper-right region is classified by the binary classifier that recognises class A, the lower-mid region is classified by the binary classifier of class B and the lower-left region is classified by the classifiers of classes C and D. Each classifier generates a predicted label and a  $p_{value}$  for the new image. There are three different alternatives:

- **Only one binary classifier identifies the image:** the predicted label is the class of the classifier that has recognised the image. The confidence and the credibility of the predicted label are computed using the  $p_{value}$  of this classifier (and the second largest  $p_{value}$ ).
- **Two or more binary classifiers identify the image:** the predicted label is the class of the classifier that has obtained the largest  $p_{value}$ .

The conformal measures are computed using this  $p_{value}$  and the second largest one.

- **The image is not recognised by any of the classifiers:** the image is labelled as *unknown*. It is not possible to recognise the image's class.

Next section contains the application of the RSIC methodology to the analysis of the TJ-II Thomson scattering images.

### 5.2.2 Analysis of the TJ-II Thomson Scattering Images

The CCD camera of the TJ-II (see Section 2.3.2) Thomson scattering diagnostic (Herranz et al., 2003) generates 2-D images of the plasma spectra, with the horizontal and vertical axes displaying, respectively, scattered wavelength and position along a plasma chord. Using the Thomson scattering diagnostic, it is possible to measure radial profiles of both plasma density and temperature. Each Thomson scattering image belongs to only one of five different classes: cut-off (CFF), electron cyclotron heating phase (ECH), background (BCK), neutron beam injection phase (NBI) and stray light without plasma or collapsed discharge (STR).

So far, different methods to classify the TJ-II Thomson scattering images have been tested: SVM (Vega et al., 2005), (Makili et al., 2010), neural networks (Farias et al., 2005) and conformal predictors (Vega et al., 2010b), (Makili et al., 2011) and (Vega et al., 2012). Although these works differ in the methods that they used to classify the TJ-II Thomson scattering images, they have in common that the complete images were used to train the systems and to classify new samples regardless of the different amount of information provided by different image regions. They also have in common that they used a wavelet transform of level 4 to reduce the dimensionality of the original images. Their best results oscillate between 90% (Farias et al., 2005) and 98.68% (Makili et al., 2010).

The maximum number of images analysed in the previous works was 599 (Makili et al., 2011). In the present case, 1,272 images were used to test the RSIC methodology. The type of image generated by the Thomson scattering depends on the experiment carried out in the TJ-II. As a consequence, the number of images available in each class is different: 42 CFF, 517 ECH, 124 BCK, 366 NBI and 223 STR. The resolution of the Thomson scattering images is  $576 \times 385$  pixels. In order to speed up the RSIC process, the images' dimensionality was reduced to  $144 \times 97$  pixels using the approximation wavelet coefficients of level 2 (see Section 3.2.3.1). The set of 1,272 images was randomly split into a proper training set (25% of each class), a calibration set (25% of each class) and a test set (50% of each class). As a result, the proper training set and the calibration set contained 319 images each: 11 CFF, 129 ECH, 31 BCK, 92 NBI and 56 STR. The test set held 634 images: 20 CFF, 259 ECH, 62 BCK, 182 NBI and 111 STR.

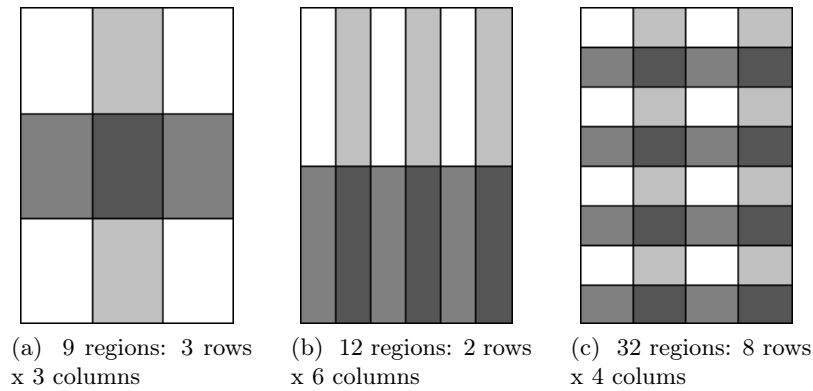
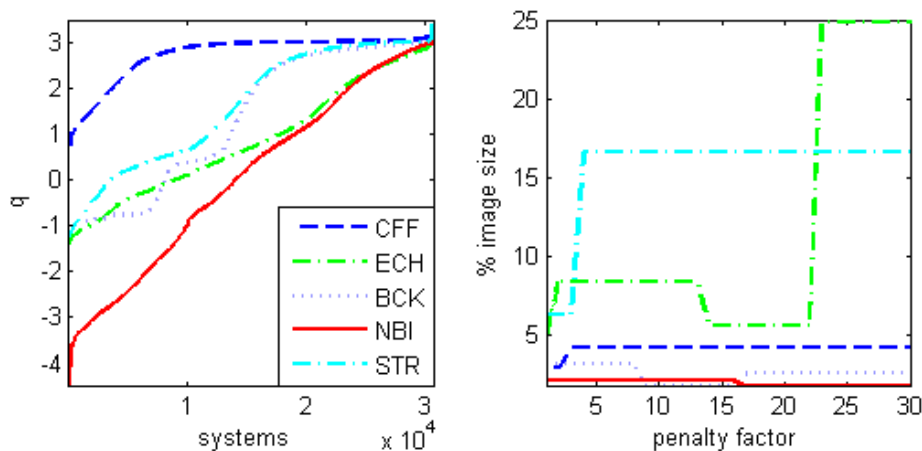


Figure 5.9: Example of the division of the TJ-II Thomson scattering images into regions

No expert knowledge was applied to cut up the images into regions in the *first step* of the RSIC methodology (Section 5.2.1.1). It is known that the centre of the Thomson scattering images contain the most of the information but some irrelevant regions had to be included to test the performance of the RSIC methodology. As an alternative, the images were divided into rectangular regions. The height and the width of the images were cut up from 2 to 8 pieces, testing all combinations (e.g. 2 rows and 2 columns —4 regions—, 2 rows and 3 columns —6 regions—, . . . , 2 rows and 8 columns —16 regions—, 3 rows and 2 columns —6 regions—, . . . , 8 rows and 8 columns —64 regions—). Therefore, 1,225 different regions were created. Figure 5.9 contains three different examples of image division. In Figure 5.9a, the image was divided into 3 rows and 3 columns (9 regions). Figure 5.9b depicts an image divided into 2 rows and 6 columns (12 regions). Finally, Figure 5.9c shows an image that was divided into 8 rows and 4 columns (32 regions).

The binary SVM classifiers of the OVR-SVM systems of the *second step* of the RSIC methodology (Section 5.2.1.2) were trained using RBF kernels (Eq. 3.27). The epsilon SVM parameter was set to  $1 \cdot 10^{-7}$ . The SVM parameter  $C$  and the kernel parameter  $\sigma$  must be fixed according to the complexity of the problem being solved and the size of the feature space. Since the regions size and the information contained in each region were different, it was not possible to fix the  $C$  and  $\sigma$  parameters to a unique value. Thus, 5 values of  $C$  ( $\{800, 900, 1,000, 1,100, 1,200\}$ ) and 5 values of  $\sigma$  ( $\{8, 9, 10, 11, 12\}$ ) were tested. As a result, the regions were trained using 25 different combinations of these parameters (5 values of  $C$  and 5 values of  $\sigma$ ).

According to the above figures, 1,225 regions were trained using 25 combinations of SVM parameters, making a total of 30,625 different systems. In the *third step* of the RSIC methodology (Section 5.2.1.3), the performance of



(a)  $q$  value of the 30,625 systems trained in the experiment (b) Size of the selected regions for different values of the PF

Figure 5.10: Results of the classification of the Thomson scattering images

the 30,625 systems to classify each Thomson scattering class was evaluated using Eq. 5.7 and  $PF = 3^4$ . Figure 5.10a shows the  $q$  values of the 30,625 systems trained for each one of the classes. It is important to note that the quality measure  $q$  was independently sorted in ascending order for each class.

In the *fourth step* of the RSIC methodology (Section 5.2.1.4), the best system to classify an image class is identified. Using  $PF = 3$ , the  $q$  value of the best systems were: CFF = 0.5899, ECH = -1.3824, BCK = -0.9296, NBI = -4.4750 and STR = -1.2400 (the best system on classifying a class is the one with the lowest  $q$  value, see Section 5.2.1.3). Figure 5.11 shows the selected regions for each class. Figure 5.11f contains the total region that was selected by the RSIC methodology. The size of this region was only 16.49% of the original size of the images (please note that some regions were overlapped and therefore, the total region's size was not the sum of the sizes of the different classes' regions).

Figure 5.10b shows the size of the selected regions as a percentage of the total image size for different PF values. Since the images were divided from 2 to 8 rows and columns, the maximum size of a region was 25% (2 rows and 2 columns, 4 regions) and its minimum size was 1.5625% (8 rows and 8 columns, 64 regions). Due to Eq. 5.7, large values of the PF force the selected regions not to make errors. It is possible to reduce the number of errors in two different ways: selecting a more informative region and, if it is not possible, increasing the size of the selected regions. As a consequence, bigger regions are selected for larger values of the PF. In this case, for large

<sup>4</sup>the PF value has been empirically set to 3 using Figure 5.10b

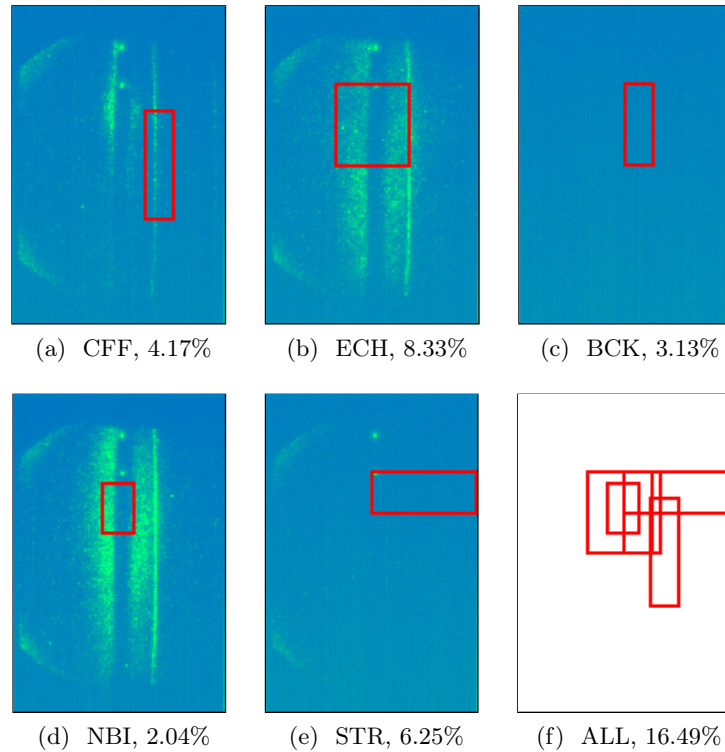


Figure 5.11: RSIC regions obtained for each Thomson scattering image class and its sizes compared to the size of the original images

values of the PF, the selected ECH region was the biggest region available.

The *fifth step* of the RSIC methodology (Section 5.2.1.5) consists in the classification of the test images. The 634 test images were classified using the selected regions. The success rates obtained were: 15.00% CFF, 96.53% ECH, 100% BCK, 98.80% STR and 98.20% STR. The total success rate taking into consideration the number of test images on each class was 95.27%. The reason of the low rate of the CFF class was the small number of training examples: only 11 images. The  $q$  values of all the regions on classifying CFF images indicated that none of the classifiers obtained good results (all the classifiers obtained  $q$  values over 0, the lowest one is the selected one:  $q = 0.5899$ ).

Table 5.3 shows a comparison of the results of the RSIC regions versus the results obtained by 5 SVM one versus rest systems trained using the entire images (instead of the ROIs). The RSIC and the entire image methods used the same proper training set, calibration set and test set. Since the entire images contained more information than the regions selected by the RSIC methodology, it was possible to build better models and therefore to obtain higher classification rates. The total success rate was 96.37% using the entire

<b>Image class</b>	<b>Rates</b>	<b>Entire image</b>	<b>RSIC</b>
CFF 20 images	Successes	11, 55.00%	3, 15.00%
	Errors	4, 20.00%	5, 25.00%
	Unknowns	5, 25.00%	12, 60.00%
	Region size	100%	4.17%
ECH 259 images	Successes	246, 94.98%	250, 96.53%
	Errors	6, 2.32%	6, 2.32%
	Unknowns	7, 2.70%	3, 1.16%
	Region size	100%	8.33%
BCK 62 images	Successes	62, 100%	62, 100%
	Errors	0, 0%	0, 0%
	Unknowns	0, 0%	0, 0%
	Region size	100%	3.13%
NBI 182 images	Successes	181, 99.45%	180, 98.80%
	Errors	1, 0.55%	0, 0%
	Unknowns	0, 0%	2, 1.1%
	Region size	100%	2.04%
STR 111 images	Successes	111, 100%	109, 98.20%
	Errors	0, 0%	2, 1.80%
	Unknowns	0, 0%	0, 0%
	Region size	100%	6.25%
Total 634 images	Successes	611, 96.37%	604, 95.27%
	Errors	11, 1.74%	13, 2.05%
	Unknowns	12, 1.89%	17, 2.68%
	Region size	100%	16.49%

Table 5.3: Comparison of the RSIC results versus the ones obtained using the entire images SVM

Image class	Data set	Entire image		RSIC	
		Time (s)	SD (s)	Time (s)	SD (s)
<b>Training</b>					
CFE 11 images	Proper training	1.206	0.026	0.075	0.001
	Calibration	6.325	0.029	1.456	0.005
ECH 129 images	Proper training	2.301	0.048	0.200	0.003
	Calibration	14.398	0.071	2.024	0.004
BCK 31 images	Proper training	1.097	0.012	0.033	0.001
	Calibration	5.228	0.037	1.318	0.006
NBI 92 images	Proper training	1.400	0.012	0.034	0.001
	Calibration	8.029	0.045	1.323	0.008
STR 56 images	Proper training	1.712	0.012	0.124	0.001
	Calibration	10.257	0.056	1.600	0.074
TOTAL 319 images	Proper training	7.715	0.062	0.465	0.004
	Calibration	44.237	0.179	7.720	0.077
<b>Test</b>					
634 images	Test	86.937	0.696	15.802	0.696

Table 5.4: Comparison of the CPU times of the RSIC method versus the entire images SVM

images versus 95.27% using the RSIC regions. It is important to note that the RSIC regions were using only the 16.49% of the size of the entire images. In spite of its reduced size, the RSIC regions success rate was slightly lower than the one obtained by the entire images. In fact, the success rate of the ECH class was higher using the RSIC regions. The highest difference in the success rate was the one obtained in the CFE class due to its small number of images (55.00% using the entire images versus 15.00% using the RSIC regions).

These classifiers were built using an Intel® Core™ 2 Quad CPU Q9300 2.50GHz, 1.95GB RAM. The CPU times consumed by the RSIC regions and the entire images were measured to quantify the effect of the complexity reduction in the CPU times. Table 5.4 shows the results obtained. The times given for both methods were the average time of 100 different runs. The standard deviation of these times is shown in the column called *SD*. The time differences between the different classes were due to, on the one hand, the different number of images in each class and, on the other hand, the different models' complexity. Using the RSIC regions, the proper training time was reduced 93.97%. The calibration time was reduced 82.55% and the test time was reduced 81.82%. The mean classification time of an image using the RSIC methodology was 0.025 s versus 0.137 s using the entire images.

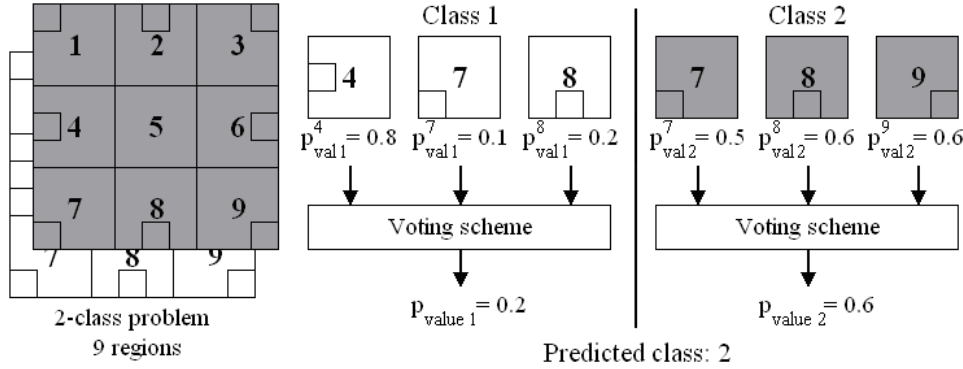


Figure 5.12: Example of a classification with multiple regions and a voting schema

### 5.2.3 Discussion

TN samples have not been included in Eq. 5.7. In multi-class problems, the number of TN is usually much larger than the number of TP (for example, in a 4 class classification problem with 10 samples per class, the number of samples in the TP can be up to 10 while the number of samples in the TN can be up to 30). Therefore, the statistical weight of TN samples is higher than the one of TP samples. As a result, if TN are included in Eq. 5.7, it may force the classifiers to obtain large distances from the TN samples to the hyperplane rather than properly classify both, the TN and the TP samples. In order to solve this issue, the TN samples were removed from Eq. 5.7 and the PF was added to penalise the systems with errors.

An alternative to Eq. 5.7 is a weighted average quality measure:

$$q(r, t) = \frac{\left( \sum_{i=1}^{\#FN} \alpha_{FN,i}^{rt} + \sum_{j=1}^{\#FP} \alpha_{FP,j}^{rt} \right) \times PF + \sum_{k=1}^{\#TP} \alpha_{TP,k}^{rt}}{(\#FN + \#FP) \times PF + \#TP} \quad (5.8)$$

With regard to the RSIC step 4 (region selection), the approach explained here uses only one region per each class. It is possible that, for very complex classification problems, several regions would be needed. There are different approaches to classify a new image using several regions per class:

- The new image is assigned to the class of the region with the largest  $p_{value}$ . In this case, all the process in step 5 is similar but instead of one  $p_{value}$  per class, it uses several  $p_{values}$ . The predicted label for the new image is the class of the largest  $p_{value}$ .
- It is possible to implement a voting scheme<sup>5</sup> for the regions of the same

<sup>5</sup>**voting scheme:** a method that given a set of predictions of different classifier generates a joint prediction

class and then, to use the output of the voting scheme as the  $p_{value}$  of each class. This alternative is shown in Figure 5.12. It contains an example of a 2-class classification problem where the images have been cut up into 9 regions. Three different regions have been chosen to classify each class. A single  $p_{value}$  is selected for each class by means of a voting scheme. Then, the resulting  $p_{values}$  are compared and the predicted label is chosen as explained in the RSIC step 5. In the example of Figure 5.12, the predicted label is 2, the credibility is 0.6 and the confidence is 0.8. It is important to note that although the largest  $p_{value}$  belongs to class 1 ( $p_{val1}^4 = 0.8$ ) since  $p_{val1}^7$  and  $p_{val1}^8$  are low, the voting scheme has rejected it. If the alternative chosen was the previous one, the predicted class would be 1.

### 5.3 Conclusions

Fusion databases are characterised by their high dimensionality and their complexity. Dozens of plasma diagnostics measure plasma magnitudes on each pulse, generating hundreds of signals (some of them correlated). The dimensionality of fusion data should be reduced in order to simplify its use for different purposes.

This chapter has introduced two techniques of dimensionality reduction: SVM-FES and RSIC

- Given a  $p$ -dimensional space, SVM-FES generates a  $q$ -dimensional space whose dimensions are a subset of the original space ( $q < p$ ). Using the reduced space, it is possible to successfully classify the samples from the original space.
- RSIC selects a region of the original images that allows the classification of the images obtaining high success rates. The classifier that uses the resulting region is faster than the one that uses the entire images. It also saves storage space.

The SVM-FES has been applied to the determination of the main features of the L/H transition. Two different models have been tested: one trained in an interval of  $\pm 100$  ms around the transition and one trained in an interval of  $\pm 500$  ms. The results obtained from these models point out that the L & H samples close to the transition are not linearly separable in the resulting feature space. Figure 5.13a shows a set of L & H samples far from the transition in the BT and TE08 space. The samples are almost linearly separable in this feature space. In contrast, Figure 5.13b depicts a set of L & H points close to the L/H transition. In this case, the L & H points are mixed in the feature space and there is not a border between the confinement modes.

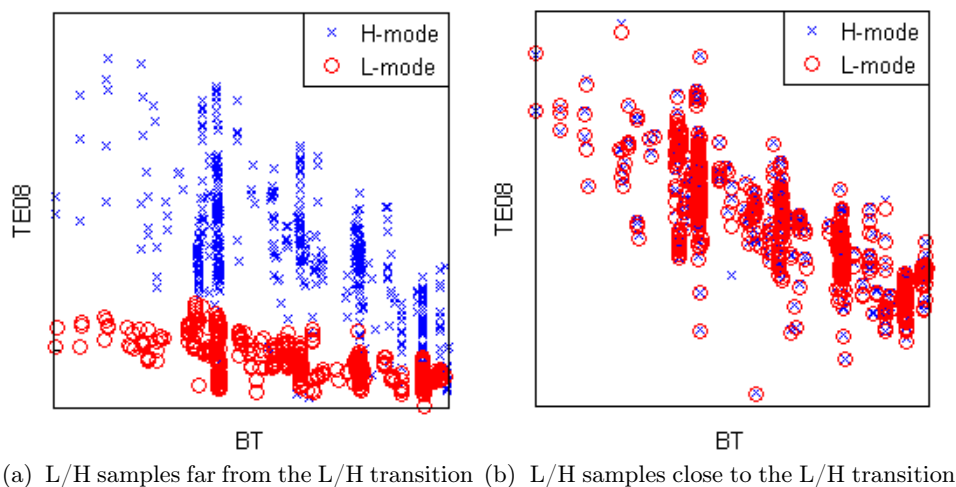


Figure 5.13: Distribution of the L/H samples in the BT and TE08 space

The results given by SVM-FES have been compared with the results given by ROC and PCA. The success rates obtained by SVM-FES, ROC and PCA for the  $\pm 100$  ms model are 93.404%, 87.852% and 57.035% respectively. In the case of the  $\pm 500$  ms model, the results are 97.436%, 91.982% and 87.635%. For both models, the results of SVM-FES exceed the ones obtained by ROC and PCA.

The feature spaces computed by SVM-FES can be seen in Table 5.1. The dimensions selected for the  $\pm 500$  ms model are a subset of the ones selected for the  $\pm 100$  ms model. This is a consequence of the non-linearity of the samples close to the L/H transition. The signals selected for the  $\pm 500$  ms model are adequate to classify the points far from the transition but, in order to obtain a high classification rate close to the transition, more signals are required.

The RSIC methodology has shown its capabilities for regions selection and classification using the TJ-II Thomson scattering images. The original images have been reduced to a region of 16.49% of their original size. The resulting region is a combination of the regions selected for each one of the classes of Thomson scattering images. In spite of the large reduction of the dimensionality of the images, the results obtained by the RSIC regions are slightly lower than the ones obtained using the entire images (95.27% versus 96.37%).

The CPU times are drastically reduced by the RSIC methodology. The training, calibration and test times are reduced 93.97%, 82.55% and 81.82% respectively. The mean classification time of an image using the RSIC regions is 0.025 s in contrast to 0.137 s using the entire images.

The regions given by the RSIC methodology help us to understand the

structure of the Thomson scattering images. Most of the area selected by RSIC belongs to the centre of the images (Figure 5.11f), so it is possible to conclude that it contains relevant information for the classification task. The height of the regions selected for the CFF and BCK classes is larger than their width. These regions identifies the vertical patterns shown in CFF, ECH and NBI images. In the case of the ECH and NBI classes (the most similar ones), the centre of the image allows the classifiers to distinguish both classes.

## Chapter 6

# Analysis of L/H & H/L transitions

During plasma operation, the plasma evolves and different phenomena take place (e.g. ELMs, L/H and H/L transitions or disruptions). Some of these events must be identified in order to study the thermonuclear processes inside the plasma and others must be avoided since they compromise the fusion machine integrity. Plasma behaviour is identified through the recognition of patterns inside waveforms. Plasma phenomena generate similar patterns on each plasma pulse and thus, the identification of several behaviours is possible using these patterns. Sometimes more than one waveform is required to identify a certain event (e.g. ELMs are recognised as spikes in the  $D_\alpha$  emission signal accompanied by drops in the plasma density).

The identification of patterns in waveforms is usually carried out by means of visual analysis. Signals are analysed by experts one by one and events are manually located. It implies the use of plenty expert manpower and long waits until the data is processed. Some pulses are sometimes not evaluated due to the lack of resources.

Present fusion databases are indexed by pulse number (a simple counter of the number of plasma discharge), the names of the diagnostics and the names of the signals (e.g. in JET, the  $D_\alpha$  emission of pulse 73337 is accessed by using the path: 73337, SA3D, AD36). The analysis of the data generated during plasma operation is performed pulse by pulse by the experts of each plasma physics field. Since the JET first pulse in 1983, more than 80,000 discharges have taken place. In the TJ-II stellarator, there have been more than 30,000 discharges since 1997. Therefore, the analysis of fusion databases is a “big numbers” problem.

JET pulses can last for more than a minute and ITER is intended to operate in steady-state (pulses longer than 30 minutes and even one hour). Therefore, the length of the signals will increase significantly in the next few years. The present paradigm of data access (pulse number, diagnostic and

signal name) will not be longer valid since it will not be possible for experts to analyse the full waveforms. In the last decade, the development of artificial intelligence and data mining methods have opened the door to an alternative data access: the *pattern oriented* paradigm (Vega and JET-EFDA contributors, 2008). Using the pattern oriented paradigm, data should no longer be indexed by pulse number and signal name but by patterns inside waveforms.

The pattern oriented paradigm is focused on events inside waveforms. Scientists can access data using the plasma phenomenon they are interested in evaluating, saving time and increasing the statistical weight of their results since they gain access to events from a large range of plasma pulses. Using this paradigm, the query is the pattern to be found in the database and the responses of the system are pulses numbers and the times where similar patterns are located.

Most of the pattern oriented data retrieval systems consist of three steps:

- **Feature extraction:** the time-domain waveforms are transformed into a set of features, usually in a lower dimension space. It speeds up the database access and simplifies the following tasks. It is a crucial step since it defines the data type that the next tasks will use. In fusion science, there are two main approaches:
  - **Fourier coefficients:** the waveform features are its major Fourier coefficients (Nakanishi et al., 2004).
  - **String methods:** the waveforms are replaced by characters based on the waveforms morphology (Dormido-Canto et al., 2008).
- **Signal indexing:** signals are indexed to speed up the retrieval process. Since the databases contain tens of thousands of pulses and hundreds of different signals, the full databases cannot be traversed and therefore an indexation is required.
- **Similar patterns retrieval:** it is carried out by means of a similarity measure. The patterns in the database are compared to the one in the query using the similarity measure. The most similar ones are retrieved to the user.

The first of the approaches for feature extraction uses the coefficients of the discrete Fourier transform. The waveforms are moved from the time domain to the frequency domain, losing the time information stored in them. The first attempt to data retrieval using this features (Nakanishi et al., 2004) was applied to search similar waveforms to the one requested by the user. The similarity between two waveforms was measured using the Euclidean distance of the  $k$  first Fourier coefficients. It was shown that  $k < 10$  was good for most cases. The drawbacks of this method were the problems dealing with high-frequency signals (it was not possible to find similar ones)

and a tendency to distinguish between waveforms whose lengths were slightly different.

Later, this method was improved to allow the recognition of patterns inside waveforms (Nakanishi et al., 2006). The Fourier complex coefficients were replaced by the power spectrum density values but there were still problems with high frequency signals and multiple zero-crossings waveforms. This problem was solved in (Hochin et al., 2008) using a similarity measure that took into consideration both the waveform frequency and its outline. Finally, an indexing method was proposed in (Hochin et al., 2010) for accelerating the data access. Waveforms were cut up into fine-grained segments that were stored into a multi-dimensional index for quick retrieval.

The second approach to feature extraction is the use of a symbolic representation of waveforms (Daw et al., 2003). Using this alternative, waveforms are replaced by a string of symbols encoding its features. The number of symbols (dimension of the feature space) depends on the degree of detail required for the representation. Two different methods of symbolic representation were evaluated:

- **Slope method:** signals were divided into segments and each segment was replaced by a label / character. There were 5 different characters. The segments were fitted using a straight line and the character assigned to the segment depends on the slope of the fitting line (Dormido-Canto et al., 2006).
- **Concavity method:** again, signals were divided into segments and each segment was replaced by a label / character. There were also 5 characters but in this case, the label of each piece was based on the classification of its concavity. The method discerned between convex, concave, increase, decrease and small horizontal oscillations (Dormido-Canto et al., 2008).

The symbolic representation has been applied to seek for entire signals and also to search for patterns within waveforms (Vega et al., 2007). To speed up the search process, the signals are indexed by means of a SVM (see Section 3.1.1) classification system (Dormido-Canto et al., 2004), (Farias et al., 2006). The combination of an SVM classification system and a symbolic representation of waveforms has been applied to the TJ-II database (Vega et al., 2008) and to the JET database (Rattá et al., 2008).

The symbolic representation of waveforms based on the slope method has the disadvantage that sometimes, in fusion databases, it is difficult to obtain an exact match of the sought pattern. In order to solve this problem, the initial set of five characters was reduced to only two characters (ascendant and descendant) and an uncertainty margin between them was fixed (Pereira et al., 2008). It increased the number of similar waveforms retrieved to the

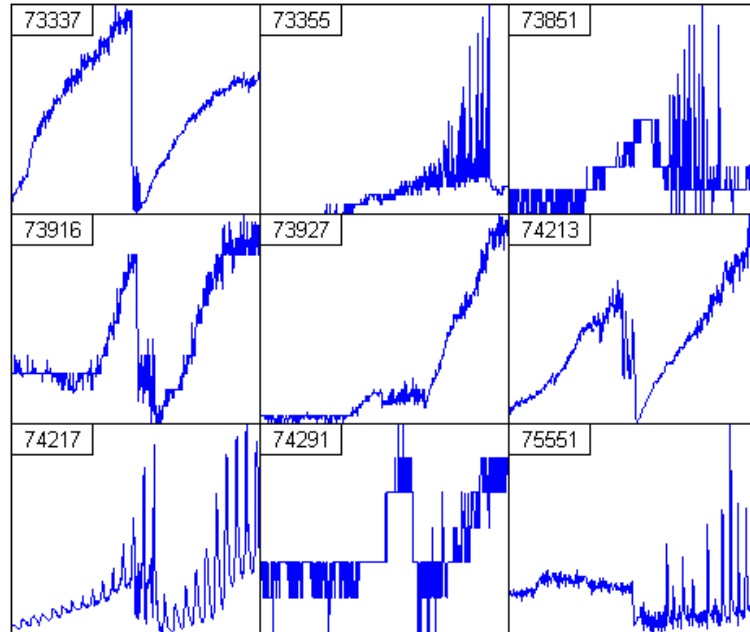


Figure 6.1: Different patterns of the L/H transition in JET

users. This methodology has also been exploited in an distributed open environment (Pereira et al., 2010). It allows scientists from different laboratories to share their data increasing the significance of the results obtained. It also grants access in larger databases to the fusion community.

One application of the pattern recognition techniques is the location of the L/H and H/L transitions (see Section 2.2.1) in a plasma discharge. The L/H transition can be identified as a sudden drop of the  $D_\alpha$  signal accompanied by a change in the slope of the plasma density waveform. The case of the H/L transition is tougher since the pattern sought in the waveforms is not well defined. However, it is not always possible to apply the mentioned pattern recognition techniques to the identification of the L/H transition. The reason is that the morphological pattern of the L/H transition varies depending on parameters such as power, temperature or density. Moreover, the time scale and the amplitude of the patterns can be significantly different. Figure 6.1 depicts different L/H transitions from 9 JET pulses.

An alternative to pattern recognition techniques for the identification of L/H transitions are data-driven models. Given a database of L/H transition times, it is possible to build a model to evaluate whether the plasma is in L-mode or in H-mode. Different techniques have been applied to obtain data-driven methods to regime identification in JET: Murari made a comparison between fuzzy logic and SVM (Murari et al., 2006), Vega combined Bayesian statistics and SVM (Vega et al., 2009b) and Meakins used neural networks

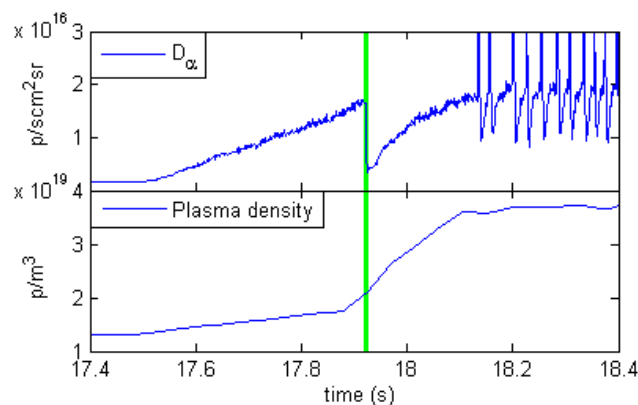


Figure 6.2: Visual location of the L/H transition, JET pulse 67707

(Meakins et al., 2010).

Data-driven models require large databases of L/H transition times. Unfortunately, the L/H transition times are not always available and these models usually misclassify the samples close to the transition. Thus, alternative methods are required to the location of the transitions. This chapter describes a new methodology to the location of L/H transitions. This methodology is introduced in Section 6.1. Section 6.2 contains the application of data-driven models of the L/H and H/L transitions using conformal predictors.

## 6.1 Automated location of L/H transitions

The Automated Transition Detector (ATD) is an unattended tool to identify L/H transitions in plasma discharges (González et al., 2012a). Given a set of pulses, the method retrieves the times of the L/H transitions together with uncertainty intervals in the estimations of the transitions. The ATD does not require human intervention.

The classical manual method of L/H transition identification consists of the location of a sudden drop of the  $D_\alpha$  waveform (JET signal PPF/-S3AD/AD36) accompanied by a change in the slope of the plasma density (Figure 6.2). Unfortunately, there are discharges where the drop of the  $D_\alpha$  waveform does not appear at all, the signal is corrupted with noise or the signal amplitude is close to the digitising limit (Figure 6.1). In addition, it is sometimes difficult to detect a change in the slope of the plasma density. Other alternative to determine the transition time could be the inspection of the ECE temperature profiles and the determination of the time when the ETB appears (see Section 2.2.1). However, the accuracy of the manual identification of the transitions is limited and it requires several manpower.

There are five reasons that emphasize the usefulness of the ATD:

- No manpower is necessary.
- All discharges are processed exactly in the same way thereby ensuring reproducibility and avoiding human errors.
- All transition times are estimated, even the ones of discharges where the transition cannot be located by means of visual analysis.
- Large databases of transition times can be generated improving the statistical significance of future studies.
- The database of transition times can be updated after each new pulse in an unattended way.

The ATD is quite general and it can be applied to other fusion devices with minor changes. In fact, it has been applied to the location of L/H transitions in JET (González et al., 2012a) and in DIII-D (Farias et al., 2012). Next section contains the workflow of the ATD and an explanation of its components. Section 6.1.2 describes the application of the ATD to the JET database and Section 6.1.3 summarizes the results of the ATD in DIII-D.

### 6.1.1 ATD workflow

The ATD consists of four software modules (Figure 6.3): *readout loop*, *discrimination loop*, *model creation* and *prediction module*.

Firstly, it is necessary to know whether the plasma achieves H-mode. Given a range of plasma pulses, the aim of the *readout loop* is to create a database containing the pulses that reach H-mode. This is achieved by means of a rough location of ELMs (just the presence of ELMs, not their times) in a discharge. If a discharge shows ELMs, it contains an L/H transition. Section 6.1.1.1 describes this module.

The *discrimination loop* (Section 6.1.1.2) classifies the transitions with H-mode into two groups accordingly with their signature (pattern) in the  $D_\alpha$  waveform:

- In the case of a *clear signature*, the time of the transition and an uncertainty interval are automatically determined. A database with the transition times and their corresponding uncertainty intervals is generated. Figure 6.4a contains an example of clear signature transition from JET pulse 73340. Clear signatures are characterized by an unambiguous drop of the  $D_\alpha$  signal.
- The transition times of the discharges showing a *non-clear signature* cannot be located within this module and thus, they are stored in an

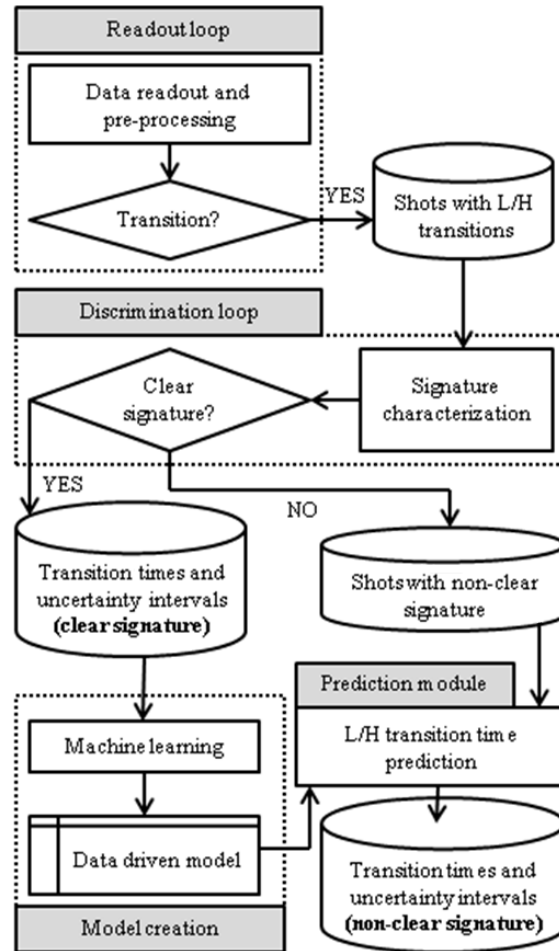


Figure 6.3: ATD workflow

intermediate database for later use. Figure 6.4b shows an example of this type of transition from JET pulse 73559. It is possible to observe that there is not a clear drop an obvious drop of the  $D_\alpha$  signal.

In order to determine the transition times in the non-clear discharges, a ICP predictor model (see Section 3.1.2.1) is trained using the discharges showing a clear transition pattern. Given an instant of a pulse, the predictor determines whether the plasma is in L-mode or in H-mode. In addition, it generates a value of confidence and credibility of the given prediction. This is accomplished with the third module of the ATD: *model creation* (Section 6.1.1.3).

Finally, in the *prediction module* (Section 6.1.1.4), the pulses in the database of non-clear signatures are used as input for the predictor generated in the previous module. The transitions of these pulses are located

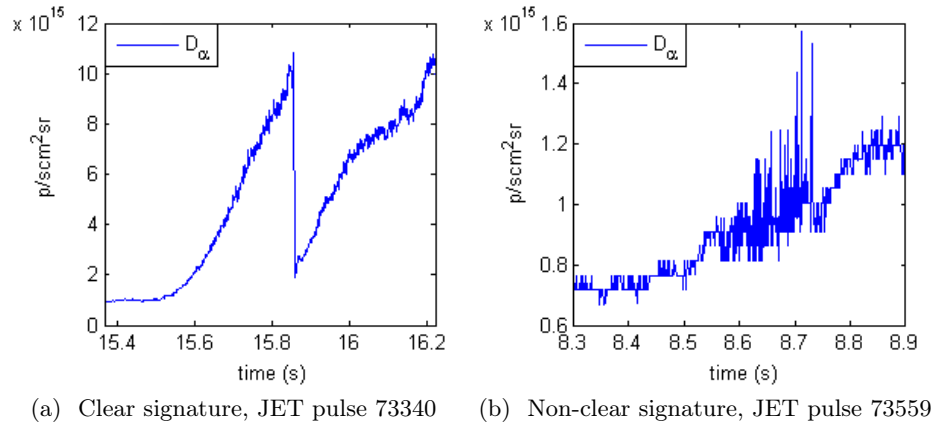


Figure 6.4: L/H transition signature types examples

at the times when the predictions change from L-mode to H-mode.

#### 6.1.1.1 Readout loop

The aim of the readout loop is the identification of the discharges that achieve H-mode and therefore contain a L/H transition. The detection of the H-mode in a discharge is carried out by means of the identification of ELMs in the discharge. Since ELMs only take place in H-mode plasmas, the detection of ELMs in a pulse means that the plasma is in H-mode.

UMEL (see Section 4.1) is used to check the presence of ELMs. A SVR regression (RBF kernel,  $K_C = 5$ ,  $K_e = 10$ ,  $K_\sigma = 0.3$ ) is computed using the  $D_\alpha$  waveform. In order to speed up the SVR computation, the waveform is decomposed using a level 2 Haar wavelet and the approximation coefficients are fitted using UMEL. The existence of ESVs reveals the presence of ELMs in the discharge.

Figure 6.5 contains two examples of the readout loop module. On the one hand, Figure 6.5a depicts a JET pulse (73351) that achieves H-mode. ESVs appear in the spikes caused by the ELMs and thus the pulse is included in the database of pulses with L/H transitions. On the other hand, Figure 6.5b shows a pulse that have not achieved H-mode. Since there are no ELMs in the pulse, no ESVs appear. Therefore, this pulse does not contain a L/H transition and is not analysed by the ATD.

#### 6.1.1.2 Discrimination loop

For every pulse with L/H transition, the discrimination loop carries out two important tasks:

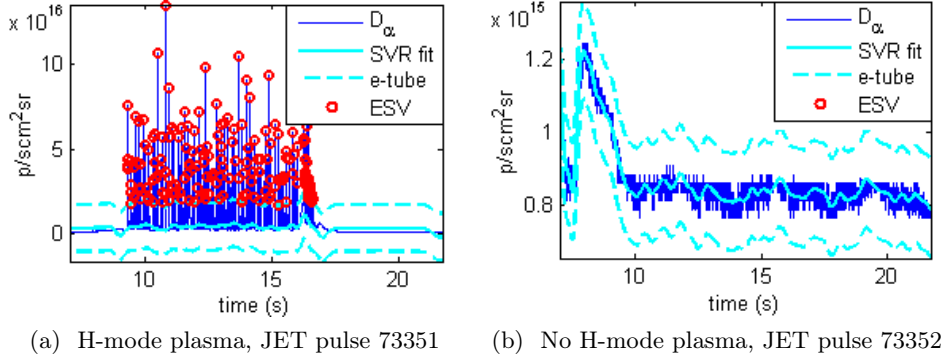


Figure 6.5: Readout loop examples

- **Location of the *L/H Transition Interval (LHTI)*:** this is a time interval where the L/H transition occurs.
- **Identification of the transition signature type:** the L/H transitions are classified into two groups according to their signature type: clear signature and non-clear signature transitions.

**Location of the LHTI.** The **first task** of the discrimination loop is the location of the LHTI. The LHTI's objectives are, first, to reduce the time slot where the transition is sought and, second, to simplify the following ATD modules. Basically, the LHTI is the time interval located between the beginning of the auxiliary input power and the appearance of the first ELM. An example of the LHTI from JET pulse 76563 is plotted in Figure 6.6. The LHTI is determined in three steps: detection of the power injection, detection of the ELMs region and residual ELMs elimination.

**Step 1: detection of the power injection.** In order to achieve the H-mode confinement regime, high auxiliary input power is necessary. However, the threshold that ensures the change of confinement is known within a wide margin. Moreover, this threshold varies with parameters such as density, temperature or magnetic field. Here, since the L/H transition must be located within the LHTI, a conservative power threshold ( $P_\tau$ ) is computed. The time when the power injected to the plasma reaches  $P_\tau$  determines the left boundary of the LHTI.  $P_\tau$  is computed as:

$$P_\tau = 0.2 \cdot \max(\text{Power}) \quad (6.1)$$

where Power is the total power injected into the plasma (JET signal PPF/-MG3/YTO).

Figure 6.7 shows the detection of the auxiliary power injection in JET pulse 73337. The horizontal red line represents  $P_\tau$ . The dotted green line is

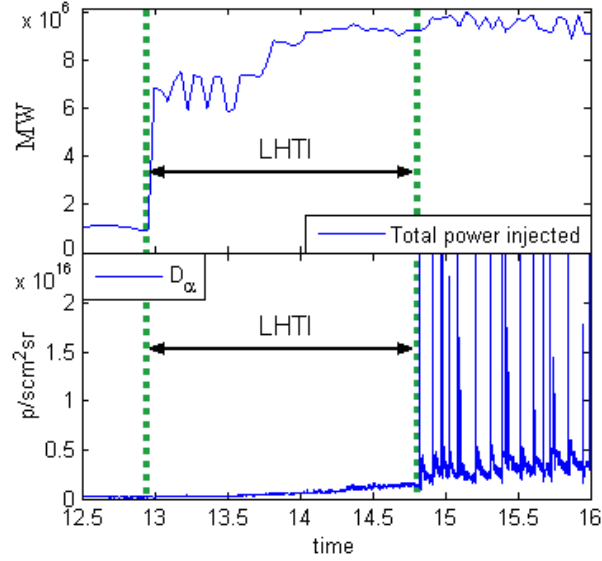


Figure 6.6: L/H Transition Interval (LHTI), JET pulse 76563

the resulting left boundary of the LHTI. In this pulse, the transition takes place at 15.844 s.

**Step 2: detection of the ELMs region.** Once the left boundary of the LHTI has been determined using the total input power, the next step is the identification of the H-mode region. ELMs only appear in H mode and therefore after the L/H transition. In this step, UMEL is applied again to locate the region with ELMs (Figure 6.8, upper graph).

To speed up the SVR computation needed in UMEL, a dimensionality reduction using a level 4 Haar wavelet is applied to the original  $D_\alpha$  signal. The approximation coefficients of the  $D_\alpha$  signal are fitted (RBF kernel,  $K_C = 4$ ,  $K_e = 18$ ,  $K_\sigma = 0.5$ ) and the ESVs are retrieved. Unfortunately, not all the ESVs appear in the ELMs. If the amplitude of the L/H transition signature is large, it is possible that some ESVs would appear in the transition. Thus, it is not possible to set the right boundary of the LHTI to the time of the first ESV. A threshold ( $ELMs_\tau$ ) is required to determine this time.

The number of ESVs retrieved by UMEL is counted in bins of 0.05 seconds (Figure 6.8, lower graph). The mean value of the ESVs in the non-empty bins is calculated (horizontal cyan line). This mean value is used to compute  $ELMs_\tau$  (horizontal red line):

$$ELMs_\tau = 0.4 \cdot \frac{\text{Number of ELMs}}{\text{Number of non-empty bins}} \quad (6.2)$$

The right boundary of the LHTI is equal to the time of the first bin with

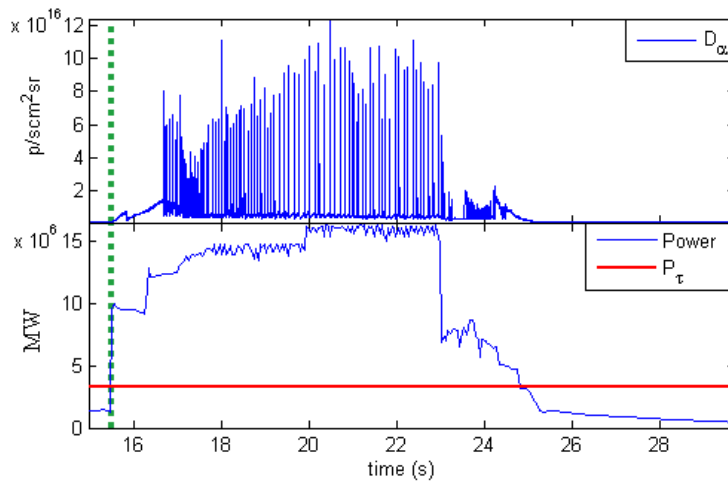


Figure 6.7: Detection of the power injection, JET pulse 73337

more ESVs than  $ELMs_{\tau}$ . Since the L/H transition is very close to the first ELM in some pulses and to ensure that the LHTI contains the transition, a margin of 0.1 s is added to the time of the right boundary of the LHTI (green dotted line). Again, this is a conservative step because it is essential that the LHTI encloses the L/H transition.

**Step 3: Residual ELMs elimination.** In the previous step, the LHTI right boundary is computed as the time of the first bin with more ESVs than  $ELMs_{\tau}$  plus a margin of 0.1 s. Therefore, it is possible that some ELMs appear at the right end of the LHTI.

The focus of the third step is to remove these ELMs in the case that they exist. The identification of the ELMs is carried out using UMEL. A complete description of how ELMs are identified using UMEL can be found in Section 4.1.3. After this step, the right boundary of the LHTI is moved to the time of the first ELM located.

**Identification of the transition signature type.** The second task of the discrimination loop is the identification of the transition signature type. Two types of transitions are considered: clear signature transitions (Figure 6.9a, upper graph) and non-clear signature transitions (Figure 6.9b, upper graph).

The Haar wavelet detail coefficients of the  $D_{\alpha}$  signal have been used to locate the characteristic drop of the transitions within the LHTI. Taking into account that the  $D_{\alpha}$  drops can be different from each other, different wavelet decomposition levels have been tested. The best results have been achieved using a level 5 wavelet decomposition. On the one hand, clear signatures

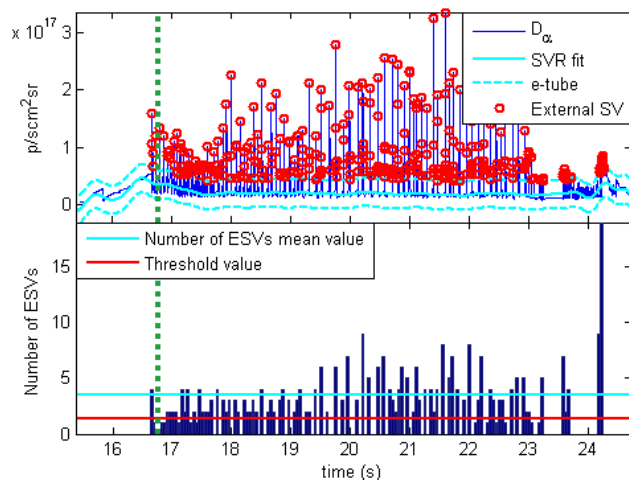


Figure 6.8: Detection of the ELMs region, JET pulse 73337

are characterized by an unambiguous drop. On the other hand, non-clear signatures do not show such an obvious drop. Therefore, the wavelet detail coefficients of the clear signature transitions show an isolated peak at the transition time (Figure 6.9a, lower graph). In contrast, since the non-clear signatures do not show a clear drop, their wavelet detail coefficients show several different peaks (Figure 6.9b, lower graph).

UMEL (RBF kernel,  $K_C = 1$ ,  $K_e = 4$ ,  $K_\sigma = 2$ ) is applied to the normalised (between 0 and 1) wavelet detail coefficients to locate the peaks. If an isolated ESV is located, the transition signature is recognised as a clear signature and the L/H transition instant is determined as the time of this ESV. On the other hand, if different ESVs are retrieved, the transition signature is identified as a non-clear signature. In this case, the transition time cannot be estimated within the discrimination loop module.

The transitions with clear signatures are included in a database of L/H transition times with their corresponding uncertainty intervals. The uncertainty interval (error bar) is related not only to the sample period ( $T_S$ ) of the  $D_\alpha$  signal but also to the wavelet decomposition level. Due to the fact that each decomposition level of the Haar wavelet transform reduces the number of samples by a factor 2, the uncertainty interval is  $\pm 2^L \cdot T_S$  around the prediction (or equivalent an error bar of  $\pm 2^{L+1} \cdot T_S$ , where  $L$  is the wavelet decomposition level). As  $T_S = 0.1$  ms and  $L = 5$ , the uncertainty interval for all transitions with a clear pattern is  $\pm 3.2$  ms.

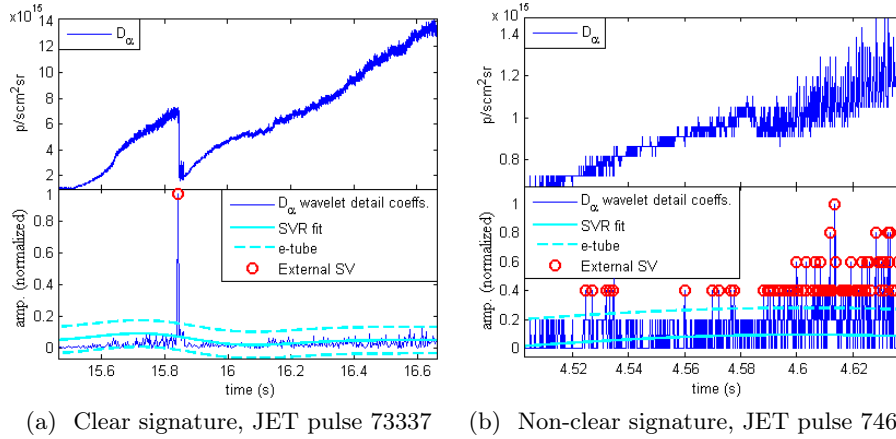


Figure 6.9: L/H transition signature types and their wavelet detail coefficients

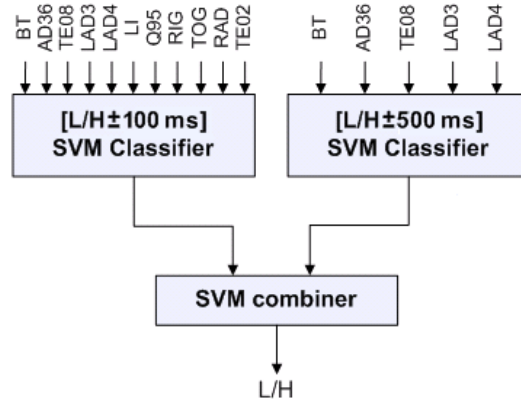


Figure 6.10: JET two-layer L/H model

### 6.1.1.3 Model creation

The L/H transition times of the non-clear signatures cannot be estimated using the wavelet transform. Several ESVs appear in the detail wavelet coefficients of the  $D_\alpha$  signal and thus it is not possible to identify which one corresponds to the real transition. As a result, an alternative method is required. A L/H classifier has been proposed to estimate the times and the *Probability Confidence Intervals* (PCIs) of the L/H transitions with non-clear signatures. The classifier is trained using the pulses with clear signatures identified in the previous module. The transition times of these pulses have been located and thus, given a certain time  $t$ , it is possible to know if the plasma is in L-mode or in H-mode. Since the classifier is built using the

automatically identified transitions, the ATD does not require a database of L/H transition times.

The first step to build a classifier is to define its input space (i.e. the space of the input samples). As it has been previously explained, dozens of diagnostics measure properties of the plasma at each instant, generating hundreds of different signals. Some of them are irrelevant for the L/H transition phenomenon and thus they can be discarded. In contrast, a small subset of signals can help in the description of the plasma confinement quite accurately.

The length of the LHFI varies from discharge to discharge. Unfortunately, the relevant features to distinguish the L and H confinement modes are different in temporal segments close to the transition ( $\pm 100$  ms around the transition time) and far from it ( $\pm 500$  ms around the transition time) and the models to distinguish the confinement mode also vary. Moreover, the position of the L/H transition in the LHFI is unknown. As a result, it is not possible to discern the best input space for a classifier. In similar cases, a combination of classifiers has achieved good results (Ratta et al., 2010, prediction of disruptions in JET).

A two-layer model (SVM based) has been proposed to locate transitions within the LHFI (Figure 6.10). The first layer consists of two classifiers. One (Figure 6.10, upper left box) is trained in a symmetric interval of  $\pm 100$  ms around the transition time with a sampling period of 1 ms (i.e. 201 samples per pulse). The second classifier in the first layer (Figure 6.10, upper right box) is trained in a symmetric interval of  $\pm 500$  ms around the transition time and a sampling period of 1 ms (i.e. 1001 samples per pulse). The focus of the classifiers in the first layer is to emphasize the automatic learning near to and far from the transition.

The feature extractor described in Section 5.1 has been applied to select the most relevant signals to predict the plasma confinement mode in both classifiers. The signals used in both models can be seen in Figure 6.10 and a complete description of the signals can be found in Appendix H. It is important to note that the signals determined as relevant for the  $\pm 500$  ms classifier, also have been selected by the SVM-FES as relevant for the  $\pm 100$  ms. It means that these signals are good enough for the phenomenological description of the decision function. However, the classifier closer to the transition needs more information to obtain a high success rate because the prediction close to the transition is more difficult.

Both classifiers have been trained using a linear kernel (Eq. 3.25) to separate the two confinement modes. Therefore, the output of the  $\pm 100$  ms classifier is a linear function:

$$D_1(u) = C_0 + \sum_{i=1}^{11} C_i \cdot u_i \quad (6.3)$$

where  $C_i$  is the weight of the plasma quantity  $i$ ,  $C_0$  is a bias and  $u = [\text{BT}, \text{AD36}, \text{TE08}, \text{LAD3}, \text{LAD4}, \text{LI}, \text{Q95}, \text{RIG}, \text{TOG}, \text{RAD}, \text{TE02}]$ . The output of the  $\pm 500$  classifier is:

$$D_2(v) = B_0 + \sum_{j=1}^5 B_j \cdot v_j \quad (6.4)$$

where  $B_j$  is the weight of the plasma quantity  $j$ ,  $B_0$  is a bias and  $v = [\text{BT}, \text{AD36}, \text{TE08}, \text{LAD3}, \text{LAD4}]$ .

The training of the second layer classifier (also based on a linear SVM) called *SVM combiner* is carried out using the outputs of the first layer classifiers ( $D_1(u)$  and  $D_2(v)$ ). Thus, its output is computed as:

$$D(u, v) = A_0 + A_1 \cdot D_1(u) + A_2 \cdot D_2(v) \quad (6.5)$$

where  $A_1$  and  $A_2$  are the weights of the first layer classifiers and  $A_0$  is a bias.

The SVM combiner uses the information from both classifiers to minimize the error of the estimated transition time ( $\pm 100$  ms classifier goal) and to avoid the misclassification of points far from it ( $\pm 500$  ms classifier goal).

Finally, the plasma confinement is calculated as:

$$\text{mode} = \begin{cases} \text{L-mode} & \text{if } D(u, v) < 0 \\ \text{H-mode} & \text{if } D(u, v) \geq 0 \end{cases} \quad (6.6)$$

#### 6.1.1.4 Prediction module

This module estimates the transition times of the pulses with non-clear signatures using the model designed in the previous module. The samples within the LHTI are classified one by one in ascending temporal order. The change of the predicted confinement (i.e. the change from  $D(u_t, v_t) < 0$  to  $D(u_{t+1}, v_{t+1}) \geq 0$ ) determines the transition time.

Figure 6.11 contains two examples of prediction using JET pulses 73034 (Figure 6.11a) and 73926 (Figure 6.11b). Since there are not clear drops in the  $D_\alpha$  waveforms, the transitions cannot be located within the discrimination loop. The lower plots of Figure 6.11 contain the output of the classifiers of the previous step. The transitions predicted by the  $\pm 100$  ms ( $D_1(u)$ ) and  $\pm 500$  ms ( $D_2(v)$ ) classifiers are marked using green lines. The output of the SVM combiner ( $D(u, v)$ ) determines the predicted transition time (red line).

At this point, the model does not generate any measure of the goodness of the predicted transition time. Intuitively, samples far from the L/H transition are easier to classify (they are far from the border between L and H) and thus the predictions should have a high level of significance (high reliability). On the other hand, samples close to the transition are harder to classify and therefore the significance of the predictions should be lower

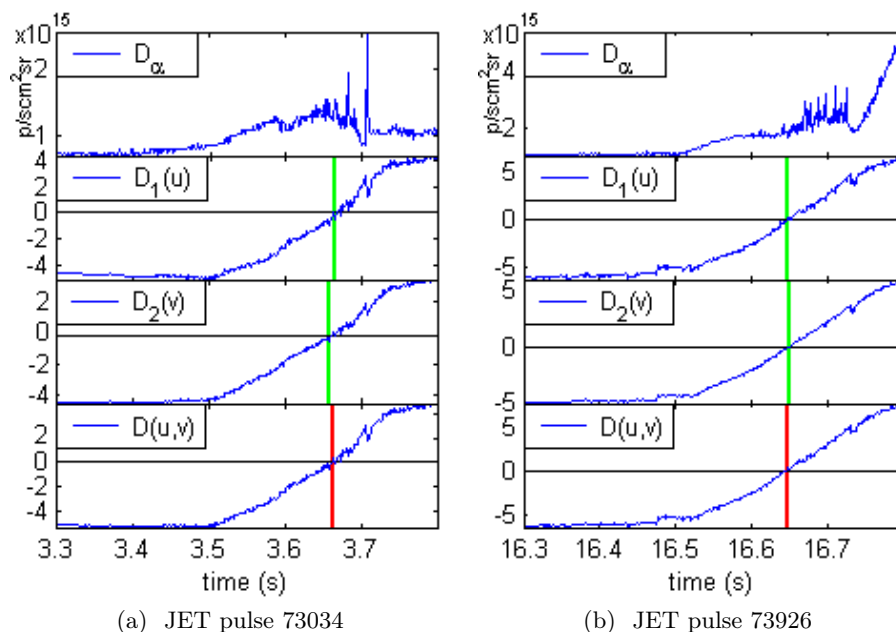


Figure 6.11: Example of the prediction module

(low reliability). The level of significance should be minimum just at the border of the L and H confinement modes. Given a reliability threshold, it defines a reliability value below which the prediction is assumed to be not very trustworthy. The time interval around the estimated transition where the reliability is below the threshold could be considered a PCI of the prediction. The ATD assures that the real L/H transition is inside the PCI but the prediction of the transition time inside the PCI is less accurate.

Figure 6.12 depicts a toy example on the computation of the PCI. Figure 6.12a shows the feature space of L (red crosses) and H samples (blue circles) and the separating hyperplane (border). The test samples are marked using green dots. The temporal evolution of the test samples is  $t_1, t_2, \dots, t_7$ . Figure 6.12b contains the computation of the PCI of the test samples. Since the test samples  $t_1$  and  $t_7$  are far from the separating hyperplane, their reliability values are high. In contrast, the samples  $t_3, t_4$  and  $t_5$  are close to the hyperplane and thus their reliability values are low. The test points located on the left of the hyperplane are classified as L-mode and the samples located on the right are classified as H-mode. The PCI is the time interval between the two first samples around the transition (one on the right and one on the left) whose reliability values are above the given threshold ( $t_3$  and  $t_6$ ).

Off-line ICPs (see Section 3.1.2.1) have been applied to compute the reliability values of the SVM combiner ( $D(u, v)$ ). The non-conformity measure

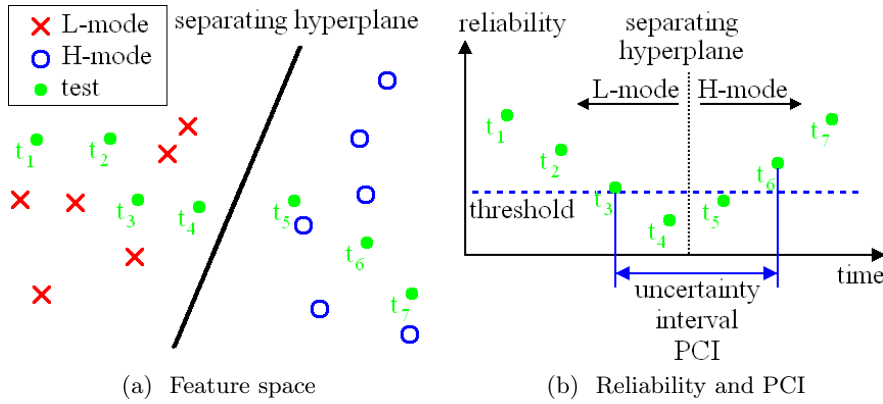


Figure 6.12: Reliability and PCI computation schema

chosen to compute the PCI is the distance from the samples to the hyperplane:

$$\alpha(x) = \begin{cases} -|distance(H, x)| & \text{if } x \text{ is properly classified} \\ |distance(H, x)| & \text{if } x \text{ is misclassified} \end{cases} \quad (6.7)$$

The reliability value of each sample is computed as the product of the conformal measures (credibility and confidence). The product of the conformal measures has been previously used obtaining good results (Makili et al., 2011). The reliability threshold has been set to 0.3. This means that, on average, the values of confidence and credibility are greater than 0.55.

Figure 6.13 shows the PCI of JET pulses 73034 (Figure 6.13a) and 73926 (Figure 6.13b). The  $D_\alpha$  signal is plotted at the top of both figures. The output of the SVM combiner ( $D(u, v)$ ) is located in the middle of the figures. The estimated transition times ( $L/H_{estimated}$ ) are located at the time when  $D(u, v) = 0$  (red line). The reliability values are plotted at the bottom of the figures. The reliability threshold (solid green line) is set to 0.3. The PCI borders (green dashed lines) are located at the times when the reliability crosses the threshold value around the transition.

It is important to note that since the PCI length depends on the reliability, it might not be a symmetric interval around the transition time (the interval on the left can be larger than the interval on the right and vice versa).

#### 6.1.1.5 Validation of L/H transition times of discharges with clear signatures

The ATD uses the time of the clear signature transitions to build a predictive model to locate the change of confinement in the pulses with non-clear signatures. In order to build a suitable model, it is important that the transition

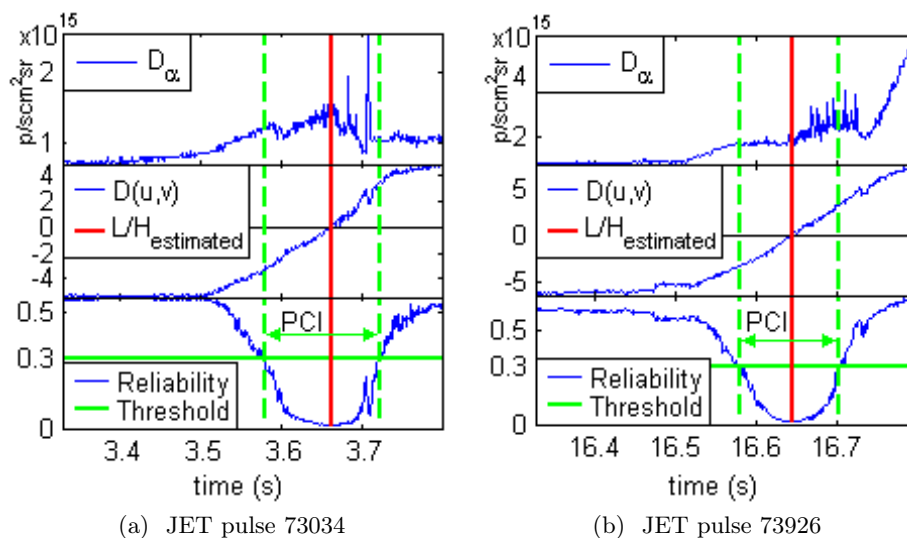


Figure 6.13: Examples of PCI

times of the discharges with clear signatures do not contain errors. Since the ATD is an automated technique, the validation of the transition times of these pulses must be carried out without human intervention.

The two-layer model described in Section 6.1.1.3 is trained with transitions that show a clear signature. Therefore, if any of these discharges is used as input of the two-layer classifier, its resulting PCI should include the transition time estimated in the discrimination loop (using the wavelet transform). If the estimated transition time is not located within the PCI, it is possible to conclude that the transition time is not properly located and hence, this transition must not be included in the training set of the two-layer model.

This method is valid for two main reasons:

1. **Low misclassification rate of the discrimination loop module:** the statistical weight of misclassified discharges is very low (there are only a few samples with a wrong classification of their confinement mode). The impact of the errors is expected to be negligible in the model determination.
2. **Use of linear kernels:** linear kernels have very high generalization ability and their sensitivity to errors is lower than other kernels. In contrast, they usually have lower success rates.

If the validation process detects misclassified transitions, the corresponding discharges are excluded from the database of discharges with clear signatures and they are included in the database of non-clear signatures. Then,

<b>Model</b>	<b>Training (Proper training set)</b>	<b>Test (Calibration Set)</b>
$\pm 100$ ms	98.62%	96.65%
$\pm 500$ ms	98.80%	97.72%
Combiner	99.17%	98.73%

Table 6.1: JET two-layer L/H model classification results

the two layer model is retrained using the new database. This process can be iterated until no more discharges are moved from the database of clear signature transition to the one of non-clear signature transitions. The transitions excluded from the clear signature database are estimated using the method described in the prediction module (Section 6.1.1.4).

### 6.1.2 Location of L/H transitions in JET

A database of 551 discharges from JET campaigns C21 to C26 was used to test the ATD methodology. The L/H transition times were determined manually by experts by means of visual analysis.

The *discrimination loop* located 143 transitions (25.95%) with clear signatures. Using these discharges, a L/H model was built. In order to reduce the computation time, a SVM parallel version was used (Ramírez et al., 2010). The set of 143 discharges was split into a proper training set (containing a random selection of 75% of the 143 shots) and a calibration set (with the remaining 25%).

After the generation of the two-layer model, the first operation was the validation of the set of 143 discharges with clear signatures (see Section 6.1.1.5). There were two pulses where the estimated transition times (in the discrimination loop using the wavelet method) were outside the PCIs. These discharges were removed from the database of clear signatures and they were included in the database of non-clear ones.

At this point, the database of clear signatures contained 141 (25.59%) transitions. Using this database, the two-layer model was retrained using 75% of the transitions as proper training set (106 transitions) and 25% as calibration set (35 transitions). The clear signature transitions were validated again and no more errors were found.

Table 6.1 summarizes the success rates achieved by the two-layer classifier using the proper training set (training set) and the calibration set (test set). Is it important to take into consideration that the higher classification rates of the  $\pm 500$  ms classifier compared to the  $\pm 100$  ms classifier do not imply that the  $\pm 500$  ms classifier locates the transition more accurately. The reason is that the  $\pm 500$  ms classifier was trained and tested in a total interval of 1 s (500 ms to the left of the transition and 500 ms to the right) while the

Signal	Original Quantities		Normalised Quantities	
	$C_i$	$B_j$	$C_i$	$B_j$
	$\pm 100$ ms	$\pm 500$ ms	$\pm 100$ ms	$\pm 500$ ms
BT	4.13	3.35	7.14	5.85
AD36	$-2.67 \cdot 10^{-16}$	$-1.16 \cdot 10^{-16}$	-9.27	-18.87
TE08	$1.66 \cdot 10^{-2}$	$9.84 \cdot 10^{-3}$	20.96	20.46
LAD3	$-1.30 \cdot 10^{-19}$	$-3.48 \cdot 10^{-19}$	-4.84	-21.48
LAD4	$5.07 \cdot 10^{-19}$	$5.56 \cdot 10^{-19}$	21.89	36.85
LI	4.82	–	2.40	–
Q95	2.07	–	4.49	–
RIG	3.40	–	6.38	–
TOG	-16.62	–	-3.65	–
RAD	$-6.28 \cdot 10^{-7}$	–	-14.23	–
TE02	$-2.44 \cdot 10^{-3}$	–	-7.50	–
bias	-11.45	$-7.53 \cdot 10^{-2}$	-15.41	-9.93

Table 6.2: JET coefficients of the first layer hyperplanes

$\pm 100$  ms classifier was trained and tested in an interval of 0.2 s (100 ms to the left of the transition and 100 ms to the right). Since the points far from the transition are easier to classify than the points close to it then the larger interval chosen the higher classification rate. For example, lets suppose a  $\pm 100$  ms classifier and a  $\pm 500$  ms classifier both using a sampling rate of 1 ms. If the  $\pm 100$  ms classifier locates a transition 5 ms after the real one then its accuracy is 97.5% (195/200). Let's suppose now that the  $\pm 500$  classifier makes a worse estimation of the transition, for example, 10 ms after the real one. In contrast, its success rate is 99% (990/1000), higher than the one of the  $\pm 100$  ms classifier.

Table 6.2 contains the hyperplane coefficients corresponding to the  $\pm 100$  classifier (Equation 6.3) and to the  $\pm 500$  classifier (Equation 6.4). The assessment of the real importance of the quantities to estimate the confinement mode can be determined with all quantities normalised in the interval  $[0, 1]$ . This normalisation is carried out using the equation:

$$S_{normalised} = \frac{S - \min(S)}{\max(S) - \min(S)} \quad (6.8)$$

It is important to note that a quantity  $S$  encloses all the pulses of a certain plasma signal. Therefore,  $\max(S)$  ( $\min(S)$ ) is not the maximum (minimum) of this signal in a single pulse but the maximum (minimum) of the signal in all the analysed pulses within the training interval.

The most important quantities to determine the confinement state of the plasma are the ones with the largest absolute coefficients (normalised). For example, in the case of the  $\pm 100$  ms classifier the most important quantities

<b>Number of non-clear signature transitions</b>	<b>410</b>
<b>Number of properly located transitions (<math>L/H_{\text{real}}</math> within the PCI)</b>	<b>397 (96.83%)</b>
mean( $ L/H_{\text{real}} - L/H_{\text{estimated}} $ )	27.9 ms
std( $ L/H_{\text{real}} - L/H_{\text{estimated}} $ )	37.6 ms
mean PCI length	225.2 ms
<b>Number of not properly located transitions (<math>L/H_{\text{real}}</math> outside the PCI)</b>	<b>13 (3.17 %)</b>
mean( $ L/H_{\text{real}} - L/H_{\text{estimated}} $ )	93.8 ms
std( $ L/H_{\text{real}} - L/H_{\text{estimated}} $ )	55.4 ms
mean PCI length	453.5 ms
Mean time between $L/H_{\text{real}}$ and the closest end of the PCI	5.96 ms

Table 6.3: Results of non-clear transitions in JET

are LAD4 (21.89), TE08 (20.96) and RAD (-14.23). The hyperplane of the SVM combiner (Equation 6.5) is:

$$D(u, v) = 0.52 \cdot D_1(u) + 0.70 \cdot D_2(v) + 0.27 \quad (6.9)$$

where  $D_1(u)$  is the output of the  $\pm 100$  ms classifier (Eq. 6.3) and  $D_2(v)$  is the output of the  $\pm 500$  ms classifier (Eq. 6.4).

Using normalised distances ( $0 < D_1(u) < 1$ ,  $0 < D_2(v) < 1$ ), the hyperplane equation is:

$$D(u, v) = 18.81 \cdot D_1(u) + 19.61 \cdot D_2(v) - 14.42 \quad (6.10)$$

It means that the  $\pm 500$  ms classifier is slightly more decisive than the  $\pm 100$  ms classifier.

The SVM combiner was applied to estimate the transition times and the PCI of the transitions with non-clear signatures (410 pulses). As previously mentioned, the reliability threshold was set to 0.3. Table 6.3 summarizes the results obtained. There were two main groups of discharges: the ones whose L/H transition time located by the experts ( $L/H_{\text{real}}$ ) lies within the computed PCI (397 pulses, 96.83%) and the ones whose  $L/H_{\text{real}}$  is outside the PCI (13 pulses, 3.17%).

With regard to the first group of discharges, Figure 6.14a shows the histogram of their PCI lengths (grouped in bins of 20 ms). The mean PCI length is 225.2 ms. It is important to mention that there were five discharges (74759, 76519, 76521, 76688 and 77634) whose PCIs vary between 710 ms and 3.91 s. These special cases were discharges with moderate input power (in all cases less than 10 MW) and/or discharges that achieve their maximum value in a non-abrupt way, with a long period of low power injection. These pulses

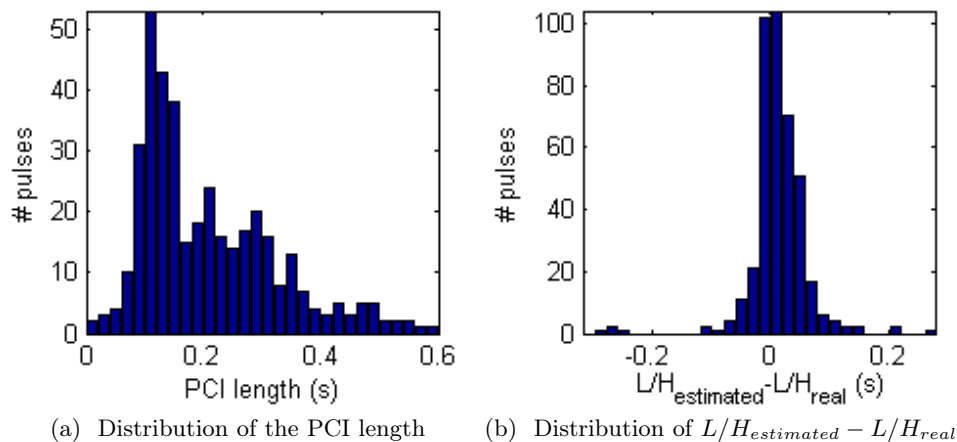


Figure 6.14: Distribution of the results obtained in the location of the non-clear signature transitions

with a long period of low injected power are not JET standard pulses and greatly increase the average PCI length in Table 6.3. If they were not taken into account, the mean PCI length becomes 206 ms. Figure 6.15 shows two of these pulses (JET pulses 77634 and 76521). It includes the input power, the  $D_\alpha$  emission, the output of the SVM combiner ( $D(u, v)$ ) and the reliability level. Figure 6.14b represents the distribution of the differences between the real L/H transition time ( $L/H_{real}$ ) and the transition time estimated by the ATD ( $L/H_{estimated}$ ). The absolute mean value is 27.9 ms and the standard deviation is 37.6 ms.

The second group of discharges in Table 6.3 was made up of the following pulses: 73559, 73576, 74611, 74622, 75066, 75222, 75740, 75741, 75742, 75743, 77009, 77054, 77179. Their  $L/H_{real}$ s were not inside the estimated PCIs. Only 13 discharges (3.17%) belonged to this group. The mean error in the location of the L/H transition was 93.8 ms and the mean PCI length was 453.5 ms. However, it is important to emphasize that in all these cases the  $L/H_{real}$  was very close to the ends of the PCI. The average difference between the  $L/H_{real}$  and the closest end of the PCI was 5.96 ms. In pulse 77009, a moderate input power was maintained for a quite long period after the transition. As a consequence, the PCI length was 4.172 s. If this pulse was ignored due to its non-standard character in JET, the mean PCI length of this group of discharges was 164.3 ms.

### 6.1.2.1 Scaling laws for the power threshold

The accuracy of the automated determination of the transition times is satisfactory and therefore the ATD can be used to increase the statistical significance of the studies of the L/H transition. For example, the ATD could be

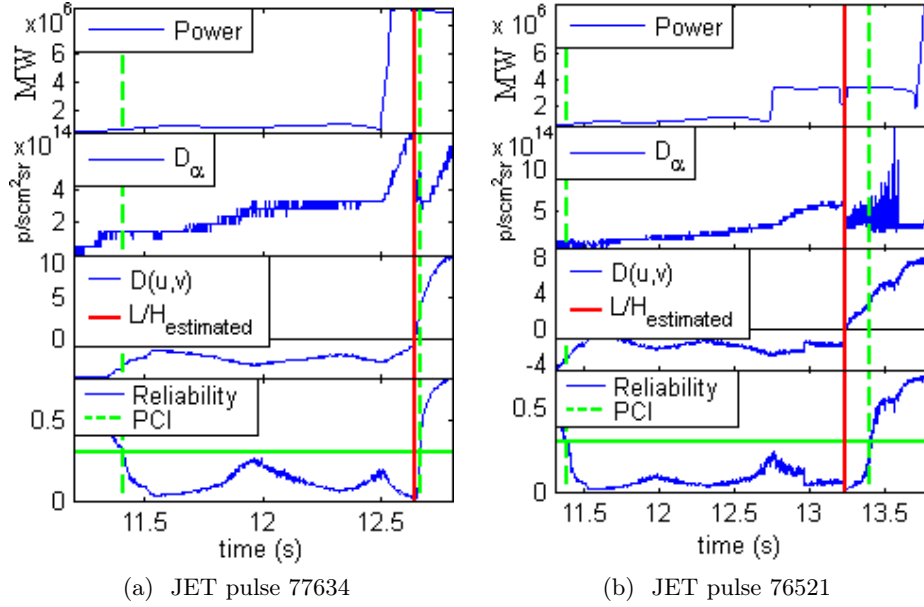


Figure 6.15: Examples of pulses with a large PCIs

Location method	Scaling law	MSE
<b>Ordinary Least Squares</b>		
Experts	$P_\tau = 10^{0.80 \pm 0.40} \cdot n_e^{0.56 \pm 0.12} \cdot B_T^{0.58 \pm 0.20} \cdot S^{0.39 \pm 0.60}$	7.082
ATD	$P_\tau = 10^{1.00 \pm 0.39} \cdot n_e^{0.64 \pm 0.08} \cdot B_T^{0.50 \pm 0.17} \cdot S^{0.23 \pm 0.60}$	8.635
<b>Ridge Regression, k = 4</b>		
Experts	$P_\tau = 10^{0.80 \pm 0.10} \cdot n_e^{0.55 \pm 0.08} \cdot B_T^{0.58 \pm 0.12} \cdot S^{0.39 \pm 0.14}$	7.077
ATD	$P_\tau = 10^{1.00 \pm 0.10} \cdot n_e^{0.64 \pm 0.07} \cdot B_T^{0.50 \pm 0.11} \cdot S^{0.23 \pm 0.13}$	8.632

Table 6.4: JET  $P_\tau$  scaling laws using  $n_e$ ,  $B_T$  and  $S$ 

used for a first data screening and then the experts could concentrate their attention only on the PCI to refine the analysis. On the other hand, it would be interesting to investigate to which extent the times determined automatically by the predictor can be used directly to perform physical studies. To assess this point, scaling laws for the power threshold to access the H-mode were determined using both the transition times determined by the ATD ( $L/H_{estimated}$ ) and the transition times identified manually by the experts ( $L/H_{real}$ ). To this end, two different regression methods were applied: OLS (see Section 3.3.1) and Ridge Regression (see Section 3.3.3). Ridge Regression was proposed to remedy collinearity among explanatory variables.

Although the L/H transition is known to depend on many parameters, it is widely accepted that the L/H transition power threshold strongly de-

Location method	Scaling law				MSE
<b>Ordinary Least Squares</b>					
Experts	$P_\tau = 10^{1.10 \pm 0.17}$	$\cdot n_e^{0.55 \pm 0.12}$	$\cdot B_T^{0.61 \pm 0.20}$	$\cdot q_{95}^{-0.14 \pm 0.23}$	7.106
ATD	$P_\tau = 10^{1.19 \pm 0.13}$	$\cdot n_e^{0.63 \pm 0.08}$	$\cdot B_T^{0.52 \pm 0.17}$	$\cdot q_{95}^{-0.10 \pm 0.22}$	8.657
<b>Ridge Regression, k = 4</b>					
Experts	$P_\tau = 10^{1.10 \pm 0.10}$	$\cdot n_e^{0.54 \pm 0.08}$	$\cdot B_T^{0.61 \pm 0.12}$	$\cdot q_{95}^{-0.14 \pm 0.12}$	7.102
ATD	$P_\tau = 10^{1.19 \pm 0.08}$	$\cdot n_e^{0.63 \pm 0.07}$	$\cdot B_T^{0.51 \pm 0.11}$	$\cdot q_{95}^{-0.10 \pm 0.12}$	8.654

Table 6.5: JET  $P_\tau$  scaling laws using  $n_e$ ,  $B_T$  and  $q_{95}$ 

depends on the plasma density, the toroidal magnetic field and the plasma size (Martin et al., 2008). Therefore, the scaling law:

$$P_\tau = K \cdot n_e^\alpha \cdot B_T^\beta \cdot S^\gamma \quad (6.11)$$

can be derived using OLS or Ridge Regression, where  $P_\tau$  is the threshold power expressed in MW,  $n_e$  is the line-average electron density (in units of  $10^{20} \text{m}^{-3}$ ),  $B_T$  is the toroidal magnetic field (T) and  $S$  is the plasma surface ( $\text{m}^2$ ). Table 6.4 shows the resulting scaling laws using the  $L/H_{real}$  (times determined by experts) and  $L/H_{estimated}$  (times estimated by the ATD) and both regression methods. The scaling laws are given using a confidence level of 95%.

Since the confidence intervals in the exponents (and in the constant) overlap each other, it appears that the scaling laws obtained using the  $L/H_{real}$  times and the  $L/H_{estimated}$  times are equivalent. Therefore, the ATD times generate scaling laws that are similar to the ones obtained using the times determined by the experts. This result is quite general since it does not apply only to the scaling laws obtained using the physical parameters  $n_e$ ,  $B_T$  and  $S$ . In order to justify this assertion, the scaling laws in Table 6.5 have been computed. They use the plasma quantities  $n_e$ ,  $B_T$  and  $q_{95}$  where  $q_{95}$  is the plasma safety factor at  $\text{PSI} = 0.95$ . Again, the confidence intervals of the exponents and the constant overlap each other.

One important topic that can be addressed using scaling laws is the difference between the clear signature transitions and the non-clear signature transitions. It is important to discover whether their difference is only a matter of the  $D_\alpha$  morphological shape or there are different underlying physical processes. To this end, scaling laws using OLS and Ridge Regression have been computed for two subsets of transitions, the ones with clear signatures and the ones with non-clear signatures. The scaling laws obtained using the ATD transition times have been compared to the ones obtained using the times given by the experts. The results, reported in Table 6.6, indicate that the two types of transitions are not governed by the same physical process and thus their scaling laws are different. This result holds for both times,

Location method	Scaling law	MSE
<b>Transitions with clear signature, Ridge Regression, k = 4</b>		
Experts	$P_\tau = 10^{2.10 \pm 0.08} \cdot n_e^{0.92 \pm 0.08} \cdot B_T^{0.25 \pm 0.09} \cdot S^{-1.15 \pm 0.10}$	2.819
ATD	$P_\tau = 10^{2.24 \pm 0.08} \cdot n_e^{0.98 \pm 0.07} \cdot B_T^{0.19 \pm 0.09} \cdot S^{-1.27 \pm 0.09}$	2.803
Experts	$P_\tau = 10^{1.39 \pm 0.07} \cdot n_e^{0.83 \pm 0.08} \cdot B_T^{0.26 \pm 0.09} \cdot q_{95}^{-0.18 \pm 0.10}$	2.890
ATD	$P_\tau = 10^{1.43 \pm 0.07} \cdot n_e^{0.87 \pm 0.08} \cdot B_T^{0.21 \pm 0.09} \cdot q_{95}^{-0.14 \pm 0.10}$	2.866
<b>Transitions with non-clear signature, Ridge Regression, k = 4</b>		
Experts	$P_\tau = 10^{0.81 \pm 0.12} \cdot n_e^{0.73 \pm 0.10} \cdot B_T^{0.50 \pm 0.13} \cdot S^{0.69 \pm 0.15}$	7.955
ATD	$P_\tau = 10^{0.84 \pm 0.10} \cdot n_e^{0.63 \pm 0.08} \cdot B_T^{0.55 \pm 0.13} \cdot S^{0.49 \pm 0.14}$	9.792
Experts	$P_\tau = 10^{1.27 \pm 0.11} \cdot n_e^{0.71 \pm 0.10} \cdot B_T^{0.53 \pm 0.13} \cdot q_{95}^{-0.12 \pm 0.13}$	8.012
ATD	$P_\tau = 10^{1.20 \pm 0.09} \cdot n_e^{0.62 \pm 0.08} \cdot B_T^{0.56 \pm 0.13} \cdot q_{95}^{-0.11 \pm 0.13}$	9.825

Table 6.6: Comparison of the JET scaling laws obtained using clear and non-clear signature transitions

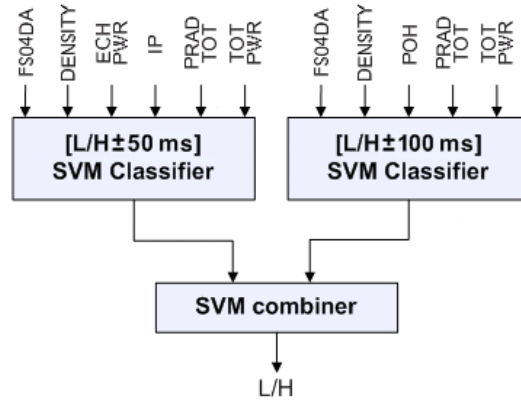


Figure 6.16: DIII-D two-layer L/H model

the ATD times and the ones given by experts.

It has been observed that the pulses with clear signatures correspond to plasmas that transit abruptly into type-I ELM phases. In contrast, in the pulses with non-clear signatures, the plasma remains in a type-III ELM phase before accessing the type-I regime. These results must be checked using a specific database chosen to this end.

### 6.1.3 Location of L/H transitions in DIII-D

The ATD methodology can be applied to different fusion devices with minor changes. (Farias et al., 2012) describes the application of the ATD in DIII-D (see Section 2.3.3).

The model described in Section 6.1.1.3 was adapted to the DIII-D data-

Signal	Original Quantities		Normalised Quantities	
	$C_i$	$B_j$	$C_i$	$B_j$
	$\pm 50$ ms	$\pm 100$ ms	$\pm 50$ ms	$\pm 100$ ms
FS04DA	$-1.65 \cdot 10^{-15}$	$-5.67 \cdot 10^{-17}$	-23.51	-14.28
DENSITY	$4.89 \cdot 10^{-13}$	$-5.09 \cdot 10^{-12}$	19.32	20.19
PRAD TOT	$-5.01 \cdot 10^{-6}$	$-3.28 \cdot 10^{-6}$	-12.21	-8.35
TOT PWR	$-4.29 \cdot 10^{-7}$	$4.14 \cdot 10^{-7}$	5.38	4.97
POH	–	$-1.14 \cdot 10^{-5}$	–	-12.33
ECH PWR	$-2.61 \cdot 10^{-7}$	–	-0.90	–
IP	$3.49 \cdot 10^{-7}$	–	0.37	–
bias	$6.29 \cdot 10^5$	50.60	3.53	1.73

Table 6.7: DIII-D coefficients of the first layer hyperplanes

base. A new SVM feature extraction process (González et al., 2010b) was carried out using a large set of 35 features. In this case, the models of the first layer were trained using intervals of  $\pm 50$  ms and  $\pm 100$  ms around the transition times. The second layer of the model was similar to the one used in the model of JET (it uses the outputs of the first layer classifiers to give a single prediction). Figure 6.16 shows the two-layer model and the signals used by each one of the classifiers. The description of the signals used by the models can be found in Appendix I.

The ATD methodology was tested using a database of 354 DIII-D pulses. The *discrimination loop* (Section 6.1.1.2) identified 291 clear signature transition. A L/H model was trained using these transition. The clear signature transitions were validated using this model (Section 6.1.1.5) and 12 transitions were removed from this set. Summarising, 279 clear signature transitions and 75 non-clear signature transitions were found.

The set of 279 was used to train a two-layer L/H model. As in the JET case, the models were trained using linear kernels. Table 6.7 describes the  $\pm 50$  ms ( $D_1$ ) and the  $\pm 100$  ms ( $D_2$ ) models obtained. The equation of the SVM combiner in the second layer of the model (Equation 6.5) was:

$$D(u, v) = -677.02 \cdot D_1(u) + 10.29 \cdot D_2(v) + 280.73 \quad (6.12)$$

Using normalised distances ( $0 < D_1(u) < 1$ ,  $0 < D_2(v) < 1$ ), the hyperplane equation was:

$$D(u, v) = 18.67 \cdot D_1(u) + 7.44 \cdot D_2(v) - 12.46 \quad (6.13)$$

It means that the  $\pm 50$  ms classifier was more relevant than the  $\pm 100$  ms classifier.

This model was applied to estimate the transition times of the non-clear signature transitions. The rate of properly located transitions ( $L/H_{real}$

within the PCI) was 95.6%. The mean error in the estimation of the transition times was 6 ms and the standard deviation was 49 ms.

The design of the ATD in DIII-D was carried out by means of a collaborative distributed environment. Since the computation of the models requires high performance computing, it was performed in the CIEMAT computer cluster EULER (Acero et al., 2009). The location of the L/H transition in new pulses was carried out in the DIII-D site. This step can be executed in an unattended manner after each pulse and therefore the models can be retrained with the new data.

#### 6.1.4 Discussion

The ATD is a novel methodology to determine L/H transition times in a completely automated way. The ATD can be used to create large databases of L/H transition times (the larger the database the more reliable the results) that can be used for several purposes, for example, L/H transition physics analysis, validation of L/H theoretical models or creation of L/H scaling laws. The ATD can be executed in an unattended way after every discharge to automatically include the new transition time in the transition times database.

According to their signature type, two different transitions can be found in JET and DIII-D: clear signature transitions and non-clear signature transitions. The first ones can be located by means of visual analysis using the  $D_\alpha$  signal and the plasma density. Approximately, 25% of JET discharges show clear signatures. In contrast, 80% of DIII-D transitions show this type of signature. The transition times of the non-clear signature transitions have been estimated using machine learning techniques (a L/H model was trained using the data of the clear signature transitions). The main difference of the ATD from previous methods is the complete absence of human intervention in the process (the ATD does not require a database of L/H transition times located previously).

In order to prove the quality of the transition times determined by the ATD, scaling laws for the input power were derived using the times determined by experts and the times determined by the ATD in JET. Two different regression methods were applied: OLS and Ridge Regression. The scaling laws were computed using different plasma quantities. For all the cases, the differences between the obtained scaling laws were not statistically significant, showing that the ATD can identify the transition times with accuracy good enough to derive the same scaling laws one would obtain with the times located by the experts (Tables 6.4 and 6.5).

The availability of several accurately determined transitions allows performing some more refined statistical test. It was found that the two types of transitions identified (the clear signature transitions leading directly to H-

mode and the non-clear transitions showing an intermediate type-III phase after the confinement change) present a different scaling law for the power threshold (Table 6.6). It must be confirmed in the future using a specific database conceived for this type of studies.

By choosing an appropriated reliability threshold, it is possible to determine a time interval (PCI) where the L/H transition is located. Conformal Predictors (CP) were chosen to generate reliability values. In this case, reliability is computed as the product of confidence and credibility. Since an off-line version of CP was used, the determination of the PCI was independent of the pulses order.

The length of the PCI is linked to the operational management of the pulses. As the plasma evolves from L-mode to H-mode, the confinement mode prediction (L or H) moves from a highly reliable L-mode (no enough power has been injected into the plasma and thus it is clearly in L-mode) to a low-reliability L-mode (the power injected into the plasma is reaching  $P_\tau$ , the threshold needed for the confinement transition). At a certain time, the classifier starts to predict H-mode (with low reliability). Reliability increases as plasma penetrates in H-mode. The transition process takes a certain time, in which the plasma moves from L-mode to H-mode, crossing an intermediate state during a variable period of time. The PCI represents this period and its length is not arbitrary and it is related to the manner in which the input power is injected into the plasma.

Figure 6.17 depicts the relationship between the PCI and the power injected into the plasma in four JET pulses. In Figures 6.17a, 6.17b and 6.17c, the power injected is lower than  $P_\tau$ , but high enough to bring the plasma closer to H-mode. As a consequence, the prediction of the ATD approaches the border between L-mode and H-mode and the reliability decreases. When additional power is injected into the plasma, the L/H transition occurs and the reliability increases fast. It leads to large PCIs (in pulse 76049, the PCI is larger than 200 ms and in pulses 74804 and 74802, the PCIs are larger than 300 ms). In contrast, Figure 6.17d shows a JET pulse where the input power is larger than  $P_\tau$  and it is injected in a single step. It leads to a fast transition between L-mode and H-mode. As a consequence, the PCI length (104 ms) is shorter than the previous ones.

This interpretation of the PCI as an interval in which the transition takes place with a certain probability and its relation with the plasma input power is confirmed by the following observations:

1. The level of reliability of the plasma confinement prediction starts to decrease in a monotonic way.
2. A minimum level is maintained during certain time.
3. The level of reliability begins to increase also in a monotonic way up to high values.

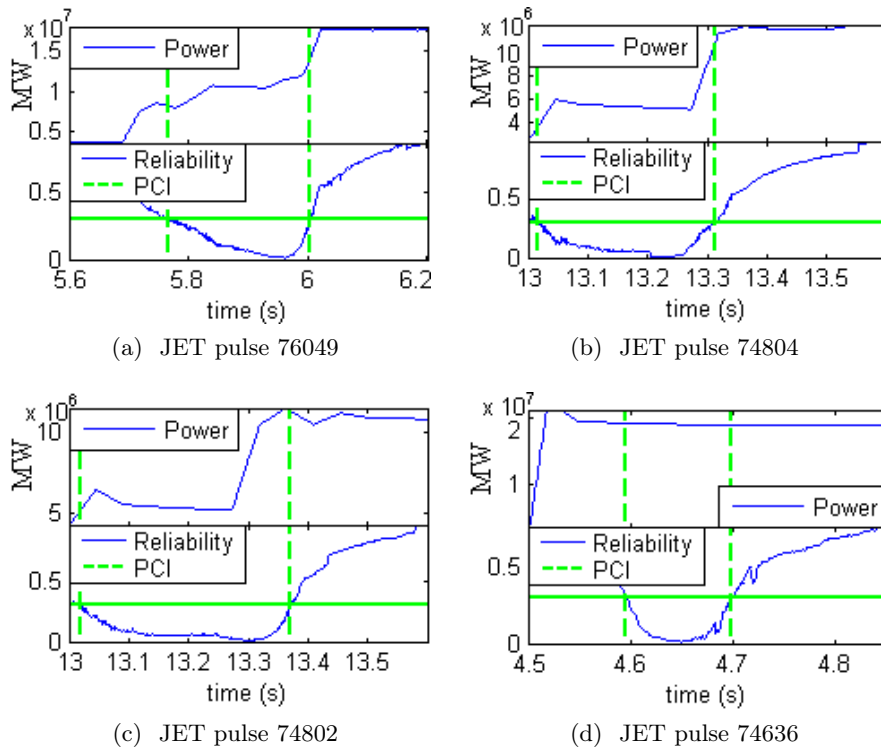


Figure 6.17: Relation of the uncertainty interval lengths and the input power

The ATD assumes that ELMs appear in all the plasma discharges that reach H-mode. As a consequence, the right border of the LHTI can be easily located using the time of the first ELM in the pulse. However, the ATD can be applied to fusion devices where there may be an H-mode without ELMs. It is possible to distinguish two cases:

- **There are pulses with an ELMy phase:** the system can identify the L/H transition in the pulses with ELMs and once the model has been trained using these pulses, it can be applied to identify the L/H transition in the pulses without ELMs.
- **There are no pulses with an ELMy phase:** since the identification of the LHTI is a rough approximation to the location of the L/H transition time, an alternative method to determine this interval can be devised and all the remaining methodology would be kept unchanged.

## 6.2 Data-driven models of L/H and H/L transitions using Conformal Predictors

A different approach to determine the plasma confinement regime consists in the creation of a L/H model using a database of L/H transition times previously determined by experts. Then, the model is applied to predict the plasma confinement in new pulses.

One of the first approaches to the identification of the plasma confinement was introduced by Martin (Martin and Bühlmann, 1998). It applied discriminant analysis to identify the confinement regime in TCV (Tokamak à Configuration Variable). Although it was trained using time slices from 670 TCV pulses, it obtained very high failure rates (between 30% and 40%).

A later approach to regime identification in ASDEX Upgrade was carried out by Giannone (Giannone et al., 2004). In this case two different discriminant analyses were compared: frequentist and formal Bayesian discriminant analysis. It used time slices from almost 1,000 discharges but only the representative ones were included in the training set. The time slices' length was 20 ms and therefore, its highest resolution was 20 ms. The training set contained 2,383 H-mode and 634 L-mode observations. The lowest failure rate was reached when using all the data in the training set (1.29%). It was pointed out that similar failure rates were obtained using 60% of the observations for training and the remaining observations for test.

In JET, many different approaches have been tested. Murari used fuzzy logic and SVM to identify the state of the plasma (Murari et al., 2006). In this case, the models were not training using time slices but single instants. They worked with a reduced database of JET pulses (25 pulses for the fuzzy model and 27 pulses for the SVM model). The success rates obtained by the models were high: 95.77% for the test set in the case of SVM and 95.7% in the case of the fuzzy model. Vega combined Bayesian analysis and SVM by means of a fuzzy operator (Vega et al., 2009b), (Vega et al., 2010c). The method was applied to a small database of 42 JET L/H transitions (33 training and 9 test) and 38 JET H/L transitions (30 training and 8 test). An interval of 2 s around the transitions was classified using the combined predictor, obtaining very high success rates: 99.22% for the L/H transitions and 96.31% for the H/L transition. Meakins applied neural networks to infer the confinement mode using plasma quantities (Meakins et al., 2010). This approach was tested using a database of 67 JET pulses. The training set contained 7,500 samples (3,896 L-mode and 3,604 H-mode) and the test set contained 11,600 samples (6,314 L-mode and 5,286 H-mode). The success rate was 98.86%. Finally, Ruiz described a real time system to determine the plasma confinement mode using the ITMS platform (Ruiz et al., 2010). They used a SVM model to analyse the plasma confinement.

This section describes the application of a different method to build L/H

	Linear kernel	RBF kernel
<b>L/H<sub>model</sub></b>		
Confidence mean value	99.86%	99.84%
Credibility mean value	64.10%	66.85%
mean( $ L/H_{real} - L/H_{estimated} $ )	22 ms	15 ms
mean( $ H/L_{real} - H/L_{estimated} $ )	236 ms	203 ms
<b>H/L<sub>model</sub></b>		
Confidence mean value	97.02%	97.53%
Credibility mean value	73.25%	73.77%
mean( $ L/H_{real} - L/H_{estimated} $ )	28 ms	33 ms
mean( $ H/L_{real} - H/L_{estimated} $ )	102 ms	106 ms

Table 6.8: L/H &amp; H/L experiments' results summary

models: CP (see Section 3.1.2). CP was applied to predict L/H and H/L transitions in JET using a database of 355 pulses and thus, increasing the statistical relevance of previous works (González et al., 2012b). CP give measures of confidence and credibility for each prediction (conformal measures).

### 6.2.1 Experiment's set-up

A initial database of 355 JET pulses was analysed by experts in order to locate the times of the L/H and H/L transitions. It was split into a training set containing 100 pulses (80 proper training set and 20 calibration set) and a test set (255 pulses). The pulses were randomly assigned to one of the sets.

Two different models were considered: a L/H model ( $L/H_{model}$ ) trained using L/H transition times and a H/L model ( $H/L_{model}$ ) trained using H/L transition times. The models were trained using 11 features selected from a set of 28 plasma signals (González et al., 2010b). These signals were the same ones that were used by the  $\pm 100$  model of the ATD methodology (see Section 6.1.1.3) and can be found in Appendix H.

The models were trained using the ICP, the inductive version of CP (see Section 3.1.2.1. Two different types of kernels were tested: linear (Eq. 3.25) and RBF (Eq. 3.27). 5 different values of the regularization parameter  $C$  ([100, 500, 1000, 2000, 3000]) were tested for the linear kernel. For the RBF kernel, all the combinations of 21 values of the  $C$  ([100, 500, 1000, 1500, ... 10000]) parameter and 21 values of the  $\sigma$  parameter ([0.1, 0.5, 1, 1.5, ..., 10]) were tested (441 combinations). The models were trained using an interval of  $\pm 0.5$  s (1 s intervals) around the L/H and H/L transitions.

### 6.2.2 L/H & H/L models' results

The SVM models were applied to the prediction of the L/H and H/L transition times of the pulses in the test set. Both models ( $L/H_{model}$  and  $H/L_{model}$ ) were used to locate both types of transitions (L/H and H/L). The performance of the models was measured using the absolute mean difference between the transition times determined by the experts ( $L/H_{real}$  and  $H/L_{real}$ ) and the transition times estimated by the models ( $L/H_{estimated}$  and  $H/L_{estimated}$ ).

Using the linear kernel, the best results were achieved using  $C = 100$ . In the case of the RBF kernel, the parameters  $C = 5500$  and  $\sigma = 3$  obtained the best performance.

Table 6.8 shows the results obtained in the experiment. The  $L/H_{model}$  and the  $H/L_{model}$  were used to estimate the L/H transition times. The absolute mean errors of the  $L/H_{model}$  were 22 ms (linear kernel) and 15 ms (RBF kernel) and the ones of the  $H/L_{model}$  were 28 ms (linear kernel) and 33 ms (RBF kernel).

The H/L transition times of the pulses were also estimated using both models. The absolute mean errors of the  $L/H_{model}$  were 236 ms (linear kernel) and 203 ms (RBF kernel). In the case of the  $H/L_{model}$ , the errors were 102 ms (linear kernel) and 106 ms (RBF kernel).

Conformal measures give key information about the accuracy and reliability of their predictions. Table 6.8 includes the mean values of confidence and credibility of the test pulses (using the whole time interval where all the signals are sampled). It can be seen that the mean credibility values of the  $H/L_{model}$  were significantly larger than the ones obtained by the  $L/H_{model}$  (73.25% versus 64.10% for the linear kernel and 73.77% versus 66.85% for the RBF kernel). It meant that the training data used for the  $H/L_{model}$  were more suitable to make predictions. As a result, the errors of the  $H/L_{model}$  in the predictions of the H/L transition times decreased by a factor of 2 comparing to the errors of the  $L/H_{model}$  while the errors in the predictions of the L/H transitions were a few milliseconds worse.

### 6.2.3 Discussion

On estimating a transition time (L/H or H/L), the models trained using this transition obtained better results than the models trained using the opposite transition. For example, the linear kernel  $L/H_{model}$  obtained an absolute mean error of 22 ms estimating L/H transition times while the linear  $H/L_{model}$  obtained 28 ms. On estimating the H/L transition times, the linear  $L/H_{model}$  obtained an absolute mean error of 236 ms while the linear  $H/L_{model}$  obtained 102 ms. This was a consequence, among others, of the difference in the trajectories of the L/H and H/L transitions (Meakins et al., 2010). The trajectory of the plasma in the feature space is not the same

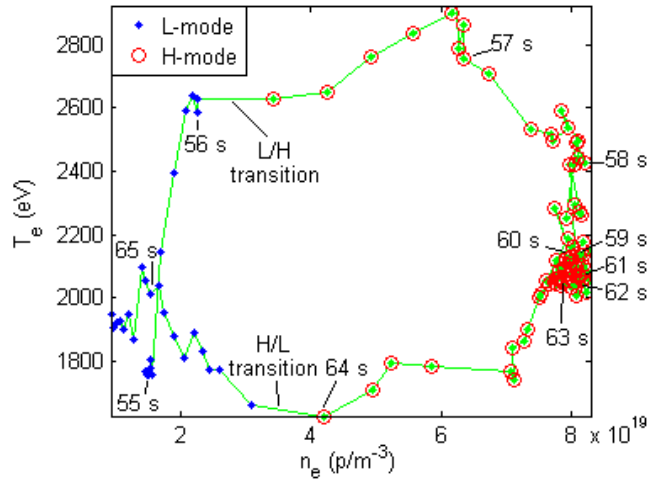


Figure 6.18: Pulse trajectory for L/H and H/L transitions in  $T_e$  and  $n_e$ , JET pulse 74323

for the L/H and H/L transitions. Figure 6.18 illustrates the trajectory of the JET pulse 74323 in the space  $T_e$  (plasma electron temperature) and  $n_e$  (plasma density). It is possible to observe that the L/H and H/L transitions take place in different points of the space and hence, it makes difficult to estimated a transition time using a model trained using the opposite transition.

It is also worth mentioning that the errors obtained in the determination of the H/L transition times were higher than the ones achieved in the determination of the L/H transition times. This was partially a consequence of the uncertainties in the location of the H/L transition times by the experts.

### 6.3 Conclusions

H-mode and the advanced operating confinement modes are key features to obtain a fusion power plant. Without them, it would be difficult to reach the high Q operating regime needed in ITER and other future fusion devices. The parameter  $P_\tau$  (the power required to access H-mode) of these devices is estimated using scaling laws. These laws use the data from existing fusion machines to predict the power that will be needed to access H-mode.

The L/H transitions are traditionally located by means of visual analysis. The first step consists in the location of an abrupt fall of the  $D_\alpha$  signal at the beginning of the pulse. Then, this tentative time is checked using the plasma edge density and the temperature profile.

The automated ATD methodology introduced in this chapter locates the L/H transitions in a set of pulses without human intervention. It is important

to note that it does not require a database of L/H transitions previously located by experts. The ATD methodology is quite general and it has been applied to the location of L/H transition in two of the biggest fusion devices with minor changes: JET and DIII-D.

The ATD distinguishes two types of L/H transitions:

- **Clear signature transitions (Figure 6.9a):** they show a clear drop in the  $D_\alpha$  signal. The transition time can be determined using the wavelet detail coefficients. The success rate on locating these pulses is 100% with an uncertainty interval of  $\pm 3.2$  ms. Approximately 25% of the JET discharges and 80% of the DIII-D pulses show clear signature transitions.
- **Non-clear signature transitions (Figure 6.9b):** the drop of the  $D_\alpha$  signal is difficult to distinguish from noise or type III ELMs, or it does not appear at all. In this case, a model trained using the previously located transitions is used to estimate the transition time. The success rate on locating these transitions is 96.83% in JET and 95.6% in DIII-D. The uncertainty interval around the predicted transition is given by conformal predictors. In JET, the mean length of this interval is 225.2 ms in the case of the properly located transitions and 453.5 ms if the transitions are not properly located.

The results obtained by the ATD have been checked using scaling laws. The laws obtained using the transition times given by the ATD are statistically similar to the ones obtained using the times given by experts. It has been shown for two different sets of explanatory variables and two regression methods. The differences in the scaling laws of the clear signature and the non-clear signature transitions point out that their access to H-mode is different. The clear signature transitions lead to type-I ELM phases while the non-clear signature transitions remains in a type-III ELM mode before accessing the type-I regime.

Using the L/H transition times determined by the ATD, it is possible to compute scaling laws to predict the power required to access H-mode in future fusion devices such as ITER. The accuracy and the statistical weight of the scaling laws increase with the number of pulses that are used to compute them. As a result, the ATD becomes a valuable tool of data analysis.

Data-driven models are a different approach to the location of transitions. They require a database of transitions located by experts that is used to build an explanatory model. Different ICP models have been trained using linear and RBF kernels. Conformal measures have shown their validity to assess the models' performance. The higher credibility level obtained by the models trained using the H/L transition points out that these models are more suitable to classify new discharges than the ones trained using L/H transitions.

---

The different trajectories of the L/H and H/L transitions in the feature space (Figure 6.18) must be taken into consideration when a plasma confinement model is under design. The trajectory that the plasma follows during the L/H transition might be different to the one that it follows during the H/L transitions. It makes the  $H/L_{model}$  results worse than the  $L/H_{model}$  ones on locating L/H transitions and the  $L/H_{model}$  results worse than the  $H/L_{model}$  ones on determining H/L transitions.



## Chapter 7

# Conclusions & Future Work

### Conclusions

This thesis attempts to solve one of the main issues of fusion by magnetic confinement: the automated analysis of the data generated in fusion devices. The growth of the data retrieved by the different plasma diagnostics and the new ones (such as cameras) developed and installed in the last few years make the visual analysis of the data unfeasible.

The identification of plasma phenomena is carried out through the identification of similar patterns in the data collected by the diagnostics. Due to the complexity of fusion databases, existing data mining and artificial intelligence techniques have problems dealing with fusion data. As a consequence, this thesis has developed a set of techniques with a general scope that are able to handle fusion data.

Firstly, UMEL has been described. It is a powerful tool to automatically locate relevant events in both waveforms and images. The design of automated methods for event location in plasma fusion requires the knowledge of experts. Expert systems (the combination of artificial intelligence and expert knowledge) are a successful option to locate events in fusion databases. The location capabilities of UMEL have been combined with expert knowledge to locate:

- **Sawteeth:** they are recognised as peaks of the soft X-ray emission at different radii. UMEL automatises the location of sawteeth and the computation of the plasma diffusivity (Vega et al., 2010a).
- **Disruptions:** a simultaneous peak of the loop voltage and a drop of the plasma current reveal the existence of a disruption. The disruptions located by UMEL can be classified using existing pattern recognition methods. The expert system created to locate JET disruptions obtained a success rate of 99.02% (Vega et al., 2010a). The located disruptions will be used by scientists with three different purposes:

- Increase the knowledge of disruptions and the statistical weight of future studies.
  - Mitigate their consequences.
  - Predict them before their occurrence.
- **ELMs:** ELMs appear in plasma waveforms as peaks of the  $D_\alpha$  signal accompanied by drops of the diamagnetic energy. These events are identified using UMEL. The ELMs locator obtained a success rate of 95% in the location of ELMs in the JET database. The study of a database of more than 226,000 ELMs revealed that the most common frequency of ELMs in JET is between 0.02 and 0.03 s (González et al., 2010a). This location method will help scientists to:
    - Increase the knowledge of ELMs and the statistical weight of future studies.
    - Mitigate the consequences of ELMs on the PFCs and the divertor.
    - Study the effects of different plasma configurations in ELMs. In particular, the temperature profile during ELMs in the JET carbon wall campaigns was analysed (González et al., 2012c).

In addition, UMEL has shown its usefulness in the analysis of plasma images and films (González et al., 2010):

- **Images:** it has been shown that the most relevant areas of an image contain high intensity gradients between neighbouring pixels. UMEL locates these gradients and therefore the relevant areas. The activity of these areas can be summarised using heat maps. Using them, scientist can analysed the different phases of the plasma during a pulse.
- **Films:** using the number of support vectors retrieved by UMEL, it is possible to locate the frames where events take place. Hot spots were detected in 10 JET infrared films, obtaining a success rate of 91.64%. Using this method, scientists will be able to analyse, for example, the heat load on the PFCs after each hot spot.

Secondly, the high dimensionality of fusion databases makes essential the use of feature selection and dimensionality reduction techniques. This thesis develops two different methods for two data types:

- **High-dimensional spaces:** it has been demonstrated that a linear separating hyperplane can be used to select a suitable group of features to classify a set of samples. This technique (dubbed SVM-FES) was applied to choose a set of features to classify L & H mode samples (González et al., 2010b). The initial feature space was made up of 28 signals. Two different time windows were considered:

- **±100 ms:** the classification success rate of the original feature space was 94.252% (using 28 signals). The feature space was reduced to 11 signals obtaining a success rate of 93.404% (only 0.848% less than the original feature space).
- **±500 ms:** the initial space obtained a success rate of 98.026% (28 signals). It was reduced to 5 signals obtaining a classification success rate of 97.436% (only 0.590% less).

Using these models, the following goals have been reached:

- Two successful L/H models have been built. In addition, a combined L/H classifier have been built using the outputs of these models.
  - The importance of the features at different distances of the L/H transitions has been studied. It was found that the classification of L/H points far from the transition is almost a linearly separable problem but it became non-separable close to the transition.
- **Images:** RSIC is a novel methodology that has shown its value to reduce the dimensionality of images in a classification task. Given a set of images that belong to two or more classes, RSIC is able to locate the most suitable regions to classify the images. It uses a non-conformity measure to evaluate the performance of the regions. In the experiment carried out using 1,272 TJ-II Thomson scattering images, the images were reduced to 16.49% of their original size obtaining a classification success rate of 95.27% versus 96.37% using the entire images (only 1.10% less). In addition, the training, calibration and test times were reduced 93.97%, 81.55% and 81.82% respectively (González et al., 2012d). The main advantages of RSIC are:
    - The reduction of the images' dimension. It shrinks the CPU time and the storage space.
    - The identification of ROIs. It helps to understand the structure of the images.

And finally, an analysis of L/H and H/L transitions has been accomplished. On the one hand, an automated locator of L/H transitions (ATD) has been described. It is a novel technique to locate L/H transitions in plasma waveforms that was successfully applied to two fusion devices, JET (González et al., 2012a) and DIII-D (Farias et al., 2012), with minor changes. The development of the ATD has revealed the existence of two different types of L/H transitions:

- **Clear signature transitions:** they are characterised by an unambiguous drop of the  $D_\alpha$  signal. They lead to type-I ELM phases.

In JET and DIII-D, all the clear signature transitions were properly located by the ATD.

- **Non-clear signature transitions:** there is not such a clear drop of the  $D_\alpha$  signal and they are followed by a type-III ELMy mode before accessing the type-I regime. In JET, 96.83% of the non-clear signature transitions were properly classified versus 95.60% in DIII-D.

Using scaling laws, it has been demonstrated that the access to H-mode is different in both transition types and the results given by the ATD have been validated. It has also been found that the length of the PCI (the probability confidence interval) is linked to the way in which the power is injected into the plasma: when it is injected abruptly, the PCI is short ( $\approx 200$ -300 ms) but if the power is injected slowly into the plasma, the PCI is longer.

The automatic location of L/H transitions is specially relevant for fusion science in two aspects:

- The automatic located transitions will increase the statistical significance of future studies.
- These transitions will be used to compute scaling laws for the power required to access H-mode in future fusion devices such as ITER.

On the other hand, CP was used to create L/H and H/L data-driven models. Using the conformal measures, it was found that the models trained using H/L transitions are more suitable to evaluate the confinement mode than the models trained using L/H transitions (González et al., 2012b).

## Future Work

This thesis has raised some interesting points that should be addressed in the future:

- Location of different plasma phenomena using UMEL: this thesis has described the application of UMEL to locate ELMs, disruptions and sawteeth in waveforms and hot spots in infrared films but there are more plasma phenomena that can be located using UMEL. For example, pellets can be tracked in films and the existence of magnetic islands or tearing modes in waveforms.
- The analysis of the temperature profile during ELMs described in Section 4.1.4 is focused in 2 ms after the ELMs. It can be easily extended to study the complete evolution of the profile from the ELM time to the time when the edge temperature gradient is completely recovered. The degradation value can be given for each instant after the ELM. In addition, the JET's new vacuum vessel wall (ITER-like wall) provides

a new opportunity to measure the degradation of the temperature gradient during ELMs under new conditions.

- The analysis of the complexity of the SVM-FES models may be done using only SVs and not SVs plus errors: the feature extractor described in Section 5.1 estimate the complexity of the models using the number of SVs. These SVs include the samples that are misclassified. In order to perform a more accurate study of the complexity, the number of errors could be subtracted from the total number of SVs.
- Regarding the RSIC methodology described in Section 5.2.1, it uses only one region per each class. It is possible that, for very complex classification problems, several regions would be needed. The performance of the system if more than one region per class is chosen should be tested.
- The ATD methodology described in Section 6.1 can be applied to locate L/H transition in the new JET pulses with the ITER-like wall. In addition, a careful analysis of the two types of L/H transitions detected (clear and non-clear signature) should be done using a specific database. It is worth studying the access to H-mode in both types of transitions because it is a key point for ITER.



## Part II

# Resumen en español



## Chapter 8

# Introducción

Plasma es el cuarto estado de la materia (líquido, sólido, gaseoso y plasma). Se trata de un gas ionizado casi neutral en el que los iones y los electrones se mueven independientemente. Si el plasma se calienta lo suficiente (y se alcanzan las condiciones adecuadas), los átomos del plasma se fusionan creando átomos más pesados y liberando energía. Este proceso es conocido como fusión del plasma.

La fusión del plasma es una prometedora fuente de energía limpia. Desafortunadamente, la tecnología necesaria para producir energía de fusión barata y segura está todavía en desarrollo. Existen dos alternativas para obtener energía por fusión del plasma:

1. **Fusión por confinamiento magnético:** el plasma se aísla por un campo magnético dentro de una cámara de vacío. Entonces, se calienta hasta que alcanza condiciones termonucleares y los átomos se fusionan. Esta tesis está centrada en el análisis de los datos generados por máquinas de fusión por confinamiento magnético.
2. **Fusión por confinamiento inercial:** pequeñas bolas de combustible (del tamaño de la cabeza de un alfiler) se calientan y comprimen mediante haces láser. Los átomos del combustible (habitualmente deuterio y tritio) se fusionan liberando energía.

Multitud de diagnósticos diferentes monitorizan el estado del plasma durante la operación. Estos diagnósticos generan señales e imágenes que deben ser evaluadas por expertos. A medida que los diagnósticos han mejorado su rendimiento en los últimos años, la cantidad de información generada ha crecido exponencialmente. Ya no es posible para los expertos examinar los datos a través de su visualización.

El análisis de los datos producidos en las máquinas de fusión por confinamiento magnético se ha convertido en un problema de “big numbers” (grandes números). Las técnicas de minería de datos e inteligencia artifi-

cial deben jugar un papel relevante en el análisis de la información en los próximos años. Las principales ventajas de estas técnicas son:

- **Precisión:** la precisión obtenida por estos métodos difícilmente puede ser igualada por humanos.
- **Rapidez:** la mayoría de estas técnicas están diseñadas para trabajar con grandes conjuntos de datos y pueden ser paralelizadas. Sus resultados pueden estar disponibles poco después de cada pulso de plasma.
- **Coste:** a pesar de que el coste inicial de una aplicación que use minería de datos o inteligencia artificial pueda ser caro, estas técnicas requieren poco mantenimiento y pueden ser ejecutadas miles de veces sin coste adicional.
- **Libres de errores humanos:** esto no significa que estas técnicas no contengan errores sino que están libres de los errores producidos por descuidos o despistes.

Por otro lado, presentan las siguientes desventajas:

- **Complejidad de las bases de datos de fusión:** el gran número de diferentes fenómenos del plasma que tienen lugar en las máquinas de fusión y sus correlaciones dificultan la aplicación de estos métodos.
- **Conocimiento experto:** la mayoría de estas aplicaciones requieren conocimiento experto durante su desarrollo y ejecución. A veces, es complicado obtener el conocimiento requerido de los expertos.
- **Resistencia al cambio:** la información ha sido analizada visualmente desde el comienzo de la investigación de la fusión del plasma. La introducción de una nueva herramienta de análisis de datos y validación puede encontrar la resistencia de los expertos que no estén familiarizados con estas nuevas técnicas.

## 8.1 Objetivos

El propósito de esta tesis es desarrollar un conjunto de técnicas de minería de datos e inteligencia artificial de ámbito general y después, aplicarlas a las bases de datos de fusión. Más concretamente, el contenido de la misma trata de:

- **Localizar eventos relevantes en señales:** uno de los aspectos más relevantes en fusión es la localización de fenómenos del plasma usando las formas de las señales. Antes de estudiar el comportamiento del

plasma es necesario localizar estos eventos. Actualmente, su localización se lleva a cabo manualmente por expertos. Esta tesis explica UMEL—un nuevo método de localización de fenómenos del plasma en señales (Vega et al., 2010a)—. Uno de los objetivos de UMEL era la localización automática de ELMs en JET (González et al., 2010a). Además, la localización automática de ELMs permitió el estudio de la degradación del gradiente de temperatura del borde del plasma durante su aparición (González et al., 2012c).

- **Localizar eventos relevantes en imágenes:** las cámaras son uno de los nuevos diagnósticos del plasma. Su utilidad radica en proporcionar una vista de la cámara de vacío durante los pulsos de plasma. Por ello, el análisis automático de las películas del plasma se ha convertido en un aspecto clave del análisis de las bases de datos de fusión. UMEL fué adaptado para localizar eventos en películas del plasma, proporcionando una poderosa herramienta para identificar, por ejemplo, puntos calientes en películas del infrarrojo (González et al., 2010).
- **Seleccionar las principales dimensiones en un espacio multidimensional:** muchos diagnósticos diferentes miden el estado del plasma durante un pulso. Algunas de las señales generadas por los diagnósticos no son informativas y, por lo tanto, las mejores señales / dimensiones para describir un fenómeno del plasma deben ser seleccionadas. Esta tesis presenta una novedosa técnica—SVM-FES—para seleccionar las mejores características en un problema de clasificación usando Máquinas de Vectores Soporte. Esta técnica se ha aplicado a la identificación de las mejores señales para describir las transiciones L/H en JET (González et al., 2010b) y DIII-D (Farias et al., 2012).
- **Seleccionar las principales características en imágenes:** en una imagen, no todos los píxeles contienen la misma cantidad de información. Dado que el procesado de imágenes es normalmente muy lento, debe centrarse en las regiones más informativas. Esta tesis desarrolla RSIC, una técnica para identificar las regiones más relevantes de una imagen usando una medida de no conformidad. Las imágenes del Thomson scattering del TJ-II han sido analizadas usando RSIC (González et al., 2012d).
- **Analizar las transiciones L/H:** el modo de alta energía es una característica fundamental para alcanzar un reactor de fusión comercial. La transición entre los modos de baja y alta energía (transición L/H) es, por lo tanto, uno de los fenómenos más relevantes en un pulso. Esta tesis describe una técnica automática para localizar transiciones L/H en señales del plasma. Esta técnica ha sido aplicada al JET (González et al., 2012a) y al DIII-D (Farias et al., 2012). Esta tesis también

pretende estudiar las transiciones L/H y H/L usando modelos guiados por datos (González et al., 2012b).

## 8.2 Contenidos

Este resumen está estructurado de la siguiente forma:

- El **Capítulo 9** revisa los principales conceptos de la fusión de plasmas por confinamiento magnético y explica porqué la fusión debería jugar un papel clave en el mercado energético futuro. Este capítulo incluye una introducción a la física de plasmas (Sección 9.1), una descripción de algunos de los principales fenómenos que tienen lugar en los dispositivos de fusión por confinamiento magnético (Sección 9.2), e información acerca de dispositivos de fusión actuales y futuros (Sección 9.3).
- El **Capítulo 10** introduce un localizador de eventos universal. Este localizador ha sido utilizado para localizar eventos en señales (Sección 10.1) e imágenes (Sección 10.2). Usando este método, se han buscado dientes de sierra, disrupciones y modos localizados del borde en señales y puntos calientes y regiones de interés en imágenes.
- El **Capítulo 11** describe dos técnicas de reducción de dimensionalidad: la primera está pensada para la selección de características en un espacio multi-dimensional (Sección 11.1) y la segunda extrae las regiones más importantes de un conjunto de imágenes (Sección 11.2). La primera de ellas se ha utilizado para encontrar las principales características de la transición L/H. Las imágenes del Thomson scattering se han analizado utilizando la segunda de ellas.
- El **Capítulo 12** se dedica al análisis de las transiciones L/H y H/L. La Sección 12.1 explica un localizador de transiciones L/H automático en señales del plasma. Este localizador ha sido aplicado con éxito en diferentes dispositivos de fusión. La Sección 12.2 describe el uso de predictores conformales para mejorar la clasificación del modo de confinamiento del plasma.
- Finalmente, el **Capítulo 13** analiza las conclusiones y el trabajo futuro de esta Tesis.

## Chapter 9

# Fusión Nuclear: una prometedora fuente de energía limpia

Desde el principio de la historia de la humanidad, ésta ha estado buscando oportunidades para mejorar sus condiciones de vida. Como cazadores y recolectores, los humanos dependían del medio ambiente para sobrevivir. El número de humanos estaba limitado por los recursos generados por la naturaleza (Malthus, 1798, la trampa Maltusiana). Más tarde, aproximadamente en el año 10,000 a.C. aprox., el desarrollo de la agricultura y la ganadería permitió a la humanidad producir sus propios recursos. Como resultado, la población mundial creció significativamente. Este hecho es conocido como Revolución Neolítica.

12,000 años después de la Revolución Neolítica, entre la mitad del siglo XVIII y la mitad del siglo XIX, Inglaterra acogió un conjunto de transformaciones en la ciencia, y especialmente en la tecnología que dispararon un espectacular aumento de la capacidad de producción. Fue la Revolución Industrial. De acuerdo con los datos de las Naciones Unidas (United Nations, 1999), en 1750, al comienzo de la Revolución Industrial, la población mundial era de 790 millones de personas. En 1990, era de 1,650 millones de personas. La población se dobló en tan solo 250 años debido a la mejora de las condiciones de vida.

Ambas revoluciones tienen un factor en común: el aumento de la energía disponible para la humanidad (Cipolla, 1972). En el Neolítico, las plantas y animales domésticos eran más productivos (eran más eficientes energéticamente) que los de la naturaleza. El incremento de producción permitió un incremento de la población estableciendo un nuevo límite para la trampa Maltusiana. En la Revolución Industrial, los combustibles fósiles permitieron el acceso a una nueva fuente de energía que pudo ser usada para generar trabajo. La trampa Maltusiana se rompió de nuevo y la población creció

rápidamente. Al final de 2011, la población mundial ha alcanzado los 7,000 millones de personas. La predicción de la población de las Naciones Unidas dice que para 2100 la población mundial será de 10,000 millones de personas (United Nations, 2010).

El mercado energético debe responder al crecimiento futuro de la población. Además, debe contestar al crecimiento de la demanda de energía proveniente del desarrollo de los países no-OCDE (Organización para la Cooperación y el Desarrollo Económico). De acuerdo con las previsiones del año 2011 de la Agencia Internacional de Energía (International Energy Agency, 2010, IEA), el consumo energético crecerá un 33% desde el año 2010 al 2035. Los países no-OCDE representarán un 90% de este crecimiento energético. China, India, Indonesia, Brasil y Oriente Medio son las regiones donde la demanda de energía crece más rápido. La demanda energética china crece un 2.1% al año y para el 2035, esta será un 70% mayor que la demanda en USA.

En 2010, el 81% de la mezcla energética era producida por combustibles fósiles. Sin nuevas políticas en producción energética y protección medioambiental, la temperatura media crecerá más de 6°C. A pesar de que el esfuerzo en el desarrollo de nuevas estrategias y tecnologías de producción de energía limpia es alto, los combustibles fósiles mantendrán el 74% de la producción global de energía en 2035 (y ésta será un 33% mayor que en 2010). La demanda de carbón y petróleo únicamente se reducirá en los países OCDE mientras que aumentará en el resto del mundo.

El incremento en el consumo de petróleo se deberá al desarrollo del sector transporte en los países no-OCDE y especialmente al incremento del número de coches. Los coches eléctricos e híbridos necesitarán tiempo para penetrar en los mercados mientras que el número de coches crecerá hasta los 1,700 millones en 2035 (casi el doble que en 2010). La demanda de petróleo saltará desde los 87 millones de barriles al día (mb/d) en 2010 hasta los 99 mb/d. Los coches eléctricos alcanzarán el 39% de las ventas en 2035.

En este contexto, las energías renovables deberían jugar un papel fundamental. Desafortunadamente, las previsiones no son lo suficientemente buenas. En el 2035, el uso de energía renovable aumentará considerablemente pero no será suficiente para responder al crecimiento de la demanda. Por regiones, la UE estará en la cabeza de la demanda de energía renovable primaria, seguida por USA y China. Los estudios indican que habrá una reducción en el precio de la electricidad generada por energía renovable (de Vries et al., 2007).

Otro aspecto importante a tener en consideración es la disponibilidad de recursos (World Energy Council, 2010). Por un lado, los combustibles fósiles tienen recursos limitados. La producción actual de los campos de petróleo ha alcanzado ya su máximo y los suministros para los próximos años dependerán de los campos todavía sin explotar y de los campos sin

descubrir. No se espera que los campos actualmente en uso duren más que hasta la mitad del siglo. Las fuentes de carbón se cree que durarán 100 años. Las reservas de uranio no son muy grandes pero los nuevos yacimientos se cree que podrían durar durante más de un milenio. La falta de recursos causará tensión entre diferentes países que buscarán energía barata para impulsar sus economías (World Energy Council, 2007). Por otro lado, las fuentes de energía renovables son ilimitadas pero tienen problemas como la velocidad de viento mínima o la disponibilidad de tierra, entre otras, que limitan su localización.

La humanidad está en la encrucijada entre la energía fósil y la renovable. Por un lado, la energía fósil garantiza una fuente de energía barata para unas pocas décadas comprometiendo el futuro de nuestro medio ambiente. Por otro lado, la energía renovable es una fuente ilimitada de energía que no pone en peligro el medio ambiente pero todavía no es capaz de alimentar completamente el mundo. Se espera que la fusión nuclear llene el vacío entre la energía renovable y una fuente de energía que pueda reemplazar a los combustibles fósiles.

La fusión nuclear es la fuente de energía de las estrellas. En los años 20, Sir Arthur Eddington propuso que las estrellas eran esferas de gas caliente, principalmente compuestas por hidrógeno (Eddington, 1926). La temperatura causada por la presión de las fuerzas gravitacionales convierte los gases en plasma. En 1927, Lewi Tonks and Irving Langmuir dieron el nombre de *plasma* a un gas ionizado casi neutral en los que los iones y los electrones se movían independientemente. La temperatura y la presión en las estrellas hacen posible que los átomos de hidrógeno en el plasma se fusionen liberando helio y energía.

La idea detrás de la fusión es usar la energía de las estrellas para generar electricidad. En el futuro, los reactores de fusión usarán tritio (un isótopo del hidrógeno que puede ser obtenido del litio) como combustible. El litio en la batería de un ordenador portátil podría generar 200,000 kWh de electricidad (tanto como 40 toneladas de carbón) suficiente para las necesidades de una persona durante toda su vida (McCracken and Stott, 2005, p. XV).

Otro factor importante a tener en consideración es la emisión de dióxido de carbono (en gramos) por kWh (Cg/kWh). La fusión es una de las fuentes de energía con una emisión específica de dióxido de carbono más baja (6-12 Cg/kWh) cerca de la hidroeléctrica (4.8 Cg/kWh) y los reactores de fisión nuclear (5.7 Cg/kWh). Las energías fotovoltaica (16 Cg/kWh) y eólica (33.7 Cg/kWh) también tienen emisiones de CO<sub>2</sub> bajas pero están penalizadas por sus procesos de fabricación. El petróleo (200 Cg/kWh) y el carbón (270 Cg/kWh) son las fuentes de energía más contaminantes (Kikuchi, 2011, p. 183).

Una importante ventaja de la fusión nuclear frente a la fisión nuclear es la seguridad de la fusión. Al contrario de la fisión, la fusión no ocurre de forma

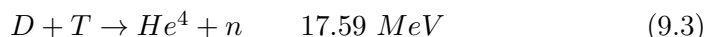
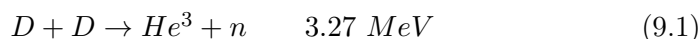
natural en la Tierra. Por lo tanto, en el caso de un accidente, la reacción de fusión se detendrá. Los estudios de la seguridad de las plantas de energía por fusión muestran que los costes asociados con un accidente están limitados por el bajo impacto radiológico del accidente (Schneider et al., 2001). La baja cantidad de radioactividad liberada a la atmósfera en el caso de un accidente no haría necesaria la evacuación de la población cercana. Además, parece que las prohibiciones en la comida en el caso de un accidente estarán limitadas a una pequeña región alrededor de la planta de energía (dentro de un radio menor de 10 km) durante unos días (menos de una semana) y solo para la leche y la carne de ternera. Por lo tanto, el coste de un accidente está limitado y varía desde 78 millones de € hasta 1,950 millones de € en el caso de aversión al riesgo. Una conclusión de los estudios de seguridad de las futuras plantas de energía por fusión es que es posible obtener una planta de energía de fusión segura y económicamente aceptable en la base de la física de plasmas y la tecnología que serán alcanzadas en los próximos años (Ward et al., 2001).

## 9.1 Una breve introducción a la física de plasmas

Cuando un gas se calienta lo suficiente, los electrones se separan de los átomos. Cuando todos los átomos han perdido sus electrones, se dice que el gas está completamente ionizado y es conocido como plasma, el cuarto estado de la materia. La física de plasmas es la ciencia que estudia el comportamiento del plasma. Existen diferentes tipos de plasma (por ejemplo plasma solar, plasma industrial, las señales de neón, los rayos, las llamas) que difieren en su densidad y temperatura.

Las estrellas obtienen su energía de procesos de fusión nuclear. Los átomos de hidrógeno se fusionan para formar helio, liberando  $6 \times 10^8$  MJ por kilogramo de hidrógeno, alrededor de 60 millones de veces la energía por kilogramo disponible de los combustibles químicos (Wesson, 2000, p. 2). Los elementos más pesados se forman por fusión de elementos más ligeros.

La mayoría de los estudios de fusión de plasmas empiezan con deuterio (D), tanto sólo como en una mezcla con el isótopo del hidrógeno más pesado, el tritio (T). Existen tres posibles reacciones (Wesson, 2000, p. 3):



donde H es un protón, n es un neutrón y  $He^4$  es una partícula  $\alpha$ .

La sección eficaz (la probabilidad de interacción entre partículas) de estas reacciones sólo se hace suficientemente grande para ser útil a altas energías. Si se espera que las reacciones nucleares requeridas sean generadas por la

velocidad térmica de los núcleos, sería necesario alcanzar temperaturas extremadamente altas

La Figura 2.1 (EFDA-JET<sup>©</sup>) muestra la sección eficaz de las reacciones de las Ecuaciones 9.1, 9.2 y 9.3. A una temperatura de  $100 \text{ keV}^1$ , la sección eficaz de la reacción D-T es mucho mayor que las de las reacciones D-D y D-He<sup>3</sup>.

En las estrellas, las partículas a alta temperatura son mantenidas juntas por la acción de la fuerza gravitacional creada por sus masas. Desafortunadamente, la fuerza gravitacional en la Tierra no es suficiente para evitar que las partículas se escapen por su velocidad térmica (la gravedad en el Sol es 27.9 veces más grande que en la Tierra). Entonces, la cuestión fue: ¿cómo reproducir / simular las condiciones de las estrellas en la Tierra? Además, si la temperatura de las partículas debía ser extremadamente alta, ¿cómo manejar las partículas a temperaturas decenas de veces mayores que la temperatura del Sol? Por ejemplo, la temperatura en el centro del Sol es de 15 millones K mientras que la temperatura en el centro del plasma en JET puede alcanzar los 200 millones K.

Las respuestas a estas preguntas llegó estudiando las propiedades del plasma. Dado que el plasma está formado por partículas con carga eléctrica, está sujeto a una fuerza magnética: la fuerza de Lorenz. Entonces, es posible reemplazar la fuerza gravitacional que atrapa las partículas en el Sol por un campo magnético en la Tierra. Cuando una partícula cargada es afectada por un campo magnético uniforme, su movimiento tiene dos partes:

1. Un movimiento circular perpendicular al campo magnético, donde el radio del círculo se denomina radio de Larmor (Figura 2.2a).
2. Un movimiento paralelo a lo largo del campo magnético (Figura 2.2b).

La Figura 2.2 (EFDA-JET<sup>©</sup>) muestra el movimiento de una partícula cargada a lo largo de un campo magnético uniforme. El movimiento compuesto de la partícula (Figura 2.2c) es helicoidal.

Una vez que el plasma está atrapado en un campo magnético, es necesario calentarlo hasta alcanzar condiciones termonucleares. La corriente toroidal inducida por el sistema toroidal de bobinas genera calentamiento óhmico. Desafortunadamente, la resistencia del plasma cae con el aumento de la temperatura y por lo tanto el calentamiento óhmico está auto-limitado. Usando solamente calentamiento óhmico, la temperatura del plasma está lejos de la temperatura necesaria para alcanzar una sección eficaz aceptable para las reacciones de fusión nuclear. Por ello, se propusieron varios métodos de calentamiento alternativos:

---

<sup>1</sup>Un  $eV$  es la energía que un electrón recibiría pasando a través de un potencia eléctrico de un voltio.  $1 \text{ eV} = 11,600 \text{ K}$  and  $10 \text{ keV} \approx 100 \text{ millones K}$

- **Inyección de un haz de neutros (NBI, por sus siglas en inglés):** haces de alta energía de iones de hidrógeno son inyectados en el plasma incrementando su temperatura. Las partículas inyectadas en el plasma deben ser átomos neutros puesto que no podrían cruzar el campo magnético alrededor del plasma de no ser así.
- **Calentamiento por radio-frecuencia (RF, por sus siglas en inglés):** se generan ondas electromagnéticas de alta frecuencia desde una antena montada en el interior de la cámara de vacío. El calentamiento RF incluye dos métodos diferentes:
  - **Calentamiento por resonancia Ión-Ciclotrón (ICRH, por sus siglas en inglés):** el sistema ICRH usa una frecuencia entre 23 MHz (longitud de onda  $\lambda = 13$  m) y 57 MHz ( $\lambda = 5$  m) resonante con el segundo armónico del deuterio o el primer armónico del tritio y el helio.
  - **Calentamiento por resonancia Electrón-Ciclotrón (ECRH, por sus siglas en inglés):** calienta sólo los electrones del plasma. Usa una frecuencia entre 140 GHz ( $\lambda = 2.136$  mm) y 170 GHz ( $\lambda = 1.759$  mm).
  - **Calentamiento por corriente híbrida (LHCD, por sus siglas en inglés):** el calentamiento LHCD usa una frecuencia de aprox. 3.7 GHz ( $\lambda = 0.1$  m) entre las frecuencias de los ciclotrones de los iones y los electrones.

## 9.2 Fenómenos del plasma

Desafortunadamente, la operación del plasma no es tranquila y diferentes eventos tienen lugar desde el principio hasta el final de un pulso. Algunos de estos eventos, como las transiciones L/H, ayudan a los científicos a alcanzar un mejor rendimiento del plasma, pero algunos de ellos, como las disrupciones, son dañinos y potencialmente peligrosos para la integridad de las máquinas de fusión y por lo tanto deben ser evitados.

Esta sección describe cuatro fenómenos del plasma que tienen un papel fundamental en esta tesis: los modos L & H, los modos localizados del borde, los dientes de sierra y las disrupciones

### 9.2.1 Modos L & H

Los modos L (de la sigla en inglés de modo de bajo confinamiento) y H (de la sigla en inglés de modo de alto confinamiento) son dos regímenes de confinamiento diferentes del plasma en máquinas de fusión. El modo H fue descubierto por Wagner en 1982 (Wagner et al., 1982). Durante el calentamiento del plasma en el tokamak ASDEX, mientras la válvula del gas

estaba cerrada, Wagner encontró que había un incremento de la densidad causado por una repentina mejora del confinamiento de las partículas. Este fenómeno era completamente inesperado dado que no había sido predicho por ninguno de los modelos teóricos. Por suerte, el equipo de Wagner pudo reproducir el experimento y, en los años siguientes, el modo H fue alcanzado en otros tokamaks, por ejemplo, PDX en 1984 (Kaye et al., 1984), DIII-D en 1986 (Burrell et al., 1987), JET en 1987 (Tanga et al., 1987) e incluso en stellerators como el W 7-AS in 1993.

Durante el modo H, el confinamiento del plasma mejora. Típicamente, la energía de confinamiento aumenta en un factor 2. En el borde del plasma, se produce un incremento de la densidad y la temperatura, elevando el gradiente de presión. Este gradiente en el borde se conoce como barrera de transporte del borde (ETB, por sus siglas en inglés) (Wagner et al., 1984). La diferencia de presión en el plasma causada por la ETB es conocida como *pedestal*. La Figura 2.3 (EFDA-JET<sup>©</sup>) muestra un diagrama de los modos L & H, la ETB y el pedestal. En el eje  $x$  se muestra el radio normalizado del plasma y en el eje  $y$  la presión del plasma. Cuando se crea la ETB, la presión del plasma se incrementa significativamente y el pedestal aparece cerca del borde del plasma.

La transición desde el modo L al modo H (transición L/H) requiere que el calentamiento esté por encima de un determinado umbral  $P_\tau$ . Se conoce que este umbral depende de la densidad del plasma, el campo magnético y el tamaño del plasma.  $P_\tau$  es un parámetro crucial en el diseño de los dispositivos de fusión del futuro, como ITER y DEMO. El parámetro  $P_\tau$  de ITER ha sido predicho usando leyes de escala calculadas por medio de un amplio rango de tokamaks actuales (Martin et al., 2008).

La transición L/H se caracteriza por una abrupta caída de la señal  $D_\alpha$  en el borde del plasma. La señal  $D_\alpha$  mide el reciclado de deuterio entre el plasma y las superficies colindantes. Por lo tanto, una abrupta caída de esta señal indica un descenso del reciclado (Wesson, 1987, p. 188). La caída de la  $D_\alpha$  está acompañada por un incremento de la pendiente de la densidad del plasma causado por la ETB. La Figura 2.4b muestra un ejemplo de la transición L/H del pulso 73336 de JET. La transición L/H tiene lugar en el instante 15.793 s. La Figura 2.4b incluye la señal  $D_\alpha$  (arriba) y la densidad en el borde del plasma (abajo). La caída característica de la señal  $D_\alpha$  tras la transición L/H puede ser claramente apreciada. En este momento, se produce también un incremento de la pendiente de la señal de densidad del plasma.

La evolución típica de un plasma de JET puede verse en la Figura 2.4a. Al comienzo de la figura (15 s), el plasma está en modo L (el calentamiento está por debajo del umbral  $P_\tau$ ). Los sistemas de calentamiento NBI e ICRH funcionan desde 15.459 s hasta 23.805 s. Poco tiempo después de que el calentamiento esté por encima del umbral  $P_\tau$ , tiene lugar la transición L/H

y el plasma entra en modo H (segmento temporal gris). El plasma continua en modo H hasta que el calentamiento para. Entonces, poco tiempo después, el plasma vuelve a modo L (transición H/L, tiempo  $\approx 24.089$  s).

A pesar de que las ventajas del modo H son extremadamente importantes para alcanzar un reactor de fusión, también tiene algunos aspectos negativos como el incontrolado incremento de la densidad, un incremento de las impurezas y los modos localizados del borde (ELMs, por sus siglas en inglés). Los ELMs pueden ser reconocidos como picos en la señal de la emisión  $D_\alpha$  en la Figura 2.4a.

### 9.2.2 ELMs

Durante la operación de ASDEX en modo H en 1982, los científicos se dieron cuenta de que se producían picos en la señal  $H_\alpha$  (Wagner et al., 1982). Estos picos estaban asociados con una inestabilidad MHD en el borde del plasma y, en 1984, fueron bautizados con el nombre de *modos localizados del borde* (ELMs) (Keilhacker et al., 1984).

Los ELMs son inestabilidades asociadas con el modo H en tokamaks. Son reconocidos como picos en la señal  $H_\alpha$  o  $D_\alpha$  que causan una reducción de la densidad y la temperatura en la región exterior del plasma (borde). Esta reducción en la densidad y la temperatura conlleva un deterioro del confinamiento del plasma por una reducción de la ETB.

Al principio, los científicos identificaron tres tipos diferentes del ELMs en el tokamak DIII-D en 1991 (Doyle et al., 1991):

- **Tipo I, ELMs gigantes:** el borde del plasma está cerca del límite de estabilidad  $\alpha \approx \alpha_{crit}$ . Los ELMs de Tipo I aumentan su frecuencia con la energía y la densidad, y la disminuyen con un aumento de la corriente. Aparecen como grandes picos aislados de la señal de emisión ( $H_\alpha$  o  $D_\alpha$ ). Puede encontrarse un ejemplo de los ELMs de Tipo I en la Figura 2.6a. Los ELMs de Tipo I son los más peligrosos dado que las altas pérdidas de energía que provocan en el plasma conllevan una inaceptable descarga de calor en el divertor (Wesson, 1987, p. 409).
- **Tipo II, grassy ELMs:** aparecen cuando el borde del plasma está en el régimen de conexión entre el primer y el segundo regímenes “ballooning” estables. Se trata de ELMs irregulares y de pequeña amplitud (Figura 2.6b).
- **Tipo III:** son ELMs de amplitud media con una frecuencia de repetición que decrece a medida que aumenta la potencia. El gradiente de presión del plasma está por debajo del límite ideal de “ballooning” ( $0.3 \leq \alpha/\alpha_{crit} \leq 0.5$ ). La Figura 2.6c incluye un ejemplo de ELMs de Tipo III en JET.

Dado que los ELMs de Tipo II únicamente pueden ser observados bajo determinadas condiciones, se ha propuesto una clasificación de los ELMs alternativa (Zohm, 1996a):

- **Tipo I:** la frecuencia de repetición de los ELMs ( $v_{ELM}$ ) aumenta con el flujo de potencia a través de la separatrix <sup>2</sup>( $P_{sep}$ ):

$$\frac{dv_{ELM}}{dP_{sep}} > 0 \quad (9.4)$$

- **Tipo III:** la frecuencia de repetición decrece con  $P_{sep}$ :

$$\frac{dv_{ELM}}{dP_{sep}} < 0 \quad (9.5)$$

- **Ciclos dithering:** para  $P_{sep} \approx P_\tau$ , donde  $P_\tau$  es el umbral de la potencia para llevar el plasma de modo L a modo H, pueden ocurrir repetidas transiciones L-H-L. La frecuencia de repetición muestra un ligero descenso con un aumento de  $P_{sep}$ .

Los experimentos han mostrado que es posible obtener un modo H libre de ELMs. Desafortunadamente, el modo H libre de ELMs no es estacionario. Considerando  $P_\tau^{HL}$  el límite de la potencia para la transición H/L, la potencia en la separatrix  $P_{sep}$  está dada por (Zohm, 1996b):

$$P_{sep} = P_{heat} - dW/dt - P_{rad}(core) \quad (9.6)$$

La potencia radiada del centro del plasma ( $P_{rad}(core)$ ) aumenta con la densidad y el contenido de impurezas del modo H libre de ELMs, disminuyendo la potencia en la separatrix  $P_{sep}$  (Eq. 9.6).  $P_\tau^{HL}$  también sube con la densidad y llega un momento cuando  $P_{sep} < P_\tau^{HL}$  y por lo tanto, el plasma vuelve a modo L. En contraste con los pulsos en modo H libres de ELMs donde la densidad del plasma sube hasta que se produce la transición H/L, en los pulsos con el modo H con ELMs, la densidad alcanza un nivel estacionario por el efecto de los ELMs. Por lo tanto,  $P_{rad}(core)$  no sube,  $P_{sep} > P_\tau^{HL}$  y el plasma alcanza un estado estacionario.

### 9.2.3 Dientes de sierra

Los dientes de sierra son inestabilidades que causan una pérdida de energía del centro del plasma. La temperatura y la densidad siguen un ciclo regular de lentas subidas y rápidas caídas (McCracken and Stott, 2005, p. 98). En el

<sup>2</sup>**Separatrix:** última superficie de flujo cerrada. Superficie que separa el plasma confinado por las líneas de campo magnético cerradas del Scrape Off Layer (SOL, ver Figura 2.11c)

colapso de la temperatura, la energía térmica del centro del plasma se libera en forma de un pulso de calor (Wesson, 1987, p. 365).

La Figura 2.7 muestra dos ejemplos de dientes de sierra de los pulsos de JET 60903 (Figura 2.7a) y 60906 (Figura 2.7b). En los ejemplos, la temperatura de los electrones en el centro del plasma tiene un comportamiento oscilatorio similar a los dientes de una sierra. La frecuencia de las oscilaciones es ligeramente más rápida en el pulso 60906.

Desde la primera observación de la inestabilidad de los dientes de sierra en los años 70, se han propuesto diferentes teorías para explicar este fenómeno. Una de las primeras teorías fue el *modelo de Kadomtsev* (Kadomtsev, 1975). Este establece que la inestabilidad comienza cuando el valor central de  $q^3$  cae por debajo de uno. Entonces, una isla magnética aparece en el centro del plasma y causa una reconexión magnética de las líneas de campo. Como resultado, la temperatura y la densidad del plasma colapsan. Ambas suben lentamente de nuevo a medida que el perfil de  $q$  se difunde de vuelta a su estado natural. Cuando éste se vuelve inestable, la siguiente caída tiene lugar y el ciclo comienza de nuevo (Wesson, 2000, p. 90). La Figura 2.8a (EFDA-JET<sup>©</sup>) ilustra el ciclo de reconexión magnética de las líneas de campo en el centro del plasma durante un diente de sierra. Más tarde, se demostró que la difusión del perfil de  $q$  durante la fase de rampa del diente de sierra era muy baja (en contra de lo predicho por el modelo de Kadomtsev).

Después del modelo de Kadomtsev apareció la teoría “*quasi-interchange*” (Wesson, 1986) que pareció explicar el fenómeno de los dientes de sierra. Esta teoría propuso que en vez de una reconexión magnética a través de un crecimiento de una isla magnética, podría existir un movimiento convectivo debido al intercambio de líneas del campo magnético casi paralelas, produciendo la formación de una burbuja fría rodeada de plasma caliente (Wesson, 2000, p. 91). La imagen de rayos X pareció confirmar esta teoría (Figura 2.8b, EFDA-JET<sup>©</sup>) pero después de las medidas del perfil de  $q$  en el centro del plasma, se encontró que el valor de  $q$  estaba lejos de 1 y esta teoría se descartó.

La discrepancia entre el perfil de  $q$  observado en los experimentos y el teórico todavía no ha sido resuelta.

#### 9.2.4 Disrupciones

Las disrupciones son probablemente las inestabilidades más peligrosas para la seguridad de los dispositivos de fusión. Durante una disrupción, la corriente del plasma cae abruptamente y se pierde el confinamiento del plasma.

---

<sup>3</sup>**q**: factor de seguridad. Cociente del número de veces que una línea del campo magnético viaja alrededor del toro toroidalmente partido el número de veces que lo hace poloidalmente. Es llamado factor de seguridad puesto que los plasma que rotan alrededor del toro poloidalmente aproximadamente el mismo número de veces que lo hacen toroidalmente ( $q = 1$ ) son intrínsecamente menos susceptibles a determinadas inestabilidades

La dinámica de las disrupciones consta de cuatro fases (Schuller, 1995):

1. **Evento inicial:** las condiciones del plasma cambian provocando una configuración del plasma inestable.
2. **Fase de precursores:** la configuración inestable del plasma lleva a una inestabilidad MHD.
3. **Apagado térmico:** la temperatura del plasma cae bruscamente.
4. **Apagado de la corriente:** la energía magnética del campo magnético poloidal se disipa en forma de energía térmica. La deposición de esta energía puede ser muy dañina para la integridad de la cámara.

Es posible distinguir, al menos, ocho tipos de disrupciones (Savtchikov, 2003), (Murari et al., 2008):

1. **Baja  $q$ :** cuando la  $q$  en el borde del plasma alcanza el valor de 2, aparece un gradiente de densidad de corriente dentro de la superficie  $q = 2$ . La diferencia de temperatura entre el centro del plasma y el plasma más frío en el borde lleva a un rápido descenso de la temperatura de los electrones y una pérdida de la corriente del plasma.
2. **Límite de densidad:** el límite de densidad del plasma es una consecuencia de la configuración del plasma. Cuando la densidad del plasma está por encima de este límite, la potencia radiada aumenta. Esto causa una reducción de la temperatura de los electrones en el borde del plasma y finalmente, cuando la potencia radiada sobrepasa el calentamiento, la corriente del plasma se reduce y el plasma disrumpe.
3. **Transición H/L:** se trata de un caso particular del anterior. Cuando ocurre una transición H/L a alta densidad, a veces causada por una reducción del calentamiento adicional, puede llevar a una disrupción por límite de densidad.
4. **Alta potencia radiada:** es similar al caso anterior pero aquí, el aumento de la potencia radiada tiene lugar antes del aumento de la densidad del plasma. La presencia de impurezas parece la causa del aumento de la potencia radiada.
5. **Evento de desplazamiento vertical:** este tipo de disrupciones solamente ocurren en plasma elongados. Estos plasmas tienen un mejor rendimiento (la corriente del plasma es más alta dada un cierto valor de  $q$ ) pero son verticalmente inestables y por lo tanto, su posición debe ser controlada. Si el sistema de control falla, el plasma choca contra la pared de la cámara produciendo una disrupción.

6. **Límite  $\beta$ :** estas disrupciones son la consecuencia de la presencia simultánea de un valor de  $q$  bajo junto con un alto gradiente de presión local que causa inestabilidades kink y modos ballooning.
7. **Modos bloqueados:** son causadas por perturbaciones externas del campo magnético. Estas perturbaciones pueden crear presiones inestables o gradientes de corriente que lleven a la formación de islas magnéticas rotatorias (modos). Estas inestabilidades cesan de rotar y se *bloquean* con la pared, provocando una disrupción.
8. **Barrera de transporte interna:** la barrera de transporte interna (ITB, por sus siglas en inglés) es un gradiente de temperatura y presión que aparece en escenarios avanzados (Figura 2.3). La ITB reduce el transporte de partículas y energía desde el centro hasta el borde del plasma y puede causar una disrupción.

La predicción de disrupciones es un tema clave en el desarrollo de los dispositivos de fusión futuros. Rattá ha desarrollado un exitoso predictor basado en la combinación de tres clasificadores SVM (Rattá, 2010). Ha sido aplicado en la predicción de disrupciones en JET durante las campañas de la pared de carbono y está siendo actualizado para analizar los pulsos de la nueva pared semejante a la que tendrá ITER.

### 9.3 Dispositivos de fusión

Al comienzo de la investigación de la fusión, el plasma era encerrado dentro de cámaras lineales. Para evitar la pérdida de partículas en los extremos de la cámara lineal, Peter Thonemann (Thonemann and Cowhig, 1951) y Sir George Thomson (Thomson and Blackman, 1946) sugirieron hacer la cámara toroidal (como un anillo o un doughnut). En una cámara toroidal, el confinamiento no tiene límites y por tanto, no hay fugas de partículas. Alan Ware llevó a cabo experimentos usando cámaras toroidales a finales de los años 40.

En los años 50 surgió un nuevo diseño: el “*stellarator*” (generador de estado estable). Lyman Spitzer sugirió una configuración en la cual la forma helicoidal del campo magnético fuera creada por corrientes en bobinas sinusoidales externas en vez de en el plasma (Spitzer, 1951). El dispositivo de fusión español, el TJ-II, es un stellarator.

Los científicos de la Unión Soviética Sakharov y Tamm diseñaron el “*tokamak*”. Este era similar a la configuración toroidal diseñada por Thonemann y Thomson pero con un mayor campo magnético toroidal. El nombre *tokamak* proviene del nombre ruso “toroidalnaya kamera ee magnitnaya katushka”, que significa *cámara toroidal y bobinas magnéticas*. JET, DIII-D e ITER son dispositivos de fusión tipo tokamak.

Nombre	Localización	Nombre	Localización
<b>Tokamak convencionales</b>			
ALCATOR C-Mod	EE.UU.	ASDEX Upgrade	Alemania
COMPASS	Rep. Checa	DIII-D	EE.UU.
EAST	China	FTU	Italia
ISTTOK	Portugal	JET	Reino Unido
J-TEXT	China	KSTAR	Cor. del Sur
TCV	Suiza	TEXTOR	Alemania
Tore Supra	Francia	JT-60U	Japón
<b>Tokamak esféricos</b>			
LTX	EE.UU.	MAST	Reino Unido
NSTX	EE.UU.	TST-2	Japón
<b>Stellarator</b>			
H1	Australia	HSX	EE.UU.
LHD	Japón	NCSX	EE.UU.
TJ-II	España	W 7-X	Alemania

Table 9.1: Dispositivos de fusión por confinamiento magnético

La Tabla 9.1 contiene las máquinas de fusión más importantes, junto con su localización y su tipo.

### 9.3.1 JET

El JET (Joint European Torus) es, en la actualidad, el mayor tokamak del mundo. Esta situado en Culham, Oxfordshire, UK. El proceso de diseño empezó en 1973 liderado por P. H. Rebut y terminó en 1975 con la publicación del *JET Design Proposal* (Rebut and JET design team, 1976), también conocido como R5. La construcción de JET duró cuatro años entre 1979 y 1983. El primer pulso en JET tuvo lugar el 25 de junio de 1983 a la hora local 13:44.

El objetivo de JET fue establecido en la JET Design Proposal: “*el objetivo esencial de JET es obtener y estudiar el plasma en condiciones y dimensiones que se aproximen a aquellas necesarias en un reactor termonuclear. Estos estudios están destinados a definir los parámetros, el tamaño y las condiciones de trabajo de un reactor tokamak. La realización de estos objetivos involucra cuatro áreas fundamentales de trabajo:*

1. *El escalado del comportamiento del plasma con parámetros cercanos a la escala de un reactor.*
2. *La interacción plasma-pared en estas condiciones.*
3. *El estudio del calentamiento del plasma.*

4. *El estudio de la producción de partículas  $\alpha$ , confinamiento y calentamiento del plasma.*”

La figura 2.9 (EFDA-JET<sup>©</sup>) contiene el diseño original del tokamak JET. El volumen de plasma en la cámara de vacío varía entre 80 m<sup>3</sup> y 100 m<sup>3</sup>. La corriente inicial del plasma era de 3.8 MA y posteriormente se aumentó hasta los 4.8 MA. El campo magnético toroidal en el centro del plasma era inicialmente 2.8 T y fue mejorado hasta los 3.5 T.

Las bobinas de JET tienen una forma de D característica. Este diseño obedece a razones físicas: el campo magnético dentro de las bobinas toroidales decae con el radio mayor como  $1/R$  y por lo tanto existe una fuerza magnética mayor en la parte interna de las bobinas que en la parte externa. En la parte interna de las bobinas (la parte recta de la forma de D), la fuerza magnética está soportada por la estructura primaria del transformador. La parte externa de las bobinas fue diseñada para soportar las fuerzas magnéticas por sí misma. La curvatura proporciona resistencia frente al estrés de la tensión. El *campo magnético toroidal* de JET es producido por 32 bobinas en forma de D rodeando la cámara de vacío (Figura 2.10a, EFDA-JET<sup>©</sup>). Cada una de las bobinas de campo toroidales pesa 12 toneladas y está rodeada con 24 vueltas de cobre. La capacidad de conducción combinada de todas las bobinas es de 51 MA. El campo magnético podría crear una fuerza en cada bobina cercana a las 2,000 toneladas, directamente hacia el eje mayor del toro.

Las bobinas del *campo magnético poloidal* consisten en 7 bobinas circulares rodeando las bobinas del campo toroidal (Figura 2.10b, EFDA-JET<sup>©</sup>). El objetivo de la bobina interior alrededor de la columna central del núcleo del transformador de hierro (Figura 2.10c, EFDA-JET<sup>©</sup>) era actuar como la principal del transformador. Las otras 6 bobinas permiten a los científicos modificar la posición y la forma del plasma. La bobina más larga tiene un diámetro de 11 metros.

Combinando los campos magnéticos creados por los sistemas de bobinas toroidales y poloidales es posible generar plasmas con diferentes formas. La Figura 2.11 incluye tres ejemplos de configuraciones magnéticas en JET. La Figura 2.11a muestra un plasma circular en la cámara de vacío. Modificando la configuración magnética es posible obtener un plasma elíptico como el mostrado en la Figura 2.11b.

La Figura 2.11c contiene un ejemplo de una configuración magnética especial: la configuración magnética con punto X. Usando esta configuración magnética aparecen dos tipos de superficies magnéticas: las superficies magnéticas abiertas y las superficies magnéticas cerradas. La superficie magnética de flujo que separa las superficies abiertas y las cerradas se denomina *separatrix*. La capa entre la separatrix y la pared de la cámara de vacío se llama *scrape-off layer* (SOL, por sus siglas en inglés). Las líneas magnéticas fuera de la separatrix cruzan la pared de la cámara de vacío y por lo tanto

las partículas en el SOL chocan contra la pared. La superficie por debajo del punto X donde las partículas chocan contra la pared se denomina *divertor*.

La cámara de vacío estaba diseñada para maximizar el espacio dentro de las bobinas toroidales. Esta soporta un vacío que es la millonésima parte de la presión atmosférica (Wesson, 2000, p. 23). Por lo tanto, soporta una presión atmosférica de 10 toneladas por metro cuadrado en una superficie de 200 metros cuadrados. La cámara de vacío puede contener hasta 100 m<sup>3</sup> de plasma. La Figura 2.12b (United Kingdom Atomic Energy Authority<sup>©</sup>) contiene una imagen real de la cámara de vacío de JET tomada en 1998.

La forma de D de las bobinas del campo toroidal determinan la geometría de la cámara de vacío (Figura 2.12a). La proporción alto-ancho (b/a) de la cámara de vacío es de 1.6. El valor óptimo de la relación de aspecto (R/a) se estableció entre 2 y 3. El valor elegido de la relación de aspecto fue 2.4 para minimizar el coste del tokamak.

El calentamiento en JET está formado por tres sistemas diferentes: un sistema NBI con 23 MW de potencia total, una antena ICRH de hasta 32 MW y una antena de 12 MW de potencia.

Los sistemas de diagnósticos permiten a los científicos del JET medir las propiedades del plasma como la densidad, la temperatura o el voltaje y estudiar los fenómenos físicos que tienen lugar en el dispositivo de fusión. Actualmente, existen más de 90 diagnósticos funcionando y hay más de 20 en fase de diseño. En cada pulso, los diagnósticos generan hasta 40 GBytes de datos, en contraste con los 243 KBytes de datos generados en el primer pulso de JET. La base de datos de JET contiene más de 80 TBytes de datos. Los diagnósticos de JET incluyen espectrometría Thomson scattering (medidas de la temperatura de los electrones y perfiles de densidad), espectrómetros de visible, UV y rayos X (medidas de temperatura y densidad), bolómetros (medidas de la pérdida de energía del plasma), bobinas magnéticas (medidas del campo magnético, corriente y energía) o emisiones electrón-ciclotrón (medidas rápidas y de alta resolución de los perfiles de temperatura de los electrones). Los diagnósticos de JET también incluyen cámaras del espectro visible y del infrarrojo que obtienen grabaciones de video e imágenes del plasma durante un pulso.

Puede encontrarse más información acerca de JET en la página web de EFDA-JET (EFDA-JET, 2012).

### 9.3.2 TJ-II

El TJ-II es un stellarator de campo magnético bajo de tipo helicoidal con un radio mayor medio (R) de 1.5 m y un radio menor medio (a)  $\leq 0.22$  m (Alejaldre et al., 1999). Está situado en el *Laboratorio Nacional de Fusión* (LNF) en Madrid, España. Su diseño fue realizado por el equipo de físicos e ingenieros del CIEMAT en colaboración con el Oak Ridge National Labora-

tory (Hender et al., 1987). Esta propuesta estaba basada en una propuesta previa de un stellarator con configuración helicoidal flexible (Harris et al., 1985).

La Figura 2.13 muestra el diseño del TJ-II. Las bobinas de campo verticales controlan la posición horizontal del plasma. El campo toroidal está generado por 32 bobinas toroidales y es de hasta 1.2 T. El giro tridimensional del eje central de la configuración está generado por medio de dos bobinas centrales: una circular y la otra helicoidal. La cámara de vacío mantiene un vacío de  $1 \cdot 10^{-8}$  mbar.

El proceso de diseño del TJ-II empezó en 1986 cuando se creó la Asociación EURATOM-CIEMAT. El proyecto helicoidal flexible TJ-II se presentó para demostrar su interés científico y recibió respaldo preferente por parte de EURATOM para la fase I (física). En 1990, recibió soporte para la fase II (ingeniería). El primer plasma en el stellarator TJ-II tuvo lugar en diciembre de 1997. La Figura 2.14 contiene una imagen del estado del stellarator TJ-II en 2009.

Una de las características más importantes del stellarator TJ-II es su configuración helicoidal flexible. La transformada rotacional puede variar entre 0.9 y 2.2 obteniendo volúmenes de plasma desde  $0.3 \text{ m}^3$  hasta  $1.2 \text{ m}^3$ . Para valores altos de la transformada rotacional, el plasma tiene forma de alubia. El radio medio del plasma oscila entre 0.12 m y 0.22 m. Esta flexibilidad proporciona a los científicos un amplio rango de diferentes configuraciones para desarrollar sus experimentos.

Los pulsos del TJ-II duran entre 200 ms y 300 ms con una frecuencia de repetición de 7 minutos. El sistema de alimentación está formado por un generador impulsional de 140 MVA, 100 MJ a 15 kV 100 Hz. Los 96 puntos de acceso (o ventanas) en la cámara de vacío permiten a los científicos usar un amplio rango de diagnósticos del plasma como bolómetros, rayos X blandos, interferómetros, reflectómetros, Thomson scattering, espectrometría o cámaras del espectro visible e infrarrojo entre otros. Para minimizar las impurezas en el plasma, la cámara de vacío se reviste con litio o boro.

En el dispositivo TJ-II, el plasma se calienta usando dos sistemas diferentes: ECRH y NBI. El calentamiento ECRH usa dos girotrones a 53.2 GHz. La máxima potencia de cada girotrón es de 300 kW. Existen dos inyectores NBI instalados en el TJ-II, cada uno proporcionando una potencia de calentamiento de hasta 500 kW (Estrada et al., 2010). Usando el calentamiento NBI, ha sido posible obtener el modo H, alcanzando densidades de  $8 \cdot 10^{19} \text{ m}^{-3}$  y temperaturas electrónicas de 250 eV – 300 eV (Sánchez et al., 2009).

Puede encontrarse más información acerca del TJ-II en su página web (Laboratorio Nacional de Fusión, 2012).

### 9.3.3 DIII-D

El DIII-D es un dispositivo de fusión tokamak situado en San Diego, USA. Este dispositivo está operado por General Atomics. El DIII-D es la actualización del dispositivo Doublet III y fue apodado DIII-D por su nueva cámara en forma de D. Actualmente, es el tercer tokamak más grande tras JET y JT-60U (Japón).

Las características más importantes del dispositivo de fusión DIII-D son (Brooks et al., 1987): radio mayor (R) 1.67 m, radio menor (a) 0.67 m, superficie del plasma  $2 \text{ m}^2$ , volumen del plasma  $30 \text{ m}^3$ , corriente máxima del plasma 5 MA y máximo campo toroidal 2.2 T.

El objetivo del programa de investigación del DIII-D es establecer los principios científicos para la optimización del concepto de tokamak para la producción de energía. En futuro cercano, pretende posibilitar el éxito de ITER proporcionando soluciones a los principales problemas físicos como la operación en estado estacionario (General Atomics, 2012).

La Figura 2.15a contiene un esquema del tokamak DIII-D. Es posible hacerse una idea del tamaño del dispositivo comparándolo con el científico situado en su base. La Figura 2.15b muestra una imagen del interior de la cámara del DIII-D.

La página web del DIII-D (General Atomics, 2012) proporciona más información acerca de este tokamak.

### 9.3.4 ITER

ITER (Reactor Termonuclear Experimental Internacional) es un tokamak que se está construyendo en Cadarache, Francia. Se pretende que llene el vacío entre los dispositivos de fusión experimentales y la primera planta de fusión comercial (DEMO). Los miembros del proyecto ITER son: EU, China, India, Japón, Corea del Sur, Rusia y los Estados Unidos.

La Figura 2.16 muestra el diseño de ITER. Sus principales características son: radio mayor (R) 6.2 m, radio menor (a) 2.0 m, corriente máxima del plasma 15 MA y campo toroidal de 5.3 T. El objetivo científico de ITER es obtener  $Q^4 \geq 10$ .

El campo magnético de ITER será creado por bobinas superconductoras: 18 bobinas toroidales, 6 bobinas poloidales, un solenoide central y bobinas adicionales para mitigar el efecto de los ELMs. Para alcanzar la superconductividad, las bobinas se refrigeran usando helio supercrítico en el rango de  $-260^\circ\text{C}$ . El campo magnético creado por los imanes de ITER será de alrededor de 200,000 veces el campo magnético de la Tierra. El coste de los imanes de ITER se estima en 298.18 millones de € (Fusion for Energy, 2011).

Su cámara de vacío tiene un volumen de  $1,400 \text{ m}^3$ . Esta soportará un

---

<sup>4</sup>Q es el cociente entre energía de fusión y energía auxiliar inyectada en el plasma

vacío de una millonésima parte de la presión atmosférica (similar a JET). La cámara dispondrá de 44 puntos de acceso para diagnósticos del plasma y control remoto. El precio de la cámara de vacío será de 147.30 millones de €.

La temperatura en el interior de ITER alcanzará los 150 millones de grados K. Para alcanzar esta temperatura, 50 MW de potencia de calentamiento serán instalados. ITER usará dos inyectores NBI y uno adicional para tareas de diagnóstico (133.36 millones de €) y sistemas de calentamiento ICRH y ECRH (66.72 millones de €). Dado que los científicos pretenden obtener  $Q \geq 10$ , se espera que ITER genere 500 MW de energía de fusión.

Los diagnósticos de ITER incluyen 50 sistemas diferentes para analizar el estado del plasma. Incluyen rayos X, cámaras, láseres, monitores de impurezas, bolómetros, etc. Los sistemas de diagnóstico tienen un precio de 56.78 millones de €.

Los componentes de la pared en contacto con el plasma son cruciales para el éxito de ITER. Una pared de tungsteno similar a la de ITER está siendo probada actualmente en JET. La pared de ITER estará cubierta por 440 baldosas de tamaño 1 m  $\times$  1.5 m. El precio de las baldosas y otros componentes del interior de la cámara es de 130.88 millones de €. Dado que los componentes de la pared pueden ser activados por el calor extremo, es necesario un sistema de control remoto para repararlos y reemplazarlos. El sistema de control remoto que será construido en ITER cuesta 71.36 millones de €.

La preparación del lugar de construcción de ITER comenzó en enero de 2007 y la construcción de los edificios y laboratorios empezó en julio de 2010. Se espera que el ensamblaje del tokamak comience en 2015. Este estará acabado en 2018 y el primer plasma en ITER tendrá lugar en 2019. El complejo, edificios y fuentes de energía tienen unos costes de 776.27 millones de €.

Se puede encontrar más información acerca del proyecto ITER en su página web (ITER Organization, 2012).

### 9.3.5 DEMO

DEMO (planta eléctrica de DEMOstración) será el siguiente paso hacia un dispositivo de fusión comercial. DEMO pertenecerá a la 5<sup>a</sup> generación de dispositivos de fusión experimentales. Este demostrará la fiabilidad de un dispositivo de fusión de *tamaño comercial*.

Existen todavía muchas incógnitas acerca del diseño de DEMO. Sus características finales estarán basadas en los resultados obtenidos por ITER y otros dispositivos de fusión. El estudio conceptual europeo sobre una planta eléctrica de fusión (PPCS, por sus siglas en inglés) ha analizado las diferentes alternativas de diseño de DEMO basadas en el concepto tokamak

(Maisonnier et al., 2005). Los modelos de planta del PPCS han sido diseñados usando el código PROCESS. Al principio, PROCESS fue escrito para los estudios conceptuales de ITER y ha sido actualizado incorporando leyes de escala recientes usando los datos de los dispositivos de fusión existentes. Los modelos PPCS-A y PPCS-B son dispositivos de un futuro cercano (cerca del 30% mejores que el diseño base de ITER) mientras que los modelos PPCS-C y PPCS-D están basados en configuraciones del plasma y tecnologías de materiales avanzadas.

Para (Ward, 2010), DEMO debe estar basado en un dispositivo tokamak con las siguientes características: radio mayor 8.5 m con un campo toroidal de 6 T y una energía de fusión de 3 GW. La principal diferencia entre DEMO y los dispositivos de fusión existentes es la producción de energía; mientras los dispositivos de fusión actuales tienen una duración del pulso no mayor de un minuto, DEMO debe operar en estado estacionario o al menos trabajar en pulsos muy largos.

En DEMO, la producción de energía será mayor. Esta producción puede alcanzarse por medio de dos mecanismos diferentes:

- **Usando una densidad mayor:** en este caso el plasma de DEMO debe tener una forma determinada o DEMO debe funcionar con un campo magnético muy alto.
- **Usando una temperatura mayor:** esta opción es la más factible. Si la densidad de DEMO es similar a la densidad de ITER entonces la de temperatura de DEMO será mayor (temperatura media de 10 keV, alrededor de 25 keV en el centro del plasma). A esta temperatura, la sección eficaz de la fusión no varía con  $T^2$  (ver Fig. 2.1).

Para proporcionar información acerca de los materiales que se usarán en la construcción de DEMO, el laboratorio internacional de radiación de materiales de fusión (IFMIF, por si siglas en inglés) está siendo construido en Japón. Su objetivo es reducir el tiempo de diseño y construcción de DEMO para alcanzar un prototipo comercial en el menor tiempo posible (lo que se conoce como *fast track* o *vía rápida*).



## Chapter 10

# Localización de eventos relevantes en señales e imágenes

La producción futura de energía en plantas eléctricas de fusión es una función de la longitud del pulso de plasma (cuanto más largo sea el pulso, más energía se producirá). Los dispositivos de fusión actuales tienen duraciones de pulso cortas (por ejemplo, los pulsos del TJ-II duran menos de un segundo y los pulsos de JET duran entre 10 y 20 segundos, incluso un minuto bajo determinadas circunstancias). Estas duraciones de pulso se sobrepasarán en los dispositivos de fusión futuros. Se espera que ITER mantenga el plasma en estado estacionario hasta 400 segundos con  $Q \sim 5$ . Pero incluso la longitud del pulso de ITER puede ser mayor. Se espera que el modo híbrido dure hasta una hora con  $Q \sim 10$  y que el modo avanzado dure hasta 30 minutos con  $Q \sim 40$  (Stambaugh, 2006).

Durante la duración de un pulso tienen lugar cientos de eventos físicos. La identificación y localización de estos eventos se lleva a cabo a través del análisis visual de las señales del plasma. Los expertos dedican su tiempo a examinar con gran detalle cada señal para determinar el tipo de evento (por ejemplo ELMs, dientes de sierra o disrupciones) y su localización temporal. Los dispositivos de fusión actuales requieren muchos expertos para analizar los datos generados durante cada pulso y esto será inabordable en los dispositivos futuros cuando la longitud del pulso sea hasta 100 veces más larga.

Recientemente, las herramientas de minería de datos e inteligencia artificial han sido utilizadas en las bases de datos de fusión. Estos métodos proporcionan resultados rápidos y precisos en la localización e identificación de fenómenos del plasma. Además, pueden predecir fenómenos peligrosos (como disrupciones) antes de que ocurran (Ratta et al., 2010). Estas técnicas serán esenciales en los próximos años y especialmente después del primer

pulso de ITER esperado para 2019.

Un aspecto importante a tener en cuenta es el coste del análisis de los datos. El análisis visual de las señales requiere muchos trabajadores y por tanto, es caro. Los códigos de ordenador son mucho más baratos. Sus precios incluyen su diseño y mantenimiento / actualización pero pueden ser ejecutados miles de veces sin coste adicional. Esto permite el análisis de grandes cantidades de datos a un bajo coste.

Otra ventaja de las técnicas de minería de datos es su velocidad. Los códigos de ordenador son más rápidos que cualquier análisis visual llevado a cabo por los expertos. El análisis visual requiere mucho tiempo y la única forma de acelerarlo es aumentando el número de expertos y, por tanto, incrementando su coste.

El comportamiento determinista de los códigos de ordenador es también uno de sus beneficios. Los resultados de un análisis usando un código de ordenador son siempre los mismos, sin importar el número de veces que el programa se ejecute. Es importante destacar que esto no implica que los códigos estén libres de errores, simplemente significa que siempre se comenten los mismos (si existen). Esto no puede asegurarse en el análisis realizado por expertos. El mismo evento puede ser localizado por dos expertos en dos tiempos ligeramente diferentes e incluso el mismo experto puede determinar dos tiempos diferentes para el mismo evento. Las razones de estas diferencias pueden ser, entre otras, un diferente nivel de detalle en el análisis (cuanto mayor nivel de detalle, más tiempo lleva el análisis) o un simple error.

Los expertos en fusión también juegan un papel fundamental en el diseño de las herramientas de minería de datos. Dado que ellos poseen el conocimiento más extenso de los fenómenos del plasma, su asistencia es indispensable en el desarrollo de estos códigos de ordenador. Las herramientas que integran el conocimiento experto en sus sistemas se denominan *sistemas expertos*. Por una parte, los sistemas expertos son rápidos y precisos y por la otra, aplican el conocimiento de los expertos. Dado que los sistemas expertos combinan los mejores atributos de los expertos y los códigos de ordenador, se consideran una valiosa herramienta.

## 10.1 Un localizador de eventos universal

Esta Sección describe un localizador de eventos universal (UMEL, por sus siglas en inglés), una técnica para localizar eventos en señales y películas del plasma (Vega et al., 2010a). UMEL es una técnica universal porque es independiente del tipo de patrón buscado (picos, caídas o cambios de pendiente) y del tipo de señal analizada (dominio del tiempo o dominio de la frecuencia).

UMEL propociona una doble utilidad:

1. Puede ser usado como filtro para reconocer segmentos de señales o áreas en imágenes con un comportamiento relevante. El uso de UMEL como filtro permite establecer la presencia de un evento físico sin identificar su tipo.
2. Puede ser aplicado para determinar la localización exacta de puntos singulares en señales. UMEL puede localizar eventos físicos en un elevado número de experimentos y, por lo tanto, crear grandes bases de datos con una amplia base estadística de una forma automática.

UMEL basa su capacidad de búsqueda en una técnica de regresión específica: Regresión de Vectores Soporte (SVR, por sus siglas en inglés). SVR ajusta los datos de entrenamiento sin depender de factores como la frecuencia de muestreo o la distribución del ruido. Esta técnica calcula una función de ajuste y, además, devuelve una lista de puntos del conjunto de entrenamiento que se han convertido en Vectores Soporte (SVs, por sus siglas en inglés). UMEL proporciona una interpretación novedosa de estos SVs: los SVs son, en su mayoría, las muestras más difíciles de ajustar.

En SVM y SVR, la complejidad del modelo determina el número de SVs (a mayor complejidad, mayor número de SVs). La regresión de conjuntos de datos complejos requiere un gran número de SVs. En contraste, los conjuntos de datos simples requieren un menor número de SVs. Pero el número de SVs no solamente depende en la complejidad del conjunto de datos a ajustar. Esta también depende en la suavidad de la función de regresión. Las funciones de regresión suaves requieren menos SVs que las complejas.

La suavidad de un ajuste SVR es función de cuatro parámetros:

1. **Tipo de *kernel*:** determina la ecuación del ajuste SVR y por tanto, su suavidad. Existen diferentes tipos de *kernel*, por ejemplo, lineal, gaussiano, polynomial o RBF.
2. **Parámetro de regularización C:** controla la complejidad del modelo. Los valores altos de C producen ajustes más complejos. Por otra parte, valores bajos de C producen regresiones más suaves. Su valor puede ser estimado usando la siguiente ecuación (Cherkassky and Mulier, 1998, p. 449):

$$C = K_C \cdot \max(|\bar{y} + 3 \cdot \text{std}(y)|, |\bar{y} - 3 \cdot \text{std}(y)|) \quad (10.1)$$

donde:

- $\bar{y}$  : es la media de la función a ajustar
- $\text{std}(y)$  : es la desviación estándar de la función a ajustar
- $K_C$  : es una constant que varía para diferentes tipos de señal

3. **epsilon ( $e$ ):** determina el ancho de la zona  $e$ -insensitiva (también llamada  $e$ -tube puesto que parece un tubo alrededor del ajuste). Puede ser determinada usando la ecuación (Cherkassky and Mulier, 1998, p. 449):

$$e = K_e \cdot \text{std}(\text{noise}) \cdot \sqrt{\frac{\ln n}{n}} \quad (10.2)$$

donde:

- $\text{std}(\text{noise})$  : es la desviación estándar del ruido de la función  
 $n$  : es el número de muestras  
 $\ln n$  : es el logaritmo natural de  $n$   
 $K_e$  : es una constante de proporcionalidad

Desde un punto de vista práctico y dado que habitualmente el valor del ruido no es conocido, el valor de  $\text{std}(\text{noise})$  es reemplazado por  $\text{std}(y)$  donde  $y$  es la función a ajustar. Entonces, el valor de  $e$  es ajustado usando la constante de proporcionalidad  $K_e$ .

4. **Parámetro(s) del *kernel*:** algunos *kernels* incluyen un parámetro, por ejemplo el parámetro  $\sigma$  del *kernel* RBF. Este es uno de los *kernels* más habitualmente utilizados y por lo tanto, existe una ecuación para estimar el parámetro  $\sigma$  (Martinez and Martinez, 2008, p. 325):

$$\sigma_k = K_\sigma \cdot 1.06 \cdot \text{std}(y) \cdot n^{-1/5} \quad (10.3)$$

donde:

- $\text{std}(y)$  : es la desviación estándar de la función a ajustar  
 $n$  : es el número de muestras  
 $K_\sigma$  : constante dependiente del tipo de señal a ajustar

Usando UMEL, no todos los SVs tienen el mismo grado de relevancia. Los SVs que descansan en el  $e$ -tube o fuera de él se denominan SVs externos (ESVs). En contraste, los SVs dentro del  $e$ -tube son llamados SVs internos (ISVs).

$$ESV \subseteq SV \quad \forall i \in ESV, \quad |y_i - f(x_i)| \geq e \quad (10.4)$$

$$ISV \subseteq SV \quad \forall i \in ISV, \quad |y_i - f(x_i)| < e \quad (10.5)$$

Los ISVs son muestras necesarias para estimar la regresión, pero no proporcionan el mismo grado de relevancia que puede ser asignado a los ESVs. UMEL propone una interpretación novedosa de los ESVs: los SVs que se convierten en ESVs son las *muestras más difíciles de ajustar* (no pueden ser ajustadas dentro del  $e$ -tube) y estos SVs proporcionan *información esencial*

en el proceso de regresión. Los ESVs revelan la existencia de patrones especiales en una señal: picos, grandes gradientes o segmentos con diferente estructura morfológica en relación con el conjunto de la señal. La mayoría de los fenómenos del plasma están caracterizados por componentes de alta frecuencia en el dominio del tiempo (picos, caídas, rápidos cambios de la pendiente, etc.).

### 10.1.1 Localización de dientes de sierra usando UMEL

Los dientes de sierra pueden ser identificados por medio de la emisión de rayos X. Además, usando diferentes cuerdas de la emisión de rayos X a diferentes radios del plasma, es posible medir la difusividad del plasma en función de la diferencia de tiempo entre un mismo diente de sierra a diferentes radios.

Usando las cuerdas centrales (Figura 4.4 gráfico superior) es posible determinar el tiempo exacto de las caídas de los dientes de sierra. UMEL puede utilizarse para localizar las caídas en la emisión de los rayos X y por tanto, localizar los tiempos de los dientes de sierra. Los ESVs aparecen en las muestras más difíciles de ajustar, en este caso, los puntos alrededor de cada caída. Si los tiempos de los dientes de sierra son medidos a diferentes radios, pueden ser usados para cuantificar la difusividad del plasma. De acuerdo con el método pico-a-pico (Soler and Callen, 1979), es posible calcular la difusividad del plasma como:

$$\chi_e = \frac{r^2 - r_{inversion}^2}{8t_p} \quad (10.6)$$

donde:

- $r$  : es el radio del plasma donde se mide  $\chi_e$
- $r_{inversion}$  : es el radio donde el diente de sierra se invierte
- $t_p$  : es la diferencia de tiempos entre el radio de la inversión y  $r$

Dado que las coordenadas radiales de los rayos X blandos son conocidas a priori, UMEL permite la automatización del cálculo de  $\chi_e$ .

### 10.1.2 Localización de disrupciones usando UMEL

Las disrupciones pueden ser reconocidas en las señales del plasma usando la corriente del plasma y el lazo de voltaje. Cuando una disrupción tiene lugar, la corriente del plasma se desploma y aparece un pico en la señal del lazo de voltaje. La Figura 4.7b muestra el lazo de voltaje y la corriente del plasma de una descarga disruptiva (pulso de JET 71025). En las descargas no disruptivas, también es posible observar un pico en el lazo de voltaje, pero la corriente del plasma baja gradualmente hasta que alcanza el valor

<b>Disruptivas</b>	<b>343 pulsos</b>
Detectadas (verdaderos positivos)	321 (93.59%)
Fallos (falsos negativos)	22 (6.41%)
<b>No disruptivas</b>	<b>4,057 pulsos</b>
Aciertos (verdaderos negativos)	4,036 (99.48%)
Errores (falsos positivos)	21 (0.52%)
<b>Total</b>	<b>4,400 pulsos</b>
Aciertos	4,357 (99.02%)
Errores	43 (0.98%)

Table 10.1: Resultados de la localización de disrupciones

0 (Figura 4.7a, pulso de JET 71023). Ambas señales son necesarias para reconocer las disrupciones.

Para localizar las disrupciones usando UMEL, ambas señales son ajustadas usando los parámetros (RBF *kernel*,  $K_C = 1$ ,  $K_e = 30$ ,  $K_\sigma = 1$ ). Dado que las muestras más difíciles de ajustar son los puntos situados en los picos del lazo de voltaje y en las caídas de la corriente del plasma, los ESVs aparecen en estos puntos. La Figura 4.7 muestra el ajuste de la corriente del plasma y el lazo de voltaje en una descarga no disruptiva y en una disruptiva. La descarga disruptiva puede reconocerse por la aparición simultánea de ESVs en el lazo de voltaje y en la corriente del plasma.

UMEL puede utilizarse para la localización off-line de las disrupciones existentes en la base de datos de JET. Los tiempos de disrupciones determinados pueden ser usados para construir predictores de disrupciones on-line automáticos (Ratta et al., 2010). Dado que el número de muestras en ambas señales es bajo (1000 muestras de media por señal), el cómputo es muy rápido (0.33 s por señal usando un Intel® Core™ 2 Quad CPU Q9300 2.50GHz, 1.95GB RAM).

Las disrupciones de una base de datos de JET de 4,400 descargas (en el rango de pulsos desde el 65115 hasta el 70722) fueron localizadas usando UMEL. La base de datos contenía 343 pulsos disruptivos y 4,057 pulsos no disruptivos. Los resultados obtenidos por el método pueden verse en la Tabla 10.1. El porcentaje de aciertos fue del 99.02% (4,357 descargas reconocidas adecuadamente) y el porcentaje de errores fue del 0.98% (43 descargas mal clasificadas).

### 10.1.3 Localización de ELMs usando UMEL

El primer paso en la localización de ELMs es la determinación de la región donde tienen lugar. La secuencia típica de una descarga comienza con el plasma en modo L. Entonces, cuando la potencia auxiliar es inyectada al plasma por encima de un cierto umbral de potencia, el plasma alcanza el

modo H. El plasma vuelve al modo L después de que se pare la inyección de potencia. Los ELMs tienen lugar únicamente durante el tiempo que el plasma está en modo H y en JET, no hay modo H libre de ELMs. Por lo tanto, la localización del modo H implica la determinación donde aparecen ELMs y viceversa.

La localización de la región con ELMs se lleva a cabo en tres tareas secuenciales:

**Normalización de la señal  $D_\alpha$ .** Simplifica el cálculo del ajuste SVR y permite utilizar los mismos parámetros de UMEL para un amplio rango de descargas. La normalización utilizada es:

$$D_{\alpha, \text{ normalizada}} = \frac{D_\alpha - \min(D_\alpha)}{\max(D_\alpha) - \min(D_\alpha)} \quad (10.7)$$

**Reducción de dimensionalidad.** El tiempo de cálculo se reduce significativamente reduciendo el tamaño / dimensionalidad de la señal ajustada. Por ello, se reduce la dimensionalidad de la señal  $D_\alpha$  utilizando los coeficientes wavelet de aproximación de nivel 5.

**Localización del modo H.** La capacidad de UMEL para localizar segmentos temporales con comportamiento relevante ha sido utilizada para localizar el intervalo temporal en modo H de una descarga. Para ello, se usa UMEL con los parámetros (RBF *kernel*,  $K_C = 1$ ,  $K_e = 10$ ,  $K_\sigma = 20$ ). El gráfico superior de la Figura 4.8 muestra un ejemplo de los ESVs obtenidos por UMEL en el pulso de JET 73337.

Después, se calcula un histograma de los ESVs en ventanas de 0.1 s de longitud (Figura 4.8, gráfico inferior). El histograma define el segmento temporal que ha sido más difícil ajustar y, por tanto, el segmento temporal donde la señal  $D_\alpha$  contiene componentes de alta frecuencia (picos). Este segmento temporal se corresponde con la región en modo H y, por tanto, con el segmento temporal con actividad de ELMs. Los límites de la región se calculan como el primer y último punto del histograma con más ESVs que un cierto valor de decisión. Este es calculado como:

$$d_{value} = K \cdot \frac{\sum_{i=1}^N ESV_i}{N} \quad (10.8)$$

donde:

- $K$  : constante dependiente del rango de descargas
- $ESV_i$  : número de ELMs en la barra  $i$  del histograma
- $N$  : número de puntos en el histograma con ELMs

Periodo (s)	Número de ELMs	Periodo (s)	Número de ELMs
< 0.01	3,200	0.04 to 0.05	19,809
0.01 to 0.02	56,550	0.05 to 0.06	11,409
0.02 to 0.03	61,373	0.06 to 0.07	6,800
0.03 to 0.04	30,100	0.07 to 0.08	4,000

Table 10.2: Distribución de los períodos de los ELMs localizados

El siguiente paso en la localización de ELMs es localizar cada uno por separado. Habitualmente, los ELMs son localizados visualmente. El proceso consiste en reconocer los picos en las señales  $H_\alpha/D_\alpha$  que son sincronos con una caída de la energía diamagnética almacenada. El sistema automático realiza este mismo proceso dentro del intervalo que se ha determinado que contiene ELMs. Este paso se lleva a cabo mediante cuatro tareas secuenciales:

**Localización de los picos en la  $D_\alpha$ .** Dado que la señal  $D_\alpha$  tiene una proporción señal-ruido mejor que la señal de la energía diamagnética, la localización de los picos provocados por los ELMs en la señal  $D_\alpha$  es más sencilla. Estos son localizados por UMEL usando los parámetros (RBF *kernel*,  $K_C = 1$ ,  $K_e = 8$ ,  $K_\sigma = 50$ ).

**Combinación de ESVs.** Como puede observarse en la Figura 4.9a, aparece más de un ESV en cada pico de la señal  $D_\alpha$ . Esta tarea combina todos los ESVs de cada pico en uno sólo en el instante de mayor amplitud de la señal. La Figura 4.9b muestra los resultados de esta tarea.

**División de la energía diamagnética.** Para facilitar la búsqueda de las caídas en la energía diamagnética, esta se divide en trozos de una longitud de 35 ms alrededor de los picos hallados en el paso anterior. La Figura 4.10 ilustra esta tarea.

**Combinación de información.** UMEL (RBF *kernel*,  $K_C = 100$ ,  $K_e = 1$ ,  $K_\sigma = 100,000$ ) se usa de nuevo para localizar caídas en las ventanas de la señal de la energía diamagnética del paso anterior. Si uno o más ESVs aparecen en la ventana a una distancia máxima de 5 ms del pico de la  $D_\alpha$  entonces se determina que se trata de un ELM. La Figura 4.11 muestra este proceso.

Este método de localización de ELMs se aplicó a una base de datos de JET de más de 1,200 pulsos en el rango [73337, 78156]. 221,751 ELMs fueron identificados en estos pulsos.

Debido a la falta de una gran base de datos de ELMs, el rendimiento del método de localización de ELMs fue testado comparando sus resultados

con los resultados obtenidos por expertos en 20 pulsos de JET en el rango anterior. El método alcanzó un porcentaje de éxito del 95%.

La Tabla 10.2 muestra el número de ELMs localizados para diferentes períodos (la diferencia de tiempo entre un ELM y el siguiente). El período más común es entre 0.02 y 0.03 s con 61,373 ELMs.

#### 10.1.4 Análisis de los perfiles de temperatura durante los ELMs

Los ELMs causan una reducción de la densidad y la temperatura en el borde del plasma, deteriorando la Barrera de Transporte del Borde (ETB, por sus siglas en inglés) y degradando el confinamiento del plasma. Diferentes configuraciones del plasma llevan a diferentes degradaciones del confinamiento durante los ELMs y, por tanto, resulta interesante estudiar el efecto de cada parámetro en la degradación de la ETB.

La ETB puede ser reconocida como un gran gradiente en la temperatura electrónica (ET) cerca del borde del plasma en los plasmas en modo H. A este gradiente se le ha denominado *gradiente de la temperatura en el borde* (ETG). Este causa un incremento de la presión del plasma en el centro y por tanto, la temperatura de los electrones aumenta.

Para simplificar el reconocimiento automático del ETG, se ha introducido un nuevo parámetro llamado *gradiente de temperatura* (SGT). Este parámetro mide los gradientes de temperatura entre dos puntos radiales consecutivos:

$$SGT(i) = \frac{ET(i) - ET(i+1)}{r(i+1) - r(i)} \quad (10.9)$$

donde  $r(i)$  es el radio del plasma donde la  $ET(i)$  se ha medido y  $i$  es su posición radial ( $i = 1, \dots, 95$ ). Dado que el ETG ha sido definido como un gran gradiente de la ET cercano al borde del plasma, éste puede ser fácilmente localizado en plasmas en modo H en la posición radial cerca del borde donde el SGT muestra un pico.

Habitualmente, la ET del plasma desciende constantemente desde el centro del plasma hasta el borde. Como resultado el SGT oscila en torno a un determinado valor y finalmente aumenta en el ETG cerca del borde del plasma. El valor alrededor del cual el SGT oscila se ha denominado *línea base del gradiente* (SGB) y se calcula como el valor medio del SGT desde el centro del plasma hasta dos posiciones radiales antes del ETG:

$$SGB = \text{media}(SGT(c), SGT(c+1), \dots, SGT(j-2)) \quad (10.10)$$

donde  $c$  es la posición radial del centro del plasma y  $j$  es la posición radial de la ETB.

Es posible cuantificar el ETG de un plasma en modo H usando la SGB como referencia del gradiente de temperatura. Este valor ha sido denominado

coeficiente del gradiente de temperatura en el borde ( $ETG_{coef}$ ) y es estimado como el valor más alto del SGT cercano al borde del plasma ( $SGT_{ETB}$ ) partido por la SGB:

$$ETG_{coef} = \frac{SGT_{ETB}}{SGB} \quad (10.11)$$

Cuanto mayor sea la diferencia entre el  $SGT_{ETB}$  y la  $SGB$ , mayor será el coeficiente  $ETG_{coef}$ . El  $ETG_{coef}$  es igual a 1 si  $SGT_{ETG} = SGB$ . Eso implica que el SGT en el centro del plasma es igual al SGT en el borde del plasma (no hay ETB). El  $ETG_{coef}$  podría ser menor que la unidad si el gradiente de temperatura en la ETB es menor que el gradiente medio en el centro del plasma.

#### 10.1.4.1 Degradación del gradiente de temperatura entre dos tiempos

Para medir la degradación del ETG en cierto instante, es necesario determinar un tiempo de referencia para compararlo. Aquí, el  $ETG_{coef}$  del instante de referencia se ha llamado  $ETG_{coef}^{ref}$ . Entonces, la degradación del ETG entre un tiempo  $t$  ( $ETG_{coef}^t$ ) y el tiempo de referencia se calcula como:

$$degrad \left( ETG_{coef}^{ref}, ETG_{coef}^t \right) = 1 - \frac{ETG_{coef}^t - 1}{ETG_{coef}^{ref} - 1} \quad (10.12)$$

Si se estudian dos tiempos cercanos (separados por unos pocos milisegundos) la ET en la centro del plasma es casi constante. Por tanto, la SGB no se altera y es posible considerar que  $SGB^{ref} \approx SGB^t$ . Usando esta simplificación y operando se puede obtener que:

$$degrad \left( ETG_{coef}^{ref}, ETG_{coef}^t \right) = \frac{SGT_{ETB}^{ref} - SGT_{ETB}^t}{SGT_{ETB}^{ref} - SGB} \quad (10.13)$$

#### 10.1.4.2 Degradación del ETG durante los ELMs

La degradación del ETG causada por un ELM puede ser estudiada usando el perfil de la ET. La reducción de la densidad y la temperatura en el borde del plasma llevan a una caída del ETG. La densidad y temperatura suben después del ELM y el ETG aparece de nuevo en el borde del plasma.

Esta técnica de cuantificación de la degradación del ETG ha sido aplicada para analizar el ETG durante los ELMs en JET. Más de 700 pulsos de las campañas de JET desde la C15a hasta la C26 y más de 46,000 ELMs fueron analizados. El tiempo de referencia fue asignado al tiempo del ELM menos 2 ms ( $ELM - 2$ ) y el tiempo donde la degradación del ETG se ha cuantificado fue asignado al tiempo del ELM más 2 ms ( $ELM + 2$ ).

Pulsos	ELMs	ELMs con el ETG recuperado	Valor medio de la degradación del ETG (casos no recuperados)
<b>Campaña 15a</b>			
8	846	455 (53.786%)	22.710%
<b>Campaña 15b</b>			
23	1,136	463 (40.757%)	27.235%
<b>Campaña 16, 17</b>			
138	8,893	3,088 (34.724%)	22.263%
<b>Campaña 18</b>			
19	863	283 (32.797%)	20.363%
<b>Campaña 19</b>			
5	74	14 (18.919%)	37.958%
<b>Campaña 20</b>			
67	3,762	509 (13.530%)	30.761%
<b>Campaña 21</b>			
39	2,425	635 (26.186%)	28.668%
<b>Campaña 22</b>			
49	2,594	408 (15.729%)	24.791%
<b>Campaña 23</b>			
108	6,293	1,233 (19.593%)	21.642%
<b>bf Campaña 24</b>			
10	436	48 (11.009%)	33.772%
<b>Campaña 25</b>			
60	2,586	527 (20.379%)	26.126%
<b>Campaña 26</b>			
222	16,279	3,687 (22.649%)	22.376%
<b>Total</b>			
748	46,187	11,350 (24.574%)	23.948%

Table 10.3: Resultados de la degradación 2 ms después del ELM en JET

La Tabla 10.3 muestra los resultados obtenidos tras el análisis del ETG. La primera columna contiene el número de pulsos que han sido analizados en cada campaña. La segunda muestra el número de ELMs analizados en cada campaña. El número de ELMs que han recuperado el ETG inicial 2 ms después de los instantes de los ELMs ( $\text{degrad} \left( \text{ETG}_{coef}^{ELM-2}, \text{ETG}_{coef}^{ELM+2} \right) \leq 0$ ) se muestra en la tercera columna. Este experimento mostró que 11,350 (24.574%) ELMs habían recuperado su ETG 2 ms después del tiempo de los ELMs. Por lo tanto, hubo 34,837 (75.4236%) ELMs con una degradación mayor que 0. Finalmente, la última columna de la Tabla 10.3 contiene la degradación del ETG de los ELMs con una degradación mayor que 0, 2 ms después de los tiempos de los ELMs. El valor medio de la degradación del ETG fue del 23.948%.

### 10.1.5 Discusión

Habitualmente, los fenómenos del plasma están caracterizados por eventos de alta frecuencia en señales (picos o caídas). Por ello, puede pensarse que otras técnicas existentes para localizar eventos de alta frecuencia en señales, como las “wavelets”, pueden proporcionar resultados similares. Usando wavelets, es posible encontrar una base local discriminante tal como describe (Saito and Coifman, 1995). Usando esta base, pueden localizarse los eventos de alta frecuencia. Pero las capacidades de búsqueda de UMEL son están restringidas a los eventos de alta frecuencia. También localiza segmentos de señales que muestran patrones especiales aunque tengan bajas frecuencias.

La Figura 4.16 contiene un ejemplo del análisis de una función sinusoidal usando wavelets y UMEL. El valor absoluto de los coeficientes de detalle de la función sinusoidal se han dibujado en la Figura 4.16a. Es posible observar que los mayores valores de los coeficientes de detalle están situados en los segmentos rectos de la función sinusoidal (líneas verdes verticales, son los puntos con las mayores diferencias de amplitud y, por tanto, su coeficientes de detalle wavelet son los más grandes). Desafortunadamente, estos segmentos no son los que tienen la información más interesante. La Figura 4.16b muestra el análisis llevado a cabo usando UMEL. En este caso, los ESVs aparecen exactamente en los puntos donde los coeficientes de detalle wavelet son más bajos. Estos puntos donde aparecen los ESVs son los más relevantes de la señal.

Es también importante mencionar que UMEL no puede ser aplicado usando una técnica de regresión diferente. En SVR, el ajuste es función del ancho del  $e$ -tube. Como consecuencia, el ajuste es diferente para diferentes valores del parámetro  $e$ . Por tanto, los ESVs no pueden ser obtenidos usando una técnica de regresión diferente simplemente localizando las muestras con un valor residual igual o mayor que  $e$ . También es importante aclarar que los ISVs no pueden ser determinados usando una técnica de regresión diferente

y que éstos proporcionan información útil.

Finalmente, debe destacarse la importancia de la elección de los parámetros de UMEL. El *kernel* SVR,  $K_C$ ,  $K_e$  y  $K_\sigma$  deben ser elegidos de acuerdo con los fenómenos que están siendo localizados en las señales. Cada tipo de evento requiere diferentes parámetros que deben ser ajustados antes del análisis. Afortunadamente, una vez que los parámetros han sido fijados, éstos pueden ser aplicados a un amplio rango de descargas de plasma sin cambios.

## 10.2 Análisis en 2D usando UMEL

En los últimos años, el uso de cámaras como diagnósticos del plasma se ha extendido a lo largo de la comunidad de fusión. Las cámaras permiten la visualización de los procesos que tienen lugar dentro de la cámara de vacío en ambos espectros, el visible y el infrarrojo. Estos nuevos diagnósticos se han usado, entre otros, para medir la temperatura de los componentes de la pared y del divertor, el análisis de la deposición de los flujos de energía y potencia o el análisis de impurezas.

Se pretende que ITER use cámaras como una fuente principal de información para control y adquisición de datos. La red de cámaras planeada para ITER consiste en 36 cámaras del espectro visible e infrarrojo que generarán datos a una velocidad de 10 GByte/s. Como consecuencia, el análisis de los datos generados por las cámaras es una tarea abrumadora.

La única opción para interpretar los datos generados por las cámaras es probablemente el uso de herramientas de análisis automático. Estas herramientas convierten las secuencias de imágenes en señales de control, nuevas entradas en bases de datos o figuras inteligibles para diferentes estudios del plasma. Es posible distinguir dos grupos principales de aplicaciones de análisis de imágenes:

1. **Aplicaciones en tiempo real:** monitorizan el estado del plasma en tiempo real y están capacitadas para mandar señales de control, como alarmas, si detectan eventos peligrosos.
2. **Aplicaciones off-line:** sus cálculos requieren más tiempo y por tanto, no pueden ser aplicadas en el control on-line. Localizan y determinan la existencia de eventos del plasma como ELMs o MARFEs.

Dentro del primer grupo conviene destacar la medida de temperatura de los componentes de la pared de la cámara de vacío usando cámaras del espectro infrarrojo y el seguimiento de los pellets<sup>1</sup>. La medida de la temperatura de los componentes de la pared se lleva a cabo usando la intensidad de los

---

<sup>1</sup>**Pellet:** bolas milimétricas de isótopos de hidrógenos congeladas para alimentar el plasma

pixels en áreas fijas de la imagen. Esta técnica ha sido aplicada a JET (Gauthier et al., 2007) y ha sido implementada usando FPGAs en el Tore Supra (Martin et al., 2010).

La variedad de las aplicaciones del segundo grupo es mayor. El análisis off-line permite cálculos más complejos y, por tanto, estudios más sofisticados. Uno de los problemas resueltos usando análisis off-line es el seguimiento de partículas de polvo dentro de la cámara de vacío. Cuando la concentración de polvo es alta, puede poner en peligro la operación del plasma. El seguimiento de estas partículas durante la operación ha sido llevado a cabo en ASDEX y en Tore Supra en 2D (Hong et al., 2010) y en NSTX en 3D usando dos cámaras simultáneamente (Roquemore et al., 2007). Estas aplicaciones permiten el estudio de las trayectorias del polvo y cómo el plasma es afectado por ellas.

Los MARFEs también han captado la atención de los científicos. Se trata de inestabilidades que pueden reducir el confinamiento del plasma y pueden incluso causar disrupciones. Los MARFEs pueden ser identificados usando cámaras del espectro visible. Este fenómeno ha sido identificado en JET usando el método del flujo óptico (Craciunescu et al., 2011) y redes celulares no lineales (CNN) (Murari et al., 2011).

Las técnicas de reconocimiento de patrones aplicadas a imágenes también pertenecen a este segundo grupo. La búsqueda de patrones en imágenes requiere mucho tiempo y, por tanto, no puede ser aplicada on-line. Un ejemplo es la localización de patrones en películas de JET (Vega et al., 2009a). Los patrones devueltos son ordenados usando una medida de similaridad.

Los métodos de clasificación de imágenes caen en la frontera de ambos grupos. El uso de estos métodos puede ser on-line u off-line dependiendo del método usado para resolver el problema. Un ejemplo de clasificación de imágenes es la clasificación de las imágenes del Thomson scattering en el stellarator TJ-II usando predictores conformales (Vega et al., 2010b).

El análisis de imágenes usando UMEL pertenece al grupo de las aplicaciones off-line. UMEL puede ser aplicado con un doble propósito (González et al., 2010):

1. **Localización temporal de eventos:** consiste en localizar los frames donde cada evento o un conjunto de eventos tienen lugar. Los tiempos de los eventos son dados por los tiempos de los frames donde han sido localizados.
2. **Detección de regiones de interés (ROIs, por sus siglas en inglés):** en una imagen, no todos los píxeles contienen la misma cantidad de información y, por ello, no todos los píxeles tienen la misma relevancia. Por ejemplo, los píxeles del fondo de una imagen contienen menos información (son menos relevantes) que los píxeles del foco de la imagen. Una ROI es un conjunto de píxeles conectados (adyacentes) con

un alto nivel de relevancia. Usando UMEL, los píxeles donde aparecen los ESVs son los píxeles con la mayor relevancia. Además, es posible estudiar la evolución de las ROIs usando *mapas de calor*.

UMEL analiza cada frame por separado, por lo que es fácilmente paralelizable. Una vez que han sido analizados, los resultados se juntan y son interpretados para identificar los eventos y para estudiar la evolución de las ROIs. UMEL no hace distinción entre los tipos de películas y, por tanto, puede ser aplicado a películas infrarrojas y visibles.

### 10.2.1 Localización de eventos en películas

Una de las capacidades de UMEL es la localización de eventos en películas de plasma. Los SVs aparecen en aquellas áreas con un alto gradiente de intensidad entre píxeles vecinos y en aquellas que son difíciles de ajustar. En el caso de las películas del espectro infrarrojo y visible, estas zonas de altos gradientes se identifican como áreas de altas emisiones.

En las películas de infrarrojo, los eventos más interesantes son los puntos calientes. Estos eventos son choques del plasma contra los componentes de la pared que causan un incremento de su temperatura. En las películas de infrarrojo, los puntos calientes son detectados por un aumento de la intensidad de los píxeles en las zonas calientes. Esto hace que el número de SVs aumente abruptamente.

También es posible localizar eventos de interés en películas del espectro visible. En este caso, estos eventos se corresponden con MARFEs, interrupciones, pellets u OVNI<sup>2</sup>. Todos estos eventos causan un incremento de la emisión de luz del plasma y por ello un aumento de la intensidad de los píxeles.

### 10.2.2 Detección de ROIs

Un importante uso de UMEL es la localización de ROIs en imágenes. Dado que todos los píxeles no contienen la misma cantidad de información, no todas las regiones tienen el mismo nivel de relevancia. Las ROIs son áreas de una imagen donde aparecen un gran número de SVs. Los SVs aparecen en las áreas más difíciles de ajustar y donde existen grandes diferencias de intensidad entre píxeles vecinos.

Usando UMEL, existen dos opciones diferentes para localizar ROIs:

1. **Usando todos los SVs:** los SVs aparecen en las áreas de las imágenes que son relevantes para calcular la superficie de regresión. Usando esta alternativa, los SVs pueden aparecer en todos los puntos de la ROI (bordes e interior).

---

<sup>2</sup>OVNI<sup>s</sup>: Objeto Volador No Identificado

2. **Usando únicamente los ESVs:** los ESVs aparecen sólo en aquellas áreas con una alta variación entre píxeles vecinos. Por tanto, pueden ser usados para localizar los bordes de las áreas de emisión.

### 10.2.3 Evolución de las ROIs: mapas de calor

Los mapas de calor son imágenes que resumen la evolución de las ROIs a lo largo de los frames de una película. Son muy útiles para analizar un conjunto de frames usando únicamente una sola imagen. La intensidad de un píxel en mapa de calor depende de la actividad de ese píxel en un conjunto de frames (o en la película entera). Cuanta más actividad tenga el píxel, mayor será su intensidad en el mapa de calor.

La actividad de un píxel puede ser entendida de diversas maneras, por ejemplo, el valor absoluto de la intensidad, un valor booleano que muestre si la intensidad del píxel está por encima de un determinado umbral, el valor medio de la intensidad de los píxeles vecinos, etc. Aquí, la presencia o ausencia de un SV en un píxel se usa como actividad del píxel. La intensidad de los píxeles del mapa de calor es una función del número de SVs en cada píxel. Dado un píxel de un mapa de calor, su intensidad depende del número de SVs que han aparecido en este píxel en los frames analizados (cuando mayor sea el número de SVs, mayor será la intensidad del píxel en el mapa de calor).

### 10.2.4 Localización de puntos calientes

La localización de eventos en películas de plasma usando UMEL fue probada en 10 películas del infrarrojo de JET. Los puntos calientes fueron localizados usando UMEL y la transformada wavelet. Las películas contenían 819 frames cada una.

La localización de eventos usando wavelets se basa en los valores de los coeficientes de detalle. Para cada frame de las películas se calcula una transformada wavelet (familia Daubechies de orden 2). Los coeficientes de detalle horizontales, verticales y diagonales se suman y se normalizan entre 0 y 1. Para cada frame, se cuenta el número de píxeles con un valor de la suma de los coeficientes de detalle por encima de un determinado umbral. El valor del umbral se ha establecido empíricamente a 0.45.

UMEL se aplica de nuevo para localizar de forma automática los puntos calientes en ambos, el número de SVs en cada frame y el número de píxeles en cada frame con un valor wavelet mayor que el coeficiente. Los ESVs aparecen en los picos de ambos gráficos y por lo tanto, los puntos calientes son localizados sin intervención humana. La Figura 4.22 muestra los resultados obtenidos con ambos métodos. Es posible observar que la existencia de puntos calientes está mejor indicada por UMEL.

El rendimiento de la localización de puntos calientes usando UMEL y los

Método	Puntos calientes detect.	Aciertos	Falsos negativos	Falsos positivos	Tiempo (s)
<b>Pulso 73337, 97 puntos calientes</b>					
UMEL	96	90 (92.78%)	7 (7.22%)	6 (6.25%)	3,282
Wavelet	74	64 (65.98%)	33 (34.02%)	10 (13.51%)	65
<b>Pulso 73339, 152 puntos calientes</b>					
UMEL	143	142 (93.42%)	10 (6.58%)	1 (0.70%)	3,464
Wavelet	123	110 (72.37%)	42 (27.63%)	13 (9.76%)	64
<b>Pulso 73340, 143 puntos calientes</b>					
UMEL	132	130 (90.91%)	13 (9.09%)	2 (1.52%)	3,299
0.8 Wavelet	111	99 (69.23%)	44 (30.77%)	12 (10.81%)	64
<b>Pulso 73344, 134 puntos calientes</b>					
UMEL	129	127 (94.78%)	7 (5.22%)	2 (1.55%)	3,552
Wavelet	105	94 (70.15%)	40 (29.85%)	11 (10.48%)	64
<b>Pulso 73558, 91 puntos calientes</b>					
UMEL	86	84 (92.31%)	7 (7.69%)	2 (2.32%)	3,904
Wavelet	79	65 (71.43%)	26 (28.57%)	14 (17.72%)	68
<b>Pulso 73559, 107 puntos calientes</b>					
UMEL	91	90 (84.11%)	17 (15.89%)	1 (1.10%)	3,098
Wavelet	68	62 (57.94%)	45 (42.06%)	6 (8.82%)	68
<b>Pulso 73561, 98 puntos calientes</b>					
UMEL	98	88 (89.90%)	10 (10.20%)	10 (10.20%)	10,935
Wavelet	65	51 (52.04%)	47 (47.96%)	14 (21.54%)	66
<b>Pulso 74200, 45 puntos calientes</b>					
UMEL	46	44 (97.78%)	1 (2.22%)	2 (4.34%)	3,842
Wavelet	54	36 (80.00%)	9 (20.00%)	18 (33.34%)	64
<b>Pulso 74602, 134 puntos calientes</b>					
UMEL	127	119 (88.81%)	15 (11.19%)	8 (6.30%)	1,478
Wavelet	107	96 (71.64%)	38 (28.36%)	11 (10.28%)	64
<b>Pulso 74619, 64 puntos calientes</b>					
UMEL	63	62 (96.88%)	2 (3.12%)	1 (1.59%)	3,844
Wavelet	60	49 (76.56%)	15 (23.44%)	11 (18.33%)	65
<b>Total: 1,065 hot spots, 10 puntos calientes</b>					
UMEL	1011	976 (91.64%)	89 (8.36%)	35 (3.46%)	40,698
Wavelet	846	726 (68.17%)	339 (31.83%)	120 (14.18%)	652

Table 10.4: Resultados de la localización de puntos calientes

coeficientes wavelet fue probado en 10 películas infrarrojas de JET. La Tabla 10.4 contiene los resultados obtenidos por ambos métodos. Esta prueba fue ejecutada usando un procesador Intel® Core™ 2 Quad CPU Q9300 2.50GHz, 1.95GB RAM. La primera columna de la tabla corresponde con el método usado. La segunda identifica el número de puntos calientes detectados por cada método. Estos puntos calientes pueden contener errores y pueden no detectar puntos calientes reales. La tercera columna es el número de aciertos, esto es, el número de puntos calientes reales detectados por los métodos. La cuarta columna es el número de *falsos negativos* (el número de puntos calientes reales no detectados por los métodos). La quinta columna contiene el número de *falsos positivos* (el número de falsas alarmas o el número de puntos calientes detectados por los métodos que no son reales). Finalmente, la sexta columna muestra el tiempo de CPU utilizado en el análisis de cada película.

La última fila de la Tabla 10.4 resume los resultados obtenidos en las 10 películas. La tasa media de aciertos usando UMEL fue del 91.64% frente al 68.17% usando wavelets. El porcentaje medio de falsos positivos fue del 3.46% usando UMEL frente al 14.18% usando wavelets. En contraste, los tiempos de CPU de UMEL fueron mucho mayores que los obtenidos por wavelets. Esta es una consecuencia del problema de optimización cuadrática que debe ser resuelto para cada frame de las películas usando UMEL.

### 10.2.5 Discusión

La desventaja más importante de la aplicación de UMEL a imágenes es probablemente su tiempo de cálculo. Dada la alta resolución de las cámaras de plasma, el tiempo de cálculo del problema de optimización necesaria para generar la superficie de ajuste es lento. Esto hace que UMEL no pueda aplicarse a problemas de control en tiempo real. A pesar de su tiempo de cálculo, la aplicación de UMEL al análisis off-line puede ser de gran interés para analizar los fenómenos físicos. También es posible acelerar el análisis de UMEL de dos formas diferentes:

1. **Usando los coeficientes wavelet de aproximación:** es posible reducir el tamaño de las imágenes analizadas por UMEL usando wavelets. Utilizando un nivel de descomposición apropiado, es posible conseguir resultados similares a los obtenidos usando las imágenes originales. Los tiempos de CPU se reducen significativamente usando la descomposición basada en wavelets.
2. **Usando paralelización:** UMEL se aplica independientemente a cada frame. Este puede ser fácilmente paralelizado si cada frame se analiza por separado en un ordenador diferente.

Existe también una interesante discusión relacionada con el uso de mapas de calor. Dado que las películas de plasma son bastante largas y que el plasma pasa por diferentes estados, sería interesante crear un mapa de calor de estado para resumir los diferentes comportamientos del plasma. La determinación de estos estados del plasma también puede hacerse automáticamente. Las películas pueden ser analizadas usando UMEL y después, el número de SVs puede ser contado. UMEL es capaz de detectar segmentos relevantes en el número de SVs y por tanto, puede determinar diferentes grupos de frames donde los mapas de calor podrían ser calculados.

### 10.3 Conclusiones

Este capítulo ha descrito UMEL (Vega et al., 2010a), una novedosa técnica para localizar eventos relevantes en señales e imágenes del plasma. UMEL aporta una nueva interpretación de los SVs: éstos aparecen en las muestras relevantes de las señales o imágenes originales. Los fenómenos del plasma se localizan tradicionalmente a través de la inspección visual de las señales. UMEL automatiza la localización de estos eventos y genera grandes bases de datos de fenómenos del plasma. Esta técnica es extremadamente importante dado que estudios posteriores usarán estas bases de datos para aumentar la significancia estadística de sus resultados.

UMEL conlleva el cómputo de un ajuste SVR. Este ajuste define las muestras que se convierten en ESVs e ISVs. Los ISVs son SVs que caen dentro del  $e$ -tube mientras que los ESVs caen fuera. Los ISVs son muestras necesarias para calcular la regresión pero no proporcionan el mismo grado de relevancia que los ESVs. Los ESVs están localizados en las muestras más difíciles de ajustar (los puntos de la señal original que descasan fuera del  $e$ -tube). Usando estos SVs, es posible localizar eventos y segmentos relevantes en señales e imágenes.

Para crear sistemas expertos que localicen los fenómenos del plasma sin intervención humana, se necesita combinar las capacidades de búsqueda de UMEL con conocimiento experto. Los expertos deben determinar los eventos que caracterizan un cierto fenómeno y entonces, UMEL puede localizar estos eventos en las señales e imágenes.

Se han construido tres sistemas expertos diferentes para localizar fenómenos del plasma:

- **Dientes de sierra:** pueden ser localizados usando la emisión de rayos X blandos. El patrón de los dientes de sierra cambia dependiendo de la cuerda de rayos X pero el mismo código de UMEL puede aplicarse a todas ellas. Usando UMEL, es posible automatizar el cálculo de la difusividad del plasma: usando los tiempos de un diente de sierra en la cuerda central y en el eje, la difusividad del plasma se calcula aplicando

la Ecuación 10.6.

- **Disrupciones:** un pico simultáneo del lazo de voltaje y una caída de la corriente del plasma determinan la existencia de una disrupción. Usando esta información, se construyó un sistema experto para localizar disrupciones usando UMEL. Una base de datos de 343 pulsos de JET fue analizada obteniendo un porcentaje de aciertos del 99.02% (Vega et al., 2010a). Las disrupciones localizadas ayudarán a los científicos a crear mejores modelos de disrupciones para mejorar su conocimiento de ellas o incluso predecirlas antes de que ocurran.
- **ELMs:** un ELM puede ser identificado como una caída de la energía diamagnética acompañada por un pico de la señal  $D_\alpha$ . Más de 1,200 pulsos de JET fueron analizados, localizando 226,751 ELMs con una tasa de aciertos del 95%. El periodo más común de los ELMs fue entre 20 ms y 30 ms (61,373 ELMs) (González et al., 2010a). Los ELMs localizados serán útiles para mejorar los modelos teóricos de ELMs y para aumentar la significancia estadística de estudios futuros.

Una de las aplicaciones de la localización automática de ELMs es el análisis de los perfiles de temperatura durante éstos. Los perfiles de temperatura de 46,187 ELMs de 748 pulsos de JET fueron analizados automáticamente. Los resultados mostraron que en el 24.574% de los ELMs, el gradiente de temperatura estaba recuperado 2 ms después de la caída del ELM y la degradación media de los casos no recuperados fue del 23.948%. Este método automático de análisis de los perfiles de temperatura será especialmente relevante en el análisis de la degradación causada por los ELMs bajo diferentes configuraciones del plasma, especialmente después de la instalación de una nueva pared similar a la de ITER en JET.

Debido al gran desarrollo de las cámaras como diagnósticos del plasma en los últimos años, el análisis de las películas se ha convertido en un tema candente en la fusión de plasmas. UMEL será una útil herramienta para estudiar estas películas sin interacción humana (González et al., 2010). Usando el número de SVs en cada frame, UMEL localizó las ocurrencias de puntos calientes en películas del espectro infrarrojo de JET. La localización de los SVs en cada frame reveló el área más caliente de la cámara de vacío: el divertor.

El comportamiento del plasma en películas del espectro visible también se analizó usando UMEL. Los eventos del plasma están caracterizados por su alta emisión y por ello, los SVs aparecen en estas áreas. Usando mapas de calor, es posible estudiar la evolución del plasma a lo largo de los frames de una película. Los mapas de calor pueden ser calculados usando los frames de las regiones de interés calculadas por UMEL.

---

El inconveniente más importante de UMEL es probablemente su tiempo de cálculo. Este problema puede ser mitigado usando una versión paralela de SVM (Ramírez et al., 2010). En el caso de las películas, el análisis de UMEL puede ser acelerado de forma sencilla: cada frame puede ser analizado en una CPU diferente y entonces, el número total de SVs en cada frame se analiza con la versión SVM paralela (si el número de frames analizados es muy grande). También es posible calcular un ajuste SVR para cada frame usando la versión paralela de SVM.



## Chapter 11

# Técnicas de reducción de dimensionalidad

Durante la operación del plasma, docenas de diagnósticos miden propiedades del plasma tales como corriente, densidad o temperatura. Estos diagnósticos generan flujos de parejas de datos o *muestras*  $(t_i, x_i)$  donde  $x_i$  es la magnitud de la medida en el tiempo  $t_i$ . Estos flujos son habitualmente conocidos como *ondas* o *señales* y pueden contener miles de pares de datos. Algunos diagnósticos producen múltiples señales para describir la misma característica del plasma y por tanto, generan información que está correlacionada. Además, la mayoría de las magnitudes del plasma pueden ser medidas utilizando diferentes diagnósticos.

Algunas señales son relevantes para describir un cierto fenómeno físico pero otras no lo son. Dado un conjunto de datos en un espacio de características de dimensión  $p$ , el objetivo básico de las técnicas de selección de características es determinar un espacio transformado o reducido de dimensión  $q$ , donde  $q < p$ , conservando la máxima varianza del espacio de características original. En el caso de las tareas de clasificación, en vez de la varianza, los métodos deberían maximizar la tasa de aciertos de la clasificación en el espacio de características resultante.

Aquí se describen dos técnicas desarrolladas para la reducción de la dimensionalidad: un sistema de extracción de características basado en SVM para datos multidimensionales y un extractor de regiones para la clasificación de imágenes.

### 11.1 Sistema de extracción de características SVM

En un espacio de características multidimensional, no todas las dimensiones (características) tienen el mismo nivel de relevancia. Dado un problema de clasificación, las características más relevantes son aquellas que permiten la

clasificación de las muestras en el espacio de características reducido minimizando el número de errores. El objetivo del *sistema de extracción de características SVM* (SVM-FES, por sus siglas en inglés) es realizar una identificación automática de esas características en grandes conjuntos de datos.

El SVM-FES está basado en el cálculo de un *hiperplano de separación* que divide el espacio de características en dos regiones diferentes (una para cada clase). La ecuación del hiperplano de separación se usa para descartar la dimensión menos relevante del espacio de características. Dada la ecuación de un hiperplano lineal en un espacio  $n$ -dimensional:

$$C_1 \cdot X_1 + C_2 \cdot X_2 + \dots + C_n \cdot X_n + C_0 = 0 \quad (11.1)$$

donde:

- $C_i$  : coeficiente o peso de la dimensión  $i$  ( $1 \leq i \leq n$ )
- $X_i$  : dimension  $i$
- $C_0$  : término independiente

las características más relevantes son aquellas cuyos valores absolutos  $C_i$  son mayores.

Dado un modelo SVM que usa un *kernel* lineal, la ecuación del hiperplano óptimo de separación está dada por:

$$\begin{aligned} D(x) &= \sum^{SV} \alpha_i y_i [X \cdot x_i] + b_0 \\ D(x) &= \sum^{SV} \alpha_i y_i [(X_1, \dots, X_n) \cdot (x_{i,1}, \dots, x_{i,n})] + b_0 \\ D(x) &= \sum^{SV} \alpha_i y_i [x_{i,1} X_1 + \dots + x_{i,n} X_n] + b_0 \\ D(x) &= \sum^{SV} [\alpha_i y_i x_{i,1} X_1 + \dots + \alpha_i y_i x_{i,n} X_n] + b_0 \\ D(x) &= \left( \sum^{SV} \alpha_i y_i x_{i,1} \right) X_1 + \dots + \left( \sum^{SV} \alpha_i y_i x_{i,n} \right) X_n + b_0 \quad (11.2) \end{aligned}$$

donde:

- $n$  : número de dimensiones del espacio de entrada
- $y_i$  : etiqueta de  $SV_i$
- $\alpha_i$  : multiplicador de Lagrange de  $SV_i$
- $b_0$  : término independiente

Por lo tanto, dado un modelo SVM que usa un *kernel* lineal, es posible obtener la ecuación de su hiperplano de separación óptimo en la forma de la

Ecuación 11.1 donde:

$$C_j = \sum_{i=1}^{SV} \alpha_i y_i x_{i,j}, \quad 1 \leq j \leq n, \quad C_0 = b_0 \quad (11.3)$$

En un espacio de dimensión  $n$ , el SVM-FES descarta la dimensión con el coeficiente absoluto más bajo. Entonces, un nuevo hiperplano de separación es calculado en un espacio de dimensión  $n - 1$ . El proceso continua hasta que no hay más dimensiones que descartar. La dimensión resultante del espacio de características puede ser determinada usando la tasa de aciertos (el proceso se detiene cuando la tasa de aciertos cae drásticamente) o, en el caso de SVM, usando el número de SVs. El número de SVs de un modelo está dado por la complejidad del modelo y el número de muestras mal clasificadas. Por lo tanto, usando el número de SVs, el proceso se detiene cuando su número se dispara.

### 11.1.1 Extracción de características de la transición L/H

El objetivo de este experimento era encontrar el conjunto de señales (características) que mejor describan el fenómeno de la transición L/H. Se han seleccionado 28 señales como candidatas para definir la transición. La lista completa de señales puede encontrarse en el Apéndice F (en inglés).

Se consideraron dos modelos diferentes:

- **Modelo  $\pm 100$ :** modelo entrenado en el intervalo  $\pm 100$  ms alrededor de las transiciones.
- **Modelo  $\pm 500$ :** modelo entrenado en el intervalo  $\pm 500$  ms alrededor de las transiciones.

Las señales originales fueron remuestreadas a 1 kHz (1000 muestras por segundo). Por lo tanto, el modelo  $\pm 100$  ms usó 201 muestras por descarga ( $0.1 \cdot 2 \cdot 1000 = 200$  muestras + instante transición) y el modelo  $\pm 500$  ms usó 1001 muestras por descarga ( $0.5 \cdot 2 \cdot 1000 = 1000$  muestras + instante transición). El conjunto de entrenamiento incluyó 551 pulsos de JET desde la campaña C21 hasta la C26. Las muestras donde una o más señales no fueron digitalizadas fueron descartadas.

Dado que las amplitudes de las señales difieren, deben ser normalizadas para evitar problemas de escala en la selección de las más importantes. Se probaron tres normalizaciones diferentes, obteniendo los mejores resultados con la normalización entre 0 y 1:

$$S_{normalizada} = \frac{S - \min(S)}{\max(S) - \min(S)}, \quad (11.4)$$

El proceso completo del SVM-FES puede verse en las Tablas F.1, F.2, F.3 (modelo  $\pm 100$  ms), F.4, F.5 y F.6 (modelo  $\pm 500$  ms). El espacio resultante

Señal	Descripción	Coef.
<b>Modelo <math>\pm 100</math> ms</b>		
<b>BT</b>	Campo magnético toroidal	8.129
<b>LI</b>	Inductancia del plasma	-5.022
<b>Q95</b>	Factor de seguridad en $\text{PSI} = 0.95$	6.333
<b>RIG</b>	Espacio radial interior	-2.507
<b>AD36</b>	Cuerda interna de $D_\alpha$	-9.636
<b>TOG</b>	Espacio exterior superior	4.283
<b>RAD</b>	Potencia radiada	-83.827
<b>TE02</b>	Temperatura electrónica en $\text{PSI} = 0.2$	8.851
<b>LAD3</b>	Densidad de línea media en el centro del plasma	-7.452
<b>LAD4</b>	Densidad de línea media en el borde del plasma	32.191
<b>TE08</b>	Temperatura electrónica en $\text{PSI} = 0.8$	91.244
<b>Modelo <math>\pm 500</math> ms</b>		
<b>BT</b>	Campo magnético toroidal	6.719
<b>AD36</b>	Cuerda interna de $D_\alpha$	-17.809
<b>LAD3</b>	Densidad de línea media en el centro del plasma	-27.102
<b>LAD4</b>	Densidad de línea media en el borde del plasma	43.207
<b>TE08</b>	Temperatura electrónica en $\text{PSI} = 0.8$	374.425

Table 11.1: Señales seleccionadas por el SVM-FES y sus coeficientes para los modelos  $\pm 100$  ms y  $\pm 500$  ms

del modelo  $\pm 100$  ms estaba formado por las últimas 11 señales descartadas por el SVM-FES. Estas señales y sus coeficientes pueden encontrarse en la Tabla 11.1. El espacio seleccionado para el modelo  $\pm 500$  ms estaba formado por las últimas 5 dimensiones descartadas por el SVM-FES. La Tabla 11.1 contiene estas señales y sus coeficientes.

Es importante destacar que las características del modelo  $\pm 500$  ms seleccionadas por el SVM-FES eran un subconjunto de las seleccionadas para el modelo  $\pm 100$  ms. Esto significa que estas señales eran suficientemente adecuadas para la descripción fenomenológica de la función de decisión. A pesar de ello, dado que el clasificador más cercano a la transición era más complejo, necesita más información para obtener una tasa de aciertos alta.

Las tasas de acierto de los modelos fueron del 93.404% en el caso del modelo  $\pm 100$  ms y del 97.436% en el caso del modelo  $\pm 500$  ms. Es importante mencionar que una mayor tasa de aciertos del modelo  $\pm 500$  ms no significa una mayor precisión en la determinación de las transiciones L/H. De hecho, la precisión del modelo  $\pm 500$  fue menor que la del modelo  $\pm 100$  ms. Sus errores medios en la determinación de los tiempos de las transiciones L/H

son<sup>1</sup>:

$$\text{Modelo } \pm 100 \text{ ms: } (2 \cdot 100 + 1) \cdot (1 - 0.934041) = 13.258 \text{ ms}$$

$$\text{Modelo } \pm 500 \text{ ms: } (2 \cdot 500 + 1) \cdot (1 - 0.974359) = 25.667 \text{ ms}$$

Dada la alta dimensionalidad del espacio de características y el gran número de muestras, los modelos han sido entrenados usando EULER, el *cluster* de computación del CIEMAT (Acero et al., 2009). EULER usa una versión paralela de SVM (Ramírez et al., 2010) que permite entrenar modelos usando muchas muestras y dimensiones en tiempos pequeños.

### 11.1.2 Discusión

El SVM-FES asume que las muestras están distribuidas aleatoriamente en el espacio de características. Si esta suposición no es cierta, las características seleccionadas por el SVM-FES podrían no ser las características que permitan la división del espacio de características minimizando el número de errores. La Figura 5.6 contiene un ejemplo de un conjunto de datos mal condicionado. La ecuación del hiperplano de separación es  $10X - 8Y - 10 = 0$ . Usando el criterio del SVM-FES, la característica más relevante es  $X$ . El hiperplano  $X - 5.1 = 0$  (línea vertical punteada) divide el espacio cometiendo tres errores. En contraste, el hiperplano  $Y - 5 = 0$  (línea horizontal punteada) comete un solo error. Esto es una consecuencia de la distribución de las muestras en el espacio de características. Más específicamente, es una consecuencia de la muestra situada en  $[8.5, 8]$ , lejos de las muestras de su misma clase.

Los SVs considerados en la Figura 5.4 están formados por los errores del modelo y por las muestras que propiamente definen el hiperplano de separación. Para permitir una más precisa estimación de la complejidad del modelo generado por SVM, el número de errores debe ser restado del número total de SVs.

En cada paso, la metodología SVM-FES descarta la dimensión con el coeficiente más bajo. Esto implica que en un espacio  $n$ -dimensional, la metodología SVM-FES realiza  $n$  pasos. Cada paso requiere el cálculo de un modelo SVM y, si el conjunto de datos es grande, este proceso puede llevar mucho tiempo. El proceso puede ser acelerado si más de una dimensión es descartada en cada paso. Por ejemplo, las dimensiones con los  $n/t$  coeficientes más bajos pueden ser descartadas en cada paso por lo que el SVM-FES realizaría sólo  $t$  pasos. Las Tablas F.7 (modelo  $\pm 100$  ms) and F.8 (modelo  $\pm 500$  ms) del Apéndice F (en inglés) contienen los resultados del SVM-FES de la transición L/H cuando se descartan 3 características en cada paso. El espacio de características resultante del modelo  $\pm 100$  ms contiene

<sup>1</sup>dado que las señales han sido interpoladas a 1 kHz, cada muestra corresponde con 1 ms

13 características ( $\{BT, LI, Q95, ROG, AD36, TOG, RAD, TE02, CR0, RGEO, LAD3, LAD4, TE08\}$ ) y alcanza una tasa de acierto del 93.403%. El espacio de características resultante del modelo  $\pm 500$  ms está formado por 13 características ( $\{BT, ELO, TRIL, XPRL, RIG, ROG, AD36, ROG, CR0, RGEO, LAD3, LAD4, TE08\}$ ) y obtiene una tasa de aciertos del 97.750%. Dado que las señales se descartan en grupos de 3, los resultados no son tan precisos como los obtenidos anteriormente donde las señales se descartaban de una en una. También es posible fijar un valor umbral para los coeficientes del hiperplano de separación,  $C_\tau$  y entonces, todas las dimensiones con un coeficiente  $C_j < C_\tau$  son descartadas en cada paso. El proceso de extracción de características terminaría cuando no hubiera más dimensiones con coeficientes menos de  $C_\tau$ . Esta alternativa tiene el inconveniente de que el valor óptimo de  $C_\tau$  es desconocido a priori.

El SVM-FES usa una ecuación lineal para selección las dimensiones más relevantes del espacio de características. Si las muestras presentan dependencias no lineales en el espacio de características, el espacio resultante devuelto por SVM-FES puede no ser el más apropiado para clasificar las muestras. Desafortunadamente, usando por ejemplo un *kernel* RBF no es posible decidir cuáles son las características más importantes del espacio.

A pesar de que las características han sido seleccionadas usando un modelo lineal, también puede utilizarse un *kernel* RBF para generar un modelo en el espacio de características SVM-FES. En el caso del modelo  $\pm 100$  ms, el *kernel* RBF ha obtenido una tasa de aciertos del 98.861% con  $C = 200$  y  $\sigma = 0.316$  y en el caso del modelo  $\pm 500$  ms ha obtenido una tasa de aciertos del 98.261% usando los mismo parámetros.

## 11.2 Reducción de la dimensionalidad en imágenes

En una imagen, no todos los píxeles contienen la misma cantidad de información. Típicamente, los bordes de una imagen contienen menos información que el centro. Del mismo modo, los píxeles del fondo de una imagen no son tan relevantes como los situados en la parte central, que constituye el foco de interés de ésta.

Las técnicas actuales para analizar imágenes, como el flujo óptico (Horn and Schunck, 1981), son pesadas en términos de tiempos de computación. Centrándonos, por ejemplo, en un problema de clasificación SVM, éste requiere resolver un problema de optimización cuadrática para calcular el hiperplano de separación óptimo. Por tanto, la complejidad de la solución crece también cuadráticamente con el tamaño de los datos. Por ello, es necesario descartar las regiones irrelevantes de las imágenes para acelerar el cálculo de los diferentes métodos.

A continuación se describe RSIC: una metodología para la selección de regiones y la clasificación de imágenes. Una región relevante, o una región de

interés (ROI, por sus siglas en inglés) es un conjunto de píxeles conectados (adyacentes) que permiten la identificación de la clase de una imagen. La metodología está basada en una novedosa interpretación de las *medidas de no-conformidad*: son usadas para identificar la mejor ROI para clasificar la clase de una imagen. La combinación de las mejores ROI (una por clase) se usa para clasificar las nuevas imágenes.

Los objetivos de RSIC son:

1. **Identificación de las ROI de las imágenes:** una ROI contiene información adecuada para reconocer la clase de una imagen frente al resto.
2. **Reducción de la dimensión de las imágenes:** la dimensión de las imágenes originales queda reducida a la dimensión de las ROIs resultantes. Esto tiene un doble objetivo:
  - (a) **Reducción de los tiempos de entrenamiento y clasificación:** los sistemas son entrenados y las nuevas imágenes son clasificadas usando solamente un pequeño conjunto de los píxeles de las imágenes. Esto lleva a la reducción de los tiempos de CPU.
  - (b) **Reducción del espacio de almacenamiento de las imágenes:** si el objetivo de las imágenes es su clasificación, únicamente es necesario almacenar los píxeles de las ROIs.
3. **Creación de un clasificador exitoso:** aunque los tiempos de CPU y el espacio de almacenamiento fuesen reducidos, la metodología RSIC no tendría sentido si el clasificador construido usando las ROIs no obtuviese tasas de aciertos altas. Los predictores inductivos conformales (ICP, por sus siglas en inglés) son utilizados para construir el clasificador resultante. Además de la predicción, los ICP generan medidas conformales (credibilidad y confianza).

### 11.2.1 Metodología para la Selección de Regiones y la Clasificación de Imágenes

La metodología RSIC está compuesta por cinco pasos: división de las imágenes, construcción de los modelos, evaluación de las regiones, selección de las regiones y clasificación de las imágenes.

#### 11.2.1.1 Paso 1: división de las imágenes

El primer paso de la metodología RSIC conlleva la división de las imágenes en regiones más pequeñas. Este paso juega un papel fundamental en la metodología RSIC puesto que las regiones creadas aquí son las que serán evaluadas en los siguientes pasos (algunas de ellas contendrán información

adecuada para identificar la clase de una imagen y, por tanto, se convertirán en ROIs). Para obtener un buen sistema de clasificación se requiere una división apropiada o extensiva (muchas regiones diferentes a la espera de que alguna contenga información relevante) de las imágenes.

La división de las imágenes puede llevarse a cabo usando conocimiento experto. En este caso, las ROIs son identificadas por un experto. Estas ROIs contienen la información más relevante a priori. Esto ayuda al sistema a elegir las más adecuadas para identificar cada clase. En contraste, si no se dispone de conocimiento experto, las imágenes deben ser troceadas de una forma extensiva. De esta forma, se generarán muchas regiones, algunas de ellas probablemente solapadas.

### 11.2.1.2 Paso 2: construcción de los modelos

SVM en su versión uno frente al resto (OVR-SVM, por sus siglas en inglés) ha sido elegido para resolver el problema de clasificación multi-clase. En un problema de  $k$  clases, se construyen  $k$  clasificadores binarios. Cada clasificador binario genera un hiperplano de separación entre una clase y el resto ( $k-1$  clases). Una muestra nueva se asigna a la clase para la cual la distancia positiva<sup>2</sup> al hiperplano es máxima (Weston and Watkins, 1999).

Las partes de las imágenes generadas en el paso anterior se agrupan juntas por regiones (las partes de todas las imágenes de una misma región se agrupan juntas). El número de grupos es el mismo que el número de regiones. Un sistema OVR-SVM es entrenado usando cada uno de estos grupos. Los sistemas OVR-SVM son completamente independientes (son entrenados usando únicamente la información de sus regiones y deben ser capaces de clasificar imágenes usando únicamente la información de los píxeles contenidos en esas regiones). En un problema de clasificación con  $k$  clases, cada sistema OVR-SVM está formado por  $k$  clasificadores binarios. El número total de clasificadores binarios está dado por  $k \cdot r$  donde  $r$  es el número de regiones.

Para poder comparar los resultados generados por cada OVR-SVM, éstos son entrenados y calibrados usando el mismo conjunto de entrenamiento y calibración. Es importante destacar que las medidas de no-conformidad obtenidas por cada OVR-SVM no pueden ser comparadas si son entrados utilizando diferentes conjuntos.

### 11.2.1.3 Paso 3: evaluación de las regiones

El objetivo del tercer paso de la metodología RSIC es medir el rendimiento de cada OVR-SVM en la clasificación de una clase de imágenes. En un problema multi-clase, es posible que una región que identifica adecuadamente

---

<sup>2</sup>en este caso, la distancia es positiva si la muestra pertenece a la clase y negativa en caso contrario

una clase no sea capaz de distinguir otras clases. Por ello, el rendimiento de una región es calculado independientemente para cada clase. Esto permite que la metodología RSIC seleccione tantas regiones diferentes como clases.

El rendimiento del sistema OVR-SVM  $r$  (o lo que es lo mismo, una región<sup>3</sup>) en la clasificación de una clase dada  $t$  se calcula utilizando los valores de no-conformidad del conjunto de calibración del clasificador binario que distingue la clase  $t$  del resto de las clases ( $\alpha^{rt}$ ). Es importante recordar que cada sistema OVR-SVM contiene  $k$  clasificadores binarios, donde  $k$  es el número de clases.

La medida de no conformidad propuesta para la metodología RSIC está dada por la ecuación:

$$\alpha(x) = \begin{cases} -|dist(H, x)| & \text{si } x \text{ está correctamente clasificada} \\ |dist(H, x)| & \text{si } x \text{ está incorrectamente clasificada} \end{cases} \quad (11.5)$$

donde  $dist(H, x)$  es la distancia euclídea desde el hiperplano  $H$  a la muestra  $x$ . El signo de la distancia da la clase de  $x$  predicha. Por lo tanto,  $x$  está correctamente clasificada si  $signo(dist(H, x)) = y$  donde  $y$  es la clase real de  $x$  e incorrectamente clasificada en otro caso.

Usando esta medida de no-conformidad, los valores  $\alpha$  de las muestras correctamente clasificadas (verdaderos positivos -TP- y verdaderos negativos -TN-) son iguales o menores que cero ( $\alpha \leq 0$ ) y los valores  $\alpha$  de las muestras mal clasificadas (falsos positivos -FP- y falsos negativos -FN-) son positivos ( $\alpha > 0$ ). Por una parte, en la región en la que los valores  $\alpha^{rt}$  sean positivos, no ha sido posible construir un hiperplano de separación adecuado entre la clase  $t$  y el resto de las clases (existen errores de clasificación). Por otra parte, si los valores  $\alpha^{rt}$  son negativos, esto significa que el hiperplano construido por el clasificador SVM define de forma precisa la separación entre las clases (no existen errores de clasificación).

La calidad de una región  $r$  para clasificar una clase  $t$  está dada por:

$$q(r, t) = \frac{\left(\sum_{i=1}^{\#FN} \alpha_{FN,i}^{rt} + \sum_{j=1}^{\#FP} \alpha_{FP,j}^{rt}\right) \cdot PF + \sum_{k=1}^{\#TP} \alpha_{TP,k}^{rt}}{\#FN + \#FP + \#TP} \quad (11.6)$$

donde  $\#FN$ ,  $\#FP$  y  $\#TP$  son, respectivamente, el número de falsos negativos, falsos positivos y verdaderos positivos y  $PF$  es un *factor de penalización*.

Esta ecuación está formada por dos términos diferentes:

- **Términos positivos:** valores  $\alpha$  de las muestras FP y FN del conjunto de calibración. Estos valores están multiplicados por el PF. El objetivo del PF ( $PF \in [1, \infty]$ ) es penalizar los clasificadores que cometen errores.
- **Términos negativos:** valores de las muestras TP.

<sup>3</sup>cada sistema OVR-SVM se corresponde con una, y solamente una región

Cuanto más pequeño sea el valor  $q$  de la medida de calidad (un valor negativo muy grande) mejor es la región  $r$  para clasificar la clase  $t$ . Un valor pequeño de  $q$  significa que el clasificador binario de la región  $r$  ha calculado un hiperplano que maximiza la distancia desde las muestras al hiperplano de separación, y por tanto, es improbable cometer errores de clasificación. Por el contrario, un valor de  $q$  alto (un valor positivo) significa que las muestras de las clases están muy cercanas unas a otras en el espacio de características transformado, y por ello, es más probable cometer un error en la clasificación de una nueva muestra.

#### 11.2.1.4 Paso 4: selección de las regiones

La salida de la metodología RSIC es un clasificador OVR-SVM formado por los mejores clasificadores binarios. Para cada clase, todos los clasificadores binarios de las diferentes regiones son comparados y el mejor es elegido (basándose en la medida de calidad calculada en el paso anterior). Los clasificadores binarios elegidos se agrupan juntos en un único sistema OVR-SVM. El sistema OVR-SVM resultante contiene tantos clasificadores binarios como clases de imágenes (en un problema de clasificación de  $k$ -clases, contiene  $k$  clasificadores binarios, uno por cada clase).

Es posible que la misma región sea la mejor para clasificar todas las diferentes clases de imágenes. En este caso, a pesar de que la región usada por los clasificadores binarios es la misma, los clasificadores binarios son diferentes. Es importante tener en cuenta que los clasificadores son *binarios* (uno frente al resto). Por tanto, cada uno de los clasificadores debe identificar una clase frente al resto. Por otra parte, también es posible que  $k$  regiones diferentes de la imagen fuesen necesarias para construir el sistema OVR-SVM. Estas regiones pueden superponerse o pueden usar píxeles diferentes de la imagen.

### 11.2.2 Análisis de las imágenes del Thomson scattering del TJ-II

La cámara CCD del diagnóstico Thomson scattering del TJ-II (Herranz et al., 2003) genera imágenes en 2-D del espectro del plasma, con los ejes horizontales y verticales mostrando, respectivamente, la longitud de onda dispersa y la posición a lo largo de la cuerda del plasma. Usando el diagnóstico Thomson scattering se pueden medir los perfiles radiales de la densidad y la temperatura del plasma. Cada imagen del Thomson scattering pertenece a una de cinco clases diferentes: corte (CFF), fase de calentamiento electrón-ciclotrón (ECH), fondo (BCK), fase de inyección de neutros (NBI) y luz directa sin plasma o descarga colapsada (STR).

Hasta ahora, se han probado diferentes métodos para clasificar las imágenes del Thomson scattering del TJ-II: SVM(Vega et al., 2005), (Makili

et al., 2010), redes neuronales (Farias et al., 2005) y predictores conformales (Vega et al., 2010b), (Makili et al., 2011) y (Vega et al., 2012). Estos trabajos tienen en común que usan las imágenes completas para entrenar los sistemas y clasificar nuevas muestras sin tener en cuenta las diferentes cantidades de información proporcionadas por las diferentes regiones de las imágenes. También tienen en común el uso de la transformada wavelet de nivel 4 para reducir la dimensión de las imágenes originales. Sus mejores resultados oscilan entre el 90% (Farias et al., 2005) y el 98.68% (Makili et al., 2010).

El mayor número de imágenes analizadas en los trabajos anteriores es 599 (Makili et al., 2011). En este caso, 1,272 imágenes se utilizaron para probar la metodología RSIC. El tipo de imagen generada por el Thomson scattering depende del experimento llevado a cabo en el TJ-II. Por lo tanto, el número de imágenes disponibles en cada clase es diferente: 42 CFF, 517 ECH, 124 BCK, 366 NBI y 223 STR. La resolución de las imágenes del Thomson scattering es  $576 \times 385$  píxeles. Para acelerar el proceso RSIC, la dimensión de las imágenes se ha reducido a  $144 \times 97$  píxeles usando los coeficientes de aproximación wavelet de nivel 2. El conjunto de 1,272 imágenes fue aleatoriamente dividido en un conjunto de entrenamiento propio (25% de cada clase), un conjunto de calibración (25% de cada clase) y un conjunto de test (50% de cada clase). Como resultado, los conjuntos de entrenamiento propio y de calibración contenían 319 imágenes cada uno: 11 CFF, 129 ECH, 31 BCK, 92 NBI y 56 STR. El conjunto de test almacenaba 634 imágenes: 20 CFF, 259 ECH, 62 BCK, 182 NBI y 111 STR.

La división de las imágenes en el primer paso de la metodología RSIC se ha llevado a cabo sin utilizar conocimiento experto. Se sabe que el centro de las imágenes del Thomson scattering contiene la mayor parte de la información pero se debía incluir algunas regiones irrelevantes para probar el rendimiento de la metodología RSIC. Como alternativa, las imágenes han sido divididas en regiones rectangulares. La altura y la anchura de las imágenes fueron troceadas desde 2 hasta 8 partes, probando todas las combinaciones (por ejemplo, 2 filas y 2 columnas —4 regiones—, 2 filas y 3 columnas —6 regiones—, ..., 2 filas y 8 columnas —16 regiones—, 3 filas y 2 columnas —6 regiones—, ..., 8 filas y 8 columnas —64 regiones—). Por lo tanto, 1,225 regiones diferentes fueron creadas. La Figura 5.9 contiene tres ejemplos diferentes de la división de las imágenes.

Los clasificadores binarios de los sistemas OVR-SVM del segundo paso de la metodología RSIC fueron entrenados usando *kernels* RBF. El parámetro  $\epsilon$  de SVM fue fijado a  $1 \cdot 10^{-7}$ . Los parámetros  $C$  y el parámetro de la *kernel*  $\sigma$  deben ser fijados de acuerdo con la complejidad de la información del problema que se resuelve y el tamaño del espacio de características. Dado que el tamaño de las regiones y la información contenida en cada región eran diferentes, no fue posible fijar los parámetros  $C$  y  $\sigma$  a un único valor. Por lo

tanto, 5 valores de  $C$  ( $\{800, 900, 1,000, 1,100, 1,200\}$ ) y 5 valores de  $\sigma$  ( $\{8, 9, 10, 11, 12\}$ ) fueron probados. Como resultado, las regiones fueron entrenadas usando 25 combinaciones diferentes de estos parámetros (5 valores de  $C$  y 5 valores de  $\sigma$ ).

De acuerdo con estas cifras, 1,225 regiones fueron entrenadas usando 25 combinaciones de parámetros SVM, haciendo un total de 30,625 sistemas diferentes. En el tercer paso de la metodología RSIC, el rendimiento de cada uno de los 30,625 sistemas al clasificar cada clase del Thomson scattering fue evaluado utilizando la Ecuación 11.6 y  $PF = 3^4$ . La Figura 5.10a muestra los valores de  $q$  de los 30,625 sistemas entrenados para cada clase. Es importante destacar que la medida de calidad  $q$  ha sido ordenada en forma ascendente e independiente para cada clase.

En el siguiente paso de la metodología RSIC, la selección de regiones, el mejor sistema para clasificar cada clase fue identificado. Usando  $PF = 3$ , los valores de  $q$  de los mejores sistemas fueron: CFF = 0.5899, ECH = -1.3824, BCK = -0.9296, NBI = -4.4750 y STR = -1.2400 (el mejor sistema para clasificar una clase es aquel con el valor de  $q$  más bajo). La Figura 5.11 muestra las regiones seleccionadas para cada clase. El tamaño de la región resultante fue únicamente el 16.49% del tamaño original de las imágenes (algunas regiones se solaparon y por tanto, el tamaño de la región total no fue la suma de los tamaños de las regiones de las diferentes clases).

El último paso de la metodología RSIC consiste en la clasificación de las imágenes de test. Las 634 imágenes de test fueron clasificadas usando las regiones seleccionadas. Las tasas de acierto obtenidas fueron: 15.00% CFF, 96.53% ECH, 100% BCK, 98.80% STR y 98.20% STR. La tasa de aciertos total teniendo en cuenta el número de imágenes en cada clase fue del 95.27%. La razón de la baja tasa de aciertos de la clase CFF fue el pequeño número de muestras de entrenamiento: únicamente 11 imágenes. Los valores de  $q$  de todas las regiones al clasificar las imágenes CFF indican que ninguno de los clasificadores obtuvo buenos resultados (todos los clasificadores tuvieron valores de  $q$  mayores que 0, el más bajo fue el que ha sido seleccionado:  $q = 0.5899$ ).

La Tabla 11.2 muestra una comparación de los resultados de las regiones RSIC frente a los resultados obtenidos por 5 sistemas uno frente al resto SVM entrenados utilizando las imágenes completas (en vez de las ROIs). El sistema RSIC y el método con las imágenes completas usaron el mismo conjunto de entrenamiento propio, conjunto de calibración y conjunto de test. Dado que las imágenes completas contenían más información que las regiones seleccionadas por la metodología RSIC, fue posible construir mejores modelos y por tanto, obtener mejores tasas de clasificación. El porcentaje total de aciertos fue del 96.37% usando las imágenes completas frente al 95.27% usando las regiones RSIC. Es importante destacar que las regiones

<sup>4</sup>el valor de PF ha sido establecido en 3 empíricamente usando la Figura 5.10b

Clase de imagen	Tasas	Imagen completa	RSIC
CFF 20 imágenes	Aciertos	11, 55.00%	3, 15.00%
	Errores	4, 20.00%	5, 25.00%
	Desconocidas	5, 25.00%	12, 60.00%
	Tamaño	100%	4.17%
ECH 259 imágenes	Aciertos	246, 94.98%	250, 96.53%
	Errores	6, 2.32%	6, 2.32%
	Desconocidas	7, 2.70%	3, 1.16%
	Tamaño	100%	8.33%
BCK 62 imágenes	Aciertos	62, 100%	62, 100%
	Errores	0, 0%	0, 0%
	Desconocidas	0, 0%	0, 0%
	Tamaño	100%	3.13%
NBI 182 imágenes	Aciertos	181, 99.45%	180, 98.80%
	Errores	1, 0.55%	0, 0%
	Desconocidas	0, 0%	2, 1.1%
	Tamaño	100%	2.04%
STR 111 imágenes	Aciertos	111, 100%	109, 98.20%
	Errores	0, 0%	2, 1.80%
	Desconocidas	0, 0%	0, 0%
	Tamaño	100%	6.25%
Total 634 imágenes	Aciertos	611, 96.37%	604, 95.27%
	Errores	11, 1.74%	13, 2.05%
	Desconocidas	12, 1.89%	17, 2.68%
	Tamaño	100%	16.49%

Table 11.2: Comparación de los resultados del RSIC frente a los obtenidos utilizando las imágenes completas

Clase de imagen	Conjunto de datos	Imagen completa		RSIC	
		Tiempo (s)	DE (s)	Tiempo (s)	DE (s)
<b>Training</b>					
CFF 11 images	Entrenam.	1.206	0.026	0.075	0.001
	Calibración	6.325	0.029	1.456	0.005
ECH 129 images	Entrenam.	2.301	0.048	0.200	0.003
	Calibración	14.398	0.071	2.024	0.004
BCK 31 images	Entrenam.	1.097	0.012	0.033	0.001
	Calibración	5.228	0.037	1.318	0.006
NBI 92 images	Entrenam.	1.400	0.012	0.034	0.001
	Calibración	8.029	0.045	1.323	0.008
STR 56 images	Entrenam.	1.712	0.012	0.124	0.001
	Calibración	10.257	0.056	1.600	0.074
TOTAL 319 images	Entrenam.	7.715	0.062	0.465	0.004
	Calibración	44.237	0.179	7.720	0.077
<b>Test</b>					
634 images	Test	86.937	0.696	15.802	0.6958

Table 11.3: Comparación de los tiempos de CPU del método RSIC frente a SVM usando las imágenes completas

RSIC utilizaron únicamente el 16.49% del tamaño de las imágenes completas. A pesar de su reducido tamaño, la tasa de acierto de las regiones RSIC fue ligeramente inferior que la obtenida por las imágenes completas. De hecho, la tasa de aciertos de la clase ECH fue mejor usando las regiones RSIC. La mayor diferencia en las tasas de aciertos se obtuvo en la clase CFF dado el pequeño número de imágenes (55.00% usando las imágenes completas frente al 15.00% usando las regiones RSIC).

Los clasificadores fueron construidos usando un procesador Intel® Core™ 2 Quad CPU Q9300 2.50GHz, 1.95GB RAM. Los tiempos de CPU consumidos por las regiones RSIC y las imágenes completas fueron medidos para cuantificar el efecto de la reducción de la complejidad en los tiempos de CPU. La Tabla 11.3 muestra los resultados obtenidos. Los tiempos dados para ambos métodos fueron la media de 100 ejecuciones diferentes. La desviación estándar de los tiempos se muestra en la columna identificada como *DE*. Las diferencias de tiempos entre las diferentes clases se debieron, por una parte, al diferente número de imágenes en cada una, y por otra, a la diferente complejidad de los modelos. Usando las regiones RSIC, el tiempo del entrenamiento propio fue reducido un 93.97%. El tiempo de calibración se redució un 82.55% y el de test se redució un 81.82%. El tiempo medio de clasificación de una imagen usando la metodología RSIC fue de 0.025 s frente a los 0.137 s usando las imágenes completas.

### 11.2.3 Discusión

Las muestras TN (verdaderos negativos) no han sido incluidas en la Ecuación 11.6. En un problema multi-clase, el número de TN es habitualmente mucho mayor que el número de TP (por ejemplo, en un problema de clasificación de 4 clases con 10 muestras por clase, el número de muestras que pueden ser TP es 10 mientras que el número de muestras que pueden ser TN es 30). Por lo tanto, el peso estadístico de las muestras TN es mayor que el de las muestras TP. Como consecuencia, si las muestras TN se incluyen en la Ecuación 11.6, puede forzar al sistema a obtener grandes distancias entre el hiperplano y las muestras TN, en vez de intentar clasificar correctamente ambas, las muestras TN y las TP. Para solventar este problema, las muestras TN se han eliminado de la Ecuación 11.6 y se ha introducido el PF para penalizar los sistemas con errores.

Una alternativa a la Ecuación 11.6 es una medida de calidad promediada:

$$q(r, t) = \frac{\left( \sum_{i=1}^{\#FN} \alpha_{FN,i}^{rt} + \sum_{j=1}^{\#FP} \alpha_{FP,j}^{rt} \right) \times PF + \sum_{k=1}^{\#TP} \alpha_{TP,k}^{rt}}{(\#FN + \#FP) \times PF + \#TP} \quad (11.7)$$

Con respecto al paso 4 de la metodología RSIC (selección de regiones), la propuesta explicada aquí usa únicamente una región por clase. Es posible que, para problemas de clasificación muy complejos, sean necesarias varias regiones. Existen diferentes alternativas para clasificar una nueva imagen usando varias regiones por clase:

- La nueva imagen se asigna a la clase de la región con el  $p_{valor}$  mayor. En este caso, el proceso del paso 5 es similar pero en vez de un  $p_{valor}$  por clase, se usan varios  $p_{valores}$ .
- Es posible implementar un esquema de votación<sup>5</sup> para las regiones de la misma clase, y después, usar la salida del sistema de votación como  $p_{valor}$  de cada clase. Esta alternativa es la mostrada en la Figura 5.12.

## 11.3 Conclusiones

Las bases de datos de fusión están caracterizadas por su alta dimensionalidad y su complejidad. Docenas de diagnósticos del plasma miden las magnitudes del plasma en cada pulso, generando cientos de señales (algunas de ellas correlacionadas). La dimensión de los datos de fusión deben ser reducida para simplificar su uso para diferentes propósitos.

Aquí se han introducido dos técnicas de reducción de la dimensionalidad: SVM-FES y RSIC:

<sup>5</sup>**Esquema de votación:** método que dado un conjunto de predicciones de diferentes clasificadores genera una predicción conjunta

- Dado un espacio  $p$ -dimensional, SVM-FES genera un espacio  $q$ -dimensional cuyas dimensiones son un subconjunto del espacio original ( $q < p$ ). Usando el espacio reducido, es posible clasificar eficazmente las muestras del espacio original.
- RSIC selecciona una región de las imágenes originales que permite la clasificación de las imágenes obteniendo altas tasas de aciertos. El clasificador que usa la región resultante es más rápido que el que usa las imágenes completas. También ahorra espacio de almacenamiento.

El SVM-FES se aplicó a la determinación de las principales características de la transición L/H. Se probaron dos modelos diferentes: uno entrenado en un intervalo de  $\pm 100$  ms en torno a la transición y otro entrenado en un intervalo de  $\pm 500$  ms. Los resultados obtenidos de estos modelos señalaron que las muestras L y H cercanas a la transición no eran linealmente separables en el espacio de características resultante. La Figura 5.13a muestra un conjunto de muestras L y H lejos de la transición en el espacio BT y TE08. Las muestras son prácticamente linealmente separables en este espacio. En contraste, la Figura 5.13b muestra un conjunto de puntos L y H cercanos a la transición L/H. En este caso, los puntos L y H están mezclados en el espacio de características y no existe una frontera entre ambos modos de confinamiento.

Los resultados obtenidos por SVM-FES fueron comparados con los resultados obtenidos por ROC y PCA. Las tasas de acierto obtenidas por SVM-FES, ROC y PCA para el modelo de  $\pm 100$  ms fueron 93.404%, 87.852% y 57.035% respectivamente. En el caso del modelo de  $\pm 500$  ms, los resultados fueron 97.436%, 91.982% y 87.635%. Para ambos modelos, los resultados del SVM-FES superaron los obtenidos por ROC y PCA.

Los espacios de características calculados por SVM-FES pueden verse en la Tabla 11.1. Las dimensiones seleccionadas por el modelo  $\pm 500$  ms eran un subconjunto de las seleccionadas para el modelo  $\pm 100$  ms. Esto fue una consecuencia de la no linealidad de las muestras cerca de la transición L/H. Las señales seleccionadas para el modelo  $\pm 500$  ms eran adecuadas para clasificar los puntos alejados de la transición pero, para obtener una alta tasa de aciertos en la clasificación cerca de la transición, se requerían más señales.

La metodología RSIC ha demostrado sus capacidades para la selección de regiones y la clasificación usando las imágenes del Thomson scattering del TJ-II. Las imágenes originales se redujeron hasta el 16.49% del tamaño original. La región resultante fue una combinación de las regiones seleccionadas para cada una de las clases de las imágenes del Thomson scattering. A pesar de la gran reducción de la dimensionalidad de las imágenes, los resultados obtenidos por las regiones RSIC eran únicamente ligeramente inferiores a los obtenidos usando las imágenes completas (95.27% frente al 96.37%).

Los tiempos de CPU fueron drásticamente reducidos usando la metodolo-

gía RSIC. Los tiempos de entrenamiento, calibración y test fueron reducidos 93.97%, 82.55% y 81.82% respectivamente. El tiempo medio de clasificación de una imagen usando las regiones RSIC fue de 0.025 s frente a los 0.137 s usando las imágenes completas.

Las regiones seleccionadas por la metodología RSIC ayudaron a comprender la estructura de las imágenes del Thomson scattering. La mayoría del área seleccionada por RSIC pertenecía al centro de las imágenes, por lo que fue posible concluir que éste contenía información relevante para la clasificación. La altura de las regiones seleccionadas para las clases CFF y BCK fue mayor que su anchura. Estas regiones identificaron los patrones verticales que se muestran en las imágenes CFF, ECH y NBI. En el caso de las clases ECH y NBI (las más similares), el centro de la imagen permitió a los clasificadores distinguir ambas clases.



## Chapter 12

# Análisis de transiciones L/H y H/L

Durante la operación del plasma, éste evoluciona y tienen lugar diferentes fenómenos (por ejemplo ELMs, transiciones L/H y H/L o disrupciones). Algunos de estos eventos deben ser identificados para estudiar los procesos termonucleares en el plasma y otros deben ser evitados dado que comprometen la integridad de la máquina de fusión. El comportamiento del plasma es identificado a través del reconocimiento de patrones en señales. Los fenómenos del plasma generan patrones similares en cada pulso de plasma y por tanto, es posible la identificación de muchos comportamientos usando estos patrones. A veces, se necesita más de una señal para identificar un cierto evento (por ejemplo, los ELMs son reconocidos como picos en la señal de la emisión  $D_\alpha$  acompañados por caídas en la densidad del plasma).

La identificación de patrones en señales se lleva habitualmente a cabo a través del análisis visual. Las señales son analizadas por expertos una a una y los eventos localizados manualmente. Esto implica el uso de mucha fuerza de trabajo experta y largas esperas hasta que los datos son analizados. A veces, algunos pulsos no son evaluados por la falta de recursos.

Actualmente, las bases de datos de fusión están indexadas por el número de pulso (un simple contador del número de descarga de plasma), los nombres de los diagnósticos y los nombres de las señales (por ejemplo, en JET, la emisión  $D_\alpha$  del pulso 73337 es accedida usando la ruta: 73337, SA3D, AD36). Los expertos de cada campo de la física de plasmas analizan los datos generados durante la operación pulso a pulso. Desde el primer pulso de JET en 1983, han tenido lugar más de 80,000 descargas. A su vez, ha habido más de 30,000 descargas en el stellarator TJ-II desde 1997. Por lo tanto, el análisis de las base de datos de fusión es un problema de *grandes números*.

Los pulsos de JET pueden durar más de un minuto y se espera que ITER opere en régimen estacionario (pulsos de más de 30 minutos e incluso una

hora). Por ello, la longitud de las señales se incrementará significativamente en los próximos años. El paradigma de acceso de datos actual (número de pulso, diagnóstico, nombre de señal) no será válido dado que no será posible para los expertos analizar las señales completas. En la última década, el desarrollo de la inteligencia artificial y los métodos de minería de datos han abierto una puerta a un acceso de datos alternativo: el paradigma *orientado a patrones* (Vega and JET-EFDA contributors, 2008). Usando este paradigma orientado a patrones, los datos no serán indexados por el número de pulso o el nombre de la señal sino por los patrones en las señales.

El paradigma orientado a patrones está centrado en eventos dentro de señales. Los científicos pueden acceder a los datos usando el fenómeno del plasma que están interesados en evaluar, ahorrando tiempo e incrementado el peso estadístico de sus resultados, dado que consiguen acceso a eventos de un amplio rango de pulsos de plasma. Usando este paradigma, la consulta es el patrón buscado en la base de datos y las respuestas del sistema son los números de los pulsos y los tiempos donde patrones similares son localizados.

La mayoría de los sistemas de recuperación de datos orientados en patrones consisten en tres pasos:

- **Extracción de características:** las señales en el dominio temporal son transformadas en un conjunto de características, habitualmente en un espacio de dimensión menor. Esto acelera el acceso a la base de datos y simplifica las siguientes tareas. Es un paso crucial dado que define el tipo de datos que usarán las siguientes tareas. En fusión, existen dos aproximaciones principales:
  - **Coefficientes de Fourier:** las características de la señal son sus coeficientes de Fourier (Nakanishi et al., 2004) más grandes.
  - **Métodos de cadenas:** las señales son reemplazadas por caracteres basándose en la morfología de la señal (Dormido-Canto et al., 2008).
- **Indexado de las señales:** las señales son indexadas para acelerar el proceso de recuperación. Dado que las bases de datos contienen decenas de miles de pulsos de diferentes señales, las bases de datos no pueden ser recorridas completamente y por ello la indexación es necesaria.
- **Recuperación de patrones similares:** se lleva a cabo mediante el uso de una medida de similaridad. Los patrones en la base de datos son comparados con el de la consulta usando la medida de similaridad. Los más similares son devueltos al usuario.

Una aplicación de las técnicas de reconocimiento de patrones es la localización de transiciones L/H y H/L en una descarga de plasma. La transición L/H puede ser identificada como una repentina caída de la señal  $D_\alpha$  acompañada por un cambio en la pendiente de la señal de la densidad del plasma.

El caso de la transición H/L es más complicado dado que el patrón buscado en las señales no está bien definido. A pesar de ello, no siempre es posible aplicar las técnicas de reconocimiento de patrones a la identificación de la transición L/H. La razón es que el patrón morfológico de la transición L/H varía dependiendo de parámetros como la potencia, la temperatura o la densidad. Además, la escala temporal y la amplitud de los patrones pueden ser significativamente diferentes. La Figura 6.1 muestra diferentes transiciones L/H de 9 pulsos de JET.

Una alternativa a las técnicas de reconocimiento de patrones para la identificación de las transiciones L/H son los modelos basados en datos. Dada una base de datos de tiempos de transiciones L/H, es posible construir un modelo para evaluar cuándo el plasma está en modo L o en modo H. Se pueden aplicar diferentes técnicas para obtener modelos basados en datos para la identificación del régimen en JET; Murari et al. (2006) hacen una comparación entre lógica difusa y SVM, Vega et al. (2009b) combinan estadística bayesiana y SVM y Meakins et al. (2010) usan redes neuronales.

Los modelos basados en datos requieren grandes bases de datos de tiempos de transiciones L/H. Desafortunadamente, los tiempos de las transiciones L/H no siempre están disponibles y esos modelos normalmente confunden las muestras cercanas a la transición. Por ello, se requieren métodos alternativos para la localización de las transiciones.

## 12.1 Localización automatizada de transiciones L/H

El detector de transiciones automatizado (ATD, por sus siglas en inglés) es una herramienta automática, por tanto, sin intervención humana, para identificar transiciones L/H en descargas de plasma (González et al., 2012a). Dado un conjunto de pulsos, el método devuelve los tiempos de las transiciones L/H junto con los intervalos de incertidumbre de las estimaciones de las transiciones.

Existen cinco razones que justifican la utilidad del ATD:

- No es necesaria la intervención humana.
- Todas las descargas se procesan exactamente de la misma manera asegurando por tanto la reproducibilidad y evitando errores humanos.
- Todos los tiempos de las transiciones son estimados, incluso los de las descargas donde la transición no puede ser localizada por medio de análisis visual.
- Se pueden crear grandes bases de datos con tiempos de transiciones mejorando la significancia estadística de futuros estudios.

- La base de datos de tiempos de transiciones puede ser actualizada de forma automática después de cada pulso.

El ATD es bastante general y puede aplicarse a otros dispositivos de fusión con pequeños cambios. De hecho, ha sido aplicado a la localización de transiciones L/H en JET (González et al., 2012a) y en DIII-D (Farias et al., 2012).

### 12.1.1 Flujo de trabajo del ATD

El ATD consta de cuatro módulos de software (Figura 6.3): *bucle de lectura*, *bucle de discriminación*, *creación del modelo* y *módulo de predicción*.

En primer lugar, es necesario saber cuándo el plasma alcanza el modo H. Dado un rango de pulsos de plasma, el objetivo del *bucle de lectura* es crear una base de datos que contenga los pulsos que alcanzan el modo H. El *bucle de discriminación* clasifica las transiciones con modo H en dos grupos de acuerdo con su tipo (patrón) de transición en la señal  $D_\alpha$ :

- En el caso de una transición con *patrón claro*, el tiempo de la transición y el intervalo de incertidumbre son determinados automáticamente. Se genera una base de datos con los tiempos de las transiciones y sus correspondientes intervalos de incertidumbre.
- Los tiempos de transición de las descargas que muestran un *patrón no claro* no pueden ser localizados en este módulo y por tanto, se almacenan en una base de datos intermedia para su uso posterior.

Para determinar los tiempos de transición de las descargas no claras, se entrena un modelo predictor ICP usando las descargas que muestran patrones de transición claros. Dado un instante de un pulso, el predictor determina cuándo el plasma está en modo L o en modo H. Además, genera valores de confianza y credibilidad para la predicción realizada. Esto se lleva a cabo en el tercer módulo del ATD: *creación del modelo*.

Finalmente, en el *módulo de predicción* los pulsos en la base de datos de transiciones no claras son usados como entradas del predictor generado en el módulo previo. Las transiciones de estos pulsos son localizadas en el instante en que la predicción cambia de modo L a modo H.

#### 12.1.1.1 Bucle de lectura

El propósito del bucle de lectura es la identificación de las descargas que alcanzan modo H y por tanto, las que contienen una transición L/H. La detección del modo H en una descarga se lleva a cabo a través de la identificación de los ELMs de la descarga. Dado que los ELMs solamente tienen lugar en plasmas en modo H, la detección de ELMs en un pulso implica que el plasma está en modo H.

Para comprobar la presencia de ELMs se usa UMEL. Una regresión SVR (RBF *kernel*,  $K_C = 5$ ,  $K_e = 10$ ,  $K_\sigma = 0.3$ ) se calcula usando la señal  $D_\alpha$ . Para acelerar el cálculo de SVR, la señal se descompone usando la transformada wavelet de la familia Haar a nivel 2 y los coeficientes de aproximación son ajustados usando UMEL. La existencia de ESVs releva la presencia de ELMs en la descarga.

### 12.1.1.2 Bucle de discriminación

Para cada pulso con transición L/H, el bucle de discriminación lleva a cabo dos importantes tareas:

- **Localización del intervalo de transición L/H (LHTI, por sus siglas en inglés):** se trata de un intervalo donde la transición L/H tiene lugar.
- **Identificación del patrón de la transición:** las transiciones L/H se clasifican en dos grupos de acuerdo con el tipo de sus patrones: patrones claros y patrones no claros.

**Localización del intervalo LHTI.** La **primera tarea** del bucle de discriminación es la localización del LHTI. Los objetivos del LHTI son, primero, reducir el intervalo temporal donde se busca la transición y, segundo, simplificar los módulos ATD siguientes. Básicamente, el LHTI es el intervalo temporal existente entre el comienzo de la potencia auxiliar de entrada y la aparición del primer ELM. La Figura 6.6 muestra un ejemplo del LHTI del pulso de JET 76563. EL LHTI se determina en tres pasos: detección de la inyección de potencia, detección de la región con ELMs y eliminación de ELMs residuales.

- **Paso 1: detección de la inyección de potencia.** Para poder alcanzar el régimen de confinamiento en modo H se necesita una alta inyección de potencia auxiliar. No obstante, el umbral que asegura el cambio de confinamiento es conocido dentro de un amplio margen. Además, este umbral varía con parámetros como la densidad, la temperatura o el campo magnético. Aquí, dado que la transición L/H debe estar situada dentro del LHTI, se calcula un umbral de potencia ( $P_\tau$ ) conservador. El tiempo para el cuál la potencia inyectada al plasma alcanza  $P_\tau$  determina el margen izquierdo del LHTI.  $P_\tau$  se calcula como:

$$P_\tau = 0.2 \cdot \max(\text{Potencia}) \quad (12.1)$$

donde *Potencia* es la potencia total inyectada en el plasma (señal de JET PPF/MG3/YTO).

La Figura 6.7 muestra la detección de la inyección de potencia auxiliar en el pulso de JET 73337. La línea roja horizontal representa  $P_\tau$ . La línea punteada verde es el margen izquierdo resultante del LHTI. En este pulso, la transición tiene lugar en 15.844 s.

- **Paso 2: detección de la región con ELMs.** Una vez que el margen izquierdo del LHTI ha sido determinado usando la potencia total inyectada, el siguiente paso es la identificación de la región en modo H. Los ELMs solamente aparecen en modo H y por lo tanto, tras la transición L/H. En este paso UMEL se utiliza para localizar la región con ELMs (Figura 6.8, gráfico superior).

El número de ESVs devuelto por UMEL se cuenta en grupos de 0.05 segundos (Figura 6.8, gráfico inferior) y se calcula el valor medio de los ESVs en los grupos no vacíos (línea cian horizontal). Este valor medio se usa para calcular un umbral para el margen derecho del LHTI ( $ELMs_\tau$ , línea roja horizontal):

$$ELMs_\tau = 0.4 \cdot \frac{\text{Número de ELMs}}{\text{Número de grupos no vacíos}} \quad (12.2)$$

El margen derecho del LHTI es igual al tiempo del primer grupo con más ESVs que  $ELMs_\tau$ . Dado que, en algunos pulsos la transición L/H está muy cerca del primer ELMs y para asegurar que el LHTI contiene la transición, se añade un margen de 0.1 s al tiempo del margen derecho del LHTI (línea punteada verde). De nuevo, éste es un paso conservador dado que es esencial que el LHTI contenga la transición L/H.

- **Paso 3: Eliminación de ELMs residuales.** En el paso anterior, el margen derecho del LHTI se calcula como el tiempo del primer grupo con más ESVs que  $ELMs_\tau$  más un margen de 0.1 s. Por lo tanto, es posible que aparezcan algunos ELMs en el extremo derecho del LHTI.

El objetivo del tercer paso es eliminar estos ELMs en el caso de que existan. La identificación de ELMs se lleva a cabo usando UMEL. El margen derecho del LHTI se mueve hasta el tiempo del primer ELM localizado.

**Identificación del tipo de patrón de la transición.** La segunda tarea del bucle de discriminación es la identificación del tipo de patrón de la transición. Se consideran dos tipos de transiciones: transiciones con patrones claro (Figura 6.9a, gráfico superior) y transiciones con patrones no claros (Figura 6.9b, gráfico superior).

Los coeficientes de detalle de la wavelet perteneciente a la familia Haar de la señal  $D_\alpha$  se usan para localizar la caída característica de las transiciones

dentro del LHTI. Teniendo en cuenta que las caídas de la  $D_\alpha$  pueden ser diferentes unas de otras, se han probado diferentes niveles de descomposición wavelet. Los mejores resultados se han alcanzado usando un nivel 5 de descomposición wavelet. Por una parte, los patrones claros se caracterizan por una caída obvia. Por otra parte, los patrones no claros no muestran esa caída obvia. Por tanto, los coeficientes de detalle de las transiciones con patrones claros muestran un pico aislado en el instante de la transición (Figura 6.9a, gráfico inferior). En contraste, dado que los patrones no claros no muestran una caída clara, sus coeficientes de detalle wavelet muestran muchos picos diferentes (Figura 6.9b, gráfico inferior).

UMEL (RBF *kernel*,  $K_C = 1$ ,  $K_e = 4$ ,  $K_\sigma = 2$ ) se aplica a los coeficientes wavelet de detalle normalizados (entre 0 y 1). Si se localiza un ESV aislado, el tipo de transición es reconocido como claro y el tiempo de la transición L/H se determina como el tiempo del ESV. Por otro lado, si aparecen diferentes ESVs, el patrón de la transición es identificado como no claro. En este caso, el tiempo de la transición no puede ser estimado dentro del módulo del bucle de discriminación.

Las transiciones con patrones claros son incluidas en una base de datos de tiempos de transiciones L/H con sus correspondientes intervalos de incertidumbre. El intervalo de incertidumbre (barra de error) está relacionado no solo con el período de muestreo ( $T_S$  de la señal  $D_\alpha$  sino también con el nivel de descomposición wavelet. Dado que cada nivel de descomposición wavelet de la familia Haar reduce el número de muestras en un factor 2, el intervalo de incertidumbre es  $\pm 2^L T_S$  alrededor de la transición (o equivalentemente una barra de error de  $\pm 2^{L+1} T_S$ , donde  $L$  es el nivel de descomposición wavelet). Como  $T_S = 0.1$  ms y  $L = 5$ , el intervalo de incertidumbre de todas las transiciones con un patrón claro es  $\pm 3.2$  ms.

### 12.1.1.3 Creación del modelo

Los tiempos de las transiciones L/H con patrones no claros no pueden estimarse usando la transformada wavelet. Aparecen muchos ESVs en los coeficientes de detalle wavelet de la señal  $D_\alpha$  y por tanto no es posible identificar cuál se corresponde con la transición real. Por lo tanto, se requiere un método alternativo. Se ha propuesto un clasificador L/H para estimar los tiempos y los *intervalos de confianza de la predicción* (PCIs, por sus siglas en inglés) de las transiciones L/H con patrones no claros. El clasificador se entrena usando los pulsos con patrones claros identificados en el módulo previo. Los tiempos de transición de estos pulsos han sido localizados y por tanto, dado un determinado instante  $t$ , es posible saber si el plasma está en modo L o modo H. Dado que el clasificador se construye usando los tiempos de transiciones identificadas automáticamente, el ATD no requiere una base de datos de tiempos de transiciones L/H.

La longitud del LHTI varía de descarga a descarga. Desafortunadamente,

las características relevantes para distinguir los modos de confinamiento L y H son diferentes en segmentos temporales cercanos a la transición ( $\pm 100$  ms alrededor de la transición) y lejos de esta ( $\pm 500$  ms alrededor de la transición) y los modelos para distinguir el modo de confinamiento también varían. Como resultado, no es posible discernir el mejor espacio de entrada para el clasificador. En casos similares, una combinación de clasificadores ha obtenido buenos resultados (Ratta et al., 2010, predicción de interrupciones en JET).

Un modelo de dos capas (basado en SVM) se ha propuesto para localizar las transiciones dentro del LHTI (Figura 6.10). La primera capa consiste en dos clasificadores. Uno (Figura 6.10, caja superior izquierda) es entrenado en un intervalo simétrico de  $\pm 100$  ms alrededor de la transición con un período de muestreo de 1 ms (201 muestras por pulso). El segundo clasificador en la primera capa (Figura 6.10, caja superior derecha) es entrenado en un intervalo simétrico de  $\pm 500$  ms alrededor del tiempo de la transición y con un período de muestreo de 1 ms (1001 muestras por pulso). El objetivo de los clasificadores en la primera capa es enfatizar el aprendizaje automático cerca y lejos de la transición. Las señales que usa cada modelo pueden encontrarse en el Apéndice H (en inglés).

El modelo SVM combinado usa información de ambos clasificadores para minimizar el error del tiempo de transición estimado (objetivo del clasificador  $\pm 100$  ms) y para minimizar los errores en puntos lejanos a la transición (objetivo del clasificador  $\pm 500$  ms).

#### 12.1.1.4 Módulo de predicción

Este módulo estima los tiempos de transición de los pulsos con patrones no claros usando el modelo diseñado en el módulo previo. Las muestras dentro del LHTI son clasificadas una a una en orden temporal ascendente. El cambio de confinamiento predicho determina el tiempo de la transición.

En este punto, el modelo no genera ninguna medida de la bondad de las predicciones del tiempo de transición. Intuitivamente, las muestras lejos de la transición L/H son fáciles de clasificar (están lejos de la frontera entre L y H) y por tanto las predicciones deberían tener un alto nivel de fiabilidad. Por otro lado, las muestras cercanas a la transición son más difíciles de clasificar y por tanto, la fiabilidad de las predicciones debería ser menor. El nivel de fiabilidad sería mínimo junto en la frontera entre los modos de confinamiento L y H. Dado un umbral de fiabilidad, éste define un valor de fiabilidad bajo el cual las predicciones se asume que no son de confianza. El intervalo de tiempo alrededor de la transición estimada donde la fiabilidad está por debajo del umbral puede ser considerado un intervalo de confianza de la predicción (PCI) de la predicción. El ATD asegura que la transición L/H real se encuentra dentro del PCI pero la predicción del tiempo de la transición dentro del PCI es menos precisa.

Modelo	Entrenamiento (Conjunto de entrenamiento propio)	Test (Conjunto de calibración)
$\pm 100$ ms	98.62%	96.65%
$\pm 500$ ms	98.80%	97.72%
Combinado	99.17%	98.73%

Table 12.1: Resultados de clasificación del modelo SVM multicapa

La Figura 6.12 muestra un ejemplo sencillo del cálculo del PCI. La Figura 6.12a muestra el espacio de características de las muestras L (cruces rojas) y H (círculos azules) y el hiperplano de separación (frontera). Las muestras de test se señalan usando puntos verdes. La evolución temporal de las muestras de test es  $t_1, t_2, \dots, t_7$ . La Figura 6.12b contiene el cálculo del PCI de las muestras de test. Dado que las muestras de test  $t_1$  y  $t_7$  están lejos del hiperplano de separación, sus valores de fiabilidad son altos. En contraste, las muestras  $t_3, t_4$  y  $t_5$  están cerca del hiperplano y por ello, sus valores de fiabilidad son bajos. Los puntos de test localizados a la izquierda del hiperplano son clasificados como modo L y las muestras situadas a la derecha son clasificadas como modo H. El PCI es el intervalo temporal entre las dos primeras muestras alrededor de la transición (una a la derecha y otra a la izquierda) cuyos valores de fiabilidad están por encima del umbral dado ( $t_3$  y  $t_6$ ).

Un ICP (predictor conformal inductivo) off-line ha sido aplicado para calcular los valores de fiabilidad del modelo SVM combinado. El valor de fiabilidad de cada muestra se calcula como el producto de las medidas conformales (credibilidad y confianza). El producto de las medidas conformales ha sido previamente utilizado obteniendo buenos resultados (Makili et al., 2011). El umbral de fiabilidad ha sido fijado a 0.3. Esto significa que, de media, los valores de confianza y credibilidad son mayores que 0.55.

Es importante destacar que dado que la longitud del PCI depende de la fiabilidad, puede no ser un intervalo simétrico alrededor del tiempo de la transición (el intervalo a la izquierda de la transición puede ser más largo que el intervalo a la derecha y viceversa).

### 12.1.2 Localización de transiciones L/H en JET

La metodología presentada aquí fue probada con una base de datos de 551 descargas correspondientes a las campañas de JET desde la C21 hasta la C26. Los tiempos de las transiciones L/H fueron determinados manualmente por expertos analizando las descargas visualmente.

El bucle de discriminación localizó 143 transiciones claras (25.95%). Este conjunto de transiciones fue validado automáticamente y reducido a 141

<b>Número de transiciones con patrones no claros</b>	<b>410</b>
<b>Número de transiciones bien localizadas (L/H<sub>real</sub> dentro del PCI)</b>	<b>397 (96.83%)</b>
media( $ L/H_{real} - L/H_{estimado} $ )	27.9 ms
std( $ L/H_{real} - L/H_{estimado} $ )	37.6 ms
media de la longitud del PCI	225.2 ms
<b>Number de transiciones no localizadas (L/H<sub>real</sub> fuera del PCI)</b>	<b>13 (3.17 %)</b>
media( $ L/H_{real} - L/H_{estimado} $ )	93.8 ms
std( $ L/H_{real} - L/H_{estimado} $ )	55.4 ms
media de la longitud del PCI	453.5 ms
Tiempo medio entre $L/H_{real}$ y el extremo más cercano del PCI	5.96 ms

Table 12.2: Resultados de las transiciones no claras

(25.59%) transiciones. Para reducir el tiempo de cálculo se usó una versión paralela de SVM (Ramírez et al., 2010). Para poder implementar el predictor conformal de la segunda capa, las 141 transiciones se dividieron en un conjunto de entrenamiento propio (75%, 106 transiciones) y un conjunto de calibración (25%, 32 transiciones).

La Tabla 12.1 resume las tasas de aciertos alcanzadas por el clasificador de dos capas usando el conjunto de entrenamiento propio (como entrenamiento) y el conjunto de calibración (como test). Es importante tener en consideración que las tasas más altas del clasificador  $\pm 500$  ms frente al clasificador  $\pm 100$  ms no implican una predicción de la transición más precisa.

El modelo SVM combinado se aplicó para estimar los tiempos de las transiciones y los PCIs de las transiciones con patrones no claros (410 pulsos). Como se mencionó previamente, el umbral de fiabilidad se fijó a 0.3. La Tabla 12.2 resume los resultados obtenidos. Se distinguieron dos grupos principales de descargas: aquellas cuyo tiempo de la transición L/H determinado por los expertos ( $L/H_{real}$ ) cayó dentro del PCI calculado (397 pulsos, 96.83%) y aquellas cuyo  $L/H_{real}$  estaba fuera del PCI (13 pulsos, 3.17%).

Con respecto al primer grupo de descargas, la Figura 6.14a muestra el histograma de las longitudes de sus PCIs (agrupada en grupos de 20 ms). La longitud media de los PCIs fue 225.2 ms. Es importante mencionar que se identificaron cinco descargas (74759, 76519, 76521, 76688 and 77634) cuyos PCIs variaron entre 710 ms y 3.91 s. Estos casos especiales son descargas con potencia inyectada moderada (en todos los casos menos de 10 MW) y/o descargas que alcanzan su máximo valor de una forma no abrupta, con un largo período de inyección de potencia. Estos pulsos con un largo período de baja potencia inyectada no son los pulsos estándar de JET e incrementaron significativamente la longitud media del PCI en la Tabla 12.2. Si no fuesen

tenidos en cuenta, la longitud media del PCI sería de 206 ms. La Figura 6.15 muestra dos de estos pulsos (pulsos 77634 y 76521 de JET). Dicha figura incluye la potencia inyectada, la emisión  $D_\alpha$ , la salida del modelo SVM combinado ( $D(u, v)$ ) y el nivel de fiabilidad. La Figura 6.14b representa la distribución de las diferencias de tiempos entre las transiciones L/H reales ( $L/H_{real}$ ) y los tiempos estimados por el ATD ( $L/H_{estimado}$ ). El valor absoluto medio fue de 27.9 ms y la desviación estándar fue de 37.6 ms.

El segundo grupo de descargas de la Tabla 12.2 estaba formado por los siguientes pulsos: 73559, 73576, 74611, 74622, 75066, 75222, 75740, 75741, 75742, 75743, 77009, 77054, 77179. Su transición real no estaba dentro del PCI estimado. Únicamente 13 descargas (3.17%) pertenecen a este grupo. El error medio en la localización de las transiciones L/H fue de 93.8 ms y la longitud media del PCI fue de 453.5 ms. No obstante, es importante resaltar que en todos estos casos la transición real estaba muy cerca de los bordes del PCI. La diferencia media entre la transición real y el borde más cercano del PCI fue de 5.96 ms. En el pulso 77009, una potencia inyectada moderada se mantuvo durante un largo período después de la transición. Como consecuencia, la longitud del PCI fue de 4.172 s. Si este pulso fuese ignorado, dado su carácter no estándar en JET, la longitud media del PCI en este grupo de descargas sería de 164.3 ms.

### 12.1.2.1 Leyes de escala para el umbral de potencia

La precisión de la determinación automatizada de los tiempos de transición es satisfactoria y, por tanto, el ATD puede ser usado para incrementar la significancia estadística de los estudios de las transiciones L/H. Por ejemplo, el ATD puede ser usado como primera aproximación y después los expertos pueden concentrar su atención únicamente en el PCI para refinar el análisis. Por otra parte, podría ser de interés investigar hasta qué punto los tiempos determinados automáticamente por el predictor pueden ser usados directamente para realizar estudios físicos. Para resolver este punto, se han determinado leyes de escala para el umbral de potencia para acceder al modo H usando ambos, los tiempos de las transiciones determinadas por el ATD ( $L/H_{estimado}$ ) y los tiempos de las transiciones identificados manualmente por los expertos ( $L/H_{real}$ ). Para este fin, dos métodos diferentes de regresión se han aplicado: OLS (mínimos cuadrados ordinarios) y regresión Ridge. La regresión Ridge se ha propuesto para remediar la colinearidad de las variables explicativas.

A pesar de que la transición L/H se sabe que depende de varios parámetros, es ampliamente aceptado que el umbral de la potencia para la transición L/H depende fuertemente de la densidad del plasma, el campo magnético toroidal y el tamaño del plasma (Martin et al., 2008). Por tanto, la ley de escala:

$$P_\tau = K \cdot n_e^\alpha \cdot B_T^\beta \cdot S^\gamma \quad (12.3)$$

Método de localiz.	Ley de escala	MSE
<b>OLS</b>		
Expertos	$P_\tau = 10^{0.80 \pm 0.40} \cdot n_e^{0.56 \pm 0.12} \cdot B_T^{0.58 \pm 0.20} \cdot S^{0.39 \pm 0.60}$	7.082
ATD	$P_\tau = 10^{1.00 \pm 0.39} \cdot n_e^{0.64 \pm 0.08} \cdot B_T^{0.50 \pm 0.17} \cdot S^{0.23 \pm 0.60}$	8.635
<b>Regression Ridge, k = 4</b>		
Expertos	$P_\tau = 10^{0.80 \pm 0.10} \cdot n_e^{0.55 \pm 0.08} \cdot B_T^{0.58 \pm 0.12} \cdot S^{0.39 \pm 0.14}$	7.077
ATD	$P_\tau = 10^{1.00 \pm 0.10} \cdot n_e^{0.64 \pm 0.07} \cdot B_T^{0.50 \pm 0.11} \cdot S^{0.23 \pm 0.13}$	8.632

Table 12.3: Leyes de escala de  $P_\tau$  usando  $n_e$ ,  $B_T$  y  $S$ 

Método de localiz.	Ley de escala	MSE
<b>OLS</b>		
Expertos	$P_\tau = 10^{1.10 \pm 0.17} \cdot n_e^{0.55 \pm 0.12} \cdot B_T^{0.61 \pm 0.20} \cdot q_{95}^{-0.14 \pm 0.23}$	7.106
ATD	$P_\tau = 10^{1.19 \pm 0.13} \cdot n_e^{0.63 \pm 0.08} \cdot B_T^{0.52 \pm 0.17} \cdot q_{95}^{-0.10 \pm 0.22}$	8.657
<b>Regresión Ridge, k = 4</b>		
Expertos	$P_\tau = 10^{1.10 \pm 0.10} \cdot n_e^{0.54 \pm 0.08} \cdot B_T^{0.61 \pm 0.12} \cdot q_{95}^{-0.14 \pm 0.12}$	7.102
ATD	$P_\tau = 10^{1.19 \pm 0.08} \cdot n_e^{0.63 \pm 0.07} \cdot B_T^{0.51 \pm 0.11} \cdot q_{95}^{-0.10 \pm 0.12}$	8.654

Table 12.4: Leyes de escala de  $P_\tau$  using  $n_e$ ,  $B_T$  y  $q_{95}$ 

puede ser obtenida usando OLS o regresión Ridge, donde  $P_\tau$  es el umbral de la potencia expresado en MW,  $n_e$  es la densidad electrónica de línea media (en unidades de  $10^{20} \text{m}^{-3}$ ),  $B_T$  es el campo magnético toroidal (T) y  $S$  es la superficie del plasma ( $\text{m}^2$ ). La Tabla 12.3 muestra las leyes de escala resultantes usando los tiempos determinados por los expertos ( $L/H_{real}$ ) y los tiempos estimados por el ATD ( $L/H_{estimado}$ ) y ambos métodos de regresión. Las leyes de escala están dadas usando un nivel de confianza del 95%.

Dado que los intervalos de confianza en los exponentes (y en la constante) se superponen, parece que las leyes de escala obtenidas usando los tiempos  $L/H_{real}$  y  $L/H_{estimado}$  son equivalentes. Por tanto, los tiempos del ATD generan leyes de escala que son equivalentes a las obtenidas usando los tiempos determinados por expertos. Este resultado es bastante general dado que no se obtiene solo de las leyes de escala que usan los parámetros físicos  $n_e$ ,  $B_T$  y  $S$ . Para justificar esta afirmación, se han calculado las leyes de escala de la Tabla 12.4. Estas usan los parámetros del plasma  $n_e$ ,  $B_T$  y  $q_{95}$  donde  $q_{95}$  es el factor de seguridad del plasma at  $\text{PSI} = 0.95$ . De nuevo, los intervalos de confianza de los exponentes y la constante se solapan.

Un aspecto importante que puede ser tratado usando leyes de escala es la diferencia entre las transiciones con patrón claro y las transiciones con patrón no claro. Es importante descubrir si su diferencia se limita sólo a la estructura morfológica de la  $D_\alpha$  o se trata de diferentes procesos físicos

Método de localiz.	Ley de escala	MSE
<b>Transitions con patrones claros, regresión Ridge, k = 4</b>		
Expertos	$P_\tau = 10^{2.10 \pm 0.08} \cdot n_e^{0.92 \pm 0.08} \cdot B_T^{0.25 \pm 0.09} \cdot S^{-1.15 \pm 0.10}$	2.819
ATD	$P_\tau = 10^{2.24 \pm 0.08} \cdot n_e^{0.98 \pm 0.07} \cdot B_T^{0.19 \pm 0.09} \cdot S^{-1.27 \pm 0.09}$	2.803
Expertos	$P_\tau = 10^{1.39 \pm 0.07} \cdot n_e^{0.83 \pm 0.08} \cdot B_T^{0.26 \pm 0.09} \cdot q_{95}^{-0.18 \pm 0.10}$	2.890
ATD	$P_\tau = 10^{1.43 \pm 0.07} \cdot n_e^{0.87 \pm 0.08} \cdot B_T^{0.21 \pm 0.09} \cdot q_{95}^{-0.14 \pm 0.10}$	2.866
<b>Transiciones con patrones no claros, regresión Ridge, k = 4</b>		
Expertos	$P_\tau = 10^{0.81 \pm 0.12} \cdot n_e^{0.73 \pm 0.10} \cdot B_T^{0.50 \pm 0.13} \cdot S^{0.69 \pm 0.15}$	7.955
ATD	$P_\tau = 10^{0.84 \pm 0.10} \cdot n_e^{0.63 \pm 0.08} \cdot B_T^{0.55 \pm 0.13} \cdot S^{0.49 \pm 0.14}$	9.792
Expertos	$P_\tau = 10^{1.27 \pm 0.11} \cdot n_e^{0.71 \pm 0.10} \cdot B_T^{0.53 \pm 0.13} \cdot q_{95}^{-0.12 \pm 0.13}$	8.012
ATD	$P_\tau = 10^{1.20 \pm 0.09} \cdot n_e^{0.62 \pm 0.08} \cdot B_T^{0.56 \pm 0.13} \cdot q_{95}^{-0.11 \pm 0.13}$	9.825

Table 12.5: Comparación de las leyes de escala obtenidas usando transiciones con patrones claros y no claros

subyacentes. Para ello, se han calculado leyes de escala usando OLS y regresión Ridge para ambos subconjuntos de transiciones, aquellas con patrones claros y las que tienen patrones no claros. Las leyes de escala obtenidas utilizando los tiempos del ATD se compararon con aquellas obtenidas por los tiempos determinados por los expertos. Los resultados, mostrados en la Tabla 12.5, indicaron que los dos tipos de transiciones no están gobernados por el mismo proceso físico y por ello, sus leyes de escala son diferentes. Este resultado se mantuvo para ambos tiempos, los tiempos dados por el ATD y los determinados por los expertos.

Se ha observado que los pulsos con transiciones claras corresponden con plasmas que transitan abruptamente a fases con ELMs de tipo I. Por el contrario, en los pulsos con patrones no claros, el plasma permanece en una fase con ELMs de tipo III antes de acceder al régimen con ELMs de tipo I. Estos son resultados preliminares y deben ser confirmados mediante el uso de una base de datos específica para este fin.

### 12.1.3 Localización de las transiciones L/H en DIII-D

La metodología ATD puede ser aplicada con pequeños cambios a diferentes dispositivos de fusión. Farias describe la aplicación del ATD en DIII-D (Farias et al., 2012).

Se realizó un nuevo proceso de extracción de características usando SVM-FES con un conjunto inicial de 35 dimensiones. En este caso, los modelos de la primera capa se entrenaron usando intervalos de  $\pm 50$  ms y  $\pm 100$  ms alrededor de los tiempos de transición. El modelo de la segunda capa es similar al modelo de JET. Las señales utilizadas por los modelos pueden verse en el Apéndice I (en inglés).

La metodología ATD fue probada usando una base de datos de 354 pulsos de DIII-D. El *bucle de discriminación* identificó 279 transiciones con patrones claros y 75 descargas con patrones no claros.

Las transiciones con patrones claros se utilizaron para entrenar el modelo multi-capa y estimar los tiempos de las transiciones con patrones no claros. La tasa de transiciones correctamente localizadas ( $L/H_{real}$  dentro del PCI) fue del 95.6%. El error medio en la estimación de los tiempos de transiciones fue de 6 ms y la desviación estándar fue de 49 ms.

El diseño del ATD en DIII-D se llevó a cabo a través de un entorno colaborativo distribuido. Dado que el cálculo de los modelos requiere computación de alto rendimiento, ésta se lleva a cabo en el *cluster* de computación del CIEMAT (Acero et al., 2009). La localización de las transiciones L/H en los nuevos pulsos se lleva a cabo en el laboratorio del DIII-D. Este paso puede ser ejecutado de manera automática después de cada pulso y por ello, los modelos pueden ser reentrenados con nuevos datos.

#### 12.1.4 Discusión

El ATD es una metodología para determinar los tiempos de las transiciones L/H de una forma completamente automática. El ATD puede ser usado para crear grandes bases de datos de tiempos de transiciones L/H (cuanto mayores las bases de datos, más fidedignos serán los resultados) que pueden ser usadas para múltiples propósitos, por ejemplo, el análisis físico de las transiciones L/H, la validación de los modelos L/H teóricos o la creación de leyes de escala para la transición L/H. El ATD puede ser ejecutado de forma automática tras cada descarga para incluir el nuevo tiempo de la transición en la base de datos.

De acuerdo con su patrón de transición, se pueden encontrar dos tipos diferentes de transiciones en JET y DIII-D: transiciones con patrones claros y transiciones con patrones no claros. Las primeras pueden ser localizadas por un análisis visual de la señal  $D_\alpha$  y la densidad del plasma. Aproximadamente, el 25% de las descargas de JET muestran patrones claros. En contraste, el 80% de las transiciones de DIII-D muestran este tipo de patrón. Los tiempos de las transiciones con patrones no claros fueron estimados usando técnicas de aprendizaje máquina (un modelo L/H fue entrenado usando los datos de las transiciones con patrones claros). La principal diferencia entre el ATD y los métodos existentes es la completa ausencia de intervención humana en el proceso (el ATD no necesita una base de datos de tiempos de transiciones L/H localizadas previamente).

Para probar la calidad de los tiempos de transiciones determinados por el ATD, se calcularon leyes de escala para la potencia inyectada usando los tiempos determinados por expertos y los tiempos determinados por el ATD en JET. Dos métodos diferentes de regresión se aplicaron: OLS y regresión

Ridge. Las leyes de escala se calcularon usando diferentes parámetros del plasma. En todos los casos, las diferencias entre las leyes de escala obtenidas no son estadísticamente significativas, mostrando que el ATD puede identificar los tiempos de transición con precisión suficiente para derivar las mismas leyes de escala que podrían obtenerse utilizando los tiempos determinados por los expertos (Tablas 12.3 and 12.4).

La longitud del PCI está relacionada con el manejo operacional de las descargas. Según el plasma evoluciona de modo L a modo H, la predicción del modo de confinamiento (L o H) se mueve de un modo L con alta fiabilidad (no ha sido inyectada suficiente potencia en el plasma y por tanto, está claramente en modo L) a un modo L con baja fiabilidad (la potencia inyectada en el plasma está alcanzando  $P_r$ , el umbral necesario para la transición de confinamiento). En un momento dado, el clasificador empieza a predecir modo H (con baja fiabilidad). La fiabilidad aumenta según el plasma penetra en modo H. El proceso de transición requiere un cierto tiempo, en el cuál el plasma se mueve desde modo L hasta modo H, cruzando un estado intermedio durante un período de tiempo variable. El PCI representa este período y su longitud no es arbitraria y está relacionada con la forma en la que la potencia es inyectada en el plasma.

Esta interpretación del PCI como un intervalo en el cuál la transición tiene lugar con una cierta probabilidad y su relación con la potencia inyectada al plasma se confirma por las siguientes observaciones:

1. El nivel de fiabilidad de la predicción del confinamiento del plasma empieza a decrecer de forma monótona.
2. Se alcanza un nivel mínimo durante un cierto tiempo.
3. El nivel de fiabilidad comienza a aumentar también de forma monótona hasta alcanzar valores altos.

## 12.2 Modelos basados en datos de transiciones L/H y H/L usando predictores conformales

Una aproximación diferente para la determinación del modo de confinamiento del plasma consiste en la creación de un modelo L/H usando una base de datos de tiempos de transiciones L/H previamente determinados por expertos. Después, el modelo se aplica a la predicción del modo de confinamiento del plasma en nuevos pulsos.

En JET se han probado diferentes alternativas para la identificación del modo de confinamiento. Murari utilizó lógica difusa y SVM para identificar el estado del plasma (Murari et al., 2006). Este trabajo usó una base de datos de pulsos de JET reducida (25 pulsos para el modelo difuso y 27 pulsos para el modelo SVM). Las tasas de aciertos obtenidas por los modelos fueron altas:

95.77% en el conjunto de test usando SVM y 95.7% usando el modelo difuso. Vega combinó el análisis bayesiano y SVM por medio de un operador difuso (Vega et al., 2009b) y (Vega et al., 2010c). El método se aplicó a una pequeña base de datos de 42 transiciones L/H de JET (33 training y 9 test) y 38 transiciones H/L de JET (30 training y 8 test). Un intervalo de 2 s alrededor de las transiciones se clasifica usando el predictor combinado, obteniendo tasas de aciertos muy altas: 99.22% para las transiciones L/H y 96.31% para las transiciones H/L. Meakins aplicó redes neuronales para inferir el modo de confinamiento usando las características del plasma (Meakins et al., 2010). Esta aproximación fue probada usando una base de datos de 67 pulsos de JET. El conjunto de entrenamiento contenía 7,500 muestras (3,896 de modo L y 3,604 de modo H) y el conjunto de test contenía 11,600 muestras (6,314 en modo L y 5,286 en modo H). La tasa de aciertos fue del 98.86%. Finalmente, Ruiz describe un sistema en tiempo real para determinar el modo de confinamiento del plasma usando la plataforma ITMS (Ruiz et al., 2010). Usó un modelo SVM para analizar el confinamiento del plasma.

Aquí, se utilizan predictores conformales (CP) para predecir transiciones L/H y H/L en JET usando una base de datos de 355 pulsos.

### 12.2.1 Configuración del experimento

Una base de datos inicial de 355 pulsos de JET fue analizada por expertos para localizar los tiempos de las transiciones L/H y H/L. Esta base de datos se dividió en un conjunto de entrenamiento que contenía 100 pulsos (80 en el conjunto de entrenamiento propio y 20 en el conjunto de calibración) y un conjunto de test (255 pulsos). Los pulsos se asignaron aleatoriamente a uno de los conjuntos.

Se consideraron dos modelos diferentes: un modelo L/H ( $L/H_{\text{modelo}}$ ) entrenado con los tiempos de las transiciones L/H y un modelo H/L ( $H/L_{\text{modelo}}$ ) entrenado con los tiempos de las transiciones H/L. Los modelos fueron entrenados usando 11 características seleccionadas de un conjunto de 28 (Apéndice H, en inglés).

Se entrenó los modelos usando ICP, la versión inductiva de los predictores conformales y se probaron dos tipos de *kernels*: lineal y RBF. Para el *kernel* lineal, se testaron 5 valores del parámetro de regularización  $C$  ([100, 500, 1000, 2000, 3000]). Para el *kernel* RBF, todas las combinaciones de 21 valores del parámetro  $C$  ([100, 500, 1000, 1500, ... 10000]) y 21 valores del parámetro  $\sigma$  ([0.1, 0.5, 1, 1.5, ..., 10]) fueron probadas (441 combinaciones). Los modelos fueron entrenados usando un intervalo de  $\pm 0.5$  s (intervalos de longitud 1 s) alrededor de las transiciones L/H y H/L.

	Kernel lineal	Kernel RBF
<b>L/H<sub>modelo</sub></b>		
Valor medio de confianza	99.86%	99.84%
Valor medio de credibilidad	64.10%	66.85%
media( $ L/H_{real} - L/H_{estimado} $ )	22 ms	15 ms
media( $ H/L_{real} - H/L_{estimado} $ )	236 ms	203 ms
<b>H/L<sub>modelo</sub></b>		
Valor medio de confianza	97.02%	97.53%
Valor medio de credibilidad	73.25%	73.77%
media( $ L/H_{real} - L/H_{estimado} $ )	28 ms	33 ms
media( $ H/L_{real} - H/L_{estimado} $ )	102 ms	106 ms

Table 12.6: Resumen de los resultados experimentales

### 12.2.2 Resultados de los modelos L/H y H/L

Los modelos SVM se aplicaron a la predicción de los tiempos de transición L/H y H/L de los pulsos en el conjunto de entrenamiento. Ambos modelos ( $L/H_{modelo}$  y  $H/L_{modelo}$ ) fueron usados para localizar ambos tipos de transiciones (L/H y H/L). El rendimiento de los modelos fue medido usando la media del valor absoluto de la diferencia en los tiempos determinados por los expertos ( $L/H_{real}$  y  $H/L_{real}$ ) y los tiempos estimados por los modelos ( $L/H_{estimado}$  y  $H/L_{estimado}$ ).

Usando el *kernel* lineal, los mejores resultados fueron obtenidos con  $C = 100$ . El caso del *kernel* RBF, los parámetros  $C = 5500$  y  $\sigma = 3$  obtuvieron el mejor rendimiento.

La Tabla 12.6 muestra los resultados obtenidos en el experimento. Los modelos  $L/H_{modelo}$  y  $H/L_{modelo}$  se usaron para estimar los tiempos de las transiciones L/H. Los errores medios absolutos del modelo  $L/H_{modelo}$  fueron de 22 ms (*kernel* lineal) y 15 ms (*kernel* RBF) y los del modelo  $H/L_{modelo}$  fueron de 28 ms (*kernel* lineal) y 33 ms (*kernel* RBF).

Los tiempos de las transiciones H/L también fueron estimadas usando ambos modelos. Los errores medios absolutos del modelo  $L/H_{modelo}$  fueron de 236 ms (*kernel* lineal) y 203 ms (*kernel* RBF). En el caso del modelo  $H/L_{modelo}$ , los errores fueron de 102 ms (*kernel* lineal) y 106 ms (*kernel* RBF).

Los predictores conformales proporcionan información fundamental acerca de la precisión y fiabilidad de sus predicciones. La Tabla 12.6 incluye los valores medios de la confianza y la credibilidad de los pulsos de test (usando todo el intervalo temporal donde las señales están muestreadas). Puede verse que los valores de credibilidad media de los modelos  $H/L_{modelo}$  fueron significativamente mayores que los obtenidos por los modelos  $L/H_{modelo}$  (73.25% frente al 64.10% en el *kernel* lineal y 73.77% frente al 66.85% en el *ker-*

nel RBF). Esto significa que los datos de entrenamiento usados en el modelo  $H/L_{modelo}$  eran más adecuados para hacer las predicciones. Como resultado, los errores de los modelos  $H/L_{modelo}$  en las predicciones de las transiciones H/L decrecieron en un factor de 2 comparados con los errores de los modelos  $L/H_{modelo}$  mientras que los errores en la predicción de las transiciones L/H fueron únicamente unos milisegundos peores.

### 12.2.3 Discusión

A la hora de estimar el tiempo de una transición (L/H o H/L), los modelos entrenados usando esta transición obtienen mejores resultados que los modelos entrenados usando la transición opuesta. Por ejemplo, el  $L/H_{modelo}$  con *kernel* lineal obtiene un error absoluto medio de 22 ms estimando los tiempos de transición L/H mientras que el  $H/L_{modelo}$  con *kernel* lineal obtiene 28 ms. A la hora de estimar los tiempos de transición H/L, el modelo  $L/H_{modelo}$  con *kernel* lineal obtiene un error absoluto medio de 236 ms mientras que el  $H/L_{modelo}$  con *kernel* lineal obtiene 102 ms. Esto es una consecuencia, entre otras, de la diferencia en las trayectorias de las transiciones L/H y H/L (Meakins et al., 2010). La trayectoria del plasma en el espacio de características no es el mismo para las transiciones L/H y H/L. La Figura 6.18 muestra la trayectoria del pulso de JET 74323 en el espacio  $T_e$  (temperatura electrónica del plasma) y  $n_e$  (densidad del plasma). Es posible observar que las transiciones L/H y H/L tienen lugar en puntos diferentes del espacio y, por tanto, esto hace difícil estimar el tiempo de una transición usando un modelo entrenado usando la transición opuesta.

También es importante mencionar que los errores obtenidos en la determinación de los tiempos de transición H/L son mayores que los obtenidos en la determinación de los tiempos de transición L/H. Esto es parcialmente una consecuencia de la incertidumbre en la localización de los tiempos de transición H/L determinados por los expertos.

## 12.3 Conclusiones

El modo H y los modos de confinamiento avanzados son una característica fundamental para obtener una planta eléctrica de fusión. Sin ellos, sería difícil alcanzar el régimen de operación de alta Q necesario en ITER y otros dispositivos de fusión. El parámetro  $P_\tau$  (la potencia necesaria para acceder a modo H) de estos dispositivos es estimada usando leyes de escala. Estas leyes usan los datos de las máquinas de fusión actuales para predecir la potencia que será necesaria para acceder a modo H.

Las transiciones L/H son tradicionalmente localizadas a través del análisis visual de las señales del plasma. El primer paso consiste en la localización de una caída abrupta de la señal  $D_\alpha$  al comienzo del pulso. Después, este

tiempo tentativo es comprobado usando la densidad del plasma en el borde y el perfil de temperatura. La metodología automática ATD presentada en este capítulo localiza las transiciones L/H en un conjunto de pulsos sin intervención humana. Es importante destacar que no requiere una base de datos de transiciones L/H previamente localizadas por expertos. La metodología ATD es bastante general y ha sido aplicada para localizar transiciones L/H en dos de los mayores dispositivos de fusión sin apenas cambios: el JET y el DIII-D.

El ATD distingue dos tipos de transiciones:

- **Transiciones con patrones claros (Figura 6.9a):** muestran una clara caída de la señal  $D_\alpha$ . La tasa de acierto de localización de estos pulsos es del 100% con un intervalo de incertidumbre de  $\pm 3.2$  ms. Aproximadamente el 25% de las descargas de JET y el 80% de los pulsos de DIII-D muestran transiciones con patrones claros.
- **Transiciones con patrones no claros (Figura 6.9b):** la caída de la señal  $D_\alpha$  es difícil de distinguir debido al ruido o a la existencia de ELMs de tipo III, o no aparece. En este caso, un modelo entrenado usando las transiciones localizadas previamente se usa para estimar el tiempo de la transición. La tasa de aciertos de la localización de estas transiciones es del 96.83% en JET y del 95.6% en DIII-D. El intervalo de incertidumbre alrededor del tiempo predicho es dado por los predictores conformales. En JET, la longitud media del intervalo es de 225.2 ms en el caso de las transiciones localizadas correctamente y 453.5 ms en el caso de las transiciones no localizadas.

Los resultados obtenidos por el ATD han sido validados usando leyes de escala. Las leyes obtenidas usando los tiempos de transición dados por el ATD son estadísticamente similares a aquellas obtenidas usando los tiempos dados por los expertos. Esto se ha comprobado para dos conjuntos diferentes de variables explicativas y dos métodos de regresión. Las diferencias en las leyes de escala entre las transiciones con patrón claro y las transiciones con patrón no claro señalan que su acceso a modo H es diferente. Las transiciones claras llevan a fases con ELMs de tipo I mientras que las transiciones con patrones no claros permanecen en fase con ELMs de tipo III antes de acceder al régimen de ELMs de tipo I.

Usando los tiempos de las transiciones determinados por el ATD, es posible calcular leyes de escala para predecir la potencia requerida para acceder al modo H en los dispositivos de fusión futuros como ITER. La precisión y el peso estadístico de las leyes de escala aumentan con el número de pulsos que son usados para calcularlas. Por ello, el ATD se convierte en una valiosa herramienta de análisis de datos.

Los modelos basados en datos son una aproximación diferente a la localización de las transiciones. Estos requieren una base de datos de transiciones

localizadas por los expertos que es usada para construir un modelo explicativo. Diferentes modelos ICP han sido entrenados usando *kernels* lineales y RBF. Las medidas de conformidad han demostrado su utilidad para determinar el rendimiento de los modelos. El mayor nivel de credibilidad obtenido por los modelos entrenados usando puntos de las transiciones H/L indica que estos modelos son más adecuados para clasificar nuevas descargas que los entrenados usando transiciones L/H.

Las diferentes trayectorias de las transiciones L/H y H/L en el espacio de características (Figura 6.18) debe ser tenida en cuenta cuando se diseñe un modelo del confinamiento del plasma. La trayectoria que sigue el plasma durante la transición L/H puede ser diferente de la seguida durante la transición H/L. Esto hace que los resultados del  $H/L_{modelo}$  sean peores que los del  $L/H_{modelo}$  en la localización de las transiciones L/H y que los resultados del  $L/H_{modelo}$  sean peores que los del  $H/L_{modelo}$  determinando las transiciones H/L.

## Chapter 13

# Conclusiones y Trabajo Futuro

### Conclusiones

Esta tesis trata de resolver uno de los principales problemas de la fusión por confinamiento magnético: el análisis automático de los datos generados por los dispositivos de fusión. El crecimiento de los datos generados por los diferentes diagnósticos del plasma y los nuevos (como cámaras) desarrollados e instalados en los últimos años hacen que el análisis visual de los datos sea prácticamente imposible.

La identificación de los fenómenos del plasma se lleva a cabo a través de la identificación de patrones similares en los datos recogidos por los diagnósticos. Debido a la complejidad de las bases de datos de fusión, las técnicas actuales de minería de datos e inteligencia artificial tienen problemas al trabajar con datos de fusión. Como consecuencia, esta tesis ha desarrollado un conjunto de técnicas de ámbito general que pueden manejar datos de fusión.

En primer lugar, UMEL ha sido descrito. UMEL es una poderosa herramienta para localizar automáticamente eventos relevantes en ambas señales e imágenes. El diseño de métodos automáticos para localización de eventos en fusión de plasmas requiere el conocimiento de expertos. Los sistemas expertos (la combinación de la inteligencia artificial y el conocimiento experto) son una exitosa opción para localizar eventos en las bases de datos de fusión. Las capacidades de localización de UMEL han sido combinadas con conocimiento experto para localizar:

- **Dientes de sierra:** son reconocidos como picos en la emisión de rayos X débiles a diferentes radios. UMEL automatiza la localización de los dientes de sierra y el cálculo de la difusividad del plasma (Vega et al., 2010a).
- **Disrupciones:** un pico simultáneo del lazo de voltaje y una caída de la corriente del plasma revelan la existencia de una disrupción. Las disrupciones localizadas por UMEL pueden ser clasificadas usando las

técnicas existentes de reconocimiento de patrones. El sistema experto creado para localizar disrupciones en JET obtuvo una tasa de aciertos del 99.02% (Vega et al., 2010a). Las disrupciones localizadas serán usadas por los científicos con tres propósitos diferentes:

- Aumentar el conocimiento de las disrupciones y el peso estadístico de futuros estudios.
  - Mitigar sus consecuencias.
  - Predecirlas antes de que ocurran.
- **ELMs:** Los ELMs aparecen en las señales del plasma como picos de la señal  $D_\alpha$  acompañados por caídas de la energía diamagnética. Estos eventos son identificados usando UMEL. El localizador de ELMs obtuvo una tasa de aciertos del 95% en la localización de ELMs en la base de datos de JET. El estudio de una base de datos de más de 226,000 ELMs reveló que el periodo más frecuente de los ELMs en JET es entre 0.02 s y 0.03 s (González et al., 2010a). Este método de localización ayudará a los científicos a:
    - Aumentar el conocimiento de los ELMs y el peso estadístico de futuros estudios.
    - Mitigar las consecuencias de los ELMs en los componentes de la pared de la cámara de vacío y el divertor.
    - Estudiar los efectos de diferentes configuraciones del plasma en los ELMs. En particular, se analizó el perfil de temperatura durante los ELMs en las campañas de la pared de carbono de JET (González et al., 2012c).

Además, UMEL ha demostrado su utilidad en el análisis de imágenes y películas del plasma (González et al., 2010):

- **Imágenes:** se ha mostrado que las áreas más relevantes de una imagen contienen altos gradientes de intensidad entre píxeles vecinos. UMEL localiza estos gradientes y por lo tanto, las áreas relevantes. La actividad de estas áreas puede resumirse usando mapas de calor. Usando estos mapas, los científicos pueden analizar las diferentes fases del plasma durante un pulso.
- **Películas:** usando el número de vectores soporte devueltos por UMEL, es posible localizar los frames donde tienen lugar los eventos. Los puntos calientes de 10 películas infrarojas de JET fueron detectados obteniendo una tasa de aciertos del 91.64%. Usando este método, los científicos podrán analizar, por ejemplo, la carga de calor depositada en los componentes de la pared del plasma tras cada punto caliente.

En segundo lugar, la alta dimensionalidad de las bases de datos de fusión hace esencial el uso de técnicas de selección de características y reducción de dimensionalidad. Esta tesis desarrolla dos métodos diferentes para dos tipos de datos:

- **Espacios de alta dimensionalidad:** se ha demostrado que un hiperplano lineal puede ser usado para seleccionar un grupo adecuado de características para clasificar un conjunto de muestras. Esta técnica (apodada SVM-FES) se aplicó a la elección de un conjunto de características para clasificar muestras en los modos L y H. (González et al., 2010b). El espacio inicial de características estaba formado por 28 señales. Se consideraron dos ventanas temporales diferentes:
  - **$\pm 100$  ms:** la tasa de aciertos de la clasificación en el espacio original fue del 94.252% (usando 28 señales). El espacio de características fue reducido a 11 señales obteniendo un porcentaje de aciertos del 93.404% (únicamente 0.848% menor que el obtenido en el espacio de características original).
  - **$\pm 500$  ms:** el espacio inicial obtuvo una tasa de aciertos del 98.026% (28 señales). Este se redujo a 5 señales obteniendo una tasa de aciertos en la clasificación del 97.436% (únicamente un 0.590% menos).

Usando estos modelos, se han alcanzado los siguientes objetivos:

- Dos exitosos modelos L/H han sido construidos. Además, un clasificador L/H combinado ha sido construido utilizando las salidas de estos modelos.
  - Se ha estudiado la importancia de las características a diferentes distancias de la transición L/H. Se encontró que la clasificación de los puntos L/H lejos de la transición era un problema casi linealmente separable pero se volvía no separable cerca de la transición.
- **Imágenes:** RSIC es una novedosa metodología que ha demostrado su valor para reducir la dimensionalidad de las imágenes en un problema de clasificación. Dado un conjunto de imágenes pertenecientes a dos o más clases, RSIC es capaz de localizar las regiones más adecuadas para clasificar las imágenes. RSIC usa una medida de no conformidad para evaluar el rendimiento de las regiones. En el experimento llevado a cabo usando 1,272 imágenes del TJ-II Thomson scattering, las imágenes fueron reducidas hasta el 16.49% de su tamaño original obteniendo una tasa de aciertos en la clasificación del 95.27% frente al 96.37% obtenido usando las imágenes completas (únicamente un 1.10% menor). Además, los tiempos de entrenamiento, calibración y test fueron reducidos un 93.97%, 81.55% y un 81.82% respectivamente (González et al., 2012d). Las principales ventajas de RSIC son:

- La reducción de la dimensión de las imágenes. Esto acorta el tiempo de CPU y el espacio de almacenamiento.
- La identificación de las ROIs. Esto ayuda a comprender la estructura de las imágenes.

Finalmente, se ha llevado a cabo un análisis de las transiciones L/H y H/L. Por una parte, un localizador automático de transiciones L/H (ATD) ha sido descrito. Esta es una novedosa técnica de localización de transiciones L/H en señales del plasma que fue aplicada con éxito en dos dispositivos de fusión, el JET (González et al., 2012a) y el DIII-D (Farias et al., 2012) con pequeñas modificaciones. El desarrollo del ATD ha revelado la existencia de dos tipos distintos de transiciones L/H:

- **Transiciones con patrones claros:** se caracterizan por una caída inequívoca de la señal  $D_\alpha$  y llevan a fases de ELMs de tipo I. En JET y DIII-D, todas las transiciones con patrones claros fueron localizadas correctamente por el ATD.
- **Transiciones con patrones no claros:** no existe una caída clara de la señal  $D_\alpha$  y están seguidas de fases de ELMs de tipo III antes de acceder a un régimen de ELMs de tipo I. En JET, 96.83% de las transiciones con patrones no claros fueron correctamente clasificadas frente al 95.60% en DIII-D.

Usando leyes de escala, se ha demostrado que el acceso a modo H es diferente en ambos tipos de transiciones y los resultados dados por el ATD han sido validados. También se ha encontrado que la longitud del PCI (intervalo de confianza de la predicción) está relacionada con la forma en la que la potencia es inyectada al plasma: cuando es de forma abrupta, el PCI es corto ( $\approx 200\text{-}300$  ms) pero si la potencia se inyecta de forma lenta en el plasma, el PCI es más largo.

La localización automática de transiciones L/H es especialmente relevante para la fusión en dos aspectos:

- Las transiciones localizadas automáticamente aumentarán la significancia estadística de los futuros estudios.
- Estas transiciones se usarán para calcular leyes de escala para predecir la potencia requerida para acceder al modo H en dispositivos de fusión futuros como ITER.

Por otra parte, CP se utilizó para crear modelos L/H y H/L guiados por datos. Usando las medidas conformales, se encontró que los modelos entrenados usando transiciones H/L son más adecuados para evaluar el modo de confinamiento que los modelos entrenados usando las transiciones L/H (González et al., 2012b).

## Trabajo Futuro

El trabajo desarrollado ha suscitado la aparición de algunos puntos interesantes que deben ser tratados en el futuro:

- Localización de diferentes fenómenos en el plasma usando UMEL: esta tesis ha descrito la aplicación de UMEL para localizar ELMs, disrupciones y dientes de sierra en señales y puntos calientes en películas del infrarrojo pero existen más fenómenos del plasma que pueden ser localizados usando esta herramienta. Por ejemplo, los pellets pueden ser seguidos usando películas y la existencia de islas magnéticas puede ser detectada usando señales.
- El análisis de los perfiles de temperatura durante ELMs se ha limitado a 2 ms después de los ELMs. Este análisis puede ser extendido para estudiar la evolución completa del perfil desde el tiempo del ELM hasta el tiempo donde el gradiente de temperatura del borde está completamente recuperado. El valor de la degradación puede ser medido en cada instante después del ELM. Además, la nueva pared de la cámara de vacío de JET (similar a la que tendrá ITER) proporciona una nueva oportunidad de medir la degradación del gradiente de temperatura durante los ELMs bajo nuevas condiciones.
- El análisis de la complejidad del modelo SVM-FES puede ser realizado usando únicamente SVs y no SVs más errores: el extractor de características descrito en esta tesis estima la complejidad de los modelos usando el número de SVs. Estos SVs incluyen las muestras que están mal clasificadas. Para realizar un estudio más preciso de la complejidad, el número de errores podría ser restado del número total de SVs.
- Acerca de la metodología RSIC, ésta usa únicamente una región para cada clase. Es posible que, para problemas de clasificación muy complejos, se necesiten varias regiones. El rendimiento del sistema si se elige más de una región por clase debería ser probado.
- La metodología ATD puede ser aplicada para localizar transiciones en los nuevos pulsos de JET con la pared similar a la de ITER. Además, un análisis en profundidad de los dos tipos de transiciones L/H detectadas (patrones claros y no claros) debe ser realizado usando una base de datos específica. El estudio del acceso a modo H es interesante puesto que es un aspecto fundamental de ITER.



## Part III

# Appendices



# Appendix A

## List of Journal Papers & Conferences

### Journal Papers

- GONZÁLEZ, S., VEGA, J., MURARI, A., PEREIRA, A., BEURSKENS, M. AND JET-EFDA CONTRIBUTORS. Automatic ELM location in JET using a Universal Multi-Event Locator. *Fusion Science and Technology*, vol. 58(3), pages 755-762, 2010
- GONZÁLEZ, S., VEGA, J., MURARI, A. AND JET-EFDA CONTRIBUTORS. Analysis of video-movies using Support Vector Regression. *Fusion Science and Technology*, vol. 58(3), pages 763-770, 2010
- GONZÁLEZ, S., VEGA, J., MURARI, A., PEREIRA, A., RAMÍREZ, J. M., DORMIDO-CANTO, S. AND JET-EFDA CONTRIBUTORS. Support Vector Machine-based feature extractor for L/H transitions in JET. *Review of Scientific Instruments*, vol. 81(10E123), 2010
- GONZÁLEZ, S., VEGA, J., MURARI, A., PEREIRA, A., DORMIDO-CANTO, S., RAMÍREZ, J. M. AND JET-EFDA CONTRIBUTORS. Automatic location of L/H transition times for physical studies with a large statistical basis. *Plasma Physics and Controlled Fusion*, vol. 54(6), 065009, 19 pages, 2012
- GONZÁLEZ, S., VEGA, J., MURARI, A., PEREIRA, A., DORMIDO-CANTO, S., RAMÍREZ, J. M. AND JET-EFDA CONTRIBUTORS. H/L transition time estimation in JET using conformal predictors. *Fusion Engineering and Design*, 2012. In press
- GONZÁLEZ, S., VEGA, J., PEREIRA, A. AND PASTOR, I. Region selection and image classification methodology using a non-conformity

measure. *Progress in Artificial Intelligence*, vol. 1(3), pages 215-222, 2012

- GONZÁLEZ, S., VEGA, J., MURARI, A., PEREIRA, A. AND JET-EFDA CONTRIBUTORS. Automated analysis of edge pedestal gradient degradation during ELMs. *Fusion Science and Technology*, vol. 62(3), pages 403-408, 2012
- VEGA, J., MURARI, A., GONZÁLEZ, S. AND JET-EFDA CONTRIBUTORS. A universal support vector machines based method and automatic event location in waveforms and video-movies: applications to massive nuclear fusion databases. *Review of Scientific Instruments*, vol. 81(2), 023505, 11 pages, 2010
- VEGA, J., MURARI, A., PEREIRA, A., GONZÁLEZ, S. AND PASTOR, I. Accurate and reliable image classification by using conformal predictors in the TJ-II Thomson scattering. *Review of Scientific Instruments*, vol. 81(10), 10E118, 4 pages, 2010
- VEGA, J., MURARI, A., RATTÁ, G., GONZÁLEZ, S. AND DORMINDO-CANTO, S. Progress on statistical learning systems as data mining tools for the creation of automatic databases in fusion environments. *Fusion Engineering and Design*, vol. 85(3-4), pages 399-402, 2010
- RUIZ, M., VEGA, J., BARRERA, E., GONZÁLEZ, J., MURARI, A., MELÉNDEZ, R., RATTÁ, G. AND GONZÁLEZ, S. Test-bed of a real time detection system for L/H and H/L transitions implemented with the ITMS platform. *Fusion Engineering and Design*, vol. 85(3-4), pages 360-366, 2010
- VEGA, J., MURARI, A., GONZÁLEZ, S., PEREIRA, A. AND PASTOR, I. Overview of statistically hedged prediction methods: from off-line to real-time data analysis. *Fusion Engineering and Design*, 2012. In press
- FARIAS, G., VEGA, J., GONZÁLEZ, S., PEREIRA, A., LEE, X., SCHISSEL, D. AND GOHIL, P. Automatic determination of L/H transition times in DIII-D through a collaborative distributed environment. *Fusion Engineering and Design*, 2012. In press

## Conferences

- GONZÁLEZ, S., VEGA, J., MURARI, A., PEREIRA, A., BEURSKENS, M. AND JET-EFDA CONTRIBUTORS. Automatic ELM location in JET using a Universal Multi-Event Locator. 6th Fusion Data Validation Workshop, January 25-27, 2010, Madrid, Spain

- 
- GONZÁLEZ, S., VEGA, J., MURARI, A. AND JET-EFDA CONTRIBUTORS. Analysis of video-movies using Support Vector Regression. 6th Fusion Data Validation Workshop, January 25-27, 2010, Madrid, Spain
  - GONZÁLEZ, S., VEGA, J., MURARI, A., PEREIRA, A., RAMÍREZ, J. M., DORMIDO-CANTO, S. AND JET-EFDA CONTRIBUTORS. Support Vector Machine-based feature extractor for L/H transitions in JET. 18th High Temperature Plasma Diagnostics (HTPD) conference, May 16-20, 2010, Wildwood, New Jersey, USA
  - GONZÁLEZ, S., VEGA, J., MURARI, A., PEREIRA, A., DORMIDO-CANTO, S., RAMÍREZ, J. M. AND JET-EFDA CONTRIBUTORS. H/L transition time estimation in JET using conformal predictors. 8th IAEA Technical Meeting on Control, Data Acquisition and Remote Participation for Fusion Research, June 20-24, 2011, San Francisco, California, USA
  - GONZÁLEZ, S., VEGA, J., PEREIRA, A. AND PASTOR, I. Region selection and image classification methodology using a non-conformity measure. International Classification Conference, July 11-15, 2011, St. Andrews, Scotland
  - GONZÁLEZ, S., VEGA, J., MURARI, A., PEREIRA, A. AND JET-EFDA CONTRIBUTORS. Automated analysis of edge pedestal gradient degradation during ELMs. 7th Fusion Data Validation Workshop, March 26-28, 2012, Frascati, Roma, Italy
  - VEGA, J., MURARI, A., RATTÁ, G., GONZÁLEZ, S. AND DORMINDO-CANTO, S. Progress on statistical learning systems as data mining tools for the creation of automatic databases in fusion environments. 7th IAEA Technical Meeting on Control, Data Acquisition and Remote Participation for Fusion Research, 15-19 June, 2009, Aix-en-Provence, France
  - RUIZ, M., VEGA, J., BARRERA, E., GONZÁLEZ, J., MURARI, A., MELÉNDEZ, R., RATTÁ, G. AND GONZÁLEZ, S. Test-bed of a real time detection system for L/H and H/L transitions implemented with the ITMS platform. 7th IAEA Technical Meeting on Control, Data Acquisition and Remote Participation for Fusion Research, 15-19 June, 2009, Aix-en-Provence, France
  - VEGA, J., MURARI, A., PEREIRA, A., GONZÁLEZ, S. AND PASTOR, I. Accurate and reliable image classification by using conformal predictors in the TJ-II Thomson scattering. 18th High Temperature Plasma Diagnostics (HTPD) conference, May 16-20, 2010, Wildwood, New Jersey, USA

- FARIAS, G., VEGA, J., GONZÁLEZ, S., PEREIRA A., LEE, X., SCHISSEL, D. AND GOHIL, P. Automatic determination of L/H transition times in DIII-D through a collaborative distributed environment. 8th IAEA Technical Meeting on Control, Data Acquisition and Remote Participation for Fusion Research, June 20-24, 2011, San Francisco, California, USA
- VEGA, J., MURARI, A., GONZÁLEZ, S., PEREIRA, A. AND PASTOR, I. Overview of statistically hedged prediction methods: from off-line to real-time data analysis. 8th IAEA Technical Meeting on Control, Data Acquisition and Remote Participation for Fusion Research, June 20-24, 2011, San Francisco, California, USA

## Appendix B

# Fisher's Iris Data Set

Fisher's Iris data set were published by Fisher in 1936 (Fisher, 1936) to probe the usage of discriminant functions on classification. Since then, Fisher's Iris data set have been used as a benchmark to compare the results obtained by several classification algorithms. This data set consists of the measurements of the flowers of fifty plants each of the three species *Iris setosa*, *Iris versicolor*, and *Iris virginica*. It makes a total of 150 different flowers. The measurements include the *sepal length* (SL), the *sepal width* (SW), the *petal length* (PL) and the *petal width* (PW).



## Appendix C

# Wine Data Set

The Wine data set is a public data set (Frank and Asuncion, 2010) containing 178 different wines grown in the same Italian region but by three different cultivars. The data set contains 13 different measurements of wine qualities:

1. Alcohol (Alh)
2. Malic acid (MAc)
3. Ash (Ash)
4. Alcalinity of ash (Alc)
5. Magnesium (Mag)
6. Total phenols (TPh)
7. Flavanoids (Fla)
8. Non-flavanoid phenols (NF1)
9. Proanthocyanins (Pan)
10. Color intensity (CIn)
11. Hue (Hue)
12. OD280/OD315 of diluted wines (ODW)
13. Proline (Pli)

The wine's classes contains 59, 71 and 48 samples respectively. All attributes are continuous and there are no missing values.



## Appendix D

# Semeion Handwritten Digit Data Set

The Semeion handwritten digit data set was created by Tattile<sup>1</sup> Srl. and donated in 1994 to Semeion Research Center<sup>2</sup>. This is a public database and can be found in the UCI machine learning repository (Frank and Asuncion, 2010).

It contains 1593 handwritten digits from 0 to 9 written by about 80 people. Each one of the handwritten digits consists of a binary square matrix of 256 pixels where the pixels of the digit have value 1 and 0 the rest. The numbers have been stretched to fit into the 16x16 pixels matrices. The number of digits on each class can be found in Table D.1.

Figure D.1 contains an example of three different sets of digits in the Semeion data set.

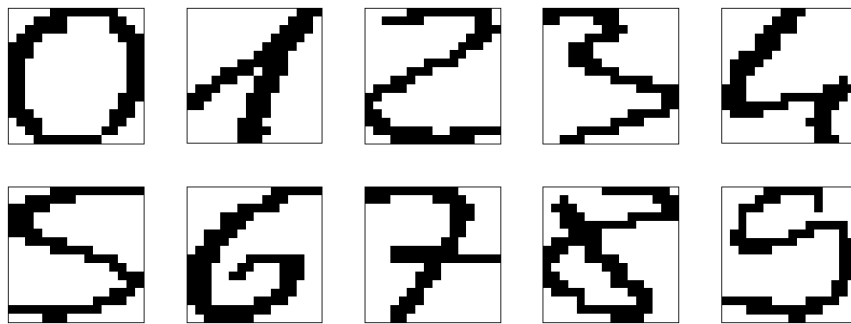
---

<sup>1</sup>Tattile Srl. via Gaetano Donizetti, 1-3-5, 25030 Mairano (Brescia), Italy

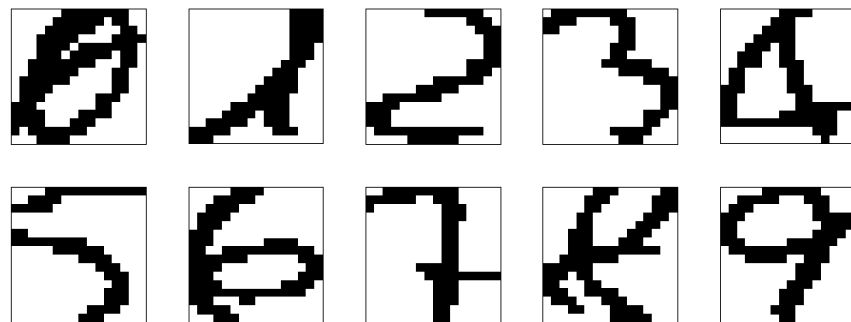
<sup>2</sup>Semeion Research Center of Sciences of Communication, via Sersale 117, 00128 Rome, Italy

Character	Number of examples	Character	Number of examples
0	161	5	159
1	162	6	161
2	159	7	158
3	159	8	155
4	161	9	158

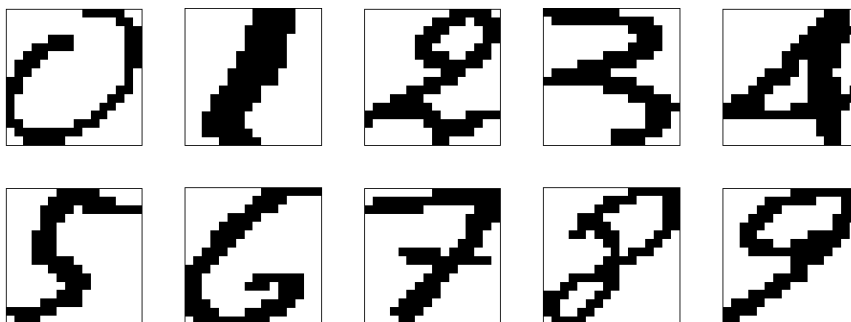
Table D.1: Number of examples of each character in the Semeion handwritten digit data set



(a) Handwritten characters set 1



(b) Handwritten characters set 2



(c) Handwritten characters set 3

Figure D.1: Three different sets of the Semeion handwritten characters

## Appendix E

# Concrete Compressive Strength Data Set

The concrete compressive strength data set contains 1,030 observations of the concrete compressive strength. It was donated by Prof. I-Cheng Yeh from the Department of Information Management of the Chung-Hua University, Taiwan (Yeh, 1998) and it can be accessed from (Frank and Asuncion, 2010).

The concrete compressive strength is a function of age and ingredients (explanatory variables). These variables include:

1. **CMT:** Cement ( $\text{kg}/\text{m}^3$ )
2. **BST:** Blast Furnace Slag ( $\text{kg}/\text{m}^3$ )
3. **FLY:** Fly Ash ( $\text{kg}/\text{m}^3$ )
4. **WTR:** Water ( $\text{kg}/\text{m}^3$ )
5. **SUP:** Superplasticizer ( $\text{kg}/\text{m}^3$ )
6. **CRS:** Coarse Aggregate ( $\text{kg}/\text{m}^3$ )
7. **FIN:** Fine Aggregate ( $\text{kg}/\text{m}^3$ )
8. **AGE:** Age (days)

The dependent variable is the concrete compressive strength (MPa).



## Appendix F

# List of signals and results of the SVM-FES of the L/H transition in JET

The initial set of 28 signals is made up of:

1. **BNDIAM:**  $\beta$  normalised with respect to the diamagnetic energy (A)  
JET address: JPF/GS/BL-BNDIAM<S
2. **BT:** Toroidal magnetic field at  $R = 2.96$  m (T)  
JET address: PPF/MAGN/BVAC
3. **ELO:** Elongation boundary  
JET address: PPF/EFIT/ELON
4. **FDWDT:** Time derivative of diamagnetic energy (A)  
JET address: JPF/GS/BL-FDWDT<S
5. **IPLA:** Plasma current (A)  
JET address: JPF/DA/C2-IPLA
6. **LI:** Plasma inductance (SI)  
JET address: PPF/MG2/XLI
7. **PTOT:** Total heating power (W)  
JET address: PPF/MG3/YTO
8. **Q95:** Safety factor (SI)  
JET address: PPF/MG3/Q95

9. **TRIL:** Lower triangulary  
JET address: PPF/EFIT/TRIL
10. **TRIU:** Upper triangulary  
JET address: PPF/EFIT/TRIU
11. **XPRL:** R coordinate lower X point (m)  
JET address: PPF/EFIT/RXPL
12. **XPZL:** Z coordinate lower X point (m)  
JET address: PPF/EFIT/ZXPL
13. **LSPRI:** R coordinate inner lower strike point (m)  
JET address: PPF/EFIT/RSIL
14. **LSPZI:** Z coordinate inner lower strike point (m)  
JET address: PPF/EFIT/ZSIL
15. **LSPRO:** R coordinate outer lower strike point (m)  
JET address: PPF/EFIT/RSOL
16. **LSPZO:** R coordinate outer lower strike point (m)  
JET address: PPF/EFIT/ZSOL
17. **RIG:** Radial inner gap (m)  
JET address: PPF/EFIT/RIG
18. **ROG:** Radial outer gap (m)  
JET address: PPF/EFIT/ROG
19. **AD36:**  $D_\alpha$  inner view (p/s · cm<sup>2</sup> · sr)  
JET address: PPF/S3AD/AD36
20. **TOG:** Top outer gap (m)  
JET address: JPF/PF/SC-TOG<XS
21. **RAD:** Radiated power (W)  
JET address: PPF/BOLO/TOPI
22. **TE02:** Electron temperature at PSI = 0.2 (eV)  
Calculate from: PPF/KK3
23. **CR0:** Plasma minor radius (m)  
JET address: PPF/EFIT/CR0

- 
24. **RGEO:** Plasma major radius (m)  
JET address: PPF/EFIT/RGEO
  25. **LAD3:** Line average electron density at the plasma core ( $\text{p/m}^3$ )  
JET address: PPF/KG1L/LAD3
  26. **LAD4:** Line average electron density at the plasma edge ( $\text{p/m}^3$ )  
JET address: PPF/KG1L/LAD4
  27. **WDIA:** Diamagnetic energy  
Calculate from: PPF/BTLI/WDIA, chain 1
  28. **TE08:** Electron temperature at  $\text{PSI} = 0.8$  (eV)  
Calculate from: PPF/KK3

The results of the SVM-FES of the  $\pm 100$  ms model are shown in Tables F.1, F.2 and F.3. Each column represents an iteration of the SVM-FES. For each column, the signal with the lowest absolute coefficient is discarded. Then, a new model of one dimension less is trained again and the process is repeated until all the signals have been discarded. The signal discarded on each iteration have been crossed out.

Tables F.4, F.5 and F.6 contains the results of the SVM-FES of the  $\pm 500$  ms model.

The SVM-FES can be sped up if more than one feature are discarded on each step. Tables F.7 and F.8 contains the SVM-FES of the  $\pm 100$  ms and  $\pm 500$  ms models respectively where 3 features are discarded on each step of the process. Therefore, the 28 signals SVM-FES is reduced to 10 steps. Figures F.1a and F.1b contain the numbers of SVs and the success rates of the  $\pm 100$  and  $\pm 500$  ms models respectively.

Signal	Hyperplane coefficients														
BNDIAM	-2.680	-2.570	-2.691	-1.077	9.827	10.022	10.110	9.549	9.599	9.051	9.042				
BT	10.019	9.999	10.083	10.022	9.827	10.022	10.110	9.549	9.599	9.051	9.042				
ELO	-5.032	-5.017	-5.532	-6.482	-7.095	-6.738	-6.821	-4.469	-3.266	-0.894	-0.938				
FDWDT	-0.609														
IPLA	-4.374	-4.350	-3.826	-4.062	-4.273	-4.478	-4.643	-3.392	-3.107	-1.495	-1.479				
LI	-8.404	-8.402	-9.383	-9.348	-8.624	-8.793	-8.758	-7.780	-8.515	-8.263	-8.272				
PTOT	-0.937	-0.937													
Q95	7.065	7.090	7.082	7.039	6.867	7.237	7.318	6.805	7.228	6.586	6.572				
TRIL	-7.438	-6.493	-9.527	-5.632	-5.590	5.060	7.351	9.031	1.958	-1.054	-1.063				
TRIU	9.336	9.339	9.476	9.934	9.928	9.622	9.621	7.962	6.891	4.876	4.928				
XPRL	-8.774	-8.207	-9.210	-7.276	-7.905	-1.406									
XPZL	5.149	4.817	3.545	4.486	5.539	2.879	2.874	-1.106	-3.000	-2.497	-2.497				
LSPRI	4.871	4.860	4.194	5.026	5.652	4.290	4.292	3.081							
LSPZI	-8.240	-8.112	-7.311	-8.082	-8.812	-7.155	-7.138	-5.062	-1.733						
LSPRO	-5.614	-5.367	-5.625	-6.089	-6.329	-2.764	-2.737								
LSPZO	-2.295	-2.160	-2.505	-2.707	-2.949										
RIG	26.619	26.973	35.022	31.824	26.444	20.332	20.012	26.432	19.678	14.316	13.675				
ROG	15.807	16.047	14.911	15.762	16.246	16.418	16.450	17.850	12.059	6.864	6.969				
AD36	-9.901	-10.006	-10.104	-10.053	-10.392	-10.665	-10.520	-10.952	-11.389	-11.607	-11.554				
TOG	18.806	19.025	19.973	18.431	15.510	15.148	14.985	16.457	16.238	15.202	15.144				
RAD	-77.240	-77.064	-80.931	-81.641	-80.463	-82.161	-82.377	-78.736	-77.381	-71.746	-71.902				
TE02	4.844	4.754	5.195	5.106	5.263	5.441	5.451	5.586	6.717	7.025	7.054				
CR0	38.795	39.461	41.351	41.064	37.832	37.144	37.374	43.088	31.279	21.697	21.509				
RGEO	13.113	12.577	6.831	7.633	11.967	9.115	7.840	5.749	3.253	-0.559					
LAD3	-15.457	-15.368	-15.056	-14.999	-14.899	-13.384	-13.397	-12.570	-12.884	-13.457	-13.432				
LAD4	43.346	43.334	43.418	43.222	42.835	40.989	40.960	39.105	39.613	39.467	39.449				
WDIA	1.353	1.080	1.084												
TE08	112.137	112.312	109.899	109.710	105.99	104.844	104.879	106.210	103.460	103.958	103.990				
Bias	-48.040	-49.329	-48.548	-49.425	-46.190	-52.203	-53.277	-62.374	-46.377	-35.750	-35.658				

Table F.1: JET  $\pm 100$  ms model hyperplanes' coefficients

Signal	Hyperplane coefficients													
BNDIAM	9.078	8.675	8.344	7.527	8.077	8.106	8.129	8.336	8.324	7.716	6.401			
BT														
ELO														
FDWDT														
IPLA	-1.486	-0.511												
LI	-8.179	-8.636	-8.625	-9.019	-7.808	-5.040	-5.022	-3.838	-3.557					
PTOT														
Q95	6.593	6.030	5.702	5.584	6.178	6.313	6.333	5.514	5.438	4.612				
TRIL	-1.076													
TRIU	4.791	5.153	5.135	3.826	2.491									
XPRL														
XPZL	-2.247	-2.822	-2.836											
LSPRI														
LSPZI														
LSPRO														
LSPZO														
RIG	13.361	17.756	17.811	4.985	-3.612	-2.682	-2.507							
ROG	6.830	8.877	8.899	3.610										
AD36	-11.536	-10.821	-10.864	-10.492	-12.012	-9.670	-9.636	-10.166	-10.804	-13.326	-11.265			
TOG	15.972	17.714	17.570	12.894	8.427	4.274	4.283	2.285						
RAD	-72.014	-72.048	-72.299	-77.620	-79.675	-83.746	-83.827	-86.959	-77.940	-49.018	-17.192			
TE02	7.081	7.281	7.212	7.031093	7.389	8.819	8.851	8.685	7.366	5.498	1.697			
CR0	21.622	27.741	27.807	13.865	2.274	-0.158								
RGEO														
LAD3	-13.369	-13.362	-13.372	-13.704	-8.998	-7.481	-7.452	-2.893	-4.019	-12.011	-18.409			
LAD4	39.409	39.213	39.308	39.135	34.646	32.233	32.191	26.044	26.081	34.074	34.936			
WDIA														
TE08	103.836	103.851	103.842	97.352	96.288	91.186	91.244	90.818	94.633	97.993	101.815			
Bias	-36.422	-43.607	-43.660	-26.121	-14.107	-13.001	-13.219	-14.239	-13.498	-14.319	-10.029			

Table F.2: JET  $\pm 100$  ms model hyperplanes' coefficients, cont. 1

Signal	Hyperplane coefficients
BNDIAM	
BT	6.206
ELO	
FDWDT	
IPLA	
LI	
PTOT	
Q95	
TRIL	
TRIU	
XPRL	
XPZL	
LSPRI	
LSPZI	
LSPRO	
LSPZO	
RIG	
ROG	
AD36	-10.861 <del>-11.887</del>
TOG	
RAD	-15.413 -38.142 -46.479 -73.297 <del>-43.103</del>
TE02	
CR0	
RGEO	
LAD3	-18.563 -18.702 <del>-23.244</del>
LAD4	34.481 34.505 37.796 <del>9.736</del>
WDIA	
TE08	110.576 62.170 64.467 72.480 90.619
Bias	-9.511 -2.796 -2.331 -3.135 -2.992

Table F.3: JET  $\pm 100$  ms model hyperplanes' coefficients, cont. 2

Signal	Hyperplane coefficients														
BNDIAM	-3.568	-3.363	-3.384	-3.425	-3.922	-4.114	-4.267	-4.283	-0.889						
BT	9.863	9.859	9.828	9.818	10.277	9.710	8.363	8.358	7.994	7.839	7.839	7.839	7.839	7.839	6.722
ELO	9.456	9.336	9.112	10.322	10.497	12.587	13.757	13.577	12.535	12.647	12.647	12.647	12.647	12.647	12.219
FDWDT	-0.519														
IPLA	-3.598	-3.604	-3.545	-3.417	-4.234	-2.820									
LI	-3.611	-3.619	-3.644	-3.571	-4.193	-5.423	-5.311	-5.357	-5.611	-5.311	-5.311	-5.311	-5.311	-5.311	-4.999
PTOT	-1.787	-1.779	-1.766	-1.767	-1.700										
Q95	5.233	5.269	5.248	5.244	5.712	4.707	3.315	3.304	2.990	2.981	2.981	2.981	2.981	2.981	
TRIL	-33.433	-32.640	-32.059	-32.033	-37.335	-58.426	-64.419	-65.972	-55.207	-52.997	-52.997	-52.997	-52.997	-52.997	-11.561
TRIU	3.344	3.347	3.316	2.971	3.778	3.972	3.655	3.653	4.414	4.326	4.326	4.326	4.326	4.326	6.026
XPRL	-20.897	-20.375	-19.958	-19.634	-22.342	-34.832	-38.758	-39.648	-32.615	-31.572	-31.572	-31.572	-31.572	-31.572	-6.411
XPZL	0.744	0.445													
LSPRI	1.460	1.456	1.284	1.021											
LSPZI	-0.861	-0.712	-0.443												
LSPRO	-2.986	-2.839	-2.612	-2.427	-2.629	-4.573	-4.870	-5.004	-4.754	-4.303	-4.303	-4.303	-4.303	-4.303	-2.576
LSPZO	-3.571	-3.521	-3.418	-3.313	-3.098	-4.753	-5.090	-5.186	-4.773	-4.563	-4.563	-4.563	-4.563	-4.563	-3.486
RIG	32.306	32.466	32.648	31.653	31.351	50.100	52.919	53.513	45.329	42.444	42.444	42.444	42.444	42.444	28.500
ROG	7.425	7.581	7.612	6.969	7.004	5.618	5.911	5.717	6.730	7.107	7.107	7.107	7.107	7.107	11.028
AD36	-19.172	-19.239	-19.256	-19.130	-19.159	-18.916	-18.873	-19.122	-19.252	-19.549	-19.549	-19.549	-19.549	-19.549	-17.808
TOG	26.973	26.972	26.768	27.485	29.266	34.285	35.272	35.173	33.640	32.682	32.682	32.682	32.682	32.682	31.494
RAD	-2.763	-2.776	-2.783	-2.438	-2.654	-2.659	-2.527								
TE02	9.159	9.087	9.119	9.249	9.322	8.512	8.281	7.803	7.304	7.194	7.194	7.194	7.194	7.194	3.138
CR0	30.591	30.921	31.027	30.269	30.067	34.820	36.263	35.928	35.094	34.331	34.331	34.331	34.331	34.331	39.868
RGE0	13.699	13.232	12.775	12.220	15.652	14.386	17.231	17.508	16.490	17.537	17.537	17.537	17.537	17.537	4.699
LAD3	-33.030	-32.998	-32.968	-33.023	-33.634	-35.883	-35.383	-35.353	-35.126	-35.285	-35.285	-35.285	-35.285	-35.285	-36.370
LAD4	53.075	53.114	53.060	53.151	54.162	56.882	56.453	56.291	55.688	55.737	55.737	55.737	55.737	55.737	54.623
WDIA	2.396	2.099	2.116	2.143	2.554	2.530	2.592	2.600							
TE08	387.798	387.827	387.840	388.189	386.970	382.244	383.934	386.946	386.350	384.825	384.825	384.825	384.825	384.825	384.615
Bias	-35.670	-36.383	-36.635	-36.582400	-34.125	-28.975	-28.666	-27.343	-30.822	-31.475	-31.475	-31.475	-31.475	-31.475	-54.844

Table F.4: JET  $\pm 500$  ms model hyperplanes' coefficients



Signal	Hyperplane coefficients			
BNDIAM				
BT	6.646	<del>6.719</del>		
ELO				
FDWDT				
IPLA				
LI				
PTOT				
Q95				
TRIL				
TRIU				
XPRL				
XPZL				
LSPRI				
LSPZI				
LSPRO				
LSPZO				
RIG				
ROG				
AD36	-17.720	-17.809	<del>-20.317</del>	
TOG	<del>1.880</del>			
RAD				
TE02				
CR0				
RGEO				
LAD3	-26.084	-27.102	-33.061	<del>-41.249</del>
LAD4	42.164	43.207	49.910	56.438
WDIA				<del>8.435</del>
TE08	381.234	374.425	245.740	242.974
Bias	-10.991	-10.509	-4.756	-4.371
				-4.232

Table F.6: JET  $\pm 500$  ms model hyperplanes' coefficients, cont. 2

Signal	Hyperplane coefficients										
	-2.680	-1.077	7.351	7.656	7.135	8.036	8.336	7.744			
BNDIAM	10.019	10.022	4.554								
BT	5.032	-6.482									
ELO	-0.609										
FDWDT	4.374	-4.062									
IPLA	-8.404	-9.348	-8.556	-7.353	-7.968	-5.114	-3.887				
LI	-0.987										
PTOT	7.065	7.039	4.653	4.835	5.314	6.244	5.514	5.048			
Q95	-7.438	-5.632	-4.583	4.705							
TRIL	9.339	9.934	8.757	6.979	5.495						
TRIU	-8.774	-7.276	-7.471	-2.819							
XPRL	5.149	4.486	2.359								
XPZL	4.871	5.026	4.112	3.276							
LSPRI	-8.240	-8.082	-6.614	-5.030	-1.254						
LSPZI	-5.614	-6.089	-2.381								
LSPRO	-2.295	-2.707									
LSPZO	26.619	31.824	22.975	26.956	-0.328						
RIG	15.807	15.762	16.296	17.214	6.329	0.044					
ROG	-9.901	-10.053	-11.279	-10.968	-11.508	-9.597	-10.166	-16.947	-24.186		
AD36	18.806	18.431	16.252	19.544	12.881	4.680	2.285				
TOG	-77.240	-81.641	-81.852	-79.577	-83.056	-82.644	-86.960	-53.923	-35.538		
RAD	4.844	5.106	5.423	5.561	6.765	8.687	8.685	6.324			
TE02	38.795	41.064	37.782	44.079	13.937	1.361					
CR0	13.113	7.633	13.857	7.527	7.726	-1.720					
RGEO	-15.457	-14.999	-13.113	-12.398	-13.684	-8.263	-2.893				
LAD3	43.346	43.222	40.968	39.203	41.251	32.960	26.044	19.757	13.346		
LAD4	1.353										
WDIA	112.137	109.710	102.543	104.836	96.006	91.523	90.818	61.722	65.193		
TE08	-48.040	-49.425	-50.677	-64.764	-28.567	-14.153	-14.239	-15.245	-3.719	-3.203	
Bias											

Table F.7: JET  $\pm 100$  ms model hyperplanes' coefficients discarding 3 features per step

Signal	Hyperplane coefficients																			
BNDIAM	-3.568	-3.425	-0.796																	
BT	9.863	9.818	9.765	7.839	6.753	7.403														
ELO	9.456	10.322	11.386	12.646	20.582	12.512	-6.755	-5.651												
FDWDT	-0.519																			
IPLA	-3.598	-3.417	-2.983																	
LI	-3.611	-3.571	-5.713	-5.311	0.358															
PTOT	-1.787	-1.767																		
Q95	5.233	5.244	4.804	2.981																
TRIL	-33.433	-32.033	-45.897	-52.997	-5.715	-12.569	-2.980													
TRIU	3.344	2.971	4.829	4.826																
XPRL	-20.897	-19.634	-26.640	-31.572	-5.556	-7.157														
XPZL	0.744																			
LSPRI	1.460	1.021																		
LSPZI	-0.861																			
LSPRO	-2.986	-2.427	-4.251	-4.303																
LSPZO	-3.571	-3.313	-4.241	-4.563	-3.494															
RIG	32.306	31.653	41.360	42.444	37.013	30.181	3.022													
ROG	7.425	6.969	6.571	7.107	7.500	2.601														
AD36	-19.172	-19.130	-19.008	-19.549	-19.271	-17.975	-15.874	-15.790	-3.3061											
TOG	26.973	27.485	32.710	32.682	29.829	20.033	-1.540													
RAD	-2.763	-2.438	-2.970																	
TE02	9.159	9.249	7.997	7.194	0.755															
CR0	30.591	30.269	33.813	34.331	38.278	22.258	-4.326	-3.467												
RGE0	13.699	12.220	12.380	17.537	-6.715	-7.400	-7.090	-5.682												
LAD3	-33.030	-33.023	-35.683	-35.285	-32.680	-29.843	-51.021	-46.922	-20.318											
LAD4	53.075	53.151	56.311	55.737	49.843	47.488	72.717	67.590	49.910											
WDIA	2.396	2.143																		
TE08	387.798	388.189	382.550	384.824	387.293	392.033	295.060	274.961	245.740	235.156										
Bias	-35.670	-36.582	-32.940	-31.475	-59.885	-36.165	4.977	2.876	-4.756	-3.624										

Table F.8: JET  $\pm 500$  ms model hyperplanes' coefficients discarding 3 features per step

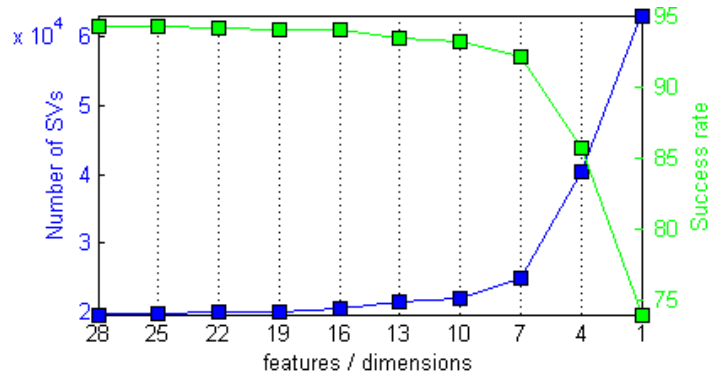
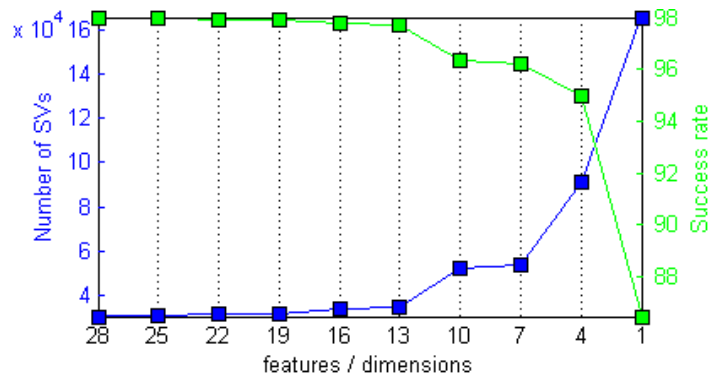
(a)  $\pm 100$  ms model(b)  $\pm 500$  ms model

Figure F.1: Success rates and numbers of SVs of the models trained in the SVM-FES discarding 3 features per step

## Appendix G

# PCA loadings of the L/H transition in JET

This Appendix contains the PCA loadings computed in Section 5.1.1.2.

Using the scree plot in Figure 5.5a it is not possible to determine the optimum number of PCs in the resulting feature space. Thus, an alternative method for determining the number of PCs has been used: the Kaiser-Guttman rule (see Section 3.2.2.2). Using this rule, the PCs with a variance value larger than the mean variance of any single original component are retained, i.e. the PCs with a percentage of the variance larger than  $100/n$  where  $n$  is the number of dimensions in the original space. In this case, all the PCs that cover a percentage of the variance larger than  $100/28 = 3.5714$  are retained. The first six PCs of the  $\pm 100$  model fulfil this condition. Their loadings are shown in Table G.1.

In the case of the  $\pm 500$  ms model the seven first PCs have a percentage of the variance larger than 3.5714. Table G.2 contains their loadings.

Signal	PC <sub>1</sub>	PC <sub>2</sub>	PC <sub>3</sub>	PC <sub>4</sub>	PC <sub>5</sub>	PC <sub>6</sub>
<b>BNDIAM</b>	0.0422	0.0225	-0.0943	0.1425	-0.0763	0.4599
<b>BT</b>	0.182	0.4303	0.1182	0.248	-0.1545	0.0263
<b>ELO</b>	-0.1638	-0.1368	0.0203	-0.0078	0.3388	-0.0643
<b>FDWDT</b>	0.0128	-0.0174	-0.0114	0.0482	-0.0184	0.1213
<b>IPLA</b>	-0.0065	0.4032	-0.0649	0.1533	0.1276	-0.0311
<b>LI</b>	0.0812	0.1255	0.3257	-0.0868	-0.1047	0.0988
<b>PTOT</b>	-0.0327	-0.2167	-0.3224	-0.1082	-0.3187	-0.2995
<b>Q95</b>	-0.1411	0.1495	-0.1209	0.0204	0.3338	-0.1467
<b>TRIL</b>	-0.3281	-0.0176	-0.054	0.1087	-0.0926	0.0209
<b>TRU</b>	-0.335	0.0621	0.3073	-0.2907	0.4723	0.1879
<b>XPRL</b>	0.2095	0.0344	-0.3994	-0.0378	0.1943	0.0414
<b>XPZL</b>	-0.1303	0.3492	-0.1136	-0.258	-0.275	-0.0692
<b>LSPRI</b>	0.0083	-0.12	0.0404	0.0089	0.151	0.2354
<b>LSPZI</b>	-0.5275	0.2263	0.2187	-0.0763	-0.3646	0.0939
<b>LSPRO</b>	0.2707	0.2933	-0.1879	-0.5137	0.0823	0.0995
<b>LSPZO</b>	-0.1798	-0.1909	0.109	0.3142	-0.0602	-0.0662
<b>RIG</b>	-0.2913	0.0566	-0.3524	0.0656	0.0809	0.0558
<b>ROG</b>	-0.0525	0.3105	0.019	-0.0371	0.0889	-0.1669
<b>AD36</b>	-0.0235	-0.0417	-0.0136	-0.1167	0.0197	0.0523
<b>TOG</b>	-0.0117	0.1263	-0.1531	0.0794	-0.1445	0.1095
<b>RAD</b>	-0.0196	-0.0215	-0.0297	-0.0415	-0.0006	-0.0012
<b>TE02</b>	-0.0667	-0.194	-0.0141	-0.1552	0.0189	-0.0131
<b>CR0</b>	0.2995	-0.156	0.3061	-0.0676	-0.1241	-0.0456
<b>RGEO</b>	-0.212	-0.035	-0.3502	0.1004	-0.0009	0.0538
<b>LAD3</b>	-0.0811	-0.1752	-0.0463	-0.4013	-0.1729	0.1847
<b>LAD4</b>	-0.0783	-0.1394	-0.0477	-0.2861	-0.1449	0.15
<b>WDIA</b>	0.0723	-0.0185	-0.1066	0.1742	-0.0354	0.6471
<b>TE08</b>	-0.0124	-0.0308	-0.0046	-0.0233	-0.0101	0.0053

Table G.1: JET  $\pm 100$  ms model PCA loadings

Signal	PC <sub>1</sub>	PC <sub>2</sub>	PC <sub>3</sub>	PC <sub>4</sub>	PC <sub>5</sub>	PC <sub>6</sub>	PC <sub>7</sub>
<b>BNDIAM</b>	0.0063	0.0481	-0.0129	0.1437	-0.1168	0.2297	-0.3437
<b>BT</b>	-0.1541	0.3475	-0.1028	-0.1181	-0.5682	-0.1576	0.3173
<b>ELO</b>	0.1813	-0.0672	0.0065	-0.0421	0.2395	-0.1259	0.3122
<b>FDWDT</b>	0.0127	-0.0164	0.0102	0.0102	-0.0246	-0.0135	-0.0145
<b>IPLA</b>	0.0315	0.4191	0.0113	0.011	-0.1096	-0.3262	-0.0703
<b>LI</b>	-0.0852	0.0332	0.0606	-0.359	-0.1038	0.0001	-0.4908
<b>PTOT</b>	0.1975	-0.2161	0.3391	0.2454	-0.3144	-0.5141	-0.1774
<b>Q95</b>	0.1601	0.2178	0.0407	0.0557	0.3436	-0.477	-0.2765
<b>TRIL</b>	0.3409	0.0096	-0.0733	0.0686	-0.1534	-0.0035	-0.0475
<b>TRU</b>	0.3917	0.0676	0.2446	-0.4787	0.2847	0.0074	-0.0391
<b>XPRL</b>	-0.1879	0.1218	0.0883	0.3321	0.2677	0.1017	0.1168
<b>XPZL</b>	0.1315	0.293	0.093	-0.0734	-0.1283	0.1232	0.0458
<b>LSPRI</b>	0.0044	-0.0902	-0.0693	-0.0345	0.1365	0.1493	-0.0871
<b>LSPZI</b>	0.4193	0.1503	-0.2288	-0.2929	-0.1483	0.2317	-0.0276
<b>LSPRO</b>	-0.2157	0.2801	0.5813	-0.0336	0.0788	0.173	-0.0002
<b>LSPZO</b>	0.1408	-0.179	-0.3748	0.0213	-0.0453	-0.0959	0.0018
<b>RIG</b>	0.3002	0.162	-0.0058	0.2945	0.0571	0.1126	0.0691
<b>ROG</b>	-0.0357	0.3253	0.0289	-0.0833	0.0365	-0.022	0.1872
<b>AD36</b>	0.0288	-0.0298	0.0619	-0.0007	-0.0024	0.0131	0.0162
<b>TOG</b>	-0.0131	0.1532	-0.0035	0.1867	-0.1389	0.178	-0.3
<b>RAD</b>	0.0136	-0.0088	0.0218	0.0073	-0.0083	-0.0116	0.0065
<b>TE02</b>	0.0374	-0.0939	0.0848	0.0062	-0.0551	-0.0535	-0.0473
<b>CR0</b>	-0.2888	-0.2761	-0.0159	-0.2648	-0.0691	-0.1549	-0.044
<b>RGEO</b>	0.2539	0.0563	-0.0324	0.3363	0.0064	0.0573	0.0396
<b>LAD3</b>	0.1732	-0.2309	0.3506	-0.0164	-0.1806	0.1439	0.1297
<b>LAD4</b>	0.1844	-0.2372	0.3387	0.0009	-0.2204	0.1317	0.1771
<b>WDIA</b>	0.0034	0.0166	-0.0008	0.1448	-0.1052	0.2323	-0.3433
<b>TE08</b>	0.0085	-0.0133	0.012	0.0045	-0.0098	-0.0086	-0.0039

Table G.2: JET  $\pm 500$  ms model PCA loadings



## Appendix H

# List of signals required by the ATD models in JET

The signals required by the models of the ATD methodology are:

- **±100 ms model**

1. **BT:** Toroidal magnetic field at  $R = 2.96$  m (T)  
JET address: PPF/MAGN/BVAC
2. **AD36:**  $D_\alpha$  inner view ( $\text{p/s} \cdot \text{cm}^2 \cdot \text{sr}$ )  
JET address: PPF/S3AD/AD36
3. **TE08:** Electron temperature at  $\text{PSI} = 0.8$  (eV)  
Calculate from: PPF/KK3
4. **LAD3:** Line average electron density at the plasma core ( $\text{p/m}^3$ )  
JET address: PPF/KG1L/LAD3
5. **LAD4:** Line average electron density at the plasma edge ( $\text{p/m}^3$ )  
JET address: PPF/KG1L/LAD4
6. **LI:** Plasma inductance (SI)  
JET address: PPF/MG2/XLI
7. **Q95:** Safety factor at  $\text{PSI} = 0.95$  (SI)  
JET address: PPF/MG3/Q95
8. **RIG:** Radial inner gap (m)  
JET address: PPF/EFIT/RIG
9. **TOG:** Top outer gap (m)  
JET address: JPF/PF/SC-TOG<XS
10. **RAD:** Radiated power (W)  
JET address: PPF/BOLO/TOPI

11. **TE02:** Electron temperature at PSI = 0.2 (eV)  
Calculate from: PPF/KK3

- **±500 ms model**

1. **BT:** Toroidal magnetic field at R = 2.96 m (T)  
JET address: PPF/MAGN/BVAC
2. **AD36:**  $D_\alpha$  inner view (p/s · cm<sup>2</sup> · sr)  
JET address: PPF/S3AD/AD36
3. **TE08:** Electron temperature at PSI = 0.8 (eV)  
Calculate from: PPF/KK3
4. **LAD3:** Line average electron density at the plasma core (p/m<sup>3</sup>)  
JET address: PPF/KG1L/LAD3
5. **LAD4:** Line average electron density at the plasma edge (p/m<sup>3</sup>)  
JET address: PPF/KG1L/LAD4

# Appendix I

## List of signals required by the ATD models in DIII-D

The signals required by the models of the ATD methodology are:

- **±50 ms model**
  1. **FS04DA:**  $D_\alpha$  signal
  2. **DENSITY:** Plasma electron density
  3. **ECH PWR:** ECH input power
  4. **IP:** Plasma current
  5. **PRAD TOT:** Radiated power
  6. **TOT PWR:** Total input power
  
- **±100 ms model**
  1. **FS04DA:**  $D_\alpha$  signal
  2. **DENSITY:** Plasma electron density
  3. **POH:** Ohmic input power
  4. **PRAD TOT:** Radiated power
  5. **TOT PWR:** Total input power



# Bibliography

ABDI, H. and WILLIAMS, L. J. Principal component analysis. *Wiley Interdisciplinary Reviews: Computational Statistics*, vol. 2(4), pages 433–459, 2010.

ACERO, A., ALBERTO, A., BLANCO, F., BLANCO, J., AN J. A. FÁBREGAS, F. C., FLORES, L. A., GIMÉNEZ, M., GONZÁLEZ, P., GUASP, J., ISEA, R., DE GUEVARA, P. L., MAYO, R., MONTES, E., MUÑOZ, A., RODRÍGUEZ, M., RUBIO-MONTERO, A. J., SERRADILLA, E. and TROIANI, S. Grid and supercomputing activities at the ICT division of CIEMAT. In *Proceedings of the Iberian Grid Infrastructure Conference 2009 (IBERGRID 2009)*, vol. 3, pages 126–136. 2009.

ALEJALDRE, C., ALONSO, J., ALMOGUERA, L., ASCASÍBAR, E., BACIERO, A., BALBÍN, R., BLAUMOSER, M., BOTIJA, J., BRAÑAS, B., DE LA CAL, E., CAPPA, A., CARRASCO, R., CASTEJÓN, F., CEPERO, J. R., CREMY, C., DONCEL, J., DULYA, C., ESTRADA, T., FERNÁNDEZ, A., FRANCÉS, M., FUENTES, C., GARCÍA, A., GARCÍA-CORTÉS, I., GUASP, J., HERRANZ, J., HIDALGO, C., JIMÉNEZ, J. A., KIRPITCHEV, I., KRIVENSKI, V., LABRADOR, I., LAPAYESE, F., LIKIN, K., LINIERS, M., LÓPEZ-FRAGUAS, A., LÓPEZ-SÁNCHEZ, A., DE LA LUNA, E., MARTÍN, R., MARTÍNEZ, A., MEDRANO, M., MÉNDEZ, P., MCCARTHY, K., MEDINA, F., VAN MILLIGEN, B., OCHANDO, M., PACIOS, L., PASTOR, I., PEDROSA, M. A., DE LA PEÑA, A., PORTAS, A., QIN, J., RODRÍGUEZ-RODRIGO, L., SALAS, A., SÁNCHEZ, E., SÁNCHEZ, J., TABARÉS, F., TAFALLA, D., TRIBALDOS, V., VEGA, J., ZURRO, B., AKULINA, D., FEDYANIN, O. I., GREBENSHCHICOV, S., KHARCHEV, N., MESHCHERYAKOV, A., BARTH, R., VAN DIJK, G., VAN DER MEIDEN, H. and PETROV, S. First plasmas in the TJ-II flexible heliac. *Plasma Physics and Controlled Fusion*, vol. 41(3A), pages A539–A548, 1999.

BOSER, B., GUYON, I. and VAPNIK, V. A training algorithm for optimal margin classifiers. *Fifth Annual Workshop on Computational Learning Theory*, pages 144–152, 1995.

- BRADLEY, A. The use of the area under the roc curve in the evaluation of machine learning algorithms. *Pattern Recognition*, vol. 30(7), pages 1145–1159, 1997.
- BREIMAN, L., FRIEDMAN, J. H., OLSHEN, R. A. and STONE, C. J. *Classification and regression trees*. Belmont, CA, Chapman and Hall, Wadsworth, 1984. ISBN 978-0412048418.
- BROOKS, N. H., PETERSEN, P. and DIII-D GROUP. Initial conditioning of the vessel wall and the graphite limiters in DIII-D. *Journal of Nuclear Materials*, vol. 145-147, pages 770–774, 1987.
- BURKE, B. *The World According to Wavelets*. A K Peters, 1996. ISBN 1-56881-047-4.
- BURRELL, K. H., EJIMA, S., SCHISSEL, D. P., BROOKS, N. H., CALLIS, R. W., CARLSTROM, T. N., COLLERAINE, A. P., DEBOO, J. C., FUKUMOTO, H., GROEBNER, R. J., HILL, D. N., HONG, R.-M., HOSOGANE, N., JACKSON, G. L., JAHNS, G. L., JANESCHITZ, G., KELLMAN, A. G., KIM, J., LAO, L. L., LEE, P., LOHR, J. M., LUXON, J. L., MAHDAVI, M. A., MOELLER, C. P., OHYABU, N., OSBORNE, T. H., OVERSKEI, D., PETERSEN, P. I., PETRIE, T. W., PHILLIPS, J. C., PRATER, R., SCOVILLE, J. T., SERAYDARIAN, R. P., SHIMADA, M., SLEAFORD, B. W., SNIDER, R. T., STAMBAUGH, R. D., STAV, R. D., ST. JOHN, H. E., STOCKDALE, R., STRAIT, E. J., TAYLOR, T., TOOKER, J. F. and YAMAGUCHI, S. Observation of an improved energy-confinement regime in neutral-beam-heated divertor discharges in the DIII-D tokamak. *Physical Review Letters*, vol. 59(13), pages 1432–1435, 1987.
- CANNAS, B., CAU, F., FANNI, A., SONATO, P., ZEDDA, M. K. and JET-EFDA CONTRIBUTORS. Automatic disruption classification at JET: comparison of different pattern recognition techniques. *Nuclear Fusion*, vol. 46(7), pages 699–708, 2006.
- CHATTERJEE, S. and HADI, A. S. *Regression Analysis by Example*. Wiley-Interscience, 2006. ISBN 978-0-471-74696-6.
- CHERKASSKY, V. and MULIER, F. *Learning from data: concepts, theory and methods*. John Wiley and Sons, 1998. ISBN 978-0-471-68182-3.
- CIPOLLA, C. M. *The economic history of world population*. Penguin, 1972. ISBN 0-140-20537-3.
- CORTES, C. and VAPNIK, V. Support-Vector Networks. *Machine Learning*, vol. 20, pages 273–297, 1995.

- CRACIUNESCU, T., MURARI, A., TISEANU, I. and LANG, P. Motion estimation within the mpeg video compressed domain for JET plasma diagnostics. *Nuclear Instruments and Methods in Physics Research Section A: Accelerators, Spectrometers, Detectors and Associated Equipment*, vol. 659(1), pages 467–476, 2011.
- DAW, C. S., FINNEY, C. E. A. and TRACY, E. R. A review of symbolic analysis of experimental data. *Review of Scientific Instruments*, vol. 74(2), pages 915–930, 2003.
- DORMIDO-CANTO, S., FARIAS, G., DORMIDO, R., VEGA, J., SÁNCHEZ, J., DURO, N., VARGAS, H., RATTÁ, G., PEREIRA, A. and PORTAS, A. Structural pattern recognition methods based on string comparison for fusion databases. *Fusion Engineering and Design*, vol. 83(2-3), pages 421–424, 2008. Proceedings of the 6th IAEA Technical Meeting on Control, Data Acquisition, and Remote Participation for Fusion Research.
- DORMIDO-CANTO, S., FARIAS, G., DORMIDO, R., VEGA, J., SÁNCHEZ, J., SANTOS, M. and THE TJ-II TEAM. TJ-II wave forms analysis with wavelets and support vector machines. *Review of Scientific Instruments*, vol. 75(10), pages 4254–4257, 2004.
- DORMIDO-CANTO, S., FARIAS, G., VEGA, J., DORMIDO, R., SÁNCHEZ, J., DURO, N., SANTOS, M., MARTIN, J. A. and PAJARES, G. Search and retrieval of plasma wave forms: structural pattern recognition approach. *Review of Scientific Instruments*, vol. 77, page 10F514, 2006.
- DOYLE, E. J., GROEBNER, R. J., BURRELL, K. H., GOHIL, P., LEHECKA, T., N. C. LUHMANN, J., MATSUMOTO, H., OSBORNE, T. H., PEEBLES, W. A. and PHILIPONA, R. Modifications in turbulence and edge electric fields at the L–H transition in the DIII-D tokamak. *Physics of Fluids B: Plasma Physics*, vol. 3(8), pages 2300–2307, 1991.
- DRAPER, N. R. and SMITH, H. *Applied Regression Analysis*. Wiley & Sons, 1998. ISBN 0-471-17082-8.
- DURO, N., DORMIDO, R., VEGA, J., DORMIDO-CANTO, S., FARIAS, G., SÁNCHEZ, J., VARGAS, H., MURARI, A. and JET-EFDA CONTRIBUTORS. Automated recognition system for ELM classification in JET. *Fusion Engineering and Design*, vol. 84(2-6), pages 712–715, 2009. Proceeding of the 25th Symposium on Fusion Technology (SOFT-25).
- EDDINGTON, A. S. *The Internal Constitution of the stars*. Cambridge University Press, 1926. ISBN 978-05-21-33708-3.
- EFDA-JET. EFDA-JET website. 2012. Available at <http://www.efda.org/jet/>.

- EGAN, J. P. *Signal detection theory and ROC analysis*. Series in Cognition and Perception. Academic Press, 1975.
- ERCKMANN, V., WAGNER, F., BALDZUHN, J., BRAKEL, R., BURHENN, R., GASPARINO, U., GRIGULL, P., HARTFUSS, H. J., HOFMANN, J. V., JAENICKE, R., NIEDERMAYER, H., OHLENDORF, W., RUDYJ, A., WELLER, A., BOGDANOV, S. D., BOMBA, B., BORSCHEGOVSKY, A. A., CATTANEI, G., DODHY, A., DORST, D., ELSNER, A., ENDLER, M., GEIST, T., GIANNONE, L., HACKER, H., HEINRICH, O., HERRE, G., HILDEBRANDT, D., HIZNYAK, V. I., IL'IN, V. I., KASPAREK, W., KARGER, F., KICK, M., KUBO, S., KUFTIN, A. N., KURBATOV, V. I., LAZAROS, A., MALYGIN, S. A., MALYGIN, V. I., MCCORMICK, K., MÜLLER, G. A., ORLOV, V. B., PECH, P., ROI, I. N., SARDEI, F., SATTLER, S., SCHNEIDER, F., SCHNEIDER, U., SCHÜLLER, P. G., SILLER, G., STROTH, U., TUTTER, M., UNGER, E., WOLFF, H., WÜRSCHING, E. and ZÖPFEL, S. *H mode of the W 7-AS stellarator*. *Physical Review Letters*, vol. 70(14), pages 2086–2089, 1993.
- ESTRADA, T., ASCASÍBAR, E., HAPPEL, T., HIDALGO, C., BLANCO, E., JIMÉNEZ-GÓMEZ, R., LINIERS, M., LÓPEZ-BRUNA, D., TABARÉS, F. and TAFALLA, D. L-H transition experiments in TJ-II. *Contributions to Plasma Physics*, vol. 50(6-7), pages 501–506, 2010.
- FARIAS, G., DORMIDO, R., SANTOS, M. and DURO, N. Image classifier for the TJ-II Thomson scattering diagnostic: Evaluation with a feed forward neural network. *Lecture Notes in Computer Science*, vol. 3562, pages 362–381, 2005.
- FARIAS, G., DORMIDO-CANTO, S., VEGA, J., SÁNCHEZ, J., DURO, N., DORMIDO, R., OCHANDO, M., SANTOS, M. and PAJARES, G. Searching for patterns in tj-ii time evolution signals. *Fusion Engineering and Design*, vol. 81(15-17), pages 1993–1997, 2006. 5th IAEA Technical Meeting on Control, Data Acquisition, and Remote Participation for Fusion Research.
- FARIAS, G., VEGA, J., GONZÁLEZ, S., PEREIRA, A., LEE, X., SCHISSEL, D. and GOHIL, P. Automatic determination of L/H transition times in DIII-D through a collaborative distributed environment. *Fusion Engineering and Design*, 2012. 8th IAEA Technical Meeting on Control, Data Acquisition and Remote Participation for Fusion Research 2011, San Francisco, California, USA. In press.
- FAWCETT, T. An introduction to ROC analysis. *Pattern Recognition Letters*, vol. 27(8), pages 861–874, 2006.
- FISHER, R. A. The use of multiple measurements in taxonomic problems. *Annals of Human Genetics*, vol. 7(2), pages 179–188, 1936.

- FLACH, P. and WU, S. Repairing concavities in ROC curves. In *Proceedings of the 2003 UK Workshop on Computational Intelligence*, pages 38–44. Springer-Verlag, 2003.
- FRANK, A. and ASUNCION, A. UCI machine learning repository. 2010. Available at <http://archive.ics.uci.edu/ml>.
- LABORATORIO NACIONAL DE FUSION. Laboratorio Nacional de Fusion, diagnostics website. 2011. Available at <http://fusionwiki.ciemat.es/fusionwiki/index.php/TJ-II#Diagnostics>.
- LABORATORIO NACIONAL DE FUSION. Laboratorio Nacional de Fusion website. 2012. Available at [http://www-fusion.ciemat.es/New\\_fusion/en/](http://www-fusion.ciemat.es/New_fusion/en/).
- FUSION FOR ENERGY. *Annual Activity Report 2010*. European Communities, 2011. ISBN 978-92-9214-012-0.
- GAMMERMAN, A., VOCK, V. and VAPNIK, V. Learning by transduction. In *Proceedings of the 14th Conference on Uncertainty in Artificial Intelligence (UAI'98)*, pages 148–155. 1998.
- GAMMERMAN, A. and VOVK, V. Hedging predictions in machine learning. *The Computer Journal*, vol. 50(2), pages 151–163, 2007.
- GAUTHIER, E., ANDREW, P., ARNOUX, G., CORRE, Y. and ROCHE, H. Plasma wall interaction during ELMs in JET. *Journal of Nuclear Materials*, vol. 363–365, pages 1026–1031, 2007. Proceedings of the 17th Plasma-Surface Interactions conference.
- GENERAL ATOMICS. DIII-D website. 2012. Available at <https://fusion.gat.com/global/DIII-D>.
- GIANNONE, L., SIPS, A. C. C., KARDAUN, O., SPREITLER, F., SUTTROP, W. and THE ASDEX UPGRADE TEAM. Regime identification in asdex upgrade. *Plasma Physics and Controlled Fusion*, vol. 46(5), pages 835–856, 2004.
- GONZÁLEZ, S., VEGA, J., MURARI, A., PEREIRA, A., BEURSKENS, M. and JET-EFDA CONTRIBUTORS. Automatic ELM location in JET using a Universal Multi-Event Locator. *Fusion Science and Technology*, vol. 58(3), pages 755–762, 2010a. 6th Fusion Data Validation Workshop 2010, Madrid, Spain.
- GONZÁLEZ, S., VEGA, J., MURARI, A., PEREIRA, A., RAMÍREZ, J. M., DORMIDO-CANTO, S. and JET-EFDA CONTRIBUTORS. Support Vector Machine-based feature extractor for L/H transitions in JET. *Review*

- of Scientific Instruments*, vol. 81(10E123), 2010b. 18th High Temperature Plasma Diagnostics (HTPD) conference 2010, Wildwood, New Jersey, USA.
- GONZÁLEZ, S., VEGA, J., MURARI, A. and JET-EFDA CONTRIBUTORS. Analysis of video-movies using Support Vector Regression. *Fusion Science and Technology*, vol. 58(3), pages 763–770, 2010. 6th Fusion Data Validation Workshop 2010, Madrid, Spain.
- GONZÁLEZ, S., VEGA, J., MURARI, A., PEREIRA, A., DORMIDO-CANTO, S., RAMÍREZ, J. M. and JET-EFDA CONTRIBUTORS. Automatic location of L/H transition times for physical studies with a large statistical basis. *Plasma Physics and Controlled Fusion*, vol. 54(6), page 065009, 2012a.
- GONZÁLEZ, S., VEGA, J., MURARI, A., PEREIRA, A., DORMIDO-CANTO, S., RAMÍREZ, J. M. and JET-EFDA CONTRIBUTORS. H/L transition time estimation in JET using conformal predictors. *Fusion Engineering and Design*, 2012b. 8th IAEA Technical Meeting on Control, Data Acquisition and Remote Participation for Fusion Research 2011, San Francisco, California, USA. In press.
- GONZÁLEZ, S., VEGA, J., MURARI, A., PEREIRA, A. and JET-EFDA CONTRIBUTORS. Automated analysis of edge pedestal gradient degradation during ELMs. *Fusion Science and Technology*, vol. 62(3), pages 403–408, 2012c. 7th Fusion Data Validation Workshop 2012, Frascati, Roma, Italy.
- GONZÁLEZ, S., VEGA, J., PEREIRA, A. and PASTOR, I. Region selection and image classification methodology using a non-conformity measure. *Progress in Artificial Intelligence*, vol. 1(3), pages 215–222, 2012d. International Classification Conference, 2011, St. Andrews, Scotland.
- HAAR, A. Zur theorie der orthogonalen funktionensysteme. *Mathematische Annalen*, vol. 69(3), pages 331–371, 1910.
- HANLEY, J. A. and MCNEIL, B. J. The meaning and use of the area under a receiver operating characteristic (ROC) curve. *Radiology*, vol. 143(1), pages 29–36, 1982.
- HANLEY, J. A. and MCNEIL, B. J. A method of comparing the areas under receiver operating characteristic curves derived from the same cases. *Radiology*, vol. 148(3), pages 839–843, 1983.
- HARRIS, J. H., CANTRELL, J. L., HENDER, T. C., CARRERAS, B. A. and MORRIS, R. N. A flexible heliac configuration. *Nuclear Fusion*, vol. 25(5), pages 623–629, 1985.

- HENDER, T. C., CANTRELL, J. L., HARRIS, J. H., CARRERAS, B. A., LYNCH, V. E., LYON, J. F., FABREGAS, J. A., GUASP, J., LOPEZ-FRAGUAS, A. and NAVARRO, A. P. Studies of a flexible heliac configuration. Technical report, Oak Ridge National Laboratory, ORNL/TM-10374 UC-20, 1987.
- HERRANZ, J., CASTEJÓN, F., PASTOR, I. and MCCARTHY, K. J. The spectrometer of the high-resolution multiposition thomson scattering diagnostic for TJ-II. *Fusion Engineering and Design*, vol. 65(4), pages 525–536, 2003.
- HOCHIN, T., KOYAMA, K., NAKANISHI, H. and KOJIMA, M. Extension of frequency-based dissimilarity for retrieving similar plasma waveforms. *Fusion Engineering and Design*, vol. 83(2-3), pages 417 – 420, 2008. Proceedings of the 6th IAEA Technical Meeting on Control, Data Acquisition, and Remote Participation for Fusion Research.
- HOCHIN, T., YAMAUCHI, Y., NAKANISHI, H., KOJIMA, M. and NOMIYA, H. Indexing of plasma waveforms for accelerating search and retrieval of their subsequences. *Fusion Engineering and Design*, vol. 85(5), pages 649 – 654, 2010.
- HOERL, A. E., KANNARD, R. W. and BALDWIN, K. F. Ridge regression: some simulations. *Communications in Statistics*, vol. 4(2), pages 105–123, 1975.
- HOERL, A. E. and KENNARD, R. W. Ridge regression: applications to nonorthogonal problems. *Technometrics*, vol. 12(1), pages 69–82, 1970a.
- HOERL, A. E. and KENNARD, R. W. Ridge regression: biased estimation for nonorthogonal problems. *Technometrics*, vol. 12(1), pages 55–67, 1970b.
- HOERL, A. E. and KENNARD, R. W. Ridge regression iterative estimation of the biasing parameter. *Communications in Statistics - Theory and Methods*, vol. 5(1), pages 77–88, 1976.
- HONG, S. H., GRISOLIA, C., ROHDE, V., GARBET, P. M., TORE SUPRA TEAM and ASDEX UPGRADE TEAM. Temporal evolution and spatial distribution of dust creation events in tore supra and in ASDEX upgrade studied by CCD image analysis. *Nuclear Fusion*, vol. 50(3), page 035002, 2010.
- HORN, B. K. and SCHUNCK, B. G. Determining optical flow. *Artificial Intelligence*, vol. 17(1-3), pages 185–203, 1981.
- HOTELLING, H. Analysis of a complex of statistical variables into principal components. *Journal of Educational Psychology*, vol. 25, pages 417–441, 1933.

- INTERNATIONAL ENERGY AGENCY. *World Energy Outlook 2011*. Organization for Economic Cooperation & Development, 2010. ISBN 978-92-64-12413-4.
- ITER ORGANIZATION. ITER website. 2012. Available at <http://www.iter.org/>.
- JACKSON, D. A. Stopping rules in principal components analysis: a comparison of heuristical and statistical approaches. *Ecology*, vol. 74(8), pages 2204–2214, 1993.
- JOLLIFFE, I. T. *Principal Component Analysis*. Springer, 2002. ISBN 0-387-95442-2.
- KADOMTSEV, B. B. On disruptive instability in tokamaks. *Soviet Journal of Plasma Physics*, vol. 1, pages 710–715, 1975.
- KAYE, S., BELL, M., BOL, K., BOYD, D., BRAU, K., BUCHENAUER, D., BUDNY, R., CAVALLO, A., COUTURE, P., CROWLEY, T., DARROW, D., EUBANK, H., FONCK, R., GOLDSTON, R., GREK, B., JAEHNIG, K., JOHNSON, D., KAITA, R., KUGEL, H., LEBLANC, B., MANICKAM, J., MANOS, D., MANSFIELD, D., MAZZUCATO, E., MCCANN, R., MCCUNE, D., MCGUIRE, K., MUELLER, D., MURDOCK, A., OKABAYASHI, M., OKANO, K., OWENS, D., POST, D., REUSCH, M., SCHMIDT, G., SESNIC, S., SLUSHER, R., SUCKEWER, S., SURKO, C., TAKAHASHI, H., TENNEY, F., TOWNER, H. and VALLEY, J. Attainment of high confinement in neutral beam heated divertor discharges in the PDX tokamak. *Journal of Nuclear Materials*, vol. 121, pages 115–125, 1984.
- KEILHACKER, M., BECKER, G., BERNHARDI, K., EBERHAGEN, A., ELSHAER, M., FUBMANN, G., GEHRE, O., GERNHARDT, J., v GIERKE, G., GLOCK, E., HAAS, G., KARGER, F., KISSEL, S., KLUBER, O., KORNHERR, K., LACKNER, K., LISITANO, G., LISTER, G. G., MASSIG, J., MAYER, H. M., MCCORMICK, K., MEISEL, D., MESERVEY, E., MULLER, E. R., MURMANN, H., NIEDERMEYER, H., POSCHENRIEDER, W., RAPP, H., RICHTER, B., ROHR, H., RYTER, F., SCHNEIDER, F., SILLER, S., SMEULDERS, P., SOLDNER, F., SPETH, E., STABLER, A., STEINMETZ, K., STEUER, K.-H., SZYMANSKI, Z., VENUS, G., VOLLMER, O. and WAGNER, F. Confinement studies in L and H-type ASDEX discharges. *Plasma Physics and Controlled Fusion*, vol. 26(1A), pages 49–63, 1984.
- KIKUCHI, M. *Frontiers in Fusion Research*. Springer, 2011. ISBN 978-1-84996-410-4.
- DE LA LUNA, E., SANCHEZ, J., TRIBALDOS, V., CONWAY, G., SUTTROP, W., FESSEY, J., PRENTICE, R., GOWERS, C., CHAREAU, J. M. and

- JET-EFDA CONTRIBUTORS. Electron cyclotron emission radiometer upgrade on the joint european torus JET tokamak. *Review of Scientific Instruments*, vol. 75(10), pages 3831–3833, 2004.
- MAISONNIER, D., COOK, I., PIERRE, S., LORENZO, B., EDGAR, B., KARIN, B., LUIGI, D. P., ROBIN, F., LUCIANO, G., STEPHAN, H., CLAUDIO, N., PRACHAI, N., ALDO, P., NEILL, T. and DAVID, W. The European power plant conceptual study. *Fusion Engineering and Design*, vol. 75-79, pages 1173–1179, 2005. Proceedings of the 23rd Symposium of Fusion Technology (SOFT 23).
- MAISONNIER, D., COOK, I., PIERRE, S., LORENZO, B., LUIGI, D. P., LUCIANO, G., PRACHAI, N. and ALDO, P. DEMO and fusion power plant conceptual studies in Europe. *Fusion Engineering and Design*, vol. 81(8-14), pages 1123–1130, 2006. Proceedings of the 7th International Symposium on Fusion Nuclear Technology.
- MAKILI, L., VEGA, J., DORMIDO-CANTO, S., PASTOR, I. and MURARI, A. Computationally efficient SVM multi-class image recognition with confidence measures. *Fusion Engineering and Design*, vol. 86(6-8), pages 1213–1216, 2011. Proceedings of the 26th Symposium of Fusion Technology (SOFT-26).
- MAKILI, L., VEGA, J., DORMIDO-CANTO, S., PASTOR, I., PEREIRA, A., FARIAS, G., PORTAS, A., PÉREZ-RISCO, D., RODRÍGUEZ-FERNÁNDEZ, M. C. and BUSCH, P. Upgrade of the automatic analysis system in the TJ-II Thomson scattering diagnostic: New image recognition classifier and fault condition detection. *Fusion Engineering and Design*, vol. 85(3-4), pages 415–418, 2010. Proceedings of the 7th IAEA Technical Meeting on Control, Data Acquisition, and Remote Participation for Fusion Research.
- MALLAT, S. G. A theory for multiresolution signal decomposition: the wavelet representation. *IEEE Transactions on Pattern Analysis and Machine Intelligence*, vol. 11(7), pages 674–693, 1989.
- MALLAT, S. G. *A wavelet tour of signal processing*. Academic Press, 1999. ISBN 0-12-466606-X.
- MALTHUS, R. T. *An essay on the principle of population*. 1798.
- MARTIN, V., DUNAND, G., MONCADA, V., JOUVE, M. and TRAVERE, J. M. New field programmable gate array-based image-oriented acquisition and real-time processing applied to plasma facing component thermal monitoring. *Review of Scientific Instruments*, vol. 81(10), page 10E113, 2010.

- MARTIN, Y. and BÜHLMANN, F. Statistical analysis of the ohmic H-mode accessibility in TCV. *Plasma Physics and Controlled Fusion*, vol. 40(5), page 697, 1998.
- MARTIN, Y. R., TAKIZUKA, T. and THE ITPA CDBM H-MODE THRESHOLD DATABASE WORKING GROUP. Power requirement for accessing the H-mode in ITER. *Journal of Physics: Conference Series*, vol. 123(1), page 012033, 2008.
- MARTINEZ, W. L. and MARTINEZ, A. R. *Computational Statistics Handbook with Matlab*. Chapman & Hall/CRC, 2008. ISBN 978-1-58488-566-5.
- MCCRACKEN, G. M. and STOTT, P. *Fusion: the energy of the universe*. Elsevier, 2005. ISBN 0-12-481851-X.
- MEAKINS, A. J., McDONALD, D. C. and EFDA-JET CONTRIBUTORS. The application of classification methods in a data driven investigation of the JET L-H transition. *Plasma Physics and Controlled Fusion*, vol. 52(7), page 075005, 2010.
- MINH, H., NIYOGI, P. and YAO, Y. Mercer's theorem, feature maps, and smoothing. In *Learning Theory*, vol. 4005 of *Lecture Notes in Computer Science*, pages 154–168. Springer, 2006.
- MURARI, A., VAGLIASINDI, G., ARENA, P., FORTUNA, L., BARANA, O., JOHNSON, M. and JET-EFDA CONTRIBUTORS. Prototype of an adaptive disruption predictor for jet based on fuzzy logic and regression trees. *Nuclear Fusion*, vol. 48(3), page 035010, 2008.
- MURARI, A., VAGLIASINDI, G., ZEDDA, M. K., FELTON, R., SAMMON, C., FORTUNA, L., ARENA, P. and JET-EFDA CONTRIBUTORS. Fuzzy logic and support vector machine approaches to regime identification in JET. *IEEE Transactions on Plasma Science*, vol. 34(3), pages 1013–1020, 2006.
- MURARI, A., VEGA, J., MAZON, D., DELMOND, J., GELFUSA, M., SZAPANOS, A. and JET-EFDA CONTRIBUTORS. Image manipulation for high temperature plasmas. *Contributions to Plasma Physics*, vol. 51(2-3), pages 187–193, 2011.
- NAKANISHI, H., HOCHIN, T. and KOJIMA, M. Search and retrieval method of similar plasma waveforms. *Fusion Engineering and Design*, vol. 71(1-4), pages 189–193, 2004. 4th IAEA Technical Meeting on Control, Data Acquisition, and Remote Participation for Fusion Research.
- NAKANISHI, H., HOCHIN, T. and KOJIMA, M. Similar pattern search for time-sectional oscillation in huge plasma waveform database. *Fusion Engineering and Design*, vol. 81(15-17), pages 2003–2007, 2006. 5th IAEA

- Technical Meeting on Control, Data Acquisition, and Remote Participation for Fusion Research.
- PEARSON, K. On lines and planes of closest fit to systems of points in space. *Philosophical Magazine*, vol. 6, pages 559–572, 1901.
- PEREIRA, A., VEGA, J., CASTRO, R. and PORTAS, A. Distributed open environment for data retrieval based on pattern recognition techniques. *Fusion Engineering and Design*, vol. 85(3-4), pages 595–597, 2010. Proceedings of the 7th IAEA Technical Meeting on Control, Data Acquisition, and Remote Participation for Fusion Research.
- PEREIRA, A., VEGA, J., PORTAS, A., CASTRO, R., MURARI, A. and JET-EFDA CONTRIBUTORS. Optimized search strategies to improve structural pattern recognition techniques. In *Proceedings of the 8th FLINS conference on computational intelligence in decision and control*. 2008.
- PERES-NETO, P. R., JACKSON, D. A. and SOMERS, K. M. How many principal components? Stopping rules for determining the number of non-trivial axes revisited. *Computational Statistics & Data Analysis*, vol. 49, pages 974–997, 2005.
- PROVOST, F. and FAWCETT, T. Analysis and visualization of classifier performance: Comparison under imprecise class and cost distributions. In *Proceedings of the Third International Conference on Knowledge Discovery and Data Mining*, pages 43–48. AAAI Press, 1997.
- PROVOST, F. and FAWCETT, T. Robust classification for imprecise environments. *Machine Learning*, vol. 42, pages 203–231, 2001.
- RAMÍREZ, J., DORMIDO-CANTO, S. and VEGA, J. Parallelization of automatic classification systems based on support vector machines: Comparison and application to JET database. *Fusion Engineering and Design*, vol. 85(3-4), pages 425–427, 2010. Proceedings of the 7th IAEA Technical Meeting on Control, Data Acquisition, and Remote Participation for Fusion Research.
- RATTÁ, G., VEGA, J., PEREIRA, A., PORTAS, A., DE LA LUNA, E., DORMIDO-CANTO, S., FARIAS, G., DORMIDO, R., SÁNCHEZ, J., DURO, N., VARGAS, H., SANTOS, M., PAJARES, G. and MURARI, A. First applications of structural pattern recognition methods to the investigation of specific physical phenomena at JET. *Fusion Engineering and Design*, vol. 83(2-3), pages 467–470, 2008. Proceedings of the 6th IAEA Technical Meeting on Control, Data Acquisition, and Remote Participation for Fusion Research.

- RATTÁ, G. A. *Técnicas de minería de datos aplicadas a fusión nuclear: predicción en tiempo real y clasificación*. Phd, Universidad Nacional de Educación a Distancia (UNED), Madrid, Spain, 2010. In Spanish.
- RATTÁ, G. A., VEGA, J. and MURARI, A. Improved feature selection based on genetic algorithms for real time disruption prediction on jet. *Fusion Engineering and Design*, 2012. In press.
- RATTA, G. A., VEGA, J., MURARI, A., VAGLIASINDI, G., JOHNSON, M. F., DE VRIES, P. C. and JET-EFDA CONTRIBUTORS. An advanced disruption predictor for JET tested in a simulated real-time environment. *Nuclear Fusion*, vol. 50(2), page 025005, 2010.
- REBUT, P. H. and JET DESIGN TEAM. The JET project - design proposal. Technical report, Commission of the European Communities EUR-5516e (EUR-JET-R5), 1976.
- ROQUEMORE, A., NISHINO, N., SKINNER, C., BUSH, C., KAITA, R., MAQUEDA, R., DAVIS, W., PIGAROV, A. and KRASHENINNIKOV, S. 3D measurements of mobile dust particle trajectories in NSTX. *Journal of Nuclear Materials*, vol. 363–365, pages 222–226, 2007. Proceedings of the 17th Plasma-Surface Interactions conference.
- RUIZ, M., VEGA, J., BARRERA, E., GONZÁLEZ, J., MURARI, A., MELÉNDEZ, R., RATTA, G. and GONZÁLEZ, S. Test-bed of a real time detection system for L/H and H/L transitions implemented with the ITMS platform. *Fusion Engineering and Design*, vol. 85(3–4), pages 360–366, 2010. 7th IAEA Technical Meeting on Control, Data Acquisition, and Remote Participation for Fusion Research 2010, Aix-en-Provence, France.
- SAITO, N. and COIFMAN, R. R. Local discriminant bases and their applications. *Journal of Mathematical Imaging and Vision*, vol. 5(4), pages 337–358, 1995.
- SAUNDERS, C., GAMMERMAN, A. and VOVK, V. Transduction with confidence and credibility. In *Sixteenth International Joint Conference on Artificial Intelligence (IJCAI '99)*, vol. 2, pages 722–726. 1999.
- SAVTCHKOV, A. *Mitigation of disruptions in a tokamak by means of large gas injection*. Inaugural dissertation, Heinrich-Heine Universität, Düsseldorf, Germany, 2003.
- SCHÖLKOPT, B. and SMOLA, A. J. *Learning with kernels: Support Vector Machines, Regularization, Optimization, and Beyond*. MIT Press, 2002. ISBN 0-262-19475-9.

- SCHNEIDER, T., LEPICARD, S., SÁEZ, R. M., CABAL, H., LECHÓN, Y., WARD, D., HAMACHER, T., AQUILONIUS, K., HALLBERG, B. and KORHONEN, R. Evaluation of radiological and economic consequences associated with an accident in a fusion power plant. *Fusion Engineering and Design*, vol. 58-59, pages 1077–1080, 2001. ISSN 0920-3796.
- SCHULLER, F. C. Disruptions in tokamaks. *Plasma Physics and Controlled Fusion*, vol. 37(11A), page A135, 1995.
- SHAFFER, G. and VOVK, V. A tutorial on conformal prediction. *Journal of Machine Learning Research*, vol. 9, pages 371–421, 2008.
- SMOLA, A. J. and SCHÖLKOPF, B. A tutorial on support vector regression. *Statistics and Computing*, vol. 14(3), pages 199–222, 2004.
- SÁNCHEZ, J., ACEDO, M., ALONSO, A., ALONSO, J., ALVAREZ, P., ASCASÍBAR, E., BACIERO, A., BALBÍN, R., BARRERA, L., BLANCO, E., BOTIJA, J., DE BUSTOS, A., DE LA CAL, E., CALVO, I., CAPPÀ, A., CARMONA, J., CARRALERO, D., CARRASCO, R., CARRERAS, B., CASTEJÓN, F., CASTRO, R., CATALÁN, G., CHMYGA, A., CHAMORRO, M., ELISEEV, L., ESTEBAN, L., ESTRADA, T., FERNÁNDEZ, A., FERNÁNDEZ-GAVILÁN, R., FERREIRA, J., FONTDECABA, J., FUENTES, C., GARCÍA, L., GARCÍA-CORTÉS, I., GARCÍA-GÓMEZ, R., GARCÍA-REGAÑA, J., GUASP, J., GUIMARAIS, L., HAPPEL, T., HERNANZ, J., HERRANZ, J., HIDALGO, C., JIMÉNEZ, J., JIMÉNEZ-DENCHE, A., JIMÉNEZ-GÓMEZ, R., JIMÉNEZ-REY, D., KIRPITCHEV, I., KOMAROV, A., KOZACHOK, A., KRUPNIK, L., LAPAYESE, F., LINIERS, M., LÓPEZ-BRUNA, D., LÓPEZ-FRAGUAS, A., LÓPEZ-RÁZOLA, J., LÓPEZ-SÁNCHEZ, A., LYSSENKO, S., MARCON, G., MARTÍN, F., MAURIN, V., MCCARTHY, K., MEDINA, F., MEDRANO, M., MELNIKOV, A., MÉNDEZ, P., VAN MILLIGEN, B., MIRONES, E., NEDZELSKIY, I., OCHANDO, M., OLIVARES, J., DE PABLOS, J., PACIOS, L., PASTOR, I., PEDROSA, M., DE LA PEÑA, A., PEREIRA, A., PÉREZ, G., PÉREZ-RISCO, D., PETROV, A., PETROV, S., PORTAS, A., PRETTY, D., RAPISARDA, D., RATTÀ, G., REYNOLDS, J., RINCÓN, E., RÍOS, L., RODRÍGUEZ, C., ROMERO, J., ROS, A., SALAS, A., SÁNCHEZ, M., SÁNCHEZ, E., SÁNCHEZ-SARABIA, E., SARKSIAN, K., SEBASTIÁN, J., SILVA, C., SCHCHEPETOV, S., SKVORTSOVA, N., SOLANO, E., SOLETO, A., TABARÉS, F., TAFALLA, D., TARANCÓN, A., TASCHEV, Y., TERA, J., TOLKACHEV, A., TRIBALDOS, V., VARGAS, V., VEGA, J., VELASCO, G., VELASCO, J., WEBER, M., WOLFERS, G. and ZURRO, B. Confinement transitions in TJ-II under Li-coated wall conditions. *Nuclear Fusion*, vol. 49(10), page 104018, 2009.

- SOLER, M. and CALLEN, J. On measuring the electron heat diffusion coefficient in a tokamak from sawtooth oscillation observations. *Nuclear Fusion*, vol. 19(6), page 703, 1979.
- SPACKMAN, K. A. Signal detection theory: valuable tools for evaluating inductive learning. In *Proceedings of the sixth international workshop on Machine learning*, pages 160–163. Morgan Kaufmann Publishers Inc., 1989.
- SPITZER, L. *A Proposed Stellarator*. Princeton University Plasma Physics Laboratory, U.S. Atomic Energy Commission, 1951.
- STAMBAUGH, R. D. Review of ITER physics issues and possible approaches to their solution. In *Proceedings of the 21st IAEA Fusion Energy Conference*. China, 2006.
- TANGA, A., BEHRINGER, K., COSTLEY, A., BRUSATI, M., DENNE, B., EDWARDS, A., GIBSON, A., GILL, R., GOTTARDI, N., GRANETZ, R., HARBOUR, P., J'CKEL, H., KEILHACKER, M., LAZZARO, E., MALACARNE, M., MORGAN, P., NOLL, P., O'ROURKE, J., STOTT, P., SUMMERS, D., TAGLE, J. and THOMAS, P. Magnetic separatrix experiments in JET. *Nuclear Fusion*, vol. 27(11), pages 1877–1895, 1987.
- TENENBAUM, J. B., DE SILVA, V. and LANGFORD, J. C. A global geometric framework for nonlinear dimensionality reduction. *Science*, vol. 290(5500), pages 2319–2323, 2000.
- THEODORIDIS, S. and KOUTROUMBAS, K. *Pattern Recognition*. Academic Press, 2009. ISBN 978-1-59749-272-0.
- THOMSON, G. P. and BLACKMAN, M. Improvements in or relating to gas discharge apparatus for producing thermonuclear reactions. *British patent 817681*, 1946.
- THONEMANN, P. C. and COWHIG, W. T. The role of the self magnetic field in high current gas discharges. *Proceedings of the Physical Society. Section B*, vol. 64(7), pages 345–354, 1951.
- TONKS, L. and LANGMUIR, I. Oscillations in ionized gases. *Physical Review*, vol. 33(2), pages 195–210, 1929.
- UNITED NATIONS. *The World at Six Billions*. Population division of the department of economic and social affairs of the united nations secretariat, 1999. Available at <http://www.un.org/esa/population/publications/sixbillion/sixbillion.htm>.
- UNITED NATIONS. *World Population Prospects: the 2010 revision*. Population division of the department of economic and social affairs of the united nations secretariat, 2010. Available at <http://esa.un.org/unpd/wup/index.htm>.

- VAGLIASINDI, G., ARENA, P., FORTUNA, L., MURARI, A. and JET-EFDA CONTRIBUTORS. Comparison between CART and fuzzy logic for confinement regime classification at JET. In *Proceedings of the 8th FLINS conference*, pages 429–434. Computational Intelligence in Decision and Control, 2008.
- VAPNIK, V. *The Nature of Statistical Learning Theory*. Springer, 2000. ISBN 0-387-98780-0.
- VAPNIK, V. *Estimation of Dependences Based on Empirical Data*. Springer, 2006. ISBN 978-0387-30865-4.
- VEGA, J. and JET-EFDA CONTRIBUTORS. Intelligent methods for data retrieval in fusion databases. *Fusion Engineering and Design*, vol. 83(2-3), pages 382–386, 2008. Proceedings of the 6th IAEA Technical Meeting on Control, Data Acquisition, and Remote Participation for Fusion Research.
- VEGA, J., MURARI, A., GONZÁLEZ, S. and JET-EFDA CONTRIBUTORS. A universal support vector machines based method for automatic event location in waveforms and video-movies: applications to massive nuclear fusion databases. *Review of Scientific Instruments*, vol. 81(2), page 023505, 2010a.
- VEGA, J., MURARI, A., GONZÁLEZ, S., PEREIRA, A. and PASTOR, I. Overview of statistically hedged prediction methods: from off-line to real-time data analysis. *Fusion Engineering and Design*, 2012. 8th IAEA Technical Meeting on Control, Data Acquisition and Remote Participation for Fusion Research 2011, San Francisco, California, USA. In press.
- VEGA, J., MURARI, A., PEREIRA, A., GONZÁLEZ, S. and PASTOR, I. Accurate and reliable image classification by using conformal predictors in the TJ-II thomson scattering. *Review of Scientific Instruments*, vol. 81(10), page 10E118, 2010b. 18th High Temperature Plasma Diagnostics (HTPD) conference 2010, Wildwood, New Jersey, USA.
- VEGA, J., MURARI, A., PEREIRA, A., PORTAS, A., RATTÁ, G., CASTRO, R. and JET-EFDA CONTRIBUTORS. Overview of intelligent data retrieval methods for waveforms and images in massive fusion databases. *Fusion Engineering and Design*, vol. 84(7-11), pages 1916–1919, 2009a. Proceeding of the 25th Symposium on Fusion Technology (SOFT-25).
- VEGA, J., MURARI, A., RATTÁ, G., GONZÁLEZ, S. and DORMIDO-CANTO, S. Progress on statistical learning systems as data mining tools for the creation of automatic databases in fusion environments. *Fusion Engineering and Design*, vol. 85(3–4), pages 399–402, 2010c. 7th IAEA Technical Meeting on Control, Data Acquisition, and Remote Participation for Fusion Research 2010, Aix-en-Provence, France.

- VEGA, J., MURARI, A., VAGLIASINDI, G., RATTÁ, G. and JET-EFDA CONTRIBUTORS. Automated estimation of L/H transition times at JET by combining bayesian statistics and support vector machines. *Nuclear Fusion*, vol. 49(8), 2009b.
- VEGA, J., PASTOR, I., CERECEDA, J. L., PEREIRA, A., HERRANZ, J., PÉREZ, D., RODRÍGUEZ, M. C., FARIAS, G., DORMIDO-CANTO, S., SÁNCHEZ, J., DORMIDO, R., DURO, N., , DORMIDO, S., PAJARES, G., SANTOS, M. and DE LA CRUZ, J. M. Application of intelligent classification techniques to the TJ-II Thomson scattering diagnostic. In *Proceedings of the 32nd EPS conference on Plasma Physics (ECA), Tarragona, Spain*, vol. 29C, pages 2090–2094. 2005.
- VEGA, J., PEREIRA, A., PORTAS, A., DORMIDO-CANTO, S., FARIAS, G., DORMIDO, R., SÁNCHEZ, J., DURO, N., SANTOS, M., SÁNCHEZ, E. and PAJARES, G. Data mining technique for fast retrieval of similar waveforms in fusion massive databases. *Fusion Engineering and Design*, vol. 83(1), pages 132–139, 2008.
- VEGA, J., RATTÁ, G., MURARI, A., CASTRO, P., DORMIDO-CANTO, S., DORMIDO, R., FARIAS, G., PEREIRA, A., PORTAS, A., DE LA LUNA, E., PASTOR, I., SÁNCHEZ, J., DURO, N., CASTRO, R., SANTOS, M. and VARGAS, H. Recent results on structural pattern recognition for fusion massive databases. In *Proceedings of the IEEE International Symposium on intelligent signal processing (WISP)*. 2007.
- VOVK, V., GAMMERMAN, A. and SHAFER, G. *Algorithmic Learning in a Random World*. Springer, 2005. ISBN 978-0387-00152-4.
- DE VRIES, B. J. M., VAN VUUREN, D. P. and HOOGWIJK, M. M. Renewable energy sources: Their global potential for the first-half of the 21st century at a global level: An integrated approach. *Energy Policy*, vol. 35(4), pages 2590–2610, 2007.
- WAGNER, F. A quarter-century of H-mode studies. *Plasma Physics and Controlled Fusion*, vol. 49(12B), pages B1–B33, 2007.
- WAGNER, F., BECKER, G., BEHRINGER, K., CAMPBELL, D., EBERHAGEN, A., ENGELHARDT, W., FUSSMANN, G., GEHRE, O., GERNHARDT, J., GIERKE, G. v., HAAS, G., HUANG, M., KARGER, F., KEILHACKER, M., KLÜBER, O., KORNHERR, M., LACKNER, K., LISITANO, G., LISTER, G. G., MAYER, H. M., MEISEL, D., MÜLLER, E. R., MURMANN, H., NIEDERMEYER, H., POSCHENRIEDER, W., RAPP, H., RÖHR, H., SCHNEIDER, F., SILLER, G., SPETH, E., STÄBLER, A., STEUER, K. H., VENUS, G., VOLLMER, O. and YÜ, Z. Regime of improved confinement and high beta in neutral-beam-heated divertor discharges of the ASDEX tokamak. *Physical Review Letters*, vol. 49(19), pages 1408–1412, 1982.

- WAGNER, F., FUSSMANN, G., GRAVE, T., KEILHACKER, M., KORNHERR, M., LACKNER, K., MCCORMICK, K., MÜLLER, E. R., STÄBLER, A., BECKER, G., BERNHARDI, K., DITTE, U., EBERHAGEN, A., GEHRE, O., GERNHARDT, J., GIERKE, G. V., GLOCK, E., GRUBER, O., HAAS, G., HESSE, M., JANESCHITZ, G., KARGER, F., KISSEL, S., KLÜBER, O., LISITANO, G., MAYER, H. M., MEISEL, D., MERTENS, V., MURMANN, H., POSCHENRIEDER, W., RAPP, H., RÖHR, H., RYTER, F., SCHNEIDER, F., SILLER, G., SMEULDERS, P., SÖLDNER, F., SPETH, E., STEUER, K. H., SZYMANSKI, Z. and VOLLMER, O. Development of an edge transport barrier at the H-Mode transition of ASDEX. *Physical Review Letters*, vol. 53(15), pages 1453–1456, 1984.
- WARD, D. J. The physics of DEMO. *Plasma Physics and Controlled Fusion*, vol. 52(12), page 124033, 2010.
- WARD, D. J., TAYLOR, N. P. and COOK, I. Economically acceptable fusion power stations with safety and environmental advantages. *Fusion Engineering and Design*, vol. 58-59, pages 1033–1036, 2001.
- WESSON, J. *Tokamaks*. Oxford University Press, 1987. ISBN 0-198-50922-7.
- WESSON, J. *The science of JET*. JET Publications Office, 2000.
- WESSON, J. A. Sawtooth oscillations. *Plasma Physics and Controlled Fusion*, vol. 28(1A), pages 243–248, 1986.
- WESTON, J., ELISSEEFF, A., BAKIR, G. and SINZ, F. The Spider. 2011. Available at <http://people.kyb.tuebingen.mpg.de/spider/main.html>.
- WESTON, J. and WATKINS, C. Support vector machines for multi-class pattern recognition. In *Proceedings of the 7th European Symposium on Artificial Neural Networks (ESANN), Bruges, Belgium*. 1999. ISBN 2-600049-9-X.
- WORLD ENERGY COUNCIL. *Deciding the Future: Energy Policy Scenarios to 2050*. 2007. ISBN 0-946121-29-X.
- WORLD ENERGY COUNCIL. *2010 Survey of Energy Resources*. 2010. ISBN 978-0-946121-021.
- YEH, I.-C. Modeling of strength of high-performance concrete using artificial neural networks. *Cement and Concrete Research*, vol. 28(12), pages 1797–1808, 1998.
- ZOHM, H. Edge localized modes (ELMs). *Plasma Physics and Controlled Fusion*, vol. 38(2), pages 105–128, 1996a.

- ZOHM, H. The physics of edge localized modes (ELMs) and their role in power and particle exhaust. *Plasma Physics and Controlled Fusion*, vol. 38(8), pages 1213–1223, 1996b.



